Linking Disrupted Cellular Ultrastructure to Human Atrial Myocyte Calcium and Voltage Instabilities: A Modeling Study

By

XIANWEI ZHANG
DISSERTATION

Submitted in partial satisfaction of the requirements for the degree of

DOCTOR OF PHILOSOPHY

in

Biophysics

in the

OFFICE OF GRADUATE STUDIES

of the

UNIVERSITY OF CALIFORNIA

DAVIS

Approved:

Eleonora Grandi, Chair

Daisuke Sato

Stefano Morotti

Committee in Charge

2022

Acknowledgement

First and foremost, I would like to thank my supervisor, Dr. Eleonora Grandi for her guidance, inspiration, and continued academic and personal support. Ele not only supported me in my Ph.D. project, but also taught me how to be an independent researcher. This dissertation work would not have been possible without her patient mentorship and wonderful leadership.

I would like to thank my research mentors Dr. Andrew Edwards, Dr. Stefano Morotti, and Dr. Daisuke Sato for all their backing and mentoring. I wish to express sincere appreciation to Dr. Haibo Ni, for his guidance, mentorship, support, and advice in all the aspects and stages of my Ph.D. research career.

I would like to express my gratitude for the amazing past and present lab members, who have made my PhD experience so enjoyable. Thanks to Stefano, Haibo, Yixuan, Charlotte, Kim, Nate, Andy and Alex. Also, many thanks to my graduate group cohorts, Gonzalo and John. I couldn't have done it without you. Thank you for coffee breaks, lunchtime, soccer/basketball/hiking/gym, retreat, Friday drink/dinner, conferences, and of course for all your help in the lab and assistance in debugging science and coding!

I appreciate my family and friends for their endless kindness, understanding and trust, with special thanks to my parents and Dingying for their endless encouragement and love, which provided me with enormous motivation and strength throughout my doctoral study.

I would express my sincere gratitude to all people who have helped me over these past five years. Finally, I am grateful to the American Heart Association for funding my research.

Abstract

Intracellular Ca^{2+} is an important regulator in cardiac electrophysiology and contraction under both physiology and pathophysiology. The regular excitation and effective contraction in healthy atrial myocytes are achieved by the well-organized transversal and axial tubular system (TATS, i.e., invaginations of cell membrane) that facilitate the coupling of key Ca^{2+}-handling proteins, such as L-type Ca^{2+} channel (LCC) and Na^{+}-Ca^{2+} exchanger (NCX) on the cell surface with ryanodine receptors (RyRs) on the sarcoplasmic reticulum (SR, intracellular Ca^{2+} storage). In atrial fibrillation (AF), the most common arrhythmia disease in the clinic, both ionic and ultrastructural remodeling have been associated with deranged Ca^{2+} signaling and electrophysiological instabilities through the altered channel and transporter expression and function, reduced density and regularity of the TATS, and subcellular re-distribution of Ca^{2+}-handling proteins. However, due to the concurrent changes in TATS and Ca^{2+}-handling protein expression and localization that occur in the disease, it is difficult to distinguish their individual contributions to the arrhythmogenic state.

To address this, we developed a novel 3D human atrial myocyte model that couples electrophysiology and Ca^{2+} handling with variable TATS organization and density. We illustrate the construction of the model, which was extensively parameterized and validated against experimental data, and its use in examining TATS regulation of subcellular Ca^{2+} release. We then demonstrate the application of the model to investigate the isolated and interactive effects of changes in expression and localization of key Ca^{2+}-handling proteins (i.e., NCX, RyR, and Calsequestrin, CSQ) and variable TATS density on Ca^{2+} abnormalities and Ca^{2+}-driven membrane instabilities.

We found that TATS loss, as seen in the disease, impairs NCX-mediated Ca^{2+} removal that increases intracellular Ca^{2+} concentration and thus elevated RyR open probability (P_O). Consequentially, these changes increase arrhythmogenic spontaneous Ca^{2+} releases (SCRs),

especially in the inner area of the cell, and subsequent voltage instabilities (i.e., delayed afterdepolarizations, DADs). Furthermore, varying the expression and distribution of NCX, RyR, and CSQ have pro- or anti-arrhythmic effects depending on the balance of opposing influences on SR Ca^{2+} leak-load and Ca^{2+}-voltage relationships. Interestingly, the effects of Ca^{2+}-handling protein changes have the most impact in cells with intermediate tubules compared to detubulated and densely tubulated myocytes.

In summary, this study demonstrates a mechanistic link between TATS remodeling and Ca^{2+}-driven proarrhythmic behavior that likely reflects AF arrhythmogenesis. We provide novel insight into the distinct and interactive consequences of TATS and Ca^{2+}-handling protein remodeling that underlie Ca^{2+} dysfunction and abnormal electrophysiology in disease. These novel model-based findings may help guide future therapeutic anti-AF strategies targeting structural remodeling.

Table of Contents

Figure List

Table List

Chapter 1 Introduction

1.1 Background and significance

Intracellular calcium (Ca^{2+}) is a key determinant of cardiac myocyte contractile and electrophysiologic function through the process of excitation-contraction coupling (ECC), which links cell membrane depolarization (excitation) to muscle cell contraction via a rapid increase in intracellular Ca^{2+} concentration. In cardiomyocytes, membrane depolarization during an action potential (AP) activates voltage-dependent L-type Ca^{2+} channels (LCCs), allowing for Ca^{2+} entry into the cell. This Ca^{2+} influx activates Ca^{2+} release from ryanodine receptor type-2 channels (RyRs) in the membrane of the sarcoplasmic reticulum (SR) in a process termed Ca^{2+}-induced Ca^{2+} release (CICR). RyR activation and release across each myocyte provides enough cytosolic Ca^{2+} to trigger contraction upon binding to troponin C (Bers, 2002). This Ca^{2+} influences not only cell contraction but also a number of other cell functions and modulates several Ca^{2+}-dependent transmembrane ion fluxes, which in turn impact membrane potential stability. Indeed, Ca^{2+} dysregulation is known to be the primary driver of derangements in the heart rhythm in specific inherited arrhythmia syndromes targeting the Ca^{2+} handling machinery (e.g., catecholaminergic polymorphic ventricular tachycardia) or drug responses (e.g., digoxin toxicity) (Denham *et al.*, 2018). Furthermore, altered Ca^{2+} signaling contributes to more common arrhythmogenic conditions with broader pathophysiological changes, such as atrial fibrillation (AF) and heart failure (HF) (Denham *et al.*, 2018). It has long been known that disease-induced remodeling in the expression, function, and regulation of proteins involved in ECC can lead to abnormal Ca^{2+} signals. Additionally,

remodeling in cardiomyocyte ultrastructure contributes to the observed alterations by disrupting the localization of these proteins and thus affecting local Ca^{2+} signals. Transverse tubules (TTs) are invaginations of the sarcolemma that play a key role in ECC in ventricular myocytes. These structures closely (<20 nm) juxtapose sarcolemmal ion channels with intracellular RyR clusters embedded in the SR membrane to facilitate rapid and synchronous activation of CICR upon cell membrane depolarization. While TTs are abundant in the ventricle, they are generally sparser and more irregularly distributed in atrial myocytes, where they are often found as axial tubules (ATs). ATs provide extensive longitudinal sarcolemmal invaginations that also serve to couple RyRs with membrane ion channels. ATs and TTs are one of the most clearly remodeled structures in HF and AF, the most common cardiac arrhythmia (Chugh *et al.*, 2014).

AF is a major public health challenge globally (Kim *et al.*, 2011), and recent estimates indicate that AF will affect 6-12 million people in the USA by 2050 and 17.9 million in Europe by 2060 (Miyasaka *et al.*, 2006; Krijthe *et al.*, 2013; Chugh *et al.*, 2014). AF is a major risk factor for ischemic stroke and causes important economic burden, along with increased morbidity (Andersson *et al.*, 2013) and mortality (Wattigney *et al.*, 2002), especially when it coexists with other diseases (Freedman *et al.*, 2016). Anti-AF pharmacological therapy is plagued by lack of efficacy and harmful side effects (Burashnikov & Antzelevitch, 2010; Rosa *et al.*, 2015; Dan & Dobrev, 2018; Verrier & Belardinelli, 2020). Catheter ablation is also characterized by complications and relative effectiveness in preventing AF recurrent (Schwarz *et al.*, 2010; Packer *et al.*, 2019). This unsatisfying situation is partly due to our poor mechanistic understanding of the triggers and substrates involved in AF, which leads to lack of effective and safe therapeutic strategies and pharmacological targets.

It is conceivable that the AF-associated remodeling of both ATs and TTs (i.e., de-tubulation, tubular disorganization) combines with changes in distribution, composition, and

phosphorylation status of Ca^{2+} handling proteins to promote Ca^{2+} abnormalities. However, the quantitative importance of atrial tubular system remodeling and heterogeneous Ca^{2+} release to AF arrhythmogenesis has not yet been established. In part, this is due to the sparsity of human data and suitable animal models of AF. Further, because structural remodeling and ionic remodeling happen simultaneously in disease, they cannot easily be separated in experiments. Computational and theoretical approaches can both fill gaps in the available human data sources and help to discriminate the contribution of structural changes versus ionic remodeling in disease. Many models of human atrial electrophysiology and AF do not possess subcellular spatial details. While these "common-pool" models (e.g., (Grandi *et al.*, 2011)) are used extensively to investigate the effects of remodeling in disease, they do not possess sufficient subcellular spatial details to study the role of subcellular structural remodeling in determining local intracellular Ca^{2+} heterogeneities and abnormalities.

1.2 Aims and outline of the dissertation

In this dissertation, we built a rigorously developed and validated a novel model of intracellular Ca^{2+} signaling, governed by the AT and TT system, to replicate and explain the measured relationship between tubular structure and Ca^{2+} signaling in human atrial myocytes. We coupled this model with our well-established model of human atrial myocyte electrophysiology to examine the relationship between tubular structure, human atrial electrophysiology, and arrhythmia.

The aims are as follows:

Aim 1. To develop a novel human atrial myocyte Ca^{2+} handling model replicating the experimental atrial tubular structure and validated against human-specific functional data collected from myocytes and tissue.

Aim 2. To investigate how atrial tubular structure influences local and global Ca^{2+} signaling and atrial electrophysiology in response to arrhythmogenic rapid pacing.

Aim 3. To investigate how atrial ionic remodeling conspires with cellular structural remodeling (as in AF) to contribute to heterogeneous Ca^{2+} release leading to rhythm disturbances in AF.

In this study, we developed and applied a new mathematical model to reveal the mechanistic link between transverse-axial tubule system (TATS) and Ca^{2+}-handling protein remodeling and Ca^{2+}-driven arrhythmia that are associated with AF pathology. Our novel model-based quantitative findings may help guide future therapeutic anti-AF strategies targeting structural remodeling, with the goal to prevent AF reoccurrence in patients and to release the burden of AF on public health.

Chapter 1 introduces the fundamental background in cardiac physiology and computational modeling. We review heart anatomy and function, myocyte structure and electrophysiology, mechanisms of cardiac arrhythmias, and multi-scale mathematical modeling of Ca^{2+} handling and electrophysiology.

Chapter 2 addresses Aims 1 and 2. This chapter illustrates how we built, parameterized, and validated a 3D human atrial myocyte model coupling electrophysiology and spatially detailed subcellular Ca^{2+} handling governed by TATS (**Fig. 1.1**). In our simulations, TATS is shown to modulate Ca^{2+} handling and ECC in atrial myocytes, with disease-associated TATS remodeling causing altered Ca^{2+} cycling and subsequent arrhythmogenesis. Simulated TATS loss causes diastolic Ca^{2+} and voltage instabilities through reduced Ca^{2+} removal via Na^{+}-Ca^{2+} exchanger (NCX), local Ca^{2+} accumulation consequent increased RyR release, thus resulting in spontaneous Ca^{2+} release and promotion of arrhythmogenic waves and delayed afterdepolarizations. At fast electrical rates typical of atrial tachycardia/fibrillation, spontaneous Ca^{2+} releases are larger and more frequent in the cell interior, devoid of TATS,

than at the periphery. These observations offer new mechanistic clues into how atrial TATS remodeling can lead to Ca^{2+}-driven instabilities that may ultimately contribute to the arrhythmogenic state.

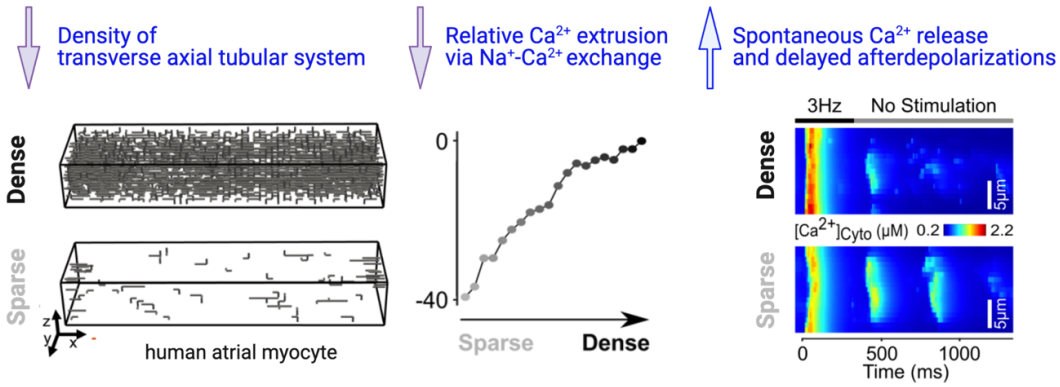

Figure 1.1 – Graphical summary of chapter 2.

A model of the human atrial myocyte action potential and subcellular Ca^{2+} handling is coupled with detailed ultrastructure to simulate varying TATS densities (*left*). Simulated TATS loss causes reduced NCX-mediated Ca^{2+} removal (*middle*) resulting in spontaneous Ca^{2+} release and promotion of arrhythmogenic Ca^{2+} waves (*right*) and delayed afterdepolarizations.

Chapter 3 details how we utilized or novel model to mechanistically examine the interactive impact of TATS loss and changes in the expression and distribution of key Ca^{2+}-handling proteins (known to be remodeled in disease) on Ca^{2+} homeostasis and electrophysiological stability (**Fig. 1.2**). Specifically, this chapter shows that varying the expression and localization of Ca^{2+}-handling proteins has variable pro- and anti-arrhythmic effects with outcomes displaying dependence on TATS density. Whereas detubulated myocytes typically appear unaffected and densely tubulated cells seem protected, the arrhythmogenic effects of Ca^{2+} handling protein remodeling are profound in intermediately tubulated cells. A mechanistic understanding of the interaction between TATS and Ca^{2+}-handling protein remodeling that underlies the Ca^{2+}-driven proarrhythmic behavior (as

observed in AF) may help to predict the effects of antiarrhythmic strategies at varying stages of ultrastructural remodeling.

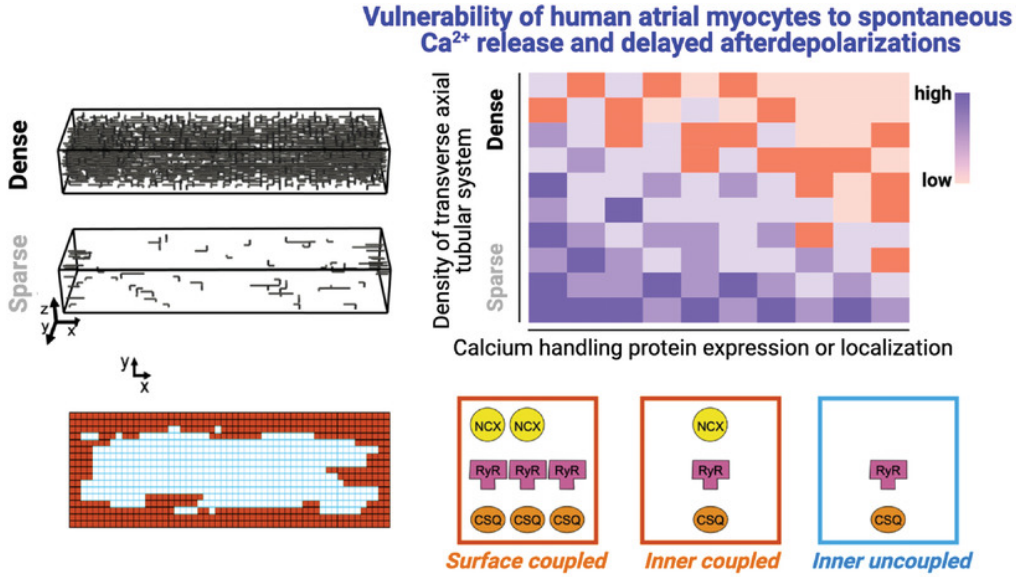

Figure 1.2 – Graphical summary of chapter 3.

A model of the human atrial myocyte AP and subcellular Ca^{2+} handling is utilized to investigate the interactive effects of changes in expression and localization of key Ca^{2+}-handling proteins (*bottom row*) and variable TATS density (*left column*) on human atrial myocyte vulnerability to Ca^{2+}-handling abnormality driven membrane instabilities (color map). Modulating the expression and distribution of NCX, RyRs, and calsequestrin (CSQ) has varying pro- and anti-arrhythmic effects depending on the balance of opposing influences on sarcoplasmic reticulum Ca^{2+} leak-load and Ca^{2+}-voltage relationships. The impact of protein remodeling on Ca^{2+}-driven proarrhythmic behavior varies dramatically depending on TATS density, with intermediately tubulated cells being more severely affected compared to sparsely and densely tubulated myocytes.

Chapter 4 summarizes the major findings and significance of this dissertation, and their translational relevance. Future directions for follow-up studies toward new insights for next-generation medicine are also discussed.

1.3 Heart anatomy and function

The human heart is a hollow muscular organ situated between the lungs and the anterior chest wall, with the bulk of the bottom (apex) stretching to the left-hand side of the chest cavity. The heart is necessary for life and functions through the circulatory system. At rest, the human heart beats from 60 to 100 times per minute, pumping oxygenated blood and nutrients through the blood vessels of the body in the systemic circuit and deoxygenated blood to the lungs in the pulmonary circuit. Because of its role throughout the body, the circulatory system is vital for hormone distribution and maintenance of body temperature, pH, and ionic homeostasis.

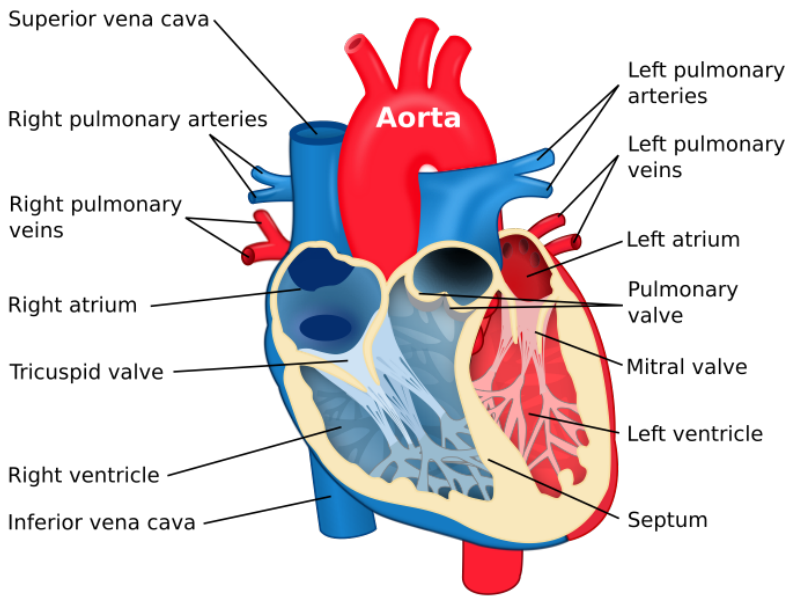

Figure 1.3 – Anatomy of the heart.

The schematic shows the major components of the heart, including left/right atria, left/right ventricles, major veins and arteries. Blue chambers are occupied by deoxygenated blood, and red chambers are occupied by oxygenated blood. Modified from Wikipedia (Anon, 2022).

The heart consists of external walls and internal cavities/chambers. The outer wall has three layers (the epicardium, myocardium, and endocardium), and the cavity is split into four,

with two upper chambers called the atria and two lower chambers termed the ventricles (**Fig. 1.3**). The left and right atria collect blood entering the heart and the left and right ventricles pump blood out of the heart. In this process, the right atrium collects deoxygenated blood via the superior and inferior vena cava and then pumps it through the tricuspid valve into the right ventricle where it is pumped to the lungs. Meanwhile, the left atrium receives the oxygenated blood from the pulmonary veins and the blood is pumped through the mitral valve into the left ventricle and then the aorta. The oxygenated blood also supplies the heart via the coronary system.

Each cardiac cycle begins with the contraction of the atria and ends with the relaxation of the ventricles. The period when the chambers contract to pump blood into circulation is called systole, with the period when the chambers relax to fill with blood called diastole. All four chambers undergo systole and diastole with the sequential order from atria to ventricles necessary for efficient filling and pumping.

Cardiac contraction is driven by the timely generation and propagation of a periodic electrical signal that is converted into mechanical activation by the process of ECC. In this process, the periodic spontaneous signal is initiated by the sinoatrial (SA) node (i.e., pacemaker cells) located in the right atrium, close to the superior vena cava. The electrical signal generated by the SA node manifests as an AP that travels as a propagating wave of depolarization to both the right and left atria to facilitate atrial contraction. Following atrial depolarization, the electrical signal passes through the atrioventricular (AV) node at the junction between the atria and ventricles, introducing a ~ 100 ms delay before activating the ventricles. As a result, the atria contract first to fill the ventricles with blood prior to ventricular activation and contraction. Connected with the AV node, the His-Purkinje system conducts the electrical pulse to the left and right ventricles facilitating their excitation and thus contraction. This electrical signal can be detected by electrocardiography (ECG) in the clinic.

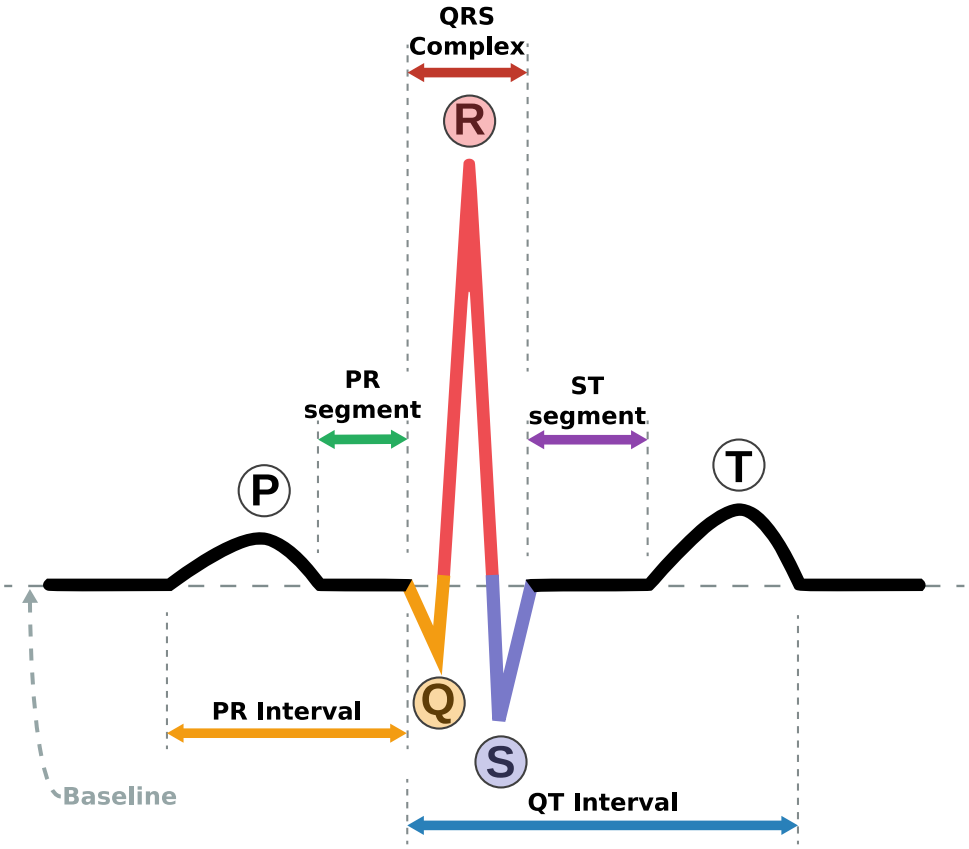

Figure 1.4 – Healthy ECG recording in a human heart.

The schematic shows the components of a typical ECG recording, including P wave, PR segment, QRS complex, ST segment, and T wave. The diastolic (baseline) level of ECG is marked as dashed line. Major biomarkers are highlighted, e.g., PR interval and QT interval. Modified from Wikipedia (Anon, n.d.).

ECG is a convenient and non-invasive technique that uses electrodes placed on the skin to monitor the time course of the heart's electrical activity, rhythm, and any abnormalities in electrical activity. A typical ECG has 10 electrodes placed on the patient's limbs and on the surface of the chest, to measure the heart's electrical potential from 12 different angles/leads. The properties of ECG have been used to understand the function of cardiac electrical activity (and thus contraction characteristics). A typical ECG signal consists of a P wave, a QRS complex, and a T wave (**Fig. 1.4**). In line with the initiation of the cardiac cycle starting with

atrial excitation, the ECG begins with a P wave, which corresponds to atrial depolarization. It is followed by the QRS complex representing the depolarization of the ventricles and the T wave which reflects ventricular repolarization. As such, the ECG signal reveals atrial contraction (systole) during the P wave, ventricular contraction (systole) in the QRS wave, and ventricular relaxation (diastole) in the T wave. Characteristics of the ECG have been used in the diagnosis of abnormal cardiac rhythms known as arrhythmias. For example, the time for ventricular depolarization and repolarization defined as the QT interval (recorded between the onset of the QRS complex and the terminal T wave) is an important readout, as a long QT interval can lead to ventricular arrhythmias, such as Torsades de Pointes (TdP), and sudden cardiac death.

The organ-level electrical activities discussed above are the macro-phenomenon of combined cellular-level activities. In the following section, I will detail cardiac electrophysiology and the coupling of excitation and contraction at the cellular level that underly these processes.

1.4 Cardiac myocyte structure and function

1.4.1 Cardiac myocyte action potential

To sustain nearly 1 billion heartbeats over the course of a lifetime, the function of the heart results from the coordinated action of a diverse array of cell types, including cardiac myocytes, which occupy the majority of the heart volume, and other cell types such as fibroblasts, endothelial cells, smooth muscle cells, and pacemaker cells. Cardiac myocytes are the basic cellular units of cardiac excitability and contractility. Whole-heart electrical activity and contraction are macroscopic phenomena of microscopic electrical activity and contraction from individual cardiac myocytes from across the heart. Each region of the heart may produce unique

AP morphologies depending on the ionic fluxes that occur (**Fig. 1.5**) and serving specialize functions. Though distinct in their characteristics depending on whether they are atrial or ventricular, healthy cardiac myocytes are cylindrically shaped with a length of around 100 µm and a diameter of 10-25µm. The surface of a cardiac myocyte is covered by a lipid bilayer membrane, namely the sarcolemma, which separates the intracellular cytosol bulk from the extracellular environment. The transmembrane movement of ions (i.e., sodium Na^+, potassium K^+, calcium Ca^{2+}, and chloride Cl^-) via sarcolemmal ion channels, ion transporters, and ionic pumps leads to changes in the transmembrane potential.

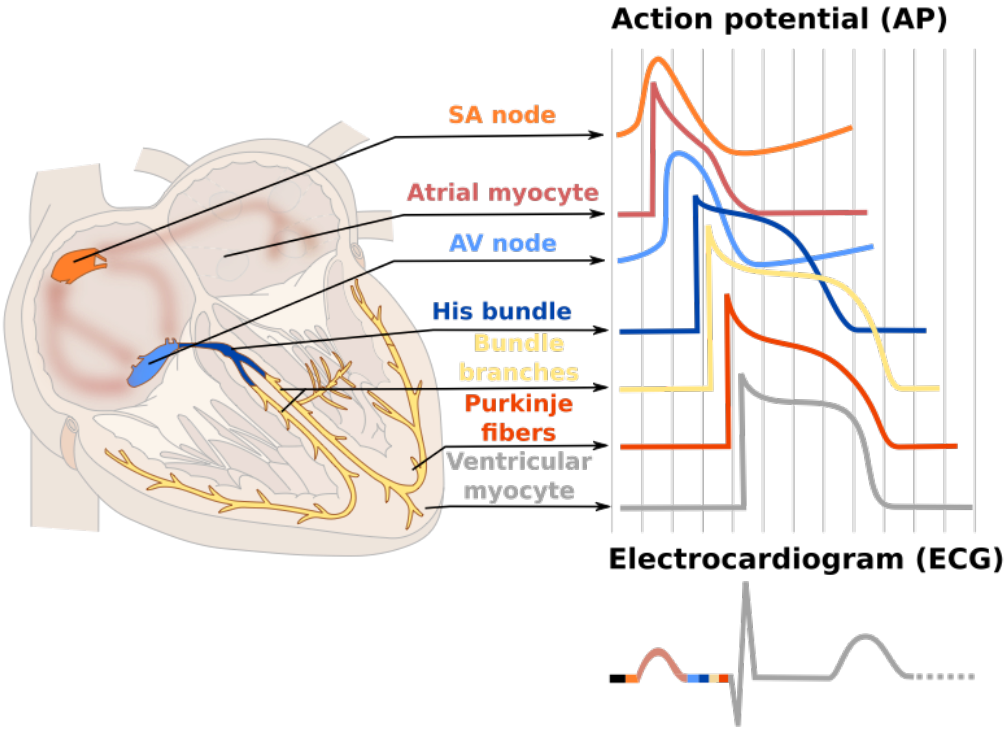

Figure 1.5 –Regional variation in AP configuration.

Varying heart region account for corresponding AP configurations. The schematic shows both region and the representative AP configuration of SA node, atrial myocyte, AV node, His bundle, Bundle branches, Purkinje fibers, and ventricular myocyte. All the AP traces are arranged with time series, reflecting the traveling of electrical signal during a normal beat. The combination of all the APs produces a normal ECG

on the bottom right. In ECG trace, the major contributors in the certain phase are marked by the corresponding colors. Modified from Wikipedia (ecgpedia, 2011).

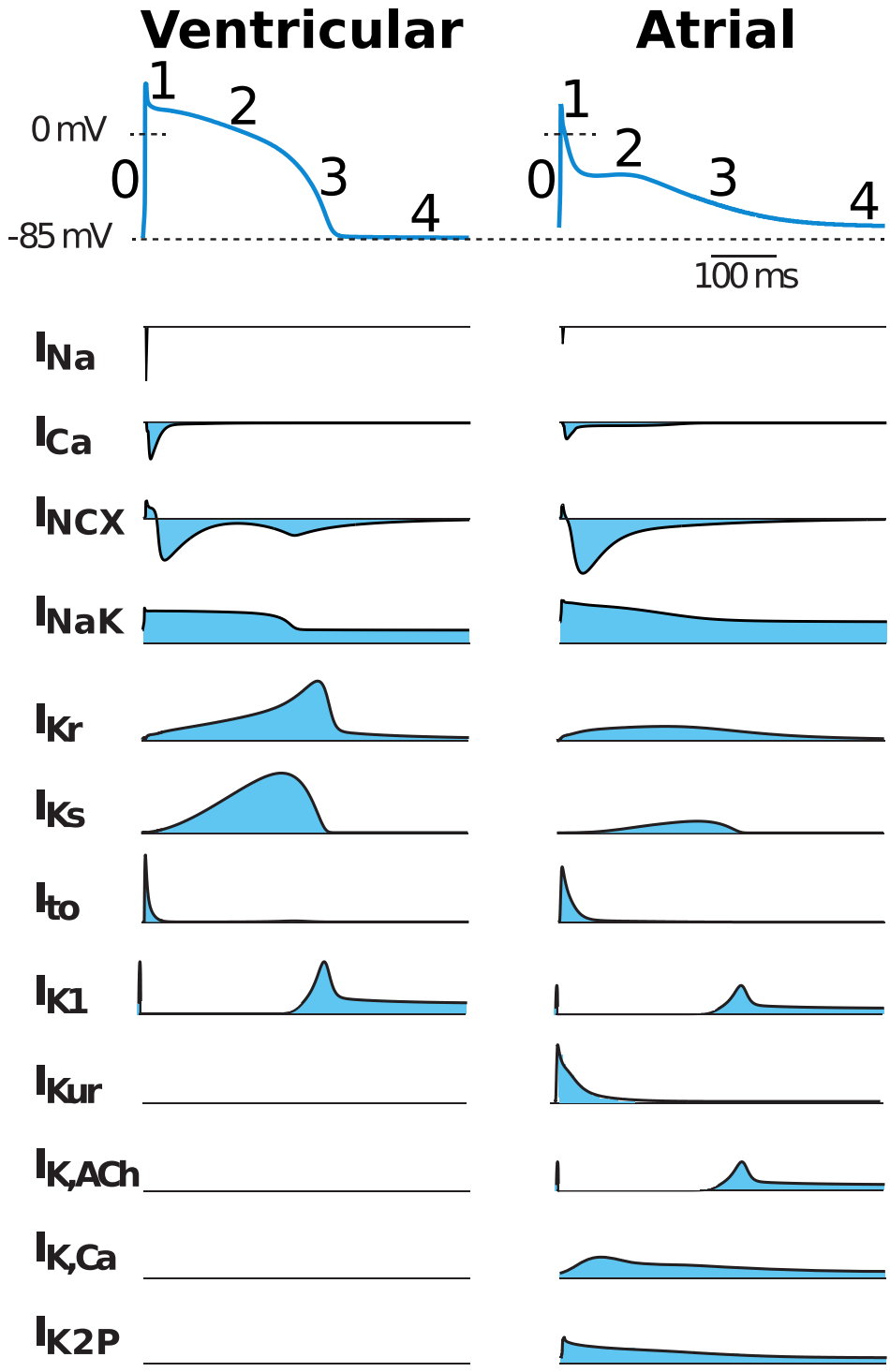

Figure 1.6 – Ventricle vs atrium AP morphology with key phases and primary ion currents.

Top: AP is divided into phases 0, 1, 2, 3, and 4 in both the ventricular myocyte (left) and atrial myocyte (right). Bottom: The contribution of multiple ion channels during all the phases, and atria-selective ion channels are included.

During the diastolic period, cardiac myocytes maintain a resting membrane voltage of around -85 mV to -90 mV in the ventricle and around -65 mV to 80 mV in the atria. When electrical excitation initiated in the SA node depolarizes the membrane potential to the threshold, an AP is initiated, which is the combined contribution by multiple ion channels. Most APs can be described within a general framework with five continuous phases (**Fig. 1.6**).

In **phase 4**, the membrane voltage is stabilized at the resting membrane potential (RMP), which is dominated by the repolarization force via the inward-rectifier K^+ current I_{K1}.

In **phase 0**, when the membrane voltage is elevated to a threshold, a large rapid Na^+ inward current (I_{Na}) is triggered to produce strong and rapid depolarization (i.e., AP upstroke), then I_{Na} is promptly inactivated. During this process, the voltage-dependent LCCs are activated to conduct inward Ca^{2+} flux.

In **phase 1**, K^+ channels rapidly open, generating, in particular, the transient outward current (I_{to}) and the ultra-rapid delayed rectifier current (I_{Kur}). These K^+ effluxes induce rapid repolarization.

In **phase 2**, the membrane potential is slowly repolarized by K^+ effluxes but balanced by depolarization from inward LCC current (I_{Ca}) leading to a plateau. During this time, the increased intracellular Ca^{2+} concentration promotes activation of the NCX; following which consequential higher intracellular Na^+ concentration increases Na^+-K^+ pump (NKA) activity. The collective contribution of these ion fluxes maintains the relatively stable voltage in phase 2.

In **phase 3**, the membrane voltage is rapidly repolarized to RMP. The slow delayed rectifier K^+ current I_{Ks} and the rapid delayed rectifying K^+ current I_{Kr} are major contributors in

the ventricles, whereas in the atria a diverse array of atrial predominant K^+ channels is also expressed and plays critical roles. These include the small-conductance Ca^{2+} activated K^+ current I_{SK}, the K2P3.1 two-pore-domain K^+ current, I_{K2P}, the ultra-rapid delayed rectifier K^+ current I_{Kur}, the acetylcholine-activated inward rectifying K^+ current I_{KAch}. Meanwhile, I_{Ca} progressively inactivates. After phase 3, another phase 4 follows, and I_{K1} contributes to the repolarization in phase 4 again. In sinoatrial cells, funny current (I_f) provides depolarization during phase 4 and regulates cardiac automaticity.

1.4.2 Excitation-contraction coupling and intracellular Ca^{2+} dynamics

Cellular excitation via AP-induced changes in membrane voltage is coupled with mechanical contraction through ECC. Intracellular Ca^{2+} is a major mediator in this process and acts by regulating ion currents and binding to the myofilaments. While most of the volume of the cell is occupied by mitochondria, which supply chemical energy and myofibrils that conduct contractile force, cardiac myocytes also contain an intracellular calcium ion store, SR, which plays a vital role in Ca^{2+} handling. Furthermore, along the sarcolemma, there are transversal membrane invaginations known as TTs that bring sarcolemmal ion channels and transporters to the inner area of the myocytes (**Fig. 1.7**). The presence of TTs ensures ion channels on the membrane are in close proximity to the SR throughout the cell. The formation of 'dyads' between SR and TTs is essential for coupling the membrane potential to intracellular Ca^{2+} signaling via ECC.

During AP phase 0, membrane depolarization leads to opening of the L-type Ca^{2+} channels, which facilitates Ca^{2+} influx into the dyadic space. The increased Ca^{2+} concentration in the dyadic space increases the opening probability of RyRs located in the closely-apposed SR membrane. RyR opening facilitates the release of a large amount of Ca^{2+} from the SR that

generates the systolic Ca^{2+} transient via CICR. The Ca^{2+} released from the SR binds to the myofilaments bringing about a conformational change that generates cell contraction.

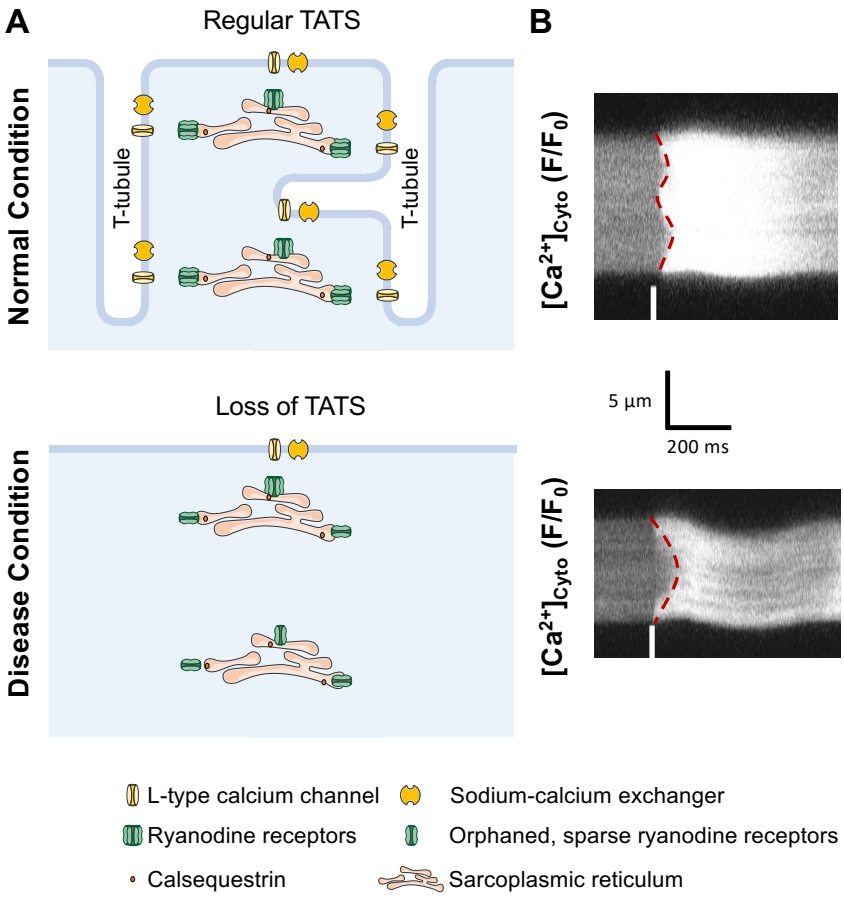

Figure 1.7 – Loss of TATS induces dyssynchronization of subcellular Ca^{2+} release in disease.

A) TATS is regular, ordered with some longitudinal branches under normal condition (top), but TATS is lack under disease condition (bottom). The schematic also indicates the location of L-type calcium channels, sodium-calcium exchanger, Ryanodine receptors, Calsequestrin, and Sarcoplasmic reticulum. **B)** Linescan images of experimental (Kirk *et al.*, 2003) atrial cells with (top) or without (bottom) tubules. The front wave of Ca^{2+} release is marked by a red dashed line.

To facilitate relaxation, Ca^{2+} is removed from the cytosol, either back into the SR by the sarcoplasmic reticulum Ca^{2+}-ATPase (SERCA), or extruded via NCX and the plasma membrane Ca^{2+} ATPase (PMCA). This restores intracellular Ca^{2+} concentration to the diastolic level with membrane voltage back to RMP. Ca^{2+} ions stored in the SR are buffered by Ca^{2+}-

binding proteins, with Ca^{2+} in the cytosol also buffered by myofilament and membrane phospholipids (Bers, 2002). The major Ca^{2+} buffer protein in the SR is CSQ. In addition to its role as an SR Ca^{2+} buffer, CSQ also regulates RyR opening and thus SR Ca^{2+} release (Terentyev *et al.*, 2003; Györke *et al.*, 2004; Knollmann *et al.*, 2006; Restrepo *et al.*, 2008). Consequential of its important role in Ca^{2+}-binding regulation, disease-related arrhythmia is induced by CSQ loss in AF (Faggioni *et al.*, 2014) with CSQ mutations observed in Catecholaminergic polymorphic ventricular tachycardia disease (Terentyev *et al.*, 2006).

As mentioned above, TTs play a key role in regulating cellular Ca^{2+} dynamics. In ventricular myocytes, rapid and synchronous CICR and thus whole-cell contraction driven is enabled by the presence of a dense and well-organized TT network. TTs are spaced approximately 2 μm apart at the z-line and project as transversal invaginations of the cell membrane with dimensions of 100-300 nm. LCCs are concentrated on TTs, and TT membranes closely juxtapose (< 20 nm) LCC clusters with intracellular RyR clusters embedded in the SR membrane, forming couplons to facilitate rapid and synchronous CICR. The Ca^{2+} removal proteins NCX and PMCA are also preferentially expressed on TTs and thus they also play an important role in Ca^{2+} extrusion.

Compared to the ventricle, atrial myocyte TTs are generally more sparse and irregular, with evidence suggesting increased prominence of ATs (**Fig. 1.7**). ATs provide extensive longitudinal sarcolemmal invaginations to form TATS that also serve to couple RyRs with membrane ion channels. TATS abundance varies with cell width, species, and location in the atria (Richards et al., 2011; Frisk et al., 2014; Glukhov et al., 2015; Gadeberg et al., 2016). These factors likely contribute to the wide-ranging diversity of atrial TATS density reported, particularly in small mammalian species, where tubules are either lacking (Huser et al., 1996; Brette et al., 2002), sparse, and often longitudinally orientated (Kirk et al., 2003; Woo et al., 2005).

A lack of TATS is associated with less synchronous Ca^{2+} release. In atrial myocytes with sparse TATS or detubulated ventricular myocytes, LCCs are mainly located on the peripheral membrane. As such, while Ca^{2+} release at the surface is triggered, to facilitate a global rise in Ca^{2+} Ca^{2+} ions must diffuse to the center of the cell and recruit inner RyRs to release Ca^{2+} and form a wave of Ca^{2+} propagation, known as fire-diffuse-fire dynamics.

While axially-dominant TATS are present in the atria of small mammals, more ventricular-like TATs are common in atria from large mammalian species e.g., sheep, cows, horses, dogs, and pigs. These TTs are reduced in density compared to the ventricle and are heterogeneous between cells and species (Wakili et al., 2010; Richards et al., 2011; Frisk et al., 2014; Gadeberg et al., 2016). Whereas TTS are present in almost 70% of human atrial cells in tissue sections (Richards et al., 2011), only sparse TTs have been reported in isolated human atrial cells (Greiser et al., 2014). These differences between studies may arise due to TATS damage, either as a result of enzymatic digestion (Chen et al., 2015) or to differences in the underlying pathophysiology of patient samples. As such, at present, the reliance on the rise of systolic Ca^{2+} on TTs in human atrial cells is not well understood.

Ca^{2+} signaling is vitally regulated by sympathetic stimulation through β-adrenergic receptors (i.e., inotropy-induced contraction and lusitropy-induced relaxation). The stimulation of β-adrenergic receptor activates both protein kinase A (PKA) and Ca^{2+}/calmodulin-dependent protein kinase II (CaMKII) pathways, which collectively modulate varying downstream Ca^{2+}-handling proteins (e.g., LCC, RyR, phospholamban (PLB), troponin I, and myosin binding protein C), and transmembrane ion channels. As such, β-adrenergic signaling is a key medicator in both subcellular and global Ca^{2+} signaling and ECC (Bers, 2002; Bers & Grandi, 2009; Bers & Morotti, 2014; Hund & Mohler, 2015).

Both ionic and ultrastructural remodeling (i.e., disrupted properties of Ca^{2+}-related protein and subcellular structures) can induce Ca^{2+} dysregulation, which in turn affects

cardiomyocyte electrical properties and stability thus leading to arrhythmia. Indeed, a clear role for Ca^{2+} abnormalities as primary drivers of arrhythmia has been well documented in both inherited arrhythmia syndromes linked to mutations in Ca^{2+} handling proteins (e.g., catecholaminergic polymorphic ventricular tachycardia) or in response to drugs (e.g., digoxin toxicity). Importantly, Ca^{2+} mishandling also contributes to more common arrhythmogenic conditions with broader pathophysiologic changes, e.g., AF and HF (Denham et al., 2018). We specifically focus on the pathology of Ca^{2+} dysregulation in AF, which will be discussed in detail in the following section.

1.5 Atrial Fibrillation

1.5.1 Pathophysiology of AF

In a healthy heart, regular electrical activity, as describes in section 1.2, maintains normal sinus rhythm (nSR). Any change from nSR to an abnormal irregular cardiac rhythm is termed an arrhythmia. Arrhythmias include situations where the heart beats too quickly (tachycardia, more than 100 BPM for the human), too slowly (bradycardia, less than 60 BPM for the human), or has disrupted electrical impulses (fibrillation). All subtypes of arrhythmia can damage the cardiac function and cause symptoms, with the most dangerous arrhythmias leading to sudden cardiac death. While the firing rate of the SA node typically determines rhythm, arrhythmias can arise from other cardiac regions, including within atrial and ventricular myocytes.

AF is the most common cardiac arrhythmia, with a prevalence of 1-2% in the general population - projected to increase to 4% by 2050 with aging of the population. AF impairs quality of life, markedly increases the risk for cerebrovascular stroke, and often coexists with other pathologies, thereby causing increased morbidity and mortality (Andrade *et al.*, 2014).

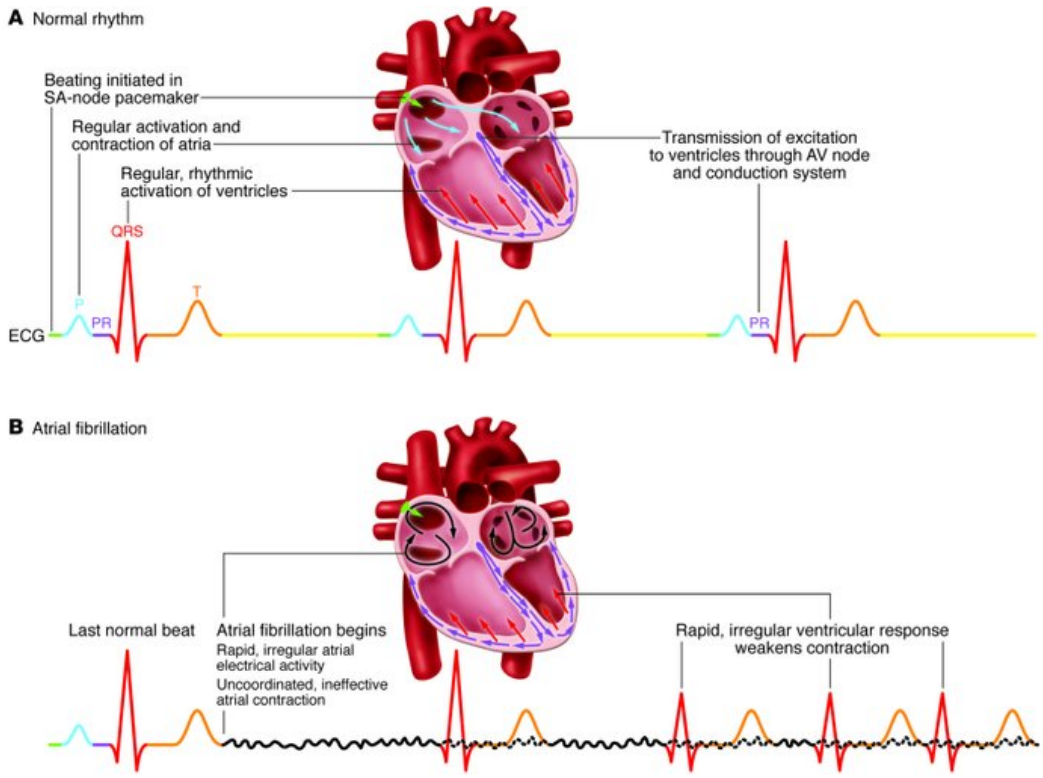

Figure 1.8 – ECG recordings of sinus rhythm and AF.

A) Bottom: A normal ECG recording showing sinus rhythm. Top: Schematics of major events in one cardiac activation cycle: rhythm is initiated by the SA node pacemaker, resulting in atrial activation, followed by atrioventricular conduction via the AV node and His-Purkinje conducting system, leading to ventricular activation. **B)** ECG showing onset of AF after one regular sinus beat. Atrial activation is now rapid and irregular, producing an undulating baseline that is visible when not obscured by larger QRS and T waves (continuous atrial activity during this phase is represented by dotted lines). During AF, rapid and uncoordinated atrial activity leads to ineffective atrial contraction. Ventricular activations (QRS complexes) now driven by the fibrillating atria occur rapidly and irregularly, weakening cardiac contraction efficiency and causing clinical symptoms. Adapted from (Wakili *et al.*, 2011).

AF may occur as a primary disease or alongside various other diseases, including diabetes, obesity, and HF. In the clinic, AF is diagnosed by rapid undulations in the P wave of the ECG (**Fig. 1.8**), reflective of irregular and rapid excitation and contraction of the atria, and subsequential reduced blood output from the ventricle. AF is categorized into paroxysmal AF

(lasting < 7 days and terminated spontaneously), persistent AF (lasting > 7 days and not self-terminating), and chronic (permanent) AF (ongoing long-term episodes) (January *et al.*, 2014). Pharmacological rhythm control is thought to be particularly applicable in early stages of AF (*paroxysmal* AF), i.e., before extensive electrical, structural, contractile, and neurohormonal (mal)adaptations lead to long-standing persistent (*chronic*) AF (cAF). However, current drugs for AF treatment have limited efficacy, may increase the risk of ventricular proarrhythmia, and are broadly outperformed by ablation procedures. While these limitations are driving a push for improved strategies in the treatment of AF, a major obstacle to next-generation pharmacotherapy is our relatively poor understanding of the molecular and cellular basis of AF initiation, progression, and maintenance.

The mechanisms underlying AF are complex and involve both (1) increased spontaneous ectopic firing of atrial cells and (2) impulse reentry through atrial tissue. At the cellular level, focal ectopic/triggered activity is likely caused by early and delayed afterdepolarizations (**EADs** and **DADs**) or enhanced automaticity. At the tissue level, afterdepolarization-prone regions overcome the surrounding stable tissue to produce ectopic activity. Focal ectopic activity can maintain AF as a driver or act on vulnerable reentrant substrates. At the cellular level, reentry is promoted by shorter AP duration (APD) and abbreviated refractoriness, and APD alternans. At the tissue level, it is favored by slow conduction velocity and heterogeneous conduction, abbreviated refractoriness, and spatially heterogeneous APD. AF emergence and progression are commonly associated with ionic and structural remodeling, which are both linked to **abnormal focal activity** and to the formation of functional and structural substrate for **reentry** (Nattel *et al.*, 2008). In the following section, we will discuss how AF-related remodeling contributes to these two determinants, and how these two factors contribute to arrhythmia (**Fig. 1.9**).

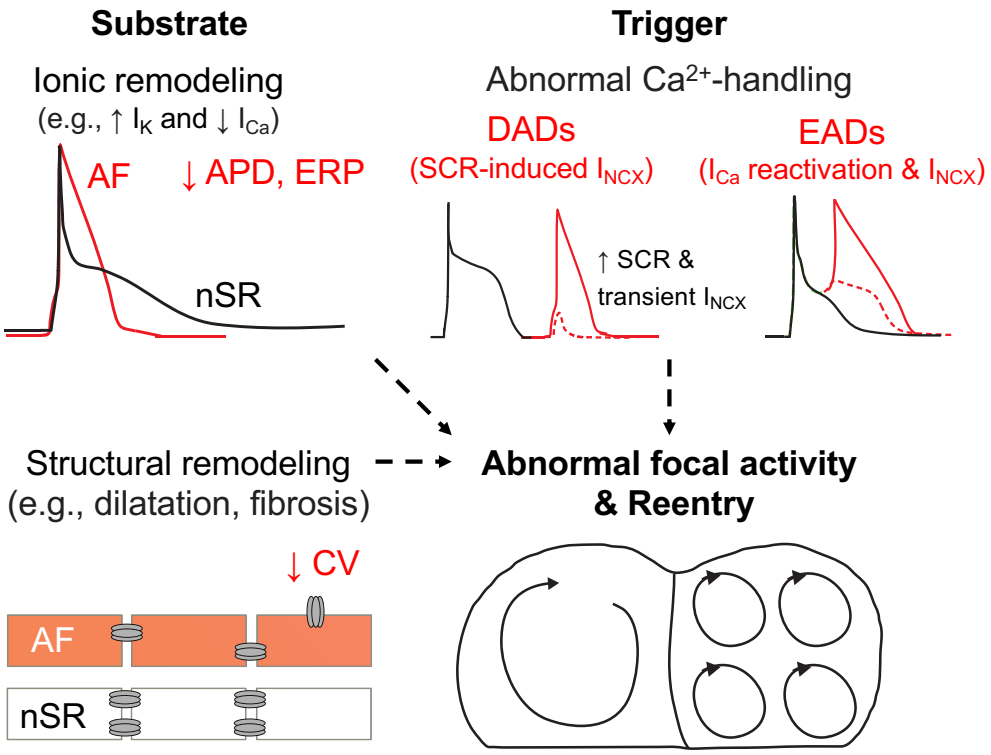

Figure 1.9 – Mechanism of arrhythmia.

Arrhythmia is commonly induced by abnormal focal activities and reentry. The underlying disease-induced changes are categorized into substrate and triggers according to their effects on arrhythmia. In substrate, ionic remodeling (e.g., increased K^+ currents and reduced Ca^{2+} currents) shorten APD and thus effective refractory period (ERP) in Atrial Fibrillation, and structural remodeling (e.g., dilatation and fibrosis) damages the conduction system (e.g., reducing conduction velocity, CV). Both ionic remodeling contribute to increased vulnerability of patients to reentry. In triggering category, abnormal focal activities are induced by DADs and EADs, medicated by abnormal Ca^{2+}-handling in disease. Spontaneous Ca^{2+} release (SCR) triggers transient I_{NCX} to depolarize the membrane voltage in phase 4 (thus induces DADs) or phase 3 (thus induces EADs). In addition, I_{Ca} reactivation during AP is also a major contributor to EADs in disease. Meanwhile, TATS loss and remodeling of Ca^{2+}-handling proteins (in both expression and distribution) induce abnormal Ca^{2+}-handling, thus trigger DADs, which will be discussed in chapter 2 and 3. The combination of all these factors collectively promote arrhythmia (i.e., abnormal focal activity and reentry) in disease conditions.

1.5.2 Arrhythmia mechanism and structural remodeling in AF

Reentry: Cardiomyocyte electrophysiology and cell-cell electrical coupling are optimized to facilitate conduction throughout the heart and appropriately timed sequence of generation and propagation of the electrical impulse to maintain nSR. In disease, cardiac remodeling involves a complex array of alterations, including changes in cell size and ultrastructure, electrophysiology, cell-cell connections, and extracellular matrix causing fibrosis and scarring. This results in a vulnerable substrate for arrhythmia, favoring unidirectional conduction block, reduced or heterogeneous refractory period, and slowed conduction velocity, which can facilitate a self-sustaining closed-loop excitation conduction circuit, namely reentry (**Fig. 1.9**). This results in faulty impulse propagation with a reentrant self-sustaining spiral wave consequently causing subsequential tachycardia and fibrillation.

There are several potential contributing factors to AF-maintaining reentry, including: 1) reduced I_{Ca} and enhanced outward K^+ current reduce AP duration and refractory period (Nattel *et al.*, 2007), 2) Ca^{2+}-dependent APD alternans that increases spatial heterogeneity in atrial refractoriness; 3) reduced I_{Na}, lower expression of gap junction channels (connexins), and fibrosis slow conduction velocity (Gaspo *et al.*, 1997; Li *et al.*, 1999; van der Velden *et al.*, 2000; Shinagawa *et al.*, 2002), 4) dilation enlarges atrial tissue size that accommodates more reentrant circuits with longer wavelengths (Zou *et al.*, 2005).

Abnormal focal activity: An imbalance between depolarization and repolarization (i.e., enhanced depolarization or reduced repolarization) may induce spontaneous electrical excitation and disrupt normal cardiac electrical conduction. This abnormal focal activity can be categorized into DADs and EADs dependent on the phase of the AP when they occur.

DADs occur in phase 4 of the AP after full repolarization (**Fig. 1.9**). Here, leaky RyRs can spontaneously release Ca^{2+} to the cytosol causing the increased intracellular Ca^{2+} concentration to drive NCX to extrude Ca^{2+} with a subsequent inward current. The NCX-

mediated depolarization could elevate the membrane voltage over a threshold for AP initiation and then trigger an additional AP. The occurrence of additional APs in the form of DADs can lead to tachycardia.

In contrast to DADs, EADs happen in AP phase 2 or phase 3 where membrane voltage has not been fully repolarized (**Fig. 1.9**). Phase-2 EADs are mainly induced by prolonged AP duration and thus reopening of recovered LCCs when the membrane potential is over -40 mV; however, phase-3 EADs happen between -70 mV to -50 mV, triggered by reopening of fast Na^+ channels and favored by rapid early repolarization. Both types of EADs can lead to tachycardia and varying arrhythmias.

Abnormal focal activity in AF is favored by several factors: 1) PKA/CaMKII hyperphosphorylation of RyR induces stronger SCR and thus DADs (Voigt *et al.*, 2014), 2) PKA/CaMKII hyperphosphorylation of PLB and loss of CSQ induces Ca^{2+} overload to increase RyR opening and thus promotion of spontaneous Ca^{2+} release (El-Armouche *et al.*, 2006; Faggioni *et al.*, 2014), 3) enhanced NCX activity increases the coupling between SCR and DADs (Voigt *et al.*, 2012). In addition, AF is associated with the loss of tubules, which inevitably contributes to I_{Ca} reduction, impaired Ca^{2+} extrusion, and increased orphaned RyRs (Denham *et al.*, 2018). In these settings, AF-induced tubular remodeling may further facilitate reduced ERP and disrupted Ca^{2+} signaling.

Given several proteins are preferentially expressed on TATs, it is conceivable that TATS remodeling (i.e., de-tubulation, tubular disorganization) combines with changes in distribution, composition, and phosphorylation status of Ca^{2+} handling proteins to promote Ca^{2+} abnormalities in diseases such as AF. Indeed, Ca^{2+} handling is remodeled in association with TT loss following 7 days of atrial pacing (a subtype of paroxysmal AF) (Wakili et al., 2010), during persistent AF (Lenaerts et al., 2009) and HF induced by both rapid ventricular pacing (Dibb et al., 2009), and myocardial infarction (Kettlewell et al., 2013). The TATS depletion

observed in disease primarily damages ECC efficacy because of reduced coupling between LTCCs and RyRs. While TATS loss occurs in AF, it may also either facilitate AF occurrence in HF or arrhythmia progression (in the absence of HF) by a number of the mechanisms discussed above. Electrically, TATS loss in the ventricle has been shown to decrease AP duration (Brette et al., 2006). Loss of atrial TATS in AF and HF is also associated with reduced I_{Ca} (Lenaerts *et al.*, 2009; Clarke *et al.*, 2015), and likely contributes to action potential shortening (Clarke *et al.*, 2015). As such, TATS remodeling in AF may exacerbate AP and thus atrial refractory period shortening, which is a hallmark feature of AF and HF-induced atrial arrhythmia.

The complex and interactive AF-associated remodeling poses substantial challenges for mechanistic understanding and prediction of the integrated effects of these arrhythmia-associated perturbations on atrial myocyte Ca^{2+} and voltage dynamics. Indeed, the distinct contributions of ionic and structural remodeling cannot easily be separated experimentally. Furthermore, enzymatic digestion during cell isolation is likely to damage the cell membrane and disrupt TATS (Chen *et al.*, 2015). In this dissertation, we have employed mathematical modeling to integrate a vast array of experimental data and knowledge from various published sources to address the critically important issue of how subcellular ultrastructure (namely, TATS) affects local and global Ca^{2+} signaling and thus regulates ECC in healthy and diseased cardiac cells.

1.6 Multiscale modeling of atrial myocyte Ca^{2+} handling

Multi-scale electrophysiology models of the heart, from cell-level models, through one-, two- and three-dimensional tissue-level simulation frameworks, to anatomically detailed models of the ventricles, atria, or whole heart, have provided remarkable insight into the normal and pathological functioning of the heart (Benson *et al.*, 2021) (**Fig. 1.10**). In the context of AF,

these models integrate structural and functional data from experimental and clinical work with knowledge of atrial electrophysiological mechanisms and dynamics to improve our mechanistic understanding of this complex arrhythmia.

Mathematical models of cardiac myocyte electrophysiology reconstruct the AP and Ca^{2+} transient of cardiac myocytes are usually represented by a system of coupled, nonlinear differential equations. These cell-level models have been developed with increasing biophysical detail and complexity for more than 50 years (Fink *et al.*, 2011) and have contributed to enhance our understanding of cellular electrophysiology and Ca^{2+} signaling in health and disease, including arrhythmias (Rudy & Silva, 2006; Roberts *et al.*, 2012; Winslow *et al.*, 2016). Transmembrane voltage in cardiac cell models is generally described by a Hodgkin and Huxley type electrical circuit model (Hodgkin & Huxley, 1952; Noble, 1960; Grandi *et al.*, 2019).

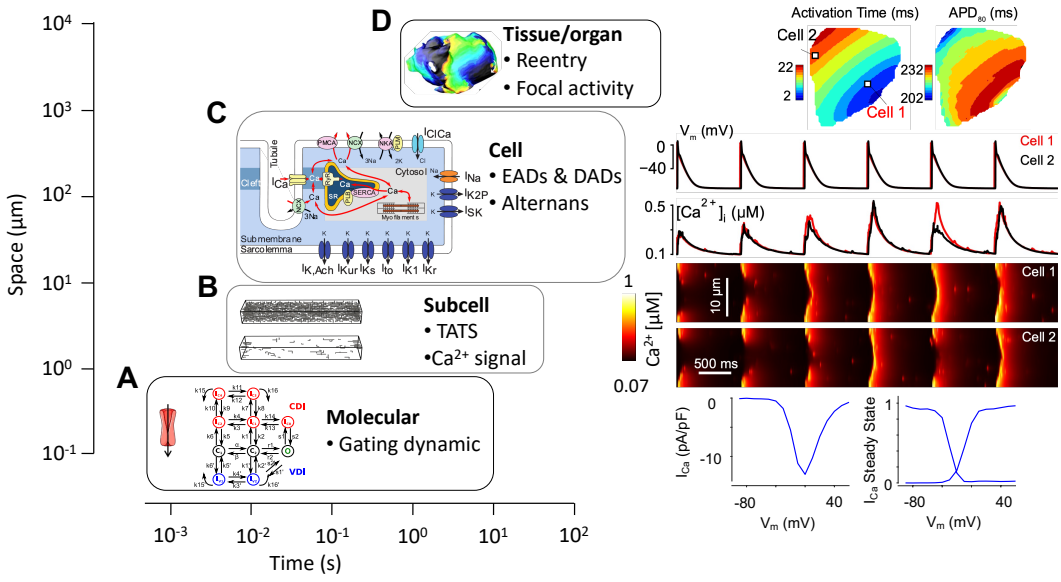

Figure 1.10 – Schematic of multi-scale cardiac modeling approaches.

The types of cardiac models are classified in to 4 categories (i.e., molecular-level, subcellular-level, cell-level, tissue/organ-level) based on the difference of space and time scales involved. From the bottom to the top, each model type captures specific aspects of cardiac biophysics: **A)** molecular-level models

replicate permeability and gating dynamics of ion channels (e.g., voltage- and Ca^{2+}- dependence of I_{Ca}), **B)** subcellular models reflect local signaling (e.g., Ca^{2+} wave initiation and propagation), **C)** cell-level models are used to study whole-cell phenomenon (e.g., voltage and Ca^{2+} transient) and arrhythmia mechanisms (e.g., EADs, DADs, and alternans), **D)** tissue/organ-level models are used to investigate phenomena emerging from spatial and temporal heterogeneity in cell-level activity and disturbances to cell-cell coupling (e.g., reentry and abnormal focal activity). The combination of multi-scale modeling approaches can reveal the mechanism in small scales under phenomena in larger scales and predict large-scale phenomena based on small-scale remodeling.

The cell membrane with the lipid bilayer is considered equivalent to an electrical capacitor, and ion channel/transporter/ pumps that conduct ion flux (mainly Na^+, K^+ and Ca^{2+}) are treated as resistors that are aligned in parallel in the circuit (**Fig. 1.11**). In quiescent cardiomyocytes, membrane net potential is in negative, which is regulated by the gradient of ions between intracellular and extracellular area. Thus, the membrane potential (V_m) is quantitatively described as follow:

$$V_m = \phi_i - \phi_e$$

Where ϕ_i and ϕ_e denote the electrical potential for intracellular and extracellular space of cell.

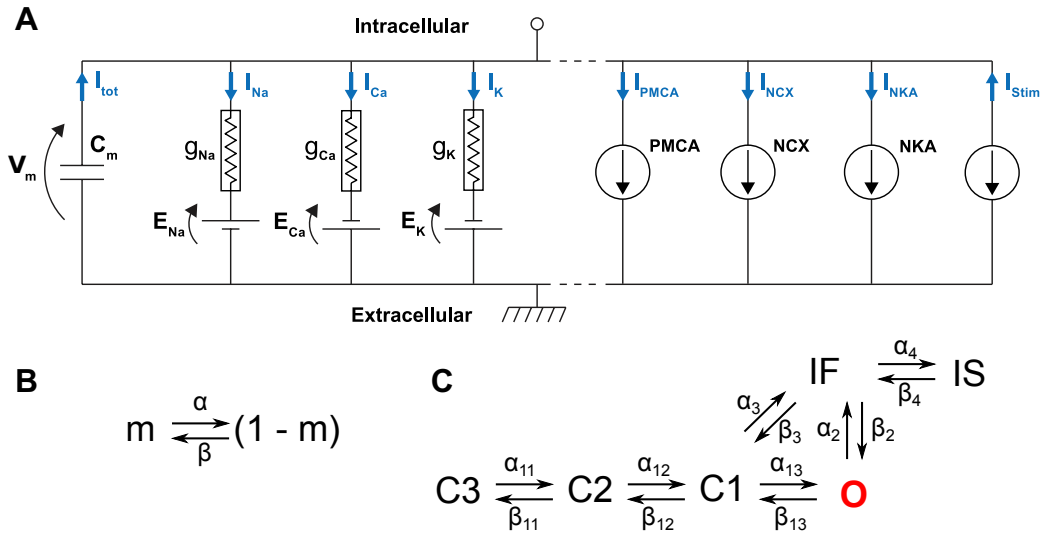

Figure 1.11 – Schematic of electric circuit model and illustrations of gating variable modeling schemes.

A) Electric circuit model describing V_m as the voltage drop across a capacitor (C_m, i.e., the lipid bilayer) and transmembrane ionic currents as resistors in parallel. **B)** A simplest Hodgkin-Huxley formalism describing gating variable (m). **C)** A Markov model that was constructed by Clancy and Rudy (Clancy & Rudy, 1999) to describe wild-type cardiac Na^+ channels, which includes three closed states (C3, C2 and C1), a conducting open state (O), and two inactivation states (fast and slow inactivation, IF and IS, respectively).

Because of the ionic concentration imbalance across the cell membrane and the ion selectively of transmembrane ionic pathways, an equilibrium is reached between the electrical force and the chemical potential. The chemical potential that is induced by ion concentration gradients is represented by a battery, and it is described by Nernst equation:

$$E_{ion} = \frac{R \cdot T}{z \cdot F} \cdot ln\left(\frac{[ion]_o}{[ion]i}\right)$$

Where R is the universal gas constant, T is the absolute temperature, F is the Faraday's constant, z is the valence number of the ion, and $[ion]_o$ and $[ion]_i$ refer to the extracellular and intracellular concentration of the ion species, respectively.

Given the cell membrane is an electrical capacitor with fixed capacitance (C_m), the stored charge (Q) is calculated as follows:

$$Q = C_m \cdot V_m$$

where V_m is the voltage drop across the capacitor. Thus, the capacitive current (I_{Cm}) can be computed using Faraday's law:

$$I_{cm} = \frac{dQ}{dt} = C_m \cdot \frac{dV_m}{dt}$$

Meanwhile, the conservation of electric charge implies that the applied current may be split in a capacitive current which charges the capacitor (via I_{Cm}) and further components that pass through the ion channel ($\sum I_{ion}$):

$$I_{cm} + \sum I_{ion} = 0$$

Combining these two equations, V_m can be described as:

$$C_m \cdot \frac{dV_m}{dt} = -\sum I_{ion}$$

Where C_m is the membrane electrical capacitance, $\sum I_{ion}$ refers to the sum of all the transmembrane currents, i.e., $\sum I_{ion} = I_{Na} + I_{Ca} + I_{to} + I_{Kur} + I_{Kr} + I_{Ks} + I_{K1} + I_{NCX} + I_{NaK} + I_{PMCA}$

Each transmembrane current is calculated based on properties of corresponding channel (e.g., ion permeability, gating/opening, etc.) to represent the whole-cell ionic current instead of the behavior of single proteins. The gating of most cardiac ion channels is voltage- and time-dependent, although other gating dynamics like ligand- and mechano- related are present. Commonly, each ionic current (I_{ion}) is described by Ohm's law:

$$I_{ion} = g_{ion} \cdot P_{ion,open} \cdot (V_m - E_{ion})$$

Where g_{ion} is the maximal conductance of the current when all corresponding channels are open; $P_{ion,open}$ is the gating variable describing the proportion of channels in the open state, which is generally is a function of V_m and time; E_{ion} is the Nernst equilibrium potential for the corresponding ion. Therefore, determining I_{ion} requires calculating the gating variables $P_{ion,open}$, which are generally defined through a system of ordinary differential equations using either the Hodgkin-Huxley (HH) formalism or Markov-type models.

In HH model, $P_{ion,open}$ is calculated based on multiple variables "gates", which undergo time and voltage dependent transitions between the open and the closed state. In the simplest case, the channel only has one state variable (m) in either open or close state, with

voltage-dependent transition rates (α and β, which are generally exponential functions of V_m) between open and close states:

$$\frac{dm}{dt} = \alpha \cdot (1 - m) - \beta \cdot m$$

The solution of this differential equation is given by:

$$m = m_\infty - (m_\infty - m_{start}) \cdot e^{-t/\tau_m}$$

where the steady state value can be calculated as $m_\infty = \frac{\alpha}{\alpha+\beta}$ (i.e., when $\frac{dm}{dt} = 0$), the decay constant is $\tau_m = \frac{1}{\alpha+\beta}$, and m_{start} is the initial value of m when $t = 0$. The variables m_∞ and τ_m describe key biophysical properties of channel kinetics, namely the voltage-dependence of steady-state activation and of the time constant of activation. Fitting of these curves, and thus model parameterization, can be determined through appropriately designed voltage clamp experiments.

In the more complex case of the Na^+ current (I_{Na}), the channel opening is described by three identical activation gates (m, increasing open probability) and one inactivation (h, decreasing open probability) gate. The transitions of this gates are considered independent, and thus I_{Na} can be computed from:

$$I_{Na} = g_{Na} \cdot m^3 \cdot h \cdot (V - E_{Na})$$

where g_{Na} is time, and E_{Na} represents the Nernst potential for Na^+.

Markov models are an alternative class of models that describe the gating behaviors using state-dependent transition frameworks and can account for activation and inactivation coupling of ion channels, i.e., to overcome the limitation of independent gates in the HH formalism. Typically, Markov models can be represented by state transition graphs with a collection of states connected with edges dictating transition rates between the states (**Fig. 1.11**). These states of Markov models are not necessarily linked to channel's structure, although such structural data can be incorporated to account for molecular level details in which individual

nodes of the graph corresponds to discrete channel conformational state (Yang *et al.*, 2020; Mangold & Silva, 2020). We have used Markov models of LCC and RyR to replicate 1) the Ca^{2+}-dependent inactivation (CDI), voltage-dependent inactivation (VDI) and time-dependence of LCC gating and 2) (both cytosol and SR) Ca^{2+}-dependence and CSQ-regulation of RyR gating. More details will be discussed in chapter 2.

Computational and theoretical approaches have been central to establishing what we know of the fundamental structure-function relationships in EC-coupling (Bers & Grandi, 2011; Heijman *et al.*, 2016). Several atrial myocyte models have been generated that include an increasingly sophisticated representation of the gradients in intracellular Ca^{2+} concentration occurring during a normal cardiac cycle. These models are discussed in this section.

1.6.1 Common-pool human atrial myocyte models

Most atrial myocyte models treat the intracellular space as single homogenized volumes, termed common-pool models. The first of such models was developed in 1987 by Hilgemann and Noble to replicate the atrial cell (rabbit) action potential (Hilgemann & Noble, 1987). In 1998, the first human atrial cell models that focused on dynamic atrial electrophysiological properties were published by Courtemanche et al. and Nygren et al. (Nygren *et al.*, 1998; Courtemanche *et al.*, 1998). These models have been updated over the last two decades to produce variants replicating atrial regional heterogeneity and to include new experimental evidence. The latter included incorporating charge conservation for the stimulus current (Jacquemet, 2007), and adding several K^+ currents to improve AP rate-dependence (Maleckar *et al.*, 2009). Despite these updates, these models still lacked detailed information specifically on human atrial cardiomyocyte Ca^{2+} handling, and as such newer models were developed to integrate more details on atrial Ca^{2+} handling. In 2011, Grandi *et al*. published a detailed human atrial cell model featuring dynamic Ca^{2+} changes in cleft and subsarcolemmal compartments,

where Ca^{2+} raises higher and more rapidly than in the bulk cytosolic space (**Fig. 1.10C**), human-specific parameterization of Ca^{2+} handling properties, and accounted for β-adrenergic and cholinergic regulation, as well as atrial AP morphology heterogeneity and differences in the right vs. left atrium. An important feature of this model was the incorporation of new human-derived data on global Ca^{2+} cycling, which allowed examining the effects of Ca^{2+} and Na^{+} homeostasis on human atrial electrophysiological properties (Grandi *et al.*, 2011). Since then, the Grandi model has been updated with new formulations of Na^{+}-dependent regulation of I_{K1} and $I_{K,Ach}$ (Voigt *et al.*, 2013), inclusion of $K_{2P}3.1$ K^{+} current (Schmidt *et al.*, 2015*a*), a Markov model of I_{Na} accounting for non-equilibrium gating (Morotti *et al.*, 2016*b*), a Markov model of I_{Kur} (Ellinwood *et al.*, 2017*a*, 2017*b*), and the formulations of I_{SK} and I_{K2P} (Schmidt *et al.*, 2015*b*; Ni *et al.*, 2020).

1.6.2 Spatial representation of atrial myocytes Ca^{2+} handling

Myocyte models commonly assume homogeneous membrane voltage throughout the cell. This is representative of the fast diffusion of membrane electrical signal which allows all membrane ion channels, transporters, and pumps to approximately share the same global voltage within a cardiac myocyte. However, because common-pool models cannot capture the underlying mechanisms and dynamics of the local Ca^{2+} handling (Sato *et al.*, 2013), recent models have begun to integrate subcellular spatial details to replicate the local Ca^{2+} signaling and thus ultrastructure-function observed in myocytes (Colman *et al.*, 2022).

Based on the Nygren and Maleckar model, in 2011, Koivumäki et al. published a human atrial myocyte model that includes atrial-specific Ca^{2+} dynamic and one-dimensional spatial representation of subcellular Ca^{2+} handling, by accounting for transversal diffusion in both the cytosol and SR (Koivumäki *et al.*, 2011). The transversal segment in the Koivumäki model

allows replication of Ca^{2+} wave propagation in the absence of TTs, which affect the properties of whole-cell Ca^{2+} transients and AP.

To better understand Ca^{2+} regulation in a higher dimension, Voigt et al. updated the Grandi model with a Markov model of RyR gating and two-dimensional (18 segments in transverse and 50 segments in longitude) spatial details of the Ca^{2+} handling and investigated how paroxysmal AF-induced RyR and SERCA dysregulations collectively cause spontaneous Ca^{2+} release and membrane voltage instability. This model was later updated to simulate altered RyR (heterogeneous and inter-band) distribution and tubular organization (adding both transversal and axial tubules) based on super-resolution subcellular RyR images (Sutanto *et al.*, 2018). Simulations with this model indicate that Ca^{2+} wave propagation is enhanced by smaller inter-band distance, and spontaneous Ca^{2+} release events are significantly larger in cells with greater RyR heterogeneity and hyperphosphorylation of RyRs close to axial-tubules. In a recent study, Vagos et al. updated this model with more recent experimental data. Their results highlight the strong effect of I_{Ca} changes in driving Ca^{2+} signal silencing (failed propagation of the Ca^{2+} wave to the myocyte center), and identify NCX and SERCA as major contributors to Ca^{2+} alternans (Vagos *et al.*, 2021).

Thul et al. developed a novel three-dimensional atrial myocyte model devoid of tubules using a lattice of discrete Ca^{2+} release units, highlighting the role of SR Ca^{2+}-release strength and RyR activation threshold in centripetal Ca^{2+} wave propagation, and generating rotating waves of partial SR Ca^{2+} release (ping waves) (Thul *et al.*, 2012). In more recent models, each CRU is further partitioned into more necessary compartments (i.e., cytosol, cleft, submembrane, junctional-SR, network-SR), and each CRU is diffusively coupled with neighboring CRUs. Importantly, new three-dimensional models of atrial myocytes were integrated with idealized tubular structures and were able to demonstrate that loss of tubules promotes pro-arrhythmic spontaneous Ca^{2+} releases (Shiferaw *et al.*, 2017; Marchena & Echebarria, 2018; Shiferaw *et*

al., 2018, 2020*a*; Marchena & Echebarria, 2020*a*; Greene & Shiferaw, 2021). Colman et al. integrated experimental image-based tubular structures into an updated three-dimensional model of human atrial myocytes, indicating loss of tubules promotes both alternans and spontaneous Ca^{2+} releases (Colman *et al.*, 2016*a*).

Major limitations of these prior models and studies include the lack of human-atria specificity and/or sufficient experiment-based validation. Furthermore, most studies do not account for the vast heterogeneity in experimental data describing human atrial subcellular structure, Ca^{2+} handling and electrophysiology. As such, to address these issues and generate a powerful tool for investigating Ca^{2+} handling and arrhythmia mechanisms in atrial cells, we developed a model of a human atrial myocyte with three-dimensional details and validation against heterogeneous human-atria-specific experimental data (**Fig. 1.10B-C**). We applied a random-walk algorithm to build a population of TATS replicating that characterized in human atrial experiments. As such, the new model reflects human-specific atrial subcellular structural details, local and global Ca^{2+} handling and electrophysiology (**Fig. 2.1Aiii and B**). Our new model allows us to mechanistically link the disruption of subcellular structures to spatial heterogeneity of Ca^{2+} handling to Ca^{2+}-driven arrhythmia in human atria.

1.6.3 Models of Ca^{2+} handling protein function

The biophysically detailed cell models described above integrate explicit descriptions of transmembrane ion channels, transporters and exchangers, and Ca^{2+} buffers that regulate transmembrane voltage and Ca^{2} dynamics, in this section, we will illustrate the main Ca^{2+}-handling proteins involved in ECC, their properties, and their mathematical descriptions (**Fig. 1.10A-C**).

1.6.3.1 Models of Ca^{2+} channels

L-type Ca^{2+} channel: LCCs are major channels regulating Ca^{2+} influx. LCC opening is low during the diastolic period but activated by voltage depolarization to conduct large and long Ca^{2+} influx. LCC opening is enhanced by phosphorylation by PKA and CaMKII (Yue *et al.*, 1990; Dzhura *et al.*, 2000). The termination (i.e., inactivation) of LCCs depends on both intracellular Ca^{2+}-binding (i.e., CDI) and membrane voltage (i.e., VDI). Reduced I_{Ca} is reported in AF (Van Wagoner *et al.*, 1999; Christ T. *et al.*, 2004; Voigt *et al.*, 2012) and thought to contribute to shorten of AP duration and refractory period, and to impair their adaptation to changes in stimulation rate (Van Wagoner *et al.*, 1999).

LCC properties and their regulation by varying intracellular pathways have been described by modern mathematical models using either the HH framework or Markovian representations. The HH framework of LCC current has a maximal current parameter (I_s) and three typical gating variables (i.e., time- and voltage-dependent activation gating variable, d, time- and voltage-dependent inactivation variable, f, voltage-independent, time- and Ca^{2+}-dependent inactivation variable, f_{Ca}):

$$I_{Ca} = d \cdot f \cdot f_{Ca} \cdot I_s$$

The maximal current parameter I_s can be quantified by the Goldman-Hodgkin-Katz current equation:

$$I_s = P_{Ca} \cdot z^2 \cdot \frac{\gamma_i \cdot [Ca^{2+}]_i \cdot e^{\frac{zVF}{RT}} - \gamma_0 \cdot [Ca^{2+}]_O}{e^{\frac{zVF}{RT}} - 1}$$

where P_{Ca} is the constant permeability and γ_i and γ_0 are ionic activity coefficients of Ca^{2+} ions in the intra- and extracellular spaces, respectively (Shannon *et al.*, 2004; Tomek *et al.*, 2019). In contrast, the Markovian representations of LCC were developed to incorporate our biophysical understanding of CDI and VDI, based on experiments using Ca^{2+} buffers and/or replacing Ca^{2+} with Ba^{2+} to limit CDI and this reveal the distinct contributions of CDI

and VDI (Jafri *et al.*, 1998; Mahajan *et al.*, 2008; Restrepo *et al.*, 2008). While the whole-cell current is the averaged behavior of an ensemble of ion channels, to replicate the stochastic single LCC channel opening and closing, randomness was integrated to regulate the transient rate between states (Mahajan *et al.*, 2008; Sato *et al.*, 2018). In our study, we extended the model to improve the fitting of LCC CDI and VDI (both single channel and whole-cell current), as described in Chapter 2 and **Fig. 2.2**.

Ryanodine receptor: RyRs are tetrameric proteins that facilitate SR Ca^{2+} release (Yuchi & Van Petegem, 2016; Williams *et al.*, 2018). RyR opening probability (P_O) is regulated by intracellular and extracellular [Ca^{2+}] (Györke & Györke, 1998) and varying binding proteins, e.g., Calsequestrin, Triadin, and Junctin (Györke *et al.*, 2004). Under a myriad of disease-induced changes, disruption of RyR properties contributes to abnormal Ca^{2+} signaling and thus arrhythmia (Dobrev *et al.*, 2011; Denham *et al.*, 2018). In particular, increased RyR channel expression in paroxysmal AF likely induced increased SCRs in myocytes isolated from patients (Beavers *et al.*, 2013; Voigt *et al.*, 2014). Conversely, a reduction in RyR expression is seen in several animal models of atrial tachycardia remodeling as part of the underlying proarrhythmic substrate (Lenaerts *et al.*, 2009; Wakili *et al.*, 2010; Lugenbiel *et al.*, 2015). Notably, despite reduced total RyR protein levels in the atria of patients with HF, RyR function was found to be increased (Molina *et al.*, 2018). Additionally, AF is associated with RyR hyperphosphorylation (Vest *et al.*, 2005; Neef *et al.*, 2010; Voigt *et al.*, 2012) and thus larger diastolic SR leak and elevated Ca^{2+} levels (Neef *et al.*, 2010).

RyRs are arranged in well-organized clusters, with transverse spacing around 1μm and inter-band spacing between longitudinally interspersed RyR clusters less than 2μm (Chen-Izu *et al.*, 2006). A surface-to-inner gradient of the RyR expression (Herraiz-Martínez *et al.*, 2022) and cluster size (Smith *et al.*, 2022) has been reported in atrial myocytes. The morphology of RyR clusters is an important mediator in the Ca^{2+} signaling (Galice *et al.*, 2018 p.20), with

disrupted morphology and distribution of RyR clusters observed in the disease (Li *et al.*, 2015; Kolstad *et al.*, 2018). Whilst these spatial differences exist in the healthy atria, complex remodeling occurs in AF involving RyR cluster fragmentation and redistribution to inter-z-line areas, with Ca^{2+} sparks increased in fragmented CRUs (Macquaide *et al.*, 2015). Multiple in-silico studies indicated that 1) larger RyR clusters, smaller spacing, and reduced RyR-RyR coupling promote larger and longer Ca^{2+} sparks (Walker *et al.*, 2014; Song *et al.*, 2016; Sato *et al.*, 2016; Galice *et al.*, 2018) and 2) disease-induced disruption of RyR clusters and their subcellular distribution (e.g., increased heterogeneity and inter-band RyR) enhances pro-arrhythmic Ca^{2+} sparks (Sutanto *et al.*, 2018). However, at present, the surface-vs-inner gradient of RyR expression on Ca^{2+} handling and arrhythmias is currently unclear. This will be further discussed in Chapter 3.

To understand the role of RyRs at multiple scales (i.e., from molecular- to organ level), a physiologically accurate mathematical description of RyR kinetics in health and disease is needed. An ideal RyR model should not only replicate the experimental observations of RyR kinetics but also conduct robustly in the context of the multiple interacting components of the subcellular or cell-level computational models of Ca^{2+} homeostasis. Multiple well-established (2-, 3-, and 4-state) RyR Markov models have been commonly used to replicate RyR kinetics (i.e., opening, closing, inactivation, and refractoriness) and systolic/diastolic Ca^{2+} regulation (e.g., SR leak, Ca^{2+} sparks, and Ca^{2+} wave) (Colman *et al.*, 2022). Each of the models is designed to replicate part of RyR kinetics and Ca^{2+} dynamic features but may be parameterized for different purposes, e.g., maintaining stable Ca^{2+} homeostasis, or reproducing spontaneous Ca^{2+} sparks at the appropriate frequency.

In our study, we used the RyR model in (Sato & Bers, 2011) and modified the model parameters to replicate (both cleft and SR) Ca^{2+}-dependence of RyR P_O (**Fig. 2.2B**). Both the subcellular and whole cell CICR properties and electrophysiology (**Figs. 2.2C, 2.3B-C, 2.4-**

2.6) are well reproduced in the whole-cell model. Furthermore, we applied this model to examine how RyR alterations (in RyR expression, regulation, and localization as reported in AF patients) affect the Ca^{2+}-driven arrhythmia (**Figs. 2.2B, 2.11 and Figs. 3.6-3.9**).

1.6.3.2 Models of Ca^{2+} pumps and exchangers

In cardiac myocytes, intracellular Ca^{2+} removal from the cytosol following contraction is mainly conducted by SERCA, NCX, and PMCA (Bers, 2002), with their relative contributions varying between myocyte types and species. As with LCC and RyR, disease-induced remodeling of Ca^{2+} removal damages the regular Ca^{2+} dynamics and thus facilitates arrhythmia.

Sarco-endoplasmic reticulum Ca^{2+}-ATPase: SERCA is the most important Ca^{2+} transporting ATPase in the heart. Its role is to return intracellular Ca^{2+} to the SR after CICR and during the diastolic period. Under steady-state conditions, SERCA uptakes the same amount of Ca^{2+} released by RyR (~ 60%–70% of the Ca^{2+} participating in CICR and cell contraction in humans (Voigt *et al.*, 2012)). SERCA uptake is regulated by cytosolic and SR $[Ca^{2+}]$, pH, ATP level, and PLB phosphorylation.

The relationship between SERCA function and cytosolic $[Ca^{2+}]$ is commonly described with Michaelis-Menten formalism:

$$J_{up} = V_{max} \cdot \frac{[Ca^{2+}]_i}{K_m + [Ca^{2+}]_i}$$

where V_{max} is the maximal pump velocity, and K_m is the Ca^{2+} concentration for half-maximal flux.

To incorporate $[Ca^{2+}]_{SR}$-dependence, two main formulations are utilized:

1) adding SR Ca^{2+} leak flux (J_{leak}) to balance SERCA uptake, which has two common formats.

$$J_{leak} = k_{leak} \cdot ([Ca^{2+}]_{SR} - [Ca^{2+}]_i) \quad \text{or} \quad J_{leak} = J_{up} \cdot \frac{[Ca^{2+}]_{SR}}{k_{SR\,max}}$$

where k_{leak} is a scaling factor (mM ms^{-1}) for SR-cytosol [Ca^{2+}] gradient to calculate a passive and constant release leak flux J_{leak}, and $k_{SR\,max}$ is the constant maximum concentration of $[Ca^{2+}]_{SR}$ where leak flux is close to uptake flux.

2) applying a thermodynamic constraint to set net SERCA flux as the sum of the forward and reverse Hill-type process (Shannon *et al.*, 2004).

$$J_{up} = \frac{V_{max,f}\left(\frac{[Ca^{2+}]_i}{k_{m,f}}\right)^2 - V_{max,r}\left(\frac{[Ca^{2+}]_{SR}}{k_{m,r}}\right)^2}{1 + \left(\frac{[Ca^{2+}]_i}{k_{m,f}}\right)^2 + \left(\frac{[Ca^{2+}]_{SR}}{k_{m,r}}\right)^2}$$

where $V_{max,f}$ and $V_{max,r}$ are constant parameters determined by SERCA number and maximal flux, and $k_{m,f}$ and $k_{m,r}$ are constant parameters regulating the dependence on $[Ca^{2+}]_i$ and $[Ca^{2+}]_{SR}$.

Other regulation factors (e.g., PLB-phosphorylation-induced changes in cytosolic Ca^{2+} affinity, PH-sensitivity, APT-sensitivity) have also been integrated into this framework (Saucerman *et al.*, 2003; Tran *et al.*, 2009; Soltis & Saucerman, 2010).

Sarcolemmal Ca^{2+} pump: PMCA is a pump embedded in the sarcolemmal membrane. It is a minor removal pathway (~2%) for the extrusion of intracellular Ca^{2+} from the cytosol to the extracellular space (Bers, 2001). It is also quantitatively described using a Michaelis-Menten scheme.

$$J_{PMCA} = V_{max} \cdot \frac{[Ca^{2+}]_i}{K_m + [Ca^{2+}]_i}$$

where V_{max} is the maximum SERCA flux parameter, K_m is the Ca^{2+} concentration constant parameter for half-maximum SERCA flux.

Sarcolemmal Na^+-Ca^{2+} exchanger: NCX conducts an electrogenic coupled antiport action between 3 Na^+ and 1 Ca^{2+} ion. In most conditions, NCXs extrude Ca^{2+} and generate inward currents, accounting for 10%~40% of Ca^{2+} removal (Voigt *et al.*, 2012). Under steady

state, Ca^{2+} efflux via NCX should be approximately equal to Ca^{2+} influx via LCC on each beat (Bers, 2002; Eisner *et al.*, 2017; Eisner, 2018). However, when the membrane voltage is larger than NCX net Nernst equilibrium ($3E_{Na^+} - 2E_{Ca^{2+}}$), NCX can also operate in reverse mode to extrude Na^+ and conduct Ca^{2+} influx.

Mathematical descriptions of NCX commonly have 1) maximal exchange velocity, 2) allosteric activation by $[Ca^{2+}]_i$, and 3) a thermodynamic component involving the full voltage- and ion-binding-dependencies of the transport mechanism (Weber *et al.*, 2001). NCX dynamics have also been described in a Markov model with full thermodynamic cycling, incorporating interaction within and between $[Ca^{2+}]$-binding domains and Ca^{2+}-independent steps in the activation (Chu *et al.*, 2016).

1.6.3.3 Models of Ca^{2+} buffers and diffusion

Ninety-nine percent of intracellular Ca^{2+} ions are associated with intracellular buffers (e.g., myofilament and membrane phospholipids in the cytosol, and CSQ in the SR), which facilitate stable Ca^{2+} cycling (Bers, 2002).

In many cardiac cell models, Ca^{2+} buffering is simulated dynamically:

$$Ca^{2+} + B \Leftrightarrow CaB$$

$$\frac{dCaB}{dt} = k_{on} \cdot [Ca^{2+}] \cdot ([B_{tot}] - [CaB]) - k_{off} \cdot [CaB]$$

where the total concentration of buffer molecules $[B_{tot}]$, the rate of association k_{on}, and the rate of dissociation k_{off} are decided based on experimental data.

Other cell models are more complex and will be discussed in the next section.

Partial differential equations (PDE) are applied to simulate the diffusion of free Ca^{2+} ions and mobile Ca^{2+} buffers (CaB, e.g., ATP and fluorophores).

$$\frac{\delta Ca^{2+}}{\delta t} = D_{Ca} \triangle [Ca^{2+}] + f(Ca) - f(CaB)$$

$$\frac{\delta CaB}{\delta t} = D_{CaB} \triangle [CaB] + f(CaB)$$

where D_{Ca} and D_{CaB} are diffusion coefficients for free Ca^{2+} and Ca^{2+} bound, $f(Ca)$ describes local Ca^{2+} net flux and $f(CaB)$ describes the sum of the various local buffering reactions. $D_{CaB} = 0$ for stationary buffers.

In these settings, the computational cost is much higher, thus the dynamics of some rapid buffers were simplified as being at equilibrium (i.e., rapid buffering approximation) to reduce the simulation cost:

$$CaB = \frac{B_{tot} \cdot [Ca^{2+}]}{K_d + [Ca^{2+}]}$$

1.6.4 Model simplification

While cellular models listed above produce mechanistic understanding of cardiac myocyte electrophysiology and pathophysiology, these frameworks can be simulated within tissue- and/or organ-level simulations for additional translational insight (**Fig. 1.10D**). Both tissue-level and organ-level simulations require the electronic coupling of numerous single-cell models, which produce tissue-specific phenomenon (i.e., reentry). However, tissue (i.e., multi-cellular) simulation based on biophysically-detailed cell models demand a high computational cost. As such, new approaches are needed to simplify model but preserve underlying stochastic dynamics and emergent phenomena, especially Ca^{2+} regulation (Rovetti *et al.*, 2007; Asfaw *et al.*, 2013; Colman *et al.*, 2022).

The spatial-detailed cell models are commonly simplified by: 1) describing LCC and RyR dynamics with less equations and variables (Williams *et al.*, 2007, 2008; Cantalapiedra *et al.*, 2017), 2) calculating CRU Ca^{2+} concentration only based on previous beat cytosol and SR Ca^{2+} concentration (Romero *et al.*, 2019), 3) describing the CRU Ca^{2+} dynamics by a 2-state (i.e., spark and non-spark) model (Chen *et al.*, 2011; Hernandez-Hernandez *et al.*, 2015).

The common-pool cell models are commonly simplified by: 1) describing the Ca^{2+} dynamics by a 2-state (i.e., release and no-release) model (Chen *et al.*, 2012), 2) simulating number of active CRUs to track the evolution of Ca^{2+} dynamics (Shiferaw *et al.*, 2018, 2020*a*) 3) describing the AP and Ca^{2+} dynamics by multi-biomarker nonlinear equations, including AP duration, diastolic interval, peak of Ca^{2+} transient, diastolic Ca^{2+} concentration, total Ca^{2+} release, and SR load (Qu *et al.*, 2007), 4) describing SR release directly based on imposed SCR waveforms (Xie *et al.*, 2010; Liu *et al.*, 2015, 2016; Ko *et al.*, 2017) or RyR states (Colman *et al.*, 2017; Colman, 2019).

Structurally detailed models based on simplified cell models are developed to understand the role of SCRs, Ca^{2+} transient alternans and related factors (e.g., ionic and structural remodeling) on arrhythmia, such as reentry and abnormal focal activity (Alvarez-Lacalle *et al.*, 2015; Campos *et al.*, 2015, 2017, 2018, 2019; Romero *et al.*, 2019; Conesa *et al.*, 2020).

1.7 Gaps in previous research

Over the past several years, substantial progress has been made in understanding the basic properties of atrial electrophysiology and ionic homeostasis in health and disease.

Experimental studies have decomposed the electro-ionic processes in atrial myocytes from AF patient samples, and mathematical models have made important contributions to our mechanistic understanding, by reintegrating those mechanisms in comprehensive mathematical and computational models of the human atrial myocyte. Nevertheless, limitations of existing experimental methods make it difficult to decouple the contributions of ionic and structural remodeling at the cellular level. The broad uncertainties and challenges in existing experimental datasets have carried through to the modeling efforts built upon them. While sophisticated models have been developed to describe detailed spatial and temporal

characteristics of cardiac myocyte ECC, simulations of perturbed TATS structure have been heuristic in their approach, rather than tightly coupled to experiments. Further, the impact of subcellular variability has only been partially investigated. No effort to date has attempted to systematically decompose the role of ultrastructural degradation specifically in human atrial arrhythmia and pathophysiology. This dissertation describes work to address these unresolved questions.

Chapter 2 Mechanisms of spontaneous Ca^{2+} release-mediated arrhythmia in a novel 3D human atrial myocyte model: I. Transverse-axial tubule variation

The content of this chapter has been published in:

Zhang X., Ni H., Morotti S., Smith C., Sato D., Louch W., Edwards A., Grandi E., "Mechanisms of spontaneous Ca2+ release-mediated arrhythmia in a novel 3D human atrial myocyte model: I. Transverse-axial tubule variation" The Journal of Physiology (2022), DOI: 10.1113/JP283363

Abstract

Intracellular calcium (Ca^{2+}) cycling is tightly regulated in the healthy heart ensuring effective contraction. This is achieved by transverse (t)-tubule membrane invaginations that facilitate close coupling of key Ca^{2+}-handling proteins such as the L-type Ca^{2+} channel (LCC) and Na^{+}-Ca^{2+} exchanger (NCX) on the cell surface with ryanodine receptors (RyRs) on the intracellular Ca^{2+} store. Though less abundant and regular than in the ventricle, t-tubules also exist in atrial myocytes as a network of transverse invaginations with axial extensions known as the transverse-axial tubule system (TATS). In heart failure and atrial fibrillation there is TATS remodeling that is associated with aberrant Ca^{2+}-handling and Ca^{2+}-induced arrhythmic activity, however the mechanism underlying this is not fully understood. To address this, we developed a novel 3D human atrial myocyte model that couples electrophysiology and Ca^{2+}-handling with variable TATS organization and density. We extensively parameterized and validated our model against experimental data to build a robust tool examining TATS regulation of subcellular Ca^{2+} release. We found that varying TATS density and thus the localization of key Ca^{2+}-handling proteins has profound effects on Ca^{2+} handling. Following TATS loss there is reduced NCX that results in increased cleft Ca^{2+} concentration through decreased Ca^{2+} extrusion. This elevated Ca^{2+} increases RyR open probability causing spontaneous Ca^{2+} releases and promotion of arrhythmogenic waves (especially in the cell interior) that leads to voltage instabilities through delayed afterdepolarizations. In summary, this study demonstrates a mechanistic link between TATS remodeling and Ca^{2+}-driven proarrhythmic behavior that likely reflects the arrhythmogenic state observed in disease.

2.1 Introduction

Intracellular Ca^{2+} is an important determinant of both contractile and electrophysiologic function of cardiac myocytes through the process of excitation-contraction coupling (ECC). Dysregulation of Ca^{2+} cycling is known to be the primary driver of arrhythmia in specific diseases or drug-responses (e.g., catecholaminergic polymorphic ventricular tachycardia, digoxin toxicity), and also contributes to more common arrhythmogenic conditions with broader pathophysiologic changes, such as atrial fibrillation (AF) and heart failure (HF) (Denham *et al.*, 2018). It has long been known that disease-induced ionic remodeling can lead to abnormal Ca^{2+} handling (Denham *et al.*, 2018); however, subcellular structural remodeling can also contribute to the observed alterations. Transverse tubules (TTs) are invaginations of the sarcolemma that play a key role in ECC in ventricular myocytes by closely (≤ 20 nm, see recent estimates in (Rog-Zielinska *et al.*, 2021*a*)) juxtaposing sarcolemmal voltage-gated L-type Ca^{2+} channels (LCCs) with ryanodine receptors (RyRs) on the membrane of the sarcoplasmic reticulum (SR) to facilitate rapid and synchronous Ca^{2+}-induced Ca^{2+} release (CICR) (Fabiato, 1983; Cheng *et al.*, 1993; Bers, 2002), and efficient fluid exchange between TT lumens and extracellular areas (Hong *et al.*, 2014; Rog-Zielinska *et al.*, 2021*b*). TTs were historically thought to be absent in atrial myocytes (Hüser *et al.*, 1996; Greiser *et al.*, 2014) thus limiting triggered CICR to the cell periphery with release in the cell interior reliant on propagation through recruitment of the inner RyRs (Blatter *et al.*, 2003). More recently, however, several studies have demonstrated an extensive TT network in the atria of a variety of species, though less dense and organized, and more variable than in ventricles. Interestingly, in contrast to the ventricle, evidence suggests that longitudinally-oriented axial tubules may be prominent in atrial myocytes and provide extensive transverse-axial tubule (TAT) extensions of sarcolemmal invaginations that also couple RyRs with membrane ion channels (Arora *et al.*, 2017; Brandenburg *et al.*, 2018, 2019). Indeed, using super resolution (stimulated emission

depletion) microscopy Brandenburg et al. (2018) clearly revealed the existence of a transverse-axial tubular system (TATS) in atrial myocytes from numerous species . Varying TATS density and organization has been reported in different cardiac regions (left/right chamber, endo-/epicardium) (Kirk *et al.*, 2003; Frisk *et al.*, 2014; Glukhov *et al.*, 2015; Arora *et al.*, 2017; Brandenburg *et al.*, 2018) and species, e.g., mouse (Yue *et al.*, 2017; Brandenburg *et al.*, 2018), rat (Kirk *et al.*, 2003; Rasmussen *et al.*, 2004; Woo *et al.*, 2005; Dibb *et al.*, 2009; Trafford *et al.*, 2013; Frisk *et al.*, 2014; Glukhov *et al.*, 2015; Brandenburg *et al.*, 2018), canine (Dolber *et al.*, 1994; Melnyk *et al.*, 2002; Trafford *et al.*, 2013), rabbit (Greiser *et al.*, 2014; Brandenburg *et al.*, 2018), pig (Frisk *et al.*, 2014; Gadeberg *et al.*, 2016; Brandenburg *et al.*, 2018), cow (Richards *et al.*, 2011), horse (Richards *et al.*, 2011), sheep (Dibb *et al.*, 2009; Lenaerts *et al.*, 2009; Caldwell *et al.*, 2014), and human (Richards *et al.*, 2011; Brandenburg *et al.*, 2018).

The importance of the TATS in atrial cells is highlighted by the impact of its remodeling in disease, namely in AF. AF is the most common cardiac arrhythmia in the clinical setting and is associated with substantial morbidity and mortality, particularly due to increased risk of stroke and worsening HF. AF patients often first display short (< 7 days) self-terminating episodes (paroxysmal AF) before exhibiting persistent and chronic states (Nattel, 2011, 2013). The cellular and molecular arrhythmogenic mechanisms have been studied extensively in both animal models and human samples from cardiac surgery patients (Dobrev & Ravens, 2003; Nattel *et al.*, 2007; Nattel & Dobrev, 2012; Andrade *et al.*, 2014; Dobrev & Wehrens, 2017; Denham *et al.*, 2018). TATS alterations are known to be a major contributor to AF (Trafford *et al.*, 2013), combining with ionic remodeling to destabilize the bidirectional interaction between electrical activation and Ca^{2+} signaling in atrial myocytes. TATS remodeling may importantly contribute to the pathology of AF, as it does in the ventricle during HF (Guo *et al.*, 2013) where it is an early remodeling event (Wei *et al.*, 2010). Currently, limitations in existing experimental methods make it difficult to separate the independent contributions of ionic and

structural remodeling at the cellular level. Furthermore, while clear, though variable, TATS are seen in human tissue (Richards *et al.*, 2011), only sparse TATS have been reported in isolated human atrial myocytes (Greiser *et al.*, 2014), most likely due to membrane damage during enzymatic digestion (Chen *et al.*, 2015). These challenges limit our mechanistic and quantitative understanding of the precise role of TATS variability in health and TATS remodeling in human AF. Indeed, while disruption of TATS architecture is associated with arrhythmia in numerous states (e.g., in ventricular myocytes in HF, and myocardial infarction (Louch *et al.*, 2006)), a direct mechanistic link between remodeling of atrial myocyte ultrastructure and arrhythmogenesis has not yet been established. In this context, mathematical models are powerful tools to both fill the gaps in the available data sources and reveal the independent contributions of TATS remodeling. Over the last decade, computational models have been developed including detailed spatial and temporal characteristics of myocyte Ca^{2+} signaling, accounting for thousands of stochastic Ca^{2+} release units, connected with the global (whole-cell) electrophysiologic behavior (Shiferaw *et al.*, 2005; Song *et al.*, 2015). These sophisticated models have been employed to study how varying cell structural properties affect local and global atrial Ca^{2+} signaling, ECC, and the development of alternans and spontaneous Ca^{2+} release (SCRs) (Colman *et al.*, 2016*b*; Shiferaw *et al.*, 2017, 2018, 2020*b*; Marchena & Echebarria, 2018, 2020*b*; Sutanto *et al.*, 2018). Experimentally, spontaneous Ca^{2+} release (SCR) and delayed afterdepolarizations (DADs) have been shown to precede the development of classical markers of ionic remodeling in AF (Voigt *et al.*, 2014), and while RyR hyperactivity is clearly involved (Voigt *et al.*, 2012, 2014), computational analyses suggest that complete detubulation could provide an additional mechanism for increased SCR and DADs during Ca^{2+} overload (Li *et al.*, 2012). Though simulations of perturbed TATS structure have been performed, they have typically been heuristic in their approach, with limited coupling to experiments and sporadic robust validation of the coupling of voltage and Ca^{2+} dynamics.

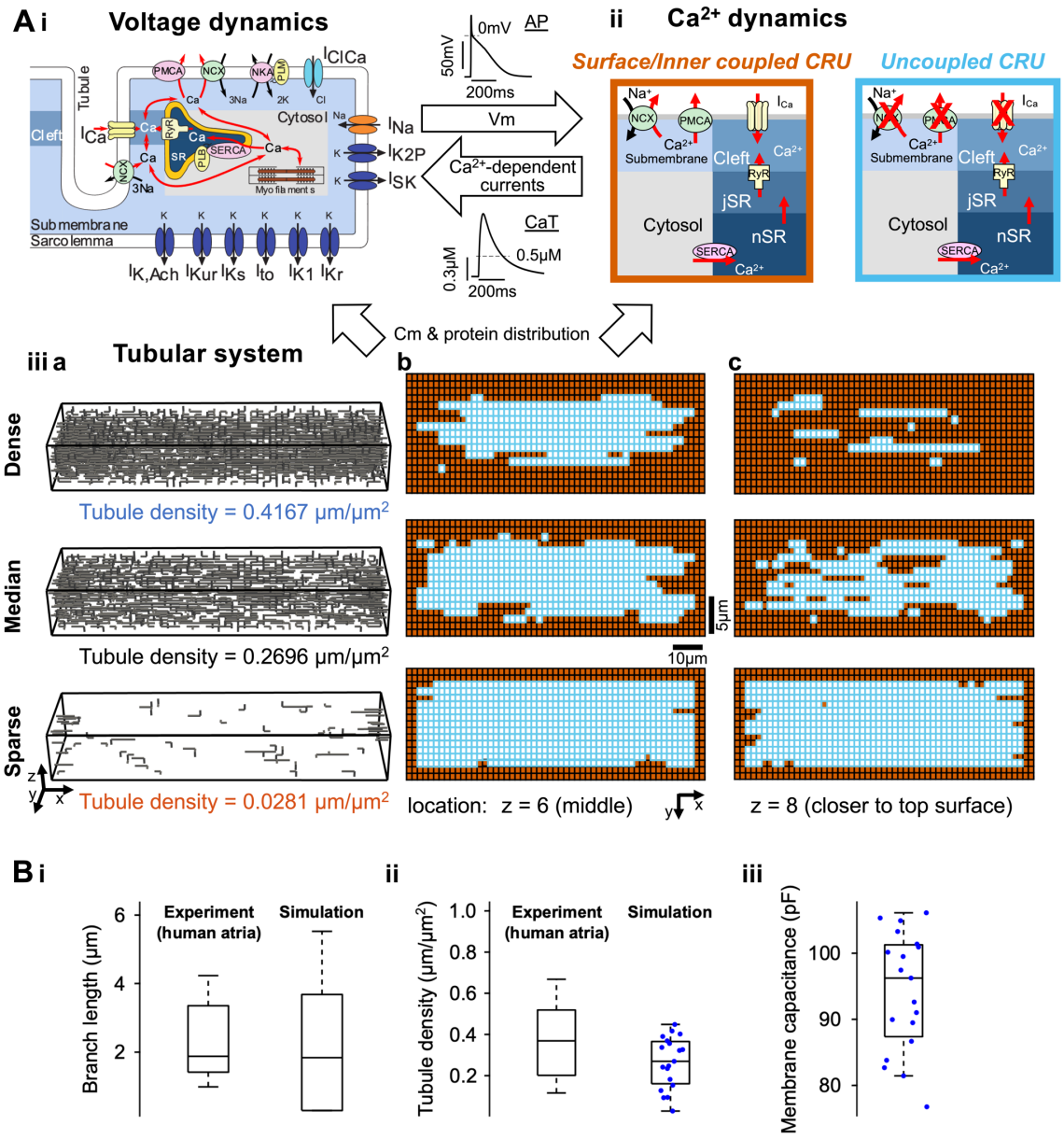

Figure 2.1 – Schematic of model structure and tubular generator features.

A) Model structure schematic showing membrane voltage dynamics (i) are coupled with Ca^{2+} dynamics (ii) by voltage and Ca^{2+}-related currents. Both are also interdependent on the tubular system (iii) whereby tubular structures govern membrane capacitance and sarcolemmal protein distribution. Dependent on ultrastructure, the cell is spatially divided into small Ca^{2+} release units (CRUs). (iiia-iiic) Representative three-dimensional (3D) structures (a) and xy-plane cross-sections of coupled CRUs in central (b) and closer to the top surface (c) of cells with dense (0.4167 μm/μm^2, top row), median (0.2696 μm/μm^2, middle row) and sparse (0.0281 μm/μm^2, bottom row) tubular densities. Due to fewer t-tubules, sparsely tubulated cells have fewer coupled CRUs (orange) in both xy-plane cross-sections. Coupled CRUs are

more abundant in upper vs. central xy-planes in both dense and median tubulated cells due to initial tubule formation from the surface sarcolemma or as branches from existing tubules. Each CRU is divided into 5 compartments: cleft, submembrane, cytosol, junctional SR (jSR), and network SR (nSR). Ca^{2+} ions travel (diffuse or get carried) between neighboring compartments and CRUs. Those CRUs coupled with tubules or surface membrane (orange boxes) possess all membrane ion channels and exchangers; the uncoupled CRUs (blue boxes) do not and are devoid of membrane ion channels and exchangers. The membrane currents include LCC Ca^{2+} current (I_{Ca}), background sarcolemmal membrane Ca^{2+} current (I_{Cabk}), Ca^{2+}-activated Cl^- current (I_{ClCa}), fast Na^+ current (I_{Na}), background Na^+ current (I_{Nabk}), small-conductance Ca^{2+}-activated K^+ current (I_{SK}), Na^+/K^+ pump current (I_{NaK}), NCX current (I_{NCX}), sarcolemmal membrane Ca^{2+} pump (I_{PMCA}), acetylcholine-activated K^+ current ($I_{K,Ach}$), ultrarapid delayed rectifier K^+ current (I_{Kur}), slowly activating delayed rectifier K^+ current (I_{KS}), transient outward K^+ current (I_{to}), inward rectifier K^+ current (I_{K1}), rapidly activating delayed rectifier K^+ current (I_{Kr}), and 2-pore-domain K^+ current (I_{K2P}). **B)** Estimated tubular branch length (i) and tubular density (ii) in experimental studies (left) and the simulated population (right). The simulated population has 19 randomly generated tubular structures that were used to calculate membrane capacitance (iii). Experimental data are adapted from (Brandenburg *et al.*, 2018).

To quantitatively understand the mechanistic link between variation in human atrial ultrastructure and myocyte function and arrhythmogenesis, we built an integrative modeling framework coupling our common-pool model of the human atrial myocyte action potential (AP) (**Fig. 2.1Ai**) (Grandi *et al.*, 2011; Morotti *et al.*, 2016*b*) with a three-dimensional (3D) model of subcellular Ca^{2+} signaling (**Fig. 2.1Aii**) based on a rabbit ventricular myocyte (Restrepo *et al.*, 2008; Sato & Bers, 2011), with varying randomly generated TATS (**Fig. 2.1Aiii**) utilizing human atrial myocyte data (Brandenburg *et al.*, 2018). We first present our integrative model parameterization and validation against broad independent functional datasets, illustrating local and global Ca^{2+} handling and AP properties in the atria, and then interrogate the model to explain the relationship between the TATS, SCRs, and DADs in human atrial myocytes. We show that reducing TATS density leads to local increases in cleft Ca^{2+} concentration through

reduced Ca^{2+} removal by the Na^{+}-Ca^{2+} exchanger (NCX). This Ca^{2+} elevation drives cleft Ca^{2+}-dependent increases in RyR open probability (P_O) and subsequent SCRs that demonstrate how atrial TATS remodeling can lead to Ca^{2+}-driven proarrhythmic behavior. In a companion paper (Chapter 3), we used this robustly validated framework to study the independent effects of varying key Ca^{2+} handling protein expression and distribution on SCRs and DADs.

2.2 Methods

To describe the coupling of electrophysiology, Ca^{2+} signaling and ultrastructure of human atrial cardiomyocytes (**Fig. 2.1**), we merged the description of surface membrane ion channels/transporters that interact nonlinearly to shape AP dynamics (**Fig. 2.1Ai**), as described in (Grandi *et al.*, 2011; Morotti *et al.*, 2016*a*, 2016*b*), with updated models of the LCC current (I_{Ca}) and RyR Ca^{2+} release (I_{rel}) (**Fig. 2.2**) that gate stochastically in individual Ca^{2+} release units (CRUs, **Fig. 2.1Aii**) (Restrepo *et al.*, 2008; Sato & Bers, 2011). A population of tubular architectures (**Fig. 2.1Aiii**) was constructed to recapitulate experimental TATS features reported in human atrial myocytes (Brandenburg *et al.*, 2018) and integrated into the model. This ultrastructural detail determines whether any given CRU is coupled with sarcolemmal fluxes or remains uncoupled. The integrative model was reparametrized to recapitulate the rate-dependent properties of electrophysiology and Ca^{2+} dynamics (**Fig. 2.3A-C**, parameters in **Tables 2.1-2.3**). Rigorous model validation was then achieved by testing the capability of the model to simulate properties of electrophysiology, subcellular and whole-cell Ca^{2+} signaling in myocytes with varying TATS structures and subjected to various physiological challenges (**Figs. 2.2C, 2.3-2.6**). Our validated model was then applied to investigate the effects of variable TATS on arrhythmogenesis.

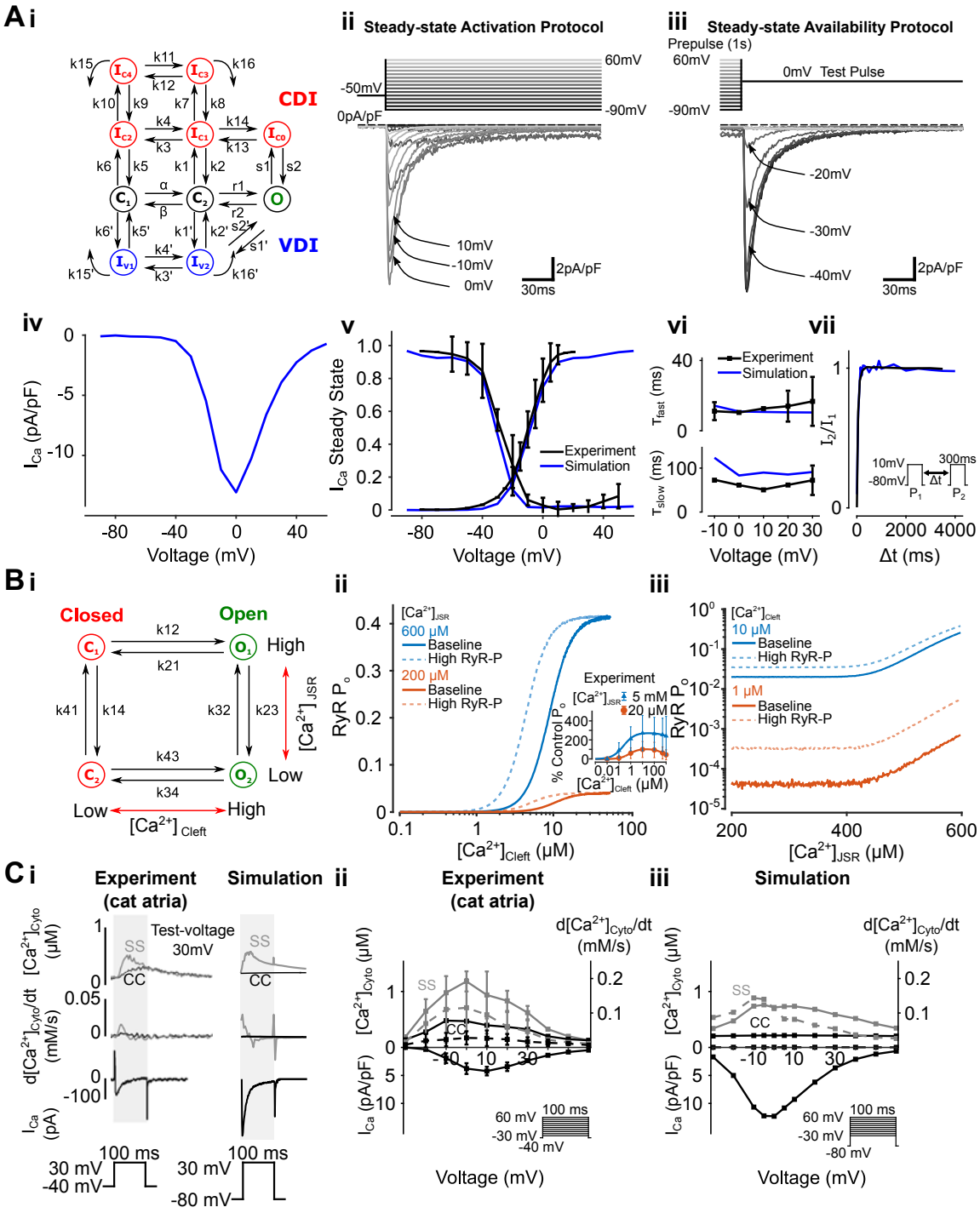

Figure 2.2 – Properties of LCC, RyR, and local Ca^{2+} signaling.

A) Schematic of LCC Markov model (i), representative traces of I_{Ca} in a cell with median tubules under steady-state activation (ii) and availability (iii) protocols. These data were used to calculate LCC current-voltage (IV) dependence (iv), activation-inactivation curve (v) and fast (top) and slow (bottom) decay time constants (vi). Time-dependent recovery was measured by P1P2 (pulse1-pulse2) protocol (insert),

with the ratio of P2- and P1-induced I_{Ca} (I_2/I_1) recovering steeply to 1.0 with increasing P1-P2 interval (Δt) (vii). Simulation results aligned with experimental observations adapted from (Li & Nattel, 1997). **B)** Schematic of RyR 4-state Markov model (i), dependence of RyR open probability (P_O) on $[Ca^{2+}]_{cleft}$ at $[Ca^{2+}]_{JSR}$ of 200 μM and 600 μM (ii), and $[Ca^{2+}]_{JSR}$ at $[Ca^{2+}]_{Cleft}$ of 1 μM and 10 μM (iii) in a bilayer RyR simulation. Experimental P_O dependence on $[Ca^{2+}]_{cleft}$ adapted from (Györke & Györke, 1998) showed a similar tendency to the simulated model (ii-inset). RyR hyperphosphorylation ('High RyR-P') shifts the dependence of RyR open probability (P_O) on $[Ca^{2+}]_{cleft}$ at $[Ca^{2+}]_{JSR}$ of 200 μM and 600 μM (ii), and increased the dependence of P_O on $[Ca^{2+}]_{JSR}$ at $[Ca^{2+}]_{Cleft}$ of 1 μM and 10 μM (iii) in the bilayer RyR simulation. **C)** Simultaneous surface (SS, grey) and cell center (CC, black) traces of subcellular $[Ca^{2+}]_{Cyto}$ (top), $d[Ca^{2+}]_{Cyto}/dt$ (derivative of $[Ca^{2+}]_{Cyto}$ transient, middle) and I_{Ca} (bottom) in an experimental (left) and simulated cell without tubules (right) (i). Voltage dependence of I_{Ca} and local $[Ca^{2+}]_{Cyto}$ in experimental (ii) and simulated (iii) cells. Top: local $[Ca^{2+}]_{Cyto}$ transient (continuous lines) and $d[Ca^{2+}]_{Cyto}/dt$ (dashed lines) in the SS space (grey) and CC region (black). Bottom: voltage dependence of peak I_{Ca} (IV curve). Experimental data represents mean ± S.D., obtained by pacing at multiple test voltages adapted from (Sheehan & Blatter, 2003), with simulated data also obtained using a voltage-clamp stepping protocol. $[Na^+]_{Cyto}$ was clamped to 0.01 mM for simulation NCX equations to replicate experimental conditions. Simulation results recapitulate the experimental observations that 1) $[Ca^{2+}]_{Cyto}$ and $d[Ca^{2+}]_{Cyto}/dt$ peaks both occur at the same test-voltage prior to the I_{Ca} peak and 2) the bell-shaped voltage-dependence of $[Ca^{2+}]_{Cyto}$ transient amplitude is steeper and increased in amplitude in SS vs. CC.

2.2.1 Subcellular Ca^{2+} signaling model structure

Our 3D Ca^{2+} signaling model of the human atrial myocyte was based on an established framework for describing rabbit ventricular Ca^{2+} signaling (Restrepo *et al.*, 2008; Sato & Bers, 2011), which accounts for spatiotemporal properties of subcellular Ca^{2+} signaling by simulating a network of CRUs (**Fig. 2.1Aii**). Here, the cell model dimensions (**Table 2.1**) and electrical capacitance (**Fig. 2.1Biii**) were modified to better describe those in human atrial myocytes (Wang *et al.*, 1993; Wang Z *et al.*, 1993; Porciatti *et al.*, 1997; Bosch *et al.*, 1999; Polontchouk *et al.*, 2001; Wettwer *et al.*, 2004; Christ T. *et al.*, 2004; Gassanov *et al.*, 2006;

Neef *et al.*, 2010; Richards *et al.*, 2011). The new 3D human atrial cell model has a dimension of 101.2 μm × 15.3 μm × 9.9 μm and comprises 10,285 (55 × 17 × 11) CRUs (**Table 2.1**). Each CRU has five Ca^{2+} compartments, namely the cytosolic, submembrane, and cleft compartments, and the network and junctional sarcoplasmic reticulum (NSR and JSR, respectively), and has a dimension of 1.84 μm × 0.9 μm × 0.9 μm (**Fig. 2.1Aii**) as in (Sato & Bers, 2011). CRUs are coupled with each other by Ca^{2+} diffusion between respective submembrane, cytosol, and NSR compartments (**Fig. 2.1Ai-ii**). The cytosolic volume in each CRU was increased to match that in our previous atrial model (Grandi *et al.*, 2011), with the JSR volume decreased to better reproduce the properties of the atrial Ca^{2+} transient (i.e., time-to-peak and amplitude) (**Table 2.1, Fig. 2.3Ci, Di**). The cleft volume was the same in each CRU and equal to the average value in (Sato & Bers, 2011). Depending on their position in the cell, we distinguished between peripheral CRUs (i.e., the first two layers close to the cell surface) and inner CRUs (**Fig. 2.1Aii-iii**). Peripheral and inner CRUs coupled with TATS possess surface membrane ion channels/transporters (i.e., I_{Ca}, NCX current, I_{NCX}, background Ca^{2+} current, I_{Cabk}, plasma membrane Ca^{2+} ATPase (PMCA) current, I_{PMCA}, fast Na^+ current, I_{Na}, background Na^+ current, I_{Nabk}, small-conductance Ca^{2+}-activated K^+ current, I_{SK}, Ca^{2+}-activated Cl^- current, I_{ClCa}, Na^+/K^+ pump current, I_{NaK}) distributed in the cleft and/or submembrane space, whereas these processes are absent in the inner CRUs that are not coupled with tubules (inner uncoupled CRUs).

Table 2.1 Structural parameters for the 3D subcellular model

Parameter	Description	Value
N	Number of CRUs	10,285
n_x	Number of CRUs along length	55

n_y	Number of CRUs along width	17
n_z	Number of CRUs along depth	11
$length_{CRU}$	Length of single CRU	1.84 μm
$width_{CRU}$	Width of single CRU	0.9 μm
$depth_{CRU}$	Depth of single CRU	0.9 μm
v_{Cyto}	Local cytosolic volume, CRU	0.969 μm^3
v_s	Local submembrane space volume, CRU	0.025 μm^3
v_{JSR}	Local JSR volume, CRU	0.015 μm^3
v_{NSR}	Local NSR volume, CRU	0.025 μm^3
v_{Cleft}	Local cleft volume, CRU	0.126 μm^3

2.2.2 Generating experiment-based TATS population

A random-walk algorithm as done in (Song *et al.*, 2018) was used to create a population of TATS that quantitatively resemble the features of those reported experimentally in human atrial myocytes (Brandenburg *et al.*, 2018). We converted the experimental TATS features measured in 2D (i.e., total tubular density, branch length, and axial-to-transverse tubule ratio) to 3D features (e.g., we added a z component to the TATS, with z-tubules having the same density as tubules in the transverse direction) and then assigned them as inputs to our random-walk-based algorithm. The constructed 3D TATS networks were subsequently verified by extracting parameters in 2D cross-sections and confirming that the TATS properties matched experimental measurements (**Fig. 2.1Bi-ii**). Our simulated population contains 20 TATS configurations with tubular density ranging from fully detubulated to that of densely tubulated atrial cardiomyocytes. Representative simulated dense/median/sparse TATS are in **Fig. 2.1Aiii**. TATS density is greater (i.e., a larger number of coupled CRUs are present) near the cell

surface than in the cell center as tubules invaginate from the cell surface and/or branch from existing tubules (Richards *et al.*, 2011).

The coupling of TATS with voltage dynamics and subcellular Ca^{2+} signaling dictated which CRUs in the network are coupled with the sarcolemma (**Fig. 2.1Aii-iii**), and affected the membrane electrical capacitance as follows:

$$C_{mem} = C_{m,specific-surface} \cdot S_{surface} + C_{m,specific-tubule} \cdot S_{tubule}$$

$$S_{surface} = 5403.42\ \mu m^2$$

$$S_{tubule} = \pi \cdot D_{tubule} \cdot L_{tubule}$$

where we assume a larger specific capacitance of the surface sarcolemma $C_{m,specific-surface} = 0.01\ pF \cdot \mu m^{-2}$ compared to the specific capacitance of tubular sarcolemma $C_{m,specific-tubule} = 0.0056\ pF \cdot \mu m^{-2}$, as estimated in experimental measurements (Pásek *et al.*, 2008*a*); $D_{tubule} = 0.3$ μm is the tubule diameter, as estimated in (Brandenburg *et al.*, 2018), and L_{tubule} is the total length of tubules, which is associated with TATS density and varies with each TATS configuration. The median C_{mem} of our cell population is 96.25 pF (**Fig. 2.1Biii**), which is similar to experimental estimates in human atrial myocytes (Van Wagoner *et al.*, 1999; Christ T. *et al.*, 2004; González de la Fuente *et al.*, 2013; Brandenburg *et al.*, 2018).

2.2.3 Ca^{2+} buffering and diffusion

Descriptions of Ca^{2+} buffering in the cleft, submembrane, and cytosolic compartments were replaced with the kinetic binding schemes in our previous models (Grandi *et al.*, 2011; Morotti *et al.*, 2016*b*). Ca^{2+} buffering by calsequestrin (CSQ) in the JSR was modeled using the rapid equilibrium approximation as done previously (Restrepo *et al.*, 2008; Sato & Bers, 2011). We

updated the CSQ dissociation constant (K_c) based on (Grandi *et al.*, 2011), and modified CSQ dimerization constant (K) to an intermediate value between those used in (Restrepo *et al.*, 2008) and (Sato & Bers, 2011), to match experimental RyR-$[Ca^{2+}]_{cleft}$ dependence (**Fig. 2.2Bii insert**) (Györke & Györke, 1998). Updated parameters are listed in **Table 2.2**.

The diffusion equations as in (Sato & Bers, 2011) were used with updated time scales of Ca^{2+} diffusion (**Table 2.2**). Specifically, we slowed the diffusion between submembrane and cytosol to prolong the time to peak of the Ca^{2+} transient, and hastened the Ca^{2+} diffusion among neighboring submembrane spaces to promote Ca^{2+} diffusion between neighboring CRUs. In addition, diffusion among neighboring cytosolic compartments was accelerated based on multiple experimental observations (Wang, 1953; Kushmerick & Podolsky, 1969; Donahue & Abercrombie, 1987; Allbritton *et al.*, 1992; Cordeiro *et al.*, 2001; Wu & Bers, 2006; Picht *et al.*, 2011) and experiment-based evaluations (Swietach *et al.*, 2010; Bers & Shannon, 2013).

Table 2.2 Updated Ca^{2+} buffering and time scale of Ca^{2+} diffusion parameters

Parameter	Description	Value
K_c	Dissociation constant of CSQ	650 μM
K	Dimerization constant of CSQ	900 μM
τ_{si}	Time scale of Ca^{2+} diffusion, submembrane to cytoplasm	0.17 ms
τ_i^T	Time scale of Ca^{2+} diffusion, transverse cytosolic	1.07 ms
τ_i^L	Time scale of Ca^{2+} diffusion, longitudinal cytosolic	1.75 ms

τ_s^T	Time scale of Ca^{2+} diffusion, transverse submembrane	1.28 ms
τ_s^L	Time scale of Ca^{2+} diffusion, longitudinal submembrane	3.06 ms

2.2.4 Dynamics of Ca^{2+} cycling in CRU

The Ca^{2+} concentration in the Ca^{2+} compartments of each CRU was calculated by accounting for all transmembrane (sarcolemmal and SR) Ca^{2+} currents and fluxes, Ca^{2+} buffers, and Ca^{2+} diffusion between neighboring compartments:

$$\frac{d[Ca^{2+}]_{Cyto}}{dt} = I_{diff,s\leftrightarrow Cyto} \cdot \frac{v_s}{v_{Cyto}} + I_{diff,Cyto} - I_{up} + I_{leak} - I_{buffer,Cyto}$$

$$\frac{d[Ca^{2+}]_s}{dt} = I_{diff,Cleft\leftrightarrow s} \cdot \frac{v_{Cleft}}{v_s} - I_{diff,Cyto\leftrightarrow s} + I_{diff,s} + I_{NCX,s} - I_{CaBk} - I_{PMCA} - I_{buffer,s}$$

$$\frac{d[Ca^{2+}]_{Cleft}}{dt} = -I_{diff,Cleft\leftrightarrow s} + I_{rel} + i_{Ca} + I_{NCX,Cleft} - I_{buffer,Cleft}$$

$$\frac{d[Ca^{2+}]_{JSR}}{dt} = \beta([Ca^{2+}]_{JSR}) \cdot \left(I_{diff,NSR\leftrightarrow JSR} - I_{rel} \cdot \frac{v_{Cleft}}{v_{JSR}}\right)$$

$$\frac{d[Ca^{2+}]_{NSR}}{dt} = -I_{diff,NSR\leftrightarrow JSR} \cdot \frac{v_{JSR}}{v_{NSR}} + I_{diff,NSR} + (I_{up} - I_{leak}) \cdot \frac{v_{Cyto}}{v_{NSR}}$$

where $[Ca^{2+}]_x$ is the local Ca^{2+} concentration in cytosolic (x: Cyto), submembrane (x: s), cleft (x: Cleft), NSR (x: NSR), or JSR (x: JSR) compartments; $I_{diff,x}$ is the diffusive current between neighboring compartments; and I_{up} is the SERCA uptake current; I_{leak} is the SR leak

current; $\beta([Ca^{2+}]_{JSR})$ is the rapid equilibrium approximation term of the CSQ Ca^{2+} buffering for $[Ca^{2+}]_{JSR}$; $I_{buffer,x}$ is the dynamic buffer current in compartments, described as follows:

$$I_{buffer,Cyto} = I_{myosin\ Ca,Cyto} + I_{myosin\ Mg,Cyto} + I_{SR,Cyto} + I_{CaM,Cyto}$$

$$+I_{TnC\ low,Cyto} + I_{TnC\ high\ Ca,Cyto} + I_{TnC\ high\ Mg,Cyto}$$

$$I_{buffer,s} = I_{CaM,s} + I_{SR,s} + I_{SL\ low,s} + I_{SL\ high,s}$$

$$I_{buffer,Cleft} = I_{CaM,Cleft} + I_{SR,Cleft} + I_{SL\ low,Cleft} + I_{SL\ high,Cleft}$$

2.2.5 Updated ion channels and transporters

An updated version of the Grandi et al. human atrial myocyte model (Grandi *et al.*, 2011) was used as described in (Morotti *et al.*, 2016*a*, 2016*b*) (**Fig. 2.1Ai**). A new Markov model of the LCC current was developed and parameters describing RyR release and SR Ca^{2+}-ATPase (SERCA) uptake were modified, as described below, to recapitulate characteristics of Ca^{2+} signaling (**Fig. 2.2C and 3C**). We further added descriptions of small-conductance Ca^{2+}-activated K^+ current (I_{SK}) as in (Morotti *et al.*, 2016*a*), and replaced the model formulations of I_{Na} and I_{NCX} with the I_{Na} model from (Courtemanche *et al.*, 1998) and the I_{NCX} model from (Soltis & Saucerman, 2010). The maximal conductance and transporter rates of I_{SK}, I_{NCX}, I_{CaBk}, I_{CaP}, I_{NaK}, I_{Na}, and I_{NaBk} were adjusted to better reproduce the rate-dependence of AP and Ca^{2+} dynamics.

All membrane ion channels and transporters are distributed uniformly to all coupled CRUs, and their density is maintained constant independent of TATS density. Within each coupled CRU, the LCCs are assumed to be in the cleft area and are closely coupled with RyRs as in (Restrepo *et al.*, 2008; Sato & Bers, 2011). NCXs are distributed with 11% of the proteins in the cleft and 89% in the submembrane as (Grandi *et al.*, 2011), similar to I_{NaBk}, I_{NaK}, I_{Na}, I_{ClCa}, I_{SK}, while I_{Cabk} and I_{PMCA} are located only in the submembrane as in (Sato & Bers, 2011).

I_{Ca} Markov model: Each CRU contains 4 LCCs, as in (Restrepo *et al.*, 2008). We developed a novel 10-state stochastic Markov model (**Fig. 2.2Ai**) based on (Morotti *et al.*, 2012) to replicate biophysical properties of I_{Ca} in human atria and recapitulate two distinct components of inactivation (Li & Nattel, 1997). This model has 1 open state (O), 2 closed states (C_1, C_2), 5 Ca^{2+}-dependent inactivation states (I_{C0}, I_{C1}, I_{C2}, I_{C3}, I_{C4}), and 2 voltage (V_m)-dependent inactivation states (I_{V1}, I_{V2}). The transition rates of the Markovian I_{Ca} current are described in **Table 2.3**.

Table 2.3 Transition rates of the LCC Markov model

Transition	Rate/Equation
$C_1 \rightarrow C_2$	$\alpha = \frac{R_2}{T_2}$
	where $R_2 = \frac{1}{1+e^{-\frac{V_m+9}{6}}}$ and $T_2 = 0.9 \cdot \left(0.59 + \frac{0.8 \cdot e^{0.052 \cdot (V_m+13)}}{1+e^{0.132 \cdot (V_m+13)}}\right)$
$C_2 \rightarrow C_1$	$\beta = \frac{1 - R_2}{T_2}$
$C_2 \rightarrow O$	$r1 = \frac{R_1}{T_1}$
	where $R_1 = \frac{0.091}{1+e^{-\frac{V_m+1000}{10}}}$ and $T_1 = \frac{0.3}{1+e^{-\frac{V_m+1000}{10}}}$
$O \rightarrow C_2$	$r2 = \frac{1 - R_2}{T_2}$
$C_2 \rightarrow I_{C1}$	$k1 = \frac{1 - R_{v1,k1k2}}{\tau_{k1k2}}$
	where $R_{v1,k1k2} = \frac{0.85}{1+e^{\frac{V_m+18+3 \cdot f_{cp}}{8}}} + 0.15$, $\tau_{k1k2} = \frac{1}{0.1 \cdot f_{cp}}$

and $f_{cp} = 0.5 \cdot \left(\frac{1}{1+\left(\frac{2.065}{3\cdot[Ca^{2+}]_{Cleft}}\right)^2} + \frac{1}{1+\left(\frac{2.065}{[Ca^{2+}]_{Cleft}}\right)^4} \right)$

$I_{C1} \rightarrow C_2$ $\quad k2 = \frac{R_{v1,k1k2}}{\tau_{k1k2}}$

$I_{C1} \rightarrow I_{C2}$ $\quad k3 = \left(1 - \frac{1}{1+e^{-\frac{V_m+27}{3}}}\right) \cdot \frac{1}{3}$

$I_{C2} \rightarrow C_1$ $\quad k5 = \frac{1}{1+e^{\frac{V_m+18+3\cdot f_{cp}}{8}}} \cdot \frac{1}{T_{v1,k5} \cdot (f_{cp}+1)}$

where $T_{v1,k5} = 20 + 30 \cdot e^{-\frac{(V_m+50)^2}{150}} + \frac{30}{1+e^{\frac{V_m+25}{5}}}$

$C_1 \rightarrow I_{C2}$ $\quad k6 = \left(1 - \frac{1}{1+e^{\frac{V_m+18+3\cdot f_{cp}}{8}}}\right) \cdot \frac{f_{cp}+1}{T_{v1,k5}}$

$I_{C2} \rightarrow I_{C1}$ $\quad k4 = \frac{\alpha \cdot k1 \cdot k3 \cdot k5}{\beta \cdot k2 \cdot k6}$

$C_2 \rightarrow I_{V2}$ $\quad k1' = \frac{R_{v1}}{T_{v1}}$

where $R_{v1} = \frac{0.85}{1+e^{-(V_m+27)\cdot 0.09}}$ and $T_{v1} = 45 + 3000 \cdot e^{-\frac{(V_m+50)^2}{150}} + \frac{200}{1+e^{-\frac{V_m+60}{3}}}$

$I_{V2} \rightarrow C_2$ $\quad k2' = \frac{1-R_{v1}}{T_{v1}}$

$I_{V1} \rightarrow I_{V2}$ $\quad k3' = k3$

$I_{V1} \rightarrow C_1$ $\quad k5' = \frac{1}{1+e^{\frac{V_m+32}{8}}} \cdot \frac{1}{T'_{v1,k5}}$

where $T'_{v1,k5} = 45 + 2000 \cdot e^{-\frac{(V_m+50)^2}{150}} + \frac{200}{1+e^{-\frac{V_m+60}{3}}}$

$C_1 \rightarrow I_{V1}$ $\quad k6' = \left(1 - \frac{1}{1+e^{\frac{V_m+32}{8}}}\right) \cdot \frac{1}{T'_{v1,k5}}$

$I_{V1} \rightarrow I_{V2}$ $$k4' = \frac{\alpha \cdot k1' \cdot k3' \cdot k5'}{\beta \cdot k2' \cdot k6'}$$

$O \rightarrow I_{V2}$ $$s1' = k1'$$

$I_{V2} \rightarrow O$ $$s2' = \frac{s1' \cdot k2' \cdot r1}{k1' \cdot r2}$$

$O \rightarrow I_{C0}$ $$s1 = k1$$

$I_{C0} \rightarrow O$ $$s2 = 0.2 \cdot k2$$

$I_{C0} \rightarrow I_{C1}$ $$k13 = r2$$

$I_{C1} \rightarrow I_{C0}$ $$k14 = \frac{s1 \cdot r1 \cdot k2 \cdot k13}{s2 \cdot r2 \cdot k1}$$

$I_{C1} \rightarrow I_{C3}$ $$k7 = \frac{1 - R_{v1,k1k2}}{50}$$

where $R_{v1,k1k2} = \frac{1}{1+e^{\frac{V_m+18+8 \cdot f_{cp}}{8}}}$

$I_{C3} \rightarrow I_{C1}$ $$k8 = \frac{R_{v1,k1k2}}{50}$$

$I_{C4} \rightarrow I_{C2}$ $$k9 = 6 \cdot \frac{R_{v1,k1k2}}{T_{v1,k9}}$$

where $T_{v1,k9} = 60 + 30 \cdot e^{-\frac{(V_m+55)^2}{150}}$

$I_{C2} \rightarrow I_{C4}$ $$k10 = 6 \cdot \frac{1 - R_{v1,k1k2}}{T_{v1,k9}}$$

$I_{C3} \rightarrow I_{C4}$ $$k12 = k3$$

$I_{C4} \rightarrow I_{C3}$ $$k11 = \frac{k4 \cdot k7 \cdot k9 \cdot k12}{k3 \cdot k8 \cdot k10}$$

$I_{C4} \rightarrow I_{V1}$ $$k15 = \frac{1 - f_{cp,k15}}{\tau_{k15}}$$

where $f_{cp,k15} = 0.5 \cdot \left(\frac{1}{1+\left(\frac{2.065}{2.5 \cdot [Ca^{2+}]_{Cleft}}\right)^2} + \frac{1}{1+\left(\frac{2.065}{[Ca^{2+}]_{Cleft}}\right)^4} \right)$

and $\tau_{k15} = \frac{1}{0.5 \cdot f_{cp,k15} + 0.01}$

$I_{V1} \rightarrow I_{C4}$ $\quad k15' = \frac{f_{cp,k15}}{\tau_{k15}}$

$I_{C3} \rightarrow I_{V2}$ $\quad k16 = \frac{1 - f_{cp,k15}}{\tau_{k16}}$

where $\tau_{k16} = \tau_{k15}$

$I_{V2} \rightarrow I_{C3}$ $\quad k16' = \frac{f_{cp,k15}}{\tau_{k16}}$

The model tracks the total number of LCCs residing in the open state, with whole-cell I_{Ca} calculated by the sum of unitary current (i_{Ca}), as described using the original model formulation in (Sato & Bers, 2011). We added descriptions of Na^+ and K^+ fluxes through LCCs from (Grandi *et al.*, 2011; Morotti *et al.*, 2016*b*). To calculate the unitary Na^+ and K^+ currents ($i_{Ca,Na}$ and $i_{Ca,K}$), the Na^+ and K^+ permeability in the original model was divided by the total number of LCCs (**Table 2.4**).

$$I_{Ca} = \sum_{n=1}^{Number\ of\ coupled\ CRUs} N_{Open,LCC} \cdot \left(i_{Ca} + i_{Ca,Na} + i_{Ca,K}\right)$$

Table 2.4 Updated human atrial myocyte ionic parameters

Parameter	Description	Value
P_{Ca}	Unitary LCC Ca^{2+} permeability (I_{Ca})	8.19 umol·C^{-1}·ms^{-1}
P_{Na}	Unitary LCC Na^+ permeability (I_{Ca})	$6.14 \cdot 10^{-13}$ cm·s^{-1}

P_K	Unitary LCC K^+ permeability (I_{Ca})	$1.1 \cdot 10^{-11}$ cm·s^{-1}
g_{SK}	Small-conductance Ca^{2+}-activated K^+ conductance per CRU (I_{SK})	$2.21 \cdot 10^{-10}$ mS
$k_{d,SK}$	Dissociation constant of intracellular Ca^{2+} (I_{SK})	$0.79 \cdot 10^{-3.45}$ mM
N_{RyR}	Number of RyRs per CRU (I_{rel})	41
J_{max}	Strength of Ca^{2+} release flux (I_{rel})	0.1321 μm^3·ms^{-1}
K_{cp}	Constant (I_{rel})	10 μM
h_{cp}	$[Ca^{2+}]_{cleft}$-dependence exponent of k_{12} and k_{43} (I_{rel})	3
v_{NCX}	Strength of the NCX Ca^{2+} flux per CRU (I_{NCX})	17.88 μM·ms^{-1}
G_{ClCa}	Ca^{2+}-dependent Cl^- conductance per CRU (I_{ClCa})	$6.5 \cdot 10^{-10}$ mS
G_{CaBk}	Strength of the background SL Ca^{2+} flux per CRU (I_{Cabk})	0.0014 μM·ms^{-1}
V_{max}	Strength of the PMCA current per CRU (I_{PMCA})	0.0097 μM·ms^{-1}
$I_{bar,NaK}$	Na^+/K^+ pump maximal transport rate per CRU, (I_{NaK})	$1.49 \cdot 10^{-14}$ A
g_{Na}	Na^+ conductance per CRU (I_{Na})	$1.07 \cdot 10^{-7}$ mS
g_{NaB}	Na^+ background conductance per CRU (I_{Nabk})	$7.09 \cdot 10^{-12}$ mS
v_{up}	Strength of uptake per CRU (I_{up})	0.36 μM·ms^{-1}
K_i	K_{mf} for SR Ca pump forward mode (I_{up})	0.615 μM

Our new I_{Ca} model reproduced steady-state activation and inactivation curves (**Fig. 2.2Aii, iiii, and v**), the fast and slow inactivation time constants (**Fig. 2.2Avi**), and time-dependent recovery (**Fig. 2.2Avii**), which resembles the experimental measurements (Li & Nattel, 1997).

SR Ca^{2+} release and uptake: The 4-state stochastic RyR Markov model (**Fig. 2.2Bi**) in (Restrepo *et al.*, 2008; Sato & Bers, 2011) was modified to incorporate human atrial myocyte-specific characteristics. This model includes 2 open states (O_1, O_2) and 2 closed states (C_1, C_2),

whereby transitions are regulated by $[Ca^{2+}]_{Cleft}$ and $[Ca^{2+}]_{JSR}$. The RyR number per CRU (N_{RyR}) was reduced to 41 based on the experimental measurement (Boyd *et al.*, 2018) and the strength of SR Ca^{2+} release flux (J_{max}) was reduced compared to (Sato & Bers, 2011) to match the rate-dependence of Ca^{2+} transient amplitude and duration (**Fig. 2.3Ci-ii**). Furthermore, we left shifted the $[Ca^{2+}]_{cleft}$-dependence (K_{cp}) and increased the hill coefficient (h_{cp}) (**Table 2.4**) to match the $[Ca^{2+}]_{Cleft}$-dependence of the RyR P_O (Györke & Györke, 1998; Fill & Gillespie, 2018). Our RyR model reproduces the changes in RyR P_O when $[Ca^{2+}]_{Cleft}$ or $[Ca^{2+}]_{JSR}$ are varied (**Fig. 2.2Bii-iii**), similar to the observations from lipid-bilayer RyR experiments (**Fig. 2.2Bii, insert**) (Györke & Györke, 1998). Finally, k_{32} was updated to impose reversibility of the Markov model. RyR hyperphosphorylation was simulated by left shifting the $[Ca^{2+}]_{cleft}$-dependence of SR release (i.e., reducing K_{cp} by 50%) to increase RyR P_O (**Fig. 2.2Bii-iii**). The transition rates of the RyR Markov model are described in **Table 2.5**.

Table 2.5 Transition rates of the RyR Markov model

Transition	Rate/Equation
$C_1 \rightarrow O_1$	$k_{12} = K_u \cdot \frac{\left([Ca^{2+}]_{Cleft}\right)^{h_{cp}}}{K_{cp}^{h_{cp}} + \left([Ca^{2+}]_{Cleft}\right)^{h_{cp}}} + w$
	where $K_{cp} = 10\ \mu M$, $h_{cp} = 3$, $K_u = 5\ ms^{-1}$ and $w = 0.000001\ ms^{-1}$
$C_2 \rightarrow O_2$	$k_{43} = K_b \cdot \frac{\left([Ca^{2+}]_{Cleft}\right)^{h_{cp}}}{K_{cp}^{h_{cp}} + \left([Ca^{2+}]_{Cleft}\right)^{h_{cp}}} + w$
	where $K_b = 0.005\ ms^{-1}$
$O_1 \rightarrow C_1$	$k_{21} = 0.5\ ms^{-1}$
$C_2 \rightarrow O_2$	$k_{34} = 3.3\ ms^{-1}$

$C_2 \rightarrow C_1$ $\quad k_{41} = 0.008\, ms^{-1}$

$C_1 \rightarrow C_2$ $\quad k_{14} = \dfrac{\widehat{M}([Ca^{2+}]_{JSR}) \cdot \tau_b^{-1} \cdot B_{CSQ}}{B_{CSQ}^0}$

where $\widehat{M}\left([Ca^{2+}]_{JSR}\right) = \frac{\sqrt{1+8\cdot\rho\cdot B_{CSQ}}-1}{4\cdot\rho\cdot B_{CSQ}}$, $\rho = \frac{5000}{1+\left(\frac{K}{[Ca^{2+}]_{JSR}}\right)^{23}}$

$\tau_b = 0.5\, ms$, $B_{CSQ} = 400\, \mu M$, $B_{CSQ}^0 = 400\, \mu M$, and $K = 900\, \mu M$

$O_1 \rightarrow O_2$ $\quad k_{23} = k_{14}$

$O_2 \rightarrow O_1$ $\quad k_{32} = \dfrac{k_{41} \cdot k_{12} \cdot k_{23} \cdot k_{34}}{k_{43} \cdot k_{21} \cdot k_{14}}$

SERCA uptake current (I_{up}) was modified from (Sato & Bers, 2011) by reducing the Ca^{2+} affinity (increasing K_i) as in (Grandi *et al.*, 2011) and adjusting the maximum Ca^{2+} uptake rate v_{up} to reproduce the rate-dependence of Ca^{2+} transient duration (**Fig. 2.3Cii**) (Kang *et al.*, 2016) and the relative contribution of SERCA to Ca^{2+} removal during the Ca^{2+} transient (**Fig. 2.3Ciii**) (Voigt *et al.*, 2012) seen experimentally. **Table 2.4** contains a list of the updated parameters.

Small-conductance Ca^{2+}-activated K^+ current (I_{SK}): I_{SK} was added to our 3D subcellular model from (Morotti *et al.*, 2016*a*) with adjusted current maximal conductance (g_{SK}),

$$I_{SK} = g_{SK} \cdot g_{SK-V} \cdot g_{SK-Ca} \cdot (V_m - E_K)$$

where V_m- and Ca^{2+}- dependent components are formulated as

$$g_{SK-V} = \left(\frac{0.27}{1 + e^{(V_m - E_K + 2.96)\cdot 0.2}} + \frac{0.28}{1 + e^{-(V_m - E_K - 86.93)\cdot 0.0064}}\right)$$

$$g_{SK-Ca} = \frac{1}{1 + e^{\frac{log_{10}^{k_{d,SK}} - log_{10}^{[Ca^{2+}]_x \cdot 10^{-3}}}{0.3}}}$$

and $[Ca^{2+}]_x$ is Ca^{2+} concentration in the cleft or submembrane space and E_K is the Nernst potential for K^+.

Other updated currents: Maximum current strength/flux parameters of I_{NCX} (Soltis & Saucerman, 2010), I_{ClCa} (Morotti *et al.*, 2016*b*), I_{Cabk} (Sato & Bers, 2011), I_{PMCA} (Sato & Bers, 2011), I_{NaK} (Morotti *et al.*, 2016*b*), I_{Na} (Courtemanche *et al.*, 1998), I_{Nabk} (Grandi *et al.*, 2011) were adjusted (**Table 2.4**) to recapitulate the rate-dependent dynamic properties of AP and Ca^{2+} (**Fig. 2.3A-C**).

2.2.6 Numerical Method

Our new 3D human atrial cell model was implemented in C++ and parallelized using OpenMP 5.1 (Dagum & Menon, 1998). The ordinary differential equations (ODEs) and subcellular Ca^{2+} diffusion were solved using an explicit Forward Euler method except that I_{Ca} and RyR gating behaviors were described stochastically as in (Restrepo *et al.*, 2008; Sato & Bers, 2011), and that ODEs of I_{Na} were solved using the Rush-Larsen scheme (Rush & Larsen, 1978). The integration time step was 0.01 ms.

2.2.7 Simulation protocols

To test the rate dependence of AP and Ca^{2+} dynamics in human atrial myocytes, a pacing-and-pause protocol was applied. The protocol starts with a 4-sec unstimulated period, followed by a 28-sec long stimulation period, in which the myocyte is paced at 0.5, 1, 2, 3, 4, or 5 Hz by injecting a depolarizing current (5 ms in duration and 12.5 pA/pF in strength), and ends with a 5-sec pause. In all simulations, the model state variables were assigned with the same initial

conditions. While our model does not describe dynamic Na^+ handling, which slowly varies (within minutes) with the stimulation frequency, we incorporated a rate-dependent description of Na^+, i.e., the intracellular Na^+ concentration ($[Na^+]_{Cyto}$, [mM]) is described as a function of the basic cycle length (BCL, [ms]) (Restrepo *et al.*, 2008; Sato & Bers, 2011) to match the Na^+-BCL relation simulated using (Grandi *et al.*, 2011). Using rate-corrected $[Na^+]_{Cyto}$ values allows the virtual cell to rapidly reach steady-state when the pacing frequency is varied.

$$[Na^+]_{Cyto} = 7.76 + \frac{7.38}{\left(1 + \left(\frac{BCL}{1.29 \cdot 10^8}\right)^{0.73}\right)^{8754.45}}$$

LCCs and RyRs gate stochastically in our model. To ensure the robustness of our main simulations results and conclusions, we simulated each cell with 10 different random seeds.

2.2.8 Detection and analysis of Ca^{2+} sparks, spontaneous Ca^{2+} release events (SCRs) and delayed after-depolarizations (DADs)

The $[Ca^{2+}]_{Cyto}$ waveform starting at the peak of the last paced beat with the subsequent no-stimulation period was used for analysis. Spark and SCR peaks were identified in MATLAB R2021 utilizing the *findpeak* function, with a 'MinPeakProminence' of 0.05 μM and 'MinPeakDistance' of 100 ms used to define sparks. Amplitudes of SCR events were calculated as the difference between the peak and the minimum $[Ca^{2+}]_{Cyto}$ values. To determine the properties of SCR, a detection threshold of 0.3 μM was used as the minimum SCR amplitude. Likewise, membrane voltage waveforms were also examined in MATLAB, with DADs detected when the membrane depolarization amplitude was greater than 10 mV (**Fig. 2.7A**). Rate threshold of SCRs and DADs was determined as the lowest pacing rate that produced the

respective arrhythmic events. To study local Ca^{2+} changes, we averaged the $[Ca^{2+}]_{Cyto}$ within surface CRUs, inner coupled CRUs (those CRUs located away from the cell surface but coupled to tubules), and inner uncoupled CRUs.

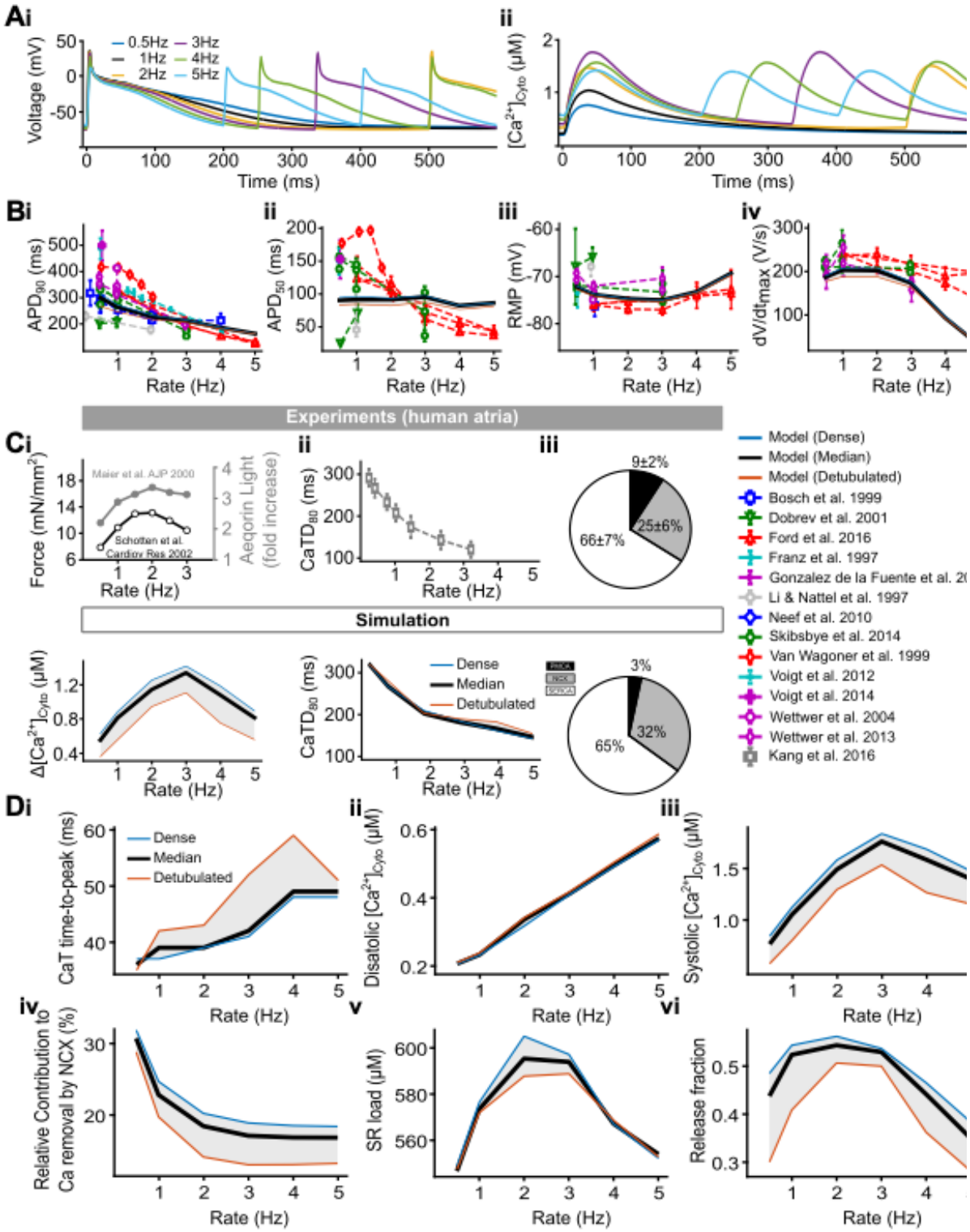

Figure 2.3 - Fitting results for AP and Ca^{2+} transient biomarkers at multiple pacing rates.

A) Representative AP (i) and Ca^{2+} transient (ii) traces in a cell with median tubules during 0.5, 1, 2, 3, 4, and 5 Hz pacing. **B)** Rate dependent changes in APD_{90} (AP duration at 90% repolarization, i), APD_{50} (ii), RMP (resting membrane potential, iii) and dV/dt_{max} (maximum upstroke velocity of depolarization, iv) in simulation and experimental observations at 0.5-5 Hz. Models of detubulated (orange), dense (blue) and median (black) tubulated cells are displayed as solid lines with data from previous studies used for fitting referenced in the key below. **C)** Comparison of contractile force/Ca^{2+} transient amplitude (i), $CaTD_{80}$ (Ca^{2+} transient duration at 80% systolic level, ii), and Ca^{2+} extrusion fractions (iii) between experimental results (top) and simulation (bottom). Experimental data of Ca^{2+} extrusion fractions at 0.5 Hz is adapted from (Voigt et al., 2012). **D)** Model prediction of Ca^{2+} signaling rate-dependence properties, including Ca^{2+} transient time to peak (i), diastolic $[Ca^{2+}]_{Cyto}$ (ii), systolic $[Ca^{2+}]_{Cyto}$ (iii), relative contribution to Ca^{2+} removal by NCX (iv), SR load (v) and release fraction (vi) in detubulated (orange), dense (blue) and median (black) tubulated cells at 0.5-5 Hz stimulation rates.

2.3 Result

2.3.1 Fitting of AP and Ca^{2+} transient biomarkers in the myocyte model against experimental observations in the human atria

To investigate the effects of varying TATS on whole-cell and subcellular Ca^{2+} signaling and electrophysiology in the human atrial myocyte, we built a mathematical model coupling voltage, spatially-detailed Ca^{2+} dynamics, and TATS (**Fig. 2.1A**) that integrates a vast array of experimental data from various published sources. A detailed description of the ultrastructural characteristics (**Fig. 2.1B, Tables 2.1-2.2**), ion channel and transporter properties (**Fig. 2.2A-B, Tables 2.3-2.5**), and subcellular Ca^{2+} handling features (**Fig. 2.2C**) in human atrial myocytes used to parameterize our model are provided in the Methods.

Given the model complexity and large number of parameters, we also included human atrial electrophysiologic and global Ca^{2+}-handling biomarkers (**Fig. 2.3**) in the fitting process.

The representative traces of steady-state APs and Ca^{2+} transients at varying pacing rates (**Fig. 2.3A**) and simulated properties indicate that fast pacing varied AP and Ca^{2+} transient biomarkers in agreement with experimental data from multiple sources (**Fig. 2.3B-C**). The model was mainly fitted to mimic the rate-dependence of the AP duration (APD, **Fig. 2.3Bi**), Ca^{2+} transient amplitude (**Fig. 2.3Ci**), and Ca^{2+} transient duration (**Fig. 2.3Cii**). Experimental observations of relative contributions to Ca^{2+} removal by PMCA, NCX, and SERCA were also replicated by our model (**Fig. 2.3Ciii**). While we utilized the model with median tubular structure (black solid lines), the AP properties above were not markedly changed when simulating models with less or more dense TATS (orange and blue solid lines, respectively). However, lack of TATS was associated with reduced Ca^{2+} transient amplitude (**Fig. 2.3Ci**) resulting from reduced systolic Ca^{2+} (**Fig. 2.3Diii**) and fractional release (**Fig. 2.3Dvi**) and longer time to peak (**Fig. 2.3Di**). In addition, the biphasic dependence of Ca^{2+} transient amplitude on the pacing rate results from analogous dependence on systolic Ca^{2+} levels (**Fig. 2.3Diii**), SR Ca^{2+} content (**Fig. 2.3Dv**), and fractional release (**Fig. 2.3Dvi**). Overall, these data indicate that our model recapitulates the main electrophysiologic and whole-cell Ca^{2+} handling properties in human-atria-specific experiments and also their rate dependence.

2.3.2 Validation of APs, subcellular and global Ca^{2+} transient and TATS biomarkers in the myocyte model against experimental observations in the human atria

Next, we validated the model to verify its ability to predict an independent experimental dataset. We focused on AP properties, subcellular Ca^{2+} spark and wave characteristics, and global Ca^{2+} transient features measured when challenging atrial myocytes with ion channel blockers or osmotic shock (to disrupt TATS). As shown in experiments (Van Wagoner *et al.*, 1999), simulating the application of the I_{Ca} blocker nifedipine shortened the APD and weakened the APD rate dependence (**Fig. 2.4B** vs. **Fig. 2.4A**). The summary data shows that the percentage

changes in APD_{90} (with respect to the value at 2 Hz pacing) are similar in the experimental (**Fig. 2.4Ci**, adapted from (Van Wagoner *et al.*, 1999) and simulation results (**Fig. 2.4Cii**). Thus, the simulated APD rate-dependence replicates the response to LCC blockade measured in human atrial myocytes.

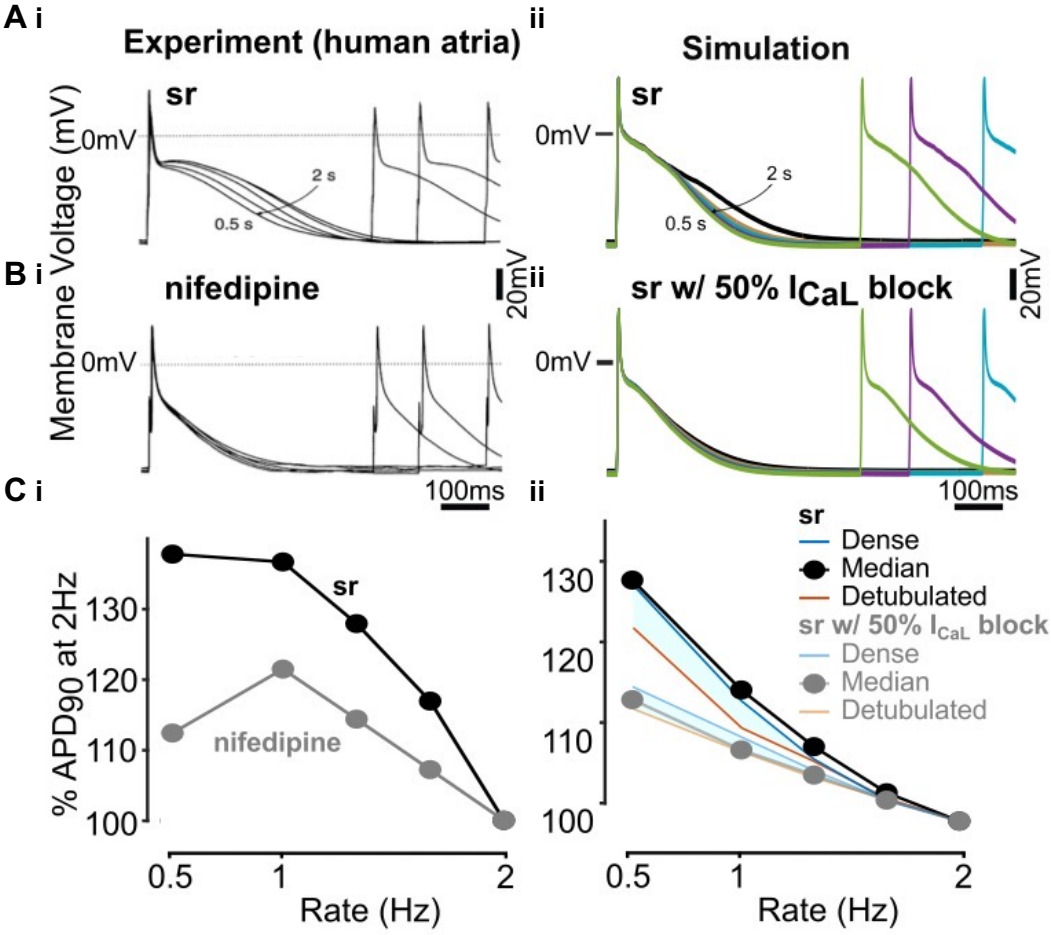

Figure 2.4 - Validation of electrophysiology by I_{Ca} block with and without nifedipine.

A) Representative AP traces showing AP rate-dependence in normal sinus rhythm (sr) in experimental (Van Wagoner David R. *et al.*, 1999) (i) and simulated (ii) cells. Simulated cells with representative tubular structures (Dense, Median, and Detubulated) were paced with the basic cycle length of 2, 1, 0.75, 0.6, and 0.5 s. **B)** Representative AP traces showing AP rate-dependence with I_{Ca} block by nifedipine or 50% I_{Ca} reduction in experimental (i) and simulated (ii) cells. In the simulation, L-type Ca^{2+} channels were blocked by 50% in the common pool model (Grandi *et al.*, 2011), then paced at the same pacing rates to steady-state. The values of steady-state $[Na^+]_{Cyto}$ in the common pool model were used to update the

$[Na^+]_{Cyto}$ equations in the 3D model prior to blocking L-type Ca^{2+} channels by 50% in the 3D model during pacing.

$$[Na^+]_{Cyto} = 7.17 + \frac{2.47}{1 + \left(\frac{BCL}{552.8}\right)^{1.52}}$$

C) Summary data showing percentage change in APD_{90} at varying stimulation rates is similar in the experiment (i) and simulation (ii) results.

To validate the predicted subcellular and whole-cell properties of Ca^{2+} signaling, we analyzed the spatiotemporal characteristics of the intracellular Ca^{2+} transients evoked by electrical stimulation and caffeine application. The simulated transversal linescan images show AP-induced Ca^{2+} waves propagating from the cell periphery to the cell center as shown in human atrial myocyte experiments (**Fig. 2.5A**) (Greiser *et al.*, 2014). The caffeine-evoked Ca^{2+} transient was larger and the release was more synchronous than the electrically evoked transient (**Fig. 2.5B**). Notably, the ratio of central to surface Ca^{2+} transient amplitude (cc/ss (ratio)) was similar between experiments in rabbit atrial myocytes (Greiser *et al.*, 2014) and human atrial myocyte simulation. Our model also recapitulates the regional differences in the surface vs. central $[Ca^{2+}]_{Cyto}$ and $d[Ca^{2+}]_{Cyto}/dt$ detected in voltage-clamp experiments in cat atrial myocytes that lack TATS, whereby $[Ca^{2+}]_{Cyto}$ and $d[Ca^{2+}]_{Cyto}/dt$ are larger at the cell surface, the bell-shaped voltage-dependence of the $[Ca^{2+}]_{Cyto}$ transient amplitude is steeper, and $[Ca^{2+}]_{Cyto}$ and $d[Ca^{2+}]_{Cyto}/dt$ peak at the same test-voltage prior to the I_{Ca} peak (**Fig. 2.2C**) (Sheehan & Blatter, 2003).

To evaluate whole-cell Ca^{2+} signaling, we compared the simulated Ca^{2+} transient characteristics with measurements in human atrial myocytes and found good agreement in the predicted vs. measured (Voigt *et al.*, 2012, 2014) diastolic and systolic twitch Ca^{2+} concentration and in the amplitude and decay time constant of the caffeine-induced Ca^{2+}

transient (**Fig. 2.5C**). Overall, simulated properties of Ca^{2+} transients and waves match experimental observations in human and rabbit atrial myocytes.

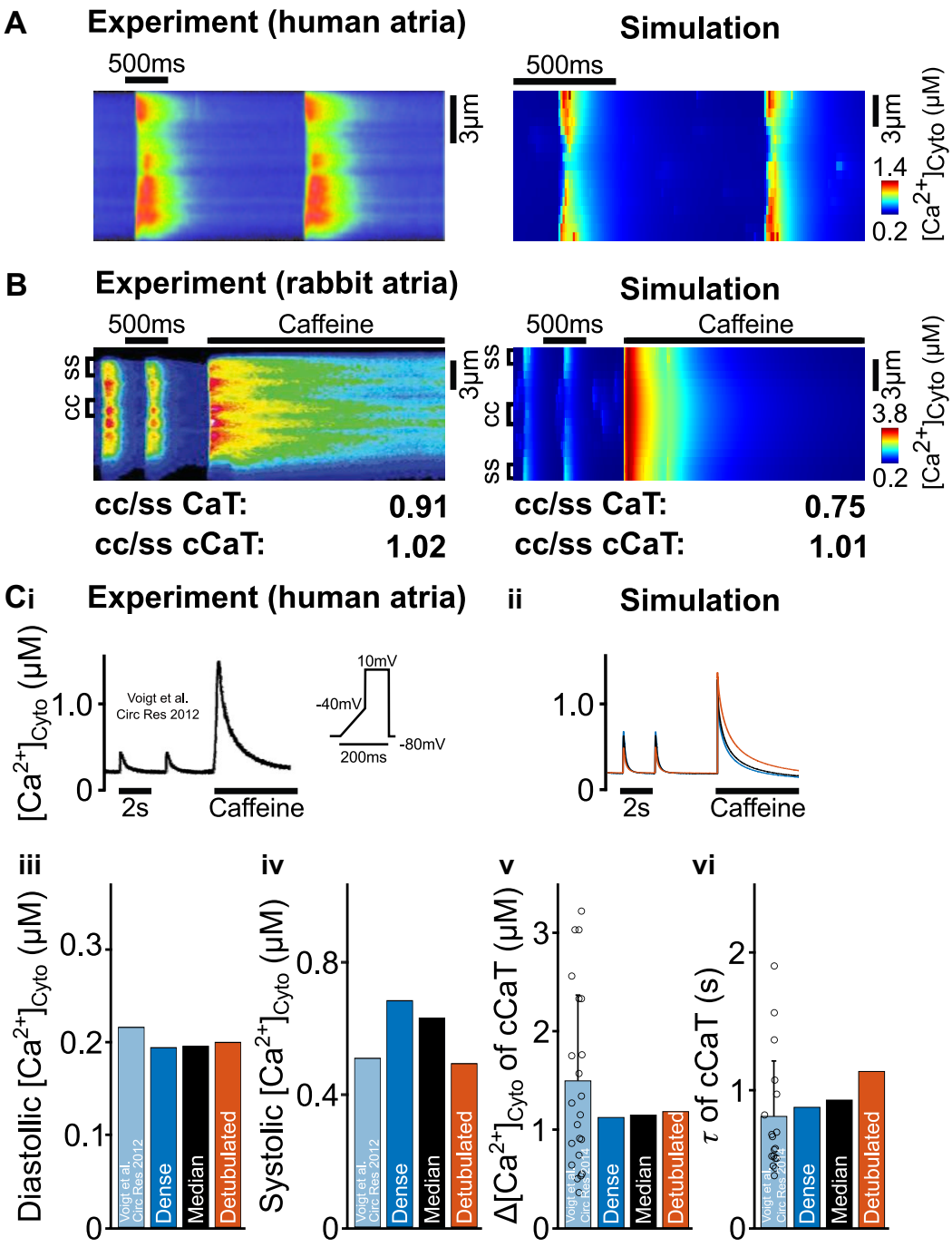

Figure 2.5 - Validation of local and global Ca^{2+} signaling with and without caffeine-evoked SR depletion.

A) Linescan images showing Ca^{2+} release in the experimental (Greiser *et al.*, 2014) (0.5 Hz, left) and simulated median tubulated (1Hz, right) atrial cells. The simulated cell was paced for 28 seconds to reach steady-state, and the local $[Ca^{2+}]_{Cyto}$ of 17 CRUs along the central y-axis during the last 2 beats was measured to get the spatiotemporal image. **B)** Linescan images showing SR Ca^{2+} release at the cell surface and in the center following respective caffeine application or clamping RyR P_O at 0.2 in experimental (Greiser *et al.*, 2014) (left) and simulated median tubulated (right) cells. The simulated cell was paced at 0.5 Hz, with caffeine application 750 ms after the last stimuli generating SR Ca^{2+} release throughout the entirety of the cell. The local electric- (CaT) and caffeine-evoked Ca^{2+} transient (cCaT) peak near the periphery (ss, 3 CRUs on each side) and central area (cc, 3 CRUs) were measured during the last 20 electric-evoked Ca^{2+} transients or caffeine stimulation and the ratio of central vs. surface electric-evoked Ca^{2+} transient peaks (cc/ss (ratio)) calculated from the average. The ratio of central vs. surface CaT and cCaT $[Ca^{2+}]_{Cyto}$ peaks (cc/ss (ratio)) are similar between experiment and simulation. **C)** Post-pacing caffeine-induced Ca^{2+} transient (cCaT) traces under 0.5 Hz voltage-clamp control in experimental (Voigt *et al.*, 2012) (i) and simulated (ii) cells. Voltage-clamp protocol is shown inset. Diastolic (iii) and systolic (iv) CaT $[Ca^{2+}]$, cCaT amplitude (v) and decay constant (vi) in experimental (Voigt *et al.*, 2012, 2014) and simulated cells with varying t-tubule densities (Dense, Median, Detubulated) as marked by respective blue, black, and orange bars.

To validate the role of TATS in subcellular Ca^{2+} signaling, we compared the spatial and temporal properties of Ca^{2+} sparks and waves in myocytes with and without tubules. Cells devoid of TATS exhibit a hallmark U-shaped Ca^{2+} wave, whereby Ca^{2+} rises at the cell periphery upon electric field stimulation and then propagates from the cell periphery to the center, as also shown in experimental linescan images (**Fig. 2.6Ai**, top) (Kirk *et al.*, 2003) and in our model (**Fig. 2.6Aii**, top). However, cells with central TATS exhibit W-shape Ca^{2+} waves (**Fig. 2.6Ai**, bottom) (Kirk *et al.*, 2003), indicating increased synchrony of Ca^{2+} release in inner areas where tubules are present. The simulation linescan images recapitulate the results of the experiment (**Fig. 2.6Aii**, bottom).

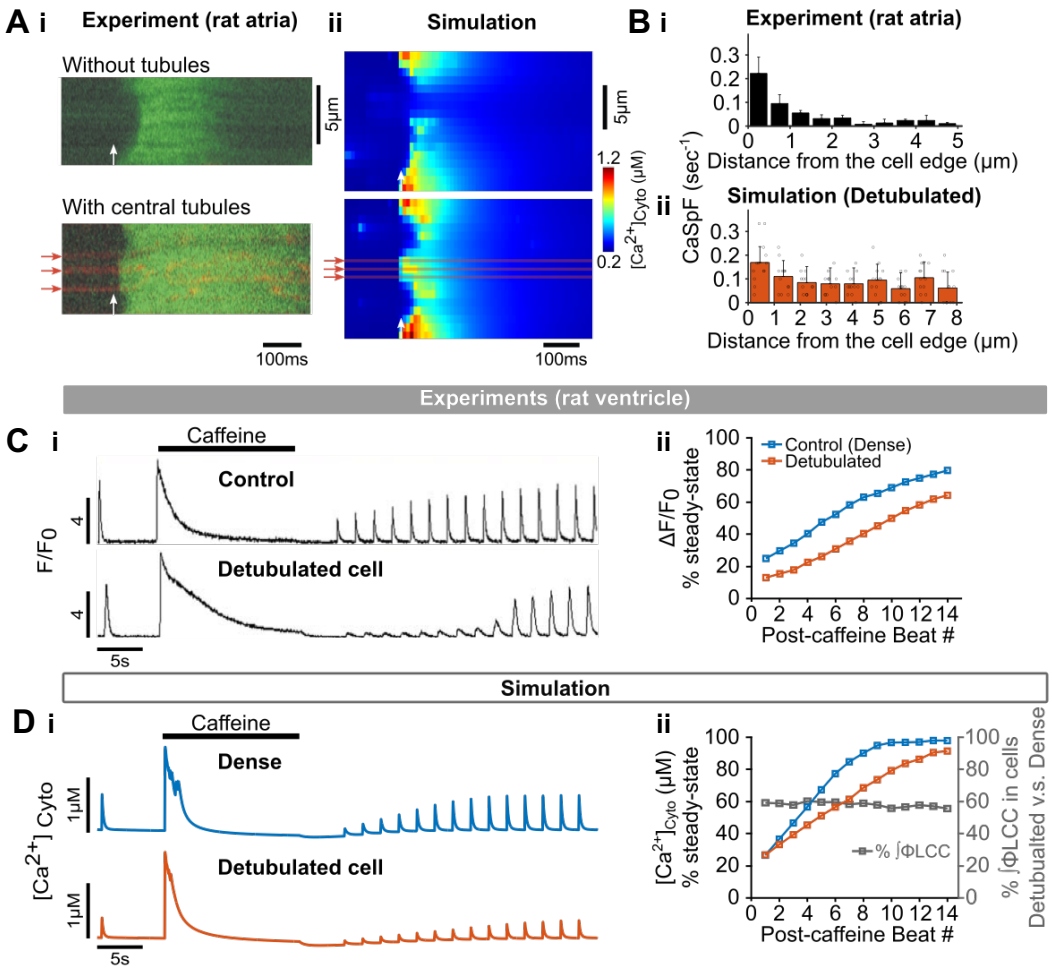

Figure 2.6 - Validation of the effects of tubule-loss on Ca^{2+} signaling.

A) Linescan images of experimental (Kirk *et al.*, 2003) (i) and simulated (ii) atrial cells without (top) or with (bottom) tubules. Tubule locations are marked by red arrows and the stimulus timing is indicated with white arrows. The axial tubules in simulated cells are 3*3 CRUs in the center x-direction with whole-cell length. **B)** Spatial distribution of Ca^{2+} sparks in experimental rat atrial cells (Brette *et al.*, 2005) (i) and simulated detubulated cells (ii). To replicate the experimental protocol, the simulated cell was paced at 0.5 Hz to steady state with a subsequent 30 s quiescence where Ca^{2+} sparks along 13 transversal scan lines (i.e., 13 y-axis lines equally distributed between 10^{th} and 46^{th} CRUs on the central x-axis) were measured and averaged. **C)** Representative CaT traces showing SR Ca^{2+} release following caffeine application and subsequent transient recovery (i) in experimental rat ventricular cells with dense tubules (top) and without tubules following detubulation (bottom) (Brette *et al.*, 2005). Post-caffeine CaT recovery from experimental observation shows slower post-caffeine CaT recovery in detubulated cells

(ii). **D)** Representative CaT traces showing SR Ca release following pseudo caffeine application (clamping RyR P_O at 0.2) and subsequent transient recovery (i) in simulated cells with dense tubules (top) and without tubules following detubulation (bottom). Simulated post-caffeine CaT recovery data (ii) is similar to experimental observation, in which the ratio of Ca^{2+} influx via LCC in detubulated vs. densely tubulated cells is reduced resulting in slower post-caffeine CaT recovery.

To investigate the subcellular regional differences of Ca^{2+} sparks properties, Brette et. al. (Brette *et al.*, 2005) measured Ca^{2+} spark frequency (CaSpF) at 1 μm intervals from the cell edge, and found that diastolic Ca^{2+} sparks in rat atrial myocytes that lack TATS occurred predominantly at the cell periphery (**Fig. 2.6Bi**). Similarly, the CaSpF in the detubulated human atrial myocyte model was higher near the cell edge compared with the cell interior (**Fig. 2.6Bii**). In the same study, caffeine was applied to rat ventricular myocytes to empty the SR and monitor the gradual recovery of the Ca^{2+} transient. In these experiments the Ca^{2+} transient amplitude recovered more slowly in detubulated ventricular cells vs. control (**Fig. 2.6Ci**) (Brette *et al.*, 2005). The experimental summary data indicates that the number of beats required for 50% recovery was ~5.5 in control cells and ~9.9 in detubulated cells (**Fig. 2.6Cii**). The model recapitulates this behavior (**Fig. 2.6Di-ii**), in which loss of TATS slows post-caffeine Ca^{2+} transient amplitude recovery. Brette et. al. (Brette *et al.*, 2005) hypothesized that the slower recovery in detubulated cells is due to the reduced Ca^{2+} influx associated with TATS loss leading to slower SR refilling. In alignment with this hypothesis, our model shows that the Ca^{2+} influx via LCCs during the post-caffeine pacing period is reduced by 40% in the detubulated cell compared with the cell with dense TATS (**Fig. 2.6Dii** grey line). Therefore, simulated effects of human atrial myocyte detubulation on subcellular and whole-cell Ca^{2+} signaling mirror experimental observations in rat atrial and ventricular myocytes. Namely, our model recapitulates 1) the spatiotemporal characteristics of Ca^{2+} waves in the presence and absence

of TATS, 2) the Ca^{2+} spark regional distribution in atrial myocytes, and 3) the time course of global $[Ca^{2+}]_{Cyto}$ transient amplitude recovery in the cells without and with TATS.

2.3.3 Loss of TATS reduces NCX-mediated Ca^{2+} extrusion, elevating cleft Ca^{2+} and RyR P_O resulting in enhanced SCR events and promotion of DADs

With our validated model, we sought to investigate how changing TATS affect arrhythmic biomarkers, namely SCRs and DADs. We subjected our population of models with varying tubular structures and densities to pacing at various cycle lengths followed by a pause to detect any diastolic (unstimulated) activity. Representative linescan images from densely and sparsely tubulated myocyte models in **Fig. 2.7Ai** show that in the sparsely tubulated cell the AP-triggered Ca^{2+} wave was less synchronous, with larger and more frequent SCRs observed in the unstimulated period compared to the cell with dense TATS. Furthermore, the cell with sparse TATS displayed a smaller AP-triggered Ca^{2+} transient, but larger SCRs (**Fig. 2.7Aii**) and DADs (**Fig. 2.7Aiii**). These results were confirmed when repeating the stochastic simulations with different random seeds (**Fig. 2.9A**). Analysis of the whole myocyte model population with varying TATS revealed that cells with sparser TATS have larger SCRs and DADs (**Fig. 2.7Bi**), and a shorter latency of SCRs and DADs (**Fig. 2.7Bii**). Since SCRs and DADs are generally more likely to occur at increasing pacing rates, we measured the pacing rate threshold for SCRs and DADs, i.e., the slowest pacing rate at which these events occurred. Our model predictions indicate that the rate thresholds for SCRs and DADs are lower in cells with sparse vs. dense TATS (**Fig. 2.7Biii**), suggesting that cells with a low density of tubules may be more susceptible to Ca^{2+}-driven arrhythmia. We further utilized the model to reveal the mechanisms by which loss of tubules promotes SCRs and DADs. We found that in cells with sparse TATS, Ca^{2+} extrusion by NCX is reduced (**Fig. 2.7Ci**) leading to elevated diastolic cleft Ca^{2+} concentration (**Fig. 2.7Cii**). The increased cleft Ca^{2+} results in augmented diastolic RyR

P_O (**Fig. 2.7Civ**) and RyR leak (**Fig. 2.7Cv**) leading to increased SCRs and DADs. Conversely, the lack of appreciable changes in SR load (**Fig. 2.7Ciii**) did not strongly affect RyR P_O.

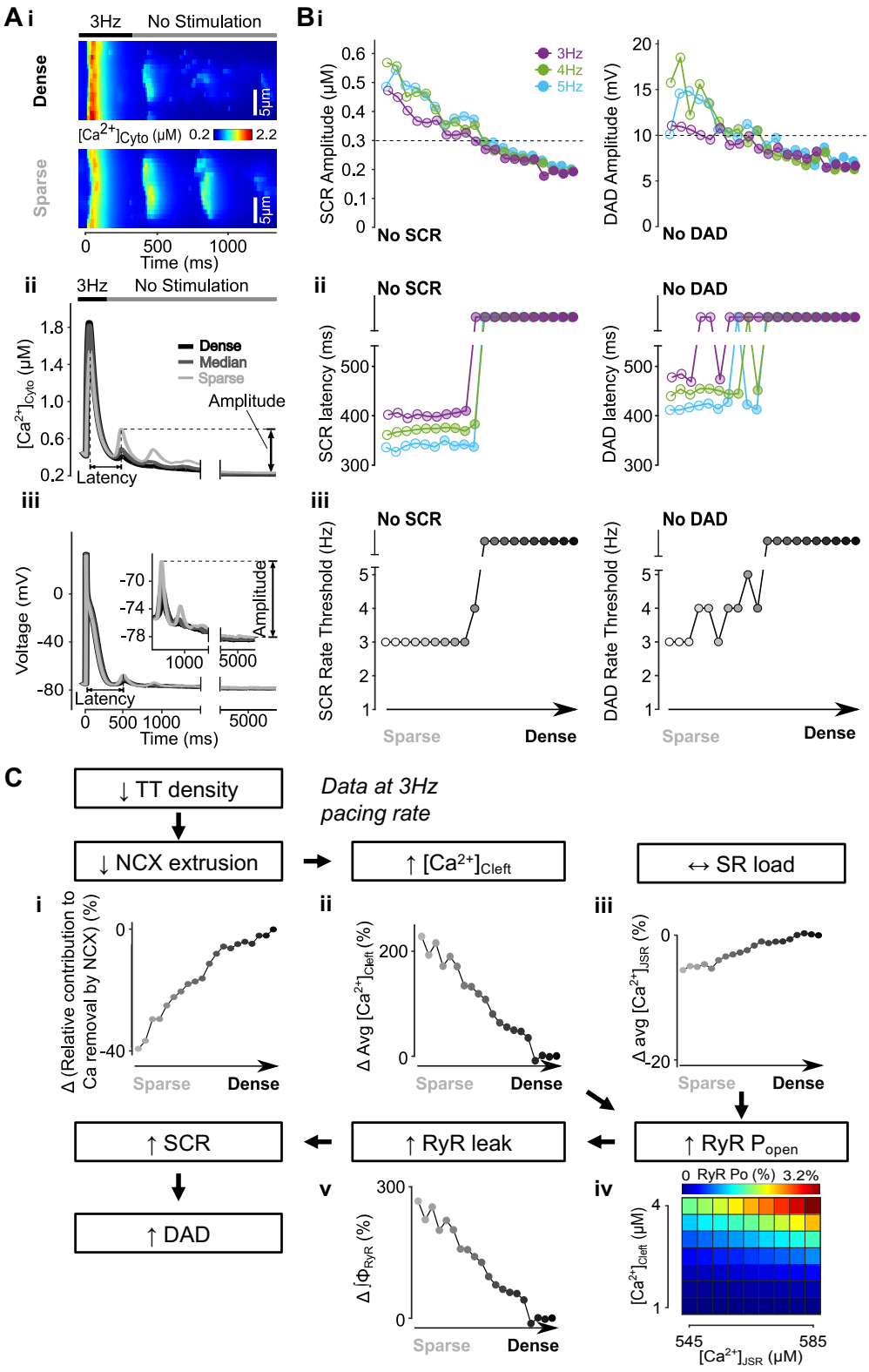

Figure 2.7 –Loss of TATS promotes spontaneous Ca^{2+} release events (SCRs) and delayed after-depolarizations (DADs).

A) Transverse line scan of cytosolic Ca^{2+} for cells with dense or sparse tubules (i), global cytosolic Ca^{2+} (ii) and voltage (iii) traces showing the final 3Hz-paced beat and subsequent no-stimulation period for observation of SCRs and DADs. SCR and DAD amplitude was calculated as the difference between the first peak maximum and the diastolic minimum in the no-stimulation period and latency as the duration between the peak of the last stimulated beat and the first peak of no-stimulation period. **B)** Amplitude (i), latency (ii) and rate threshold (iii) for SCRs and DADs with respect to increasing tubular density from detubulated to densely tubulated cells. Amplitudes over 0.3 μM and 10 mV were set as thresholds for SCRs and DADs respectively, with events under these cut-offs deemed as 'no SCR' or 'no DAD' and indicated by the dashed line. **C)** Mechanism underlying promotion of SCRs and DADs in cells with sparse tubules. Biomarkers were determined from the first 100 ms of the no-stimulation period and normalized to those of cells with dense tubules, with the Ca^{2+}-dependence of RyR P_O determined by an in-silico bilayer study. In cells with fewer tubules, Ca^{2+} removal by NCX is reduced (i) leading to elevated cleft Ca^{2+} concentration (ii) but no change in SR load (iii). Increased cleft Ca^{2+} results in augmented RyR P_O (iv) and RyR leak (v) leading to increased SCRs and DADs.

Overall, our simulations suggest that loss of TATS is associated with reduced NCX-mediated Ca^{2+} extrusion, which alters RyR function and promotes SCRs and DADs.

2.3.4 SCR properties vary between spatially distinct CRUs, with SCR threshold and latency decreased and amplitude increased in inner uncoupled CRUs

We further sought to determine whether regional variations exist in the effects of varying tubular density on the latency, amplitude, and pacing threshold for SCRs. To do so, we analyzed the averaged Ca^{2+} transient of surface CRUs, inner CRUs coupled to TATS, and inner CRU that are not coupled to TATS in each cell in the population with varying TATS and quantified the biomarkers of the local Ca^{2+} transients.

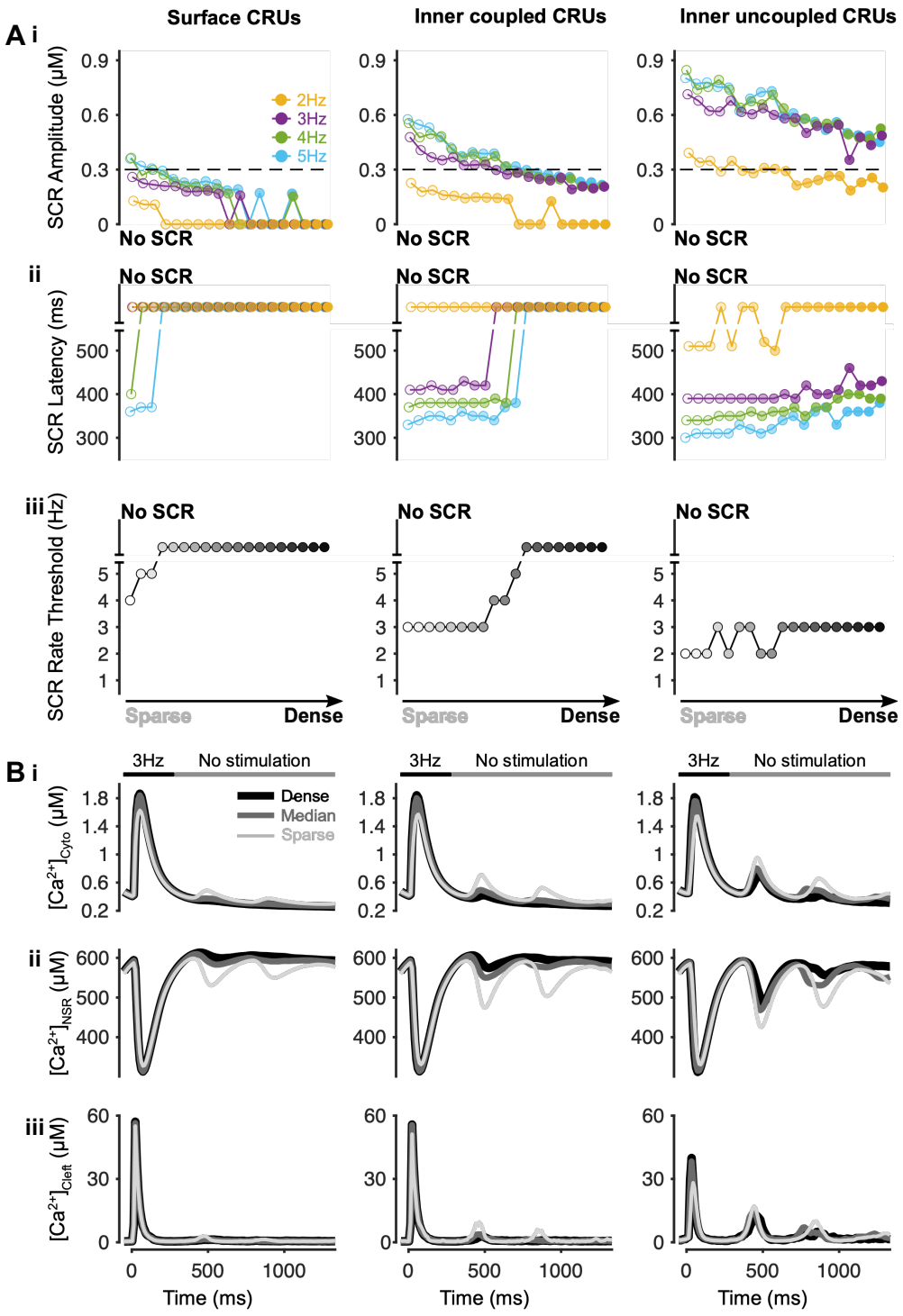

Figure 2.8 – Promotion of SCRs is greatest in inner uncoupled CRUs in cells with fewer tubules.

A) Amplitude (i), latency (ii) and rate threshold (iii) for local SCRs of surface (left), inner coupled (middle), and inner uncoupled (right) CRUs with respect to increasing tubular density. **B)** Ca^{2+} concentration in the cytosol (i), network SR (ii) and cleft (iii) of surface (left), inner coupled (middle) and inner uncoupled (right) CRUs following pacing at 3 Hz to examine SCRs.

We found that the amplitude of SCRs is larger (**Fig. 2.8Ai**) and the latency reduced (**Fig. 2.8Aii**) in inner uncoupled CRUs, where the pacing threshold for SCR is lower (**Fig. 2.8Aiii** and **2.9B**) compared to inner coupled and surface CRUs. The representative traces of average cytosolic, network SR, and cleft Ca^{2+} concentration following pacing at 3 Hz (**Fig. 2.8B**) also show larger SCRs in inner uncoupled CRUs independent of the TATS density. The simulation results indicate that while loss of TATS promotes SCRs throughout the whole cell, uncoupled CRUs may play a more important role in SCR incidence vs. inner coupled CRUs and surface CRUs.

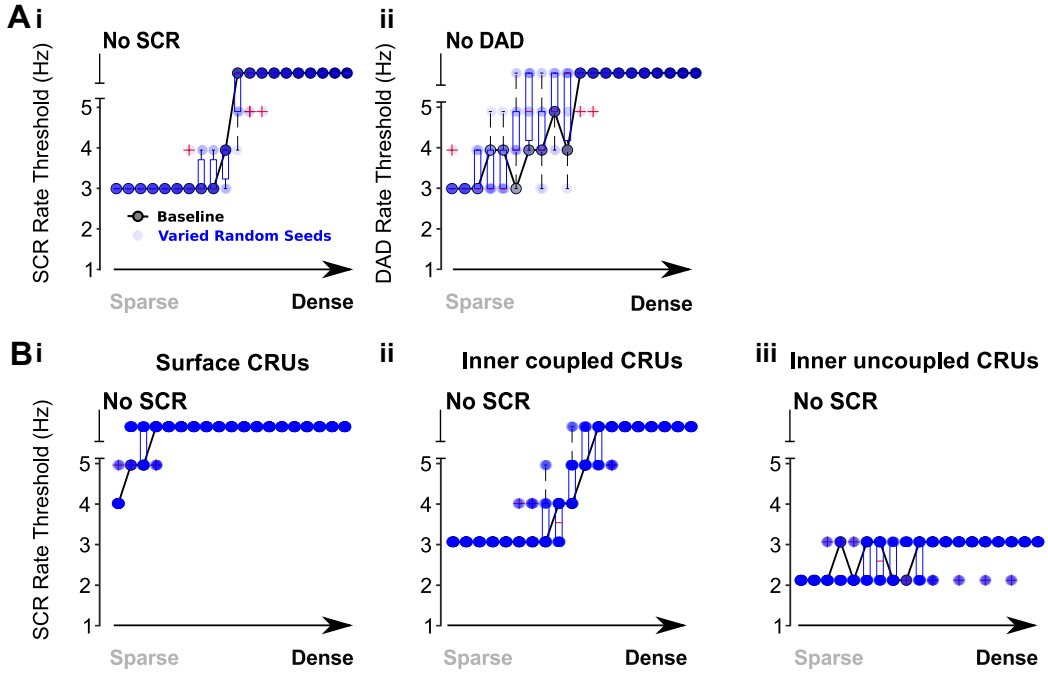

Figure 2.9 – Varying random seeds regulating stochasticity does not change the effects of TATS loss on SCRs and DADs.

A) Rate threshold for SCRs (i) and DADs (ii) with respect to increasing tubular density from detubulated to densely tubulated, with 10 different random seeds (blue). The baseline results are superimposed. **B)** TATS-loss-induced promotion of SCRs is greatest in inner uncoupled CRUs in cells with fewer tubules in all three conditions of varying uncoupled CRU compartments.

2.4 Discussion

In this study we built, parameterized, and validated a three-dimensional model of the human atrial myocyte, coupling electrophysiology and Ca^{2+} handling with subcellular spatial details governed by the TATS. This work quantitatively explains how TATS loss disrupts diastolic Ca^{2+} homeostasis and electrophysiological stability in human atrial cells. Specifically, we demonstrated that TATS loss reduces NCX-mediated Ca^{2+} removal leading to increased cleft Ca^{2+} concentration that promotes SCRs (**Fig. 2.7C**), especially in inner CRUs (**Fig. 2.8**), and subsequent DADs (**Fig. 2.7C**). These findings provide mechanistic insight into how atrial TATS remodeling can lead to Ca^{2+}-driven proarrhythmic behavior in the physiological range that may ultimately contribute to the arrhythmogenic state in both HF and AF.

2.4.1 TATS loss is associated with altered Ca^{2+} homeostasis

Previous experimental studies have shown atrial TATS loss is associated with disrupted Ca^{2+} handling in paroxysmal AF (Wakili *et al.*, 2010), persistent AF (Lenaerts *et al.*, 2009), and HF induced by both rapid ventricular pacing (Dibb *et al.*, 2009) and myocardial infarction (Kettlewell *et al.*, 2013), as also shown in the ventricle in HF (Balijepalli *et al.*, 2003; Louch *et al.*, 2004, 2006; Cannell *et al.*, 2006). The remodeling of the TATS in disease has two main functional consequences: (i) cell membrane channel localization and currents are altered and (ii) RyRs are uncoupled from LCCs and other transporters in the sarcolemma. In both atrial and ventricular myocytes, loss of TATS causes decreased LCC Ca^{2+} influx, accompanied by shortening of APD and thus refractory period that can increase vulnerability to arrhythmic activity (Bosch *et al.*, 1999; Kneller *et al.*, 2002; Brette *et al.*, 2006; Lenaerts *et al.*, 2009; Wakili *et al.*, 2010). These findings were reproduced in our simulation results, where detubulated cells had shorter APD and reduced Ca^{2+} influx compared to those with denser

TATS (**Fig. 2.4Cii** and **6Dii**). In addition to I_{Ca} and APD changes, TATS loss increases the number of uncoupled RyRs (Song *et al.*, 2006) resulting in asynchronous CICR during the systolic period (Song *et al.*, 2006; Louch *et al.*, 2006), and damaged excitability and contractility (Sacconi *et al.*, 2012). Together, the compounding effects of reduced Ca^{2+} influx and RyR coupling present in the diastolic period, with slowed post-caffeine Ca^{2+} SR reloading, reduced diastolic Ca^{2+} spark frequency (Brette *et al.*, 2005), and enhanced SCRs in uncoupled CRUs in HF (Dries *et al.*, 2018), as recapitulated in our model.

Similar to TATS loss in disease, asynchrony of CICR is also reported in various experiments of atrial cells with sparse TATS where many central RyRs are uncoupled. Here, while triggered release occurs around the cell periphery, central CICR occurs as a U-shaped wave of propagation leading to delayed and impaired Ca^{2+} release in the cell interior (Kirk *et al.*, 2003; Woo *et al.*, 2005; Dibb *et al.*, 2009; Lenaerts *et al.*, 2009; Smyrnias *et al.*, 2010; Wakili *et al.*, 2010; Frisk *et al.*, 2014; Yue *et al.*, 2017). The asynchronous CICR in atrial myocytes leads to smaller Ca^{2+} transient amplitude and longer rising duration, which is linked with weaker contractility compared to ventricular myocytes (Tanaami *et al.*, 2005; Narolska *et al.*, 2005; Walden *et al.*, 2009; Smyrnias *et al.*, 2010). Interestingly in atrial cells with extensive TATS, TAT-coupled RyRs are hyperphosphorylated which facilitates enhanced Ca^{2+} release and promotes the propagation of Ca^{2+} waves (Brandenburg *et al.*, 2016). As such, loss of TATS in these cells would disrupt both triggered and propagated Ca^{2+} release diminishing systolic contractility. In addition to the effect on Ca^{2+} transient amplitude, computational studies have predicted that TATS loss also enhances alternans susceptibility (Li *et al.*, 2012; Nivala *et al.*, 2015) and the likelihood of triggered Ca^{2+} waves during the AP due to the latency of Ca^{2+} release by the large pool of orphaned RyRs following LCC opening (Shiferaw *et al.*, 2017, 2018, 2020*b*).

2.4.2 Reduced local NCX activity underlies diastolic Ca^{2+} and V_m instabilities associated with TATS loss

While systolic Ca^{2+} abnormalities due to TATS loss have been extensively characterized, the impact of TATS remodeling on Ca^{2+} homeostasis during the diastolic period is not fully understood. Though much consideration has been given to the impact of altered LCC localization, changes in other tubular proteins, namely NCX, likely play a key role. Indeed, we predict that the effect of TATS loss on NCX function underlies diastolic Ca^{2+} and voltage instabilities. Experimental observations indicate TATS loss disrupts NCX function to promote SCRs in atrial myocytes, with preliminary data from computational studies predicting the association between the few TATS and SCRs (Colman *et al.*, 2016*b*). Both NCX and PMCA are highly expressed within the TATS (Despa *et al.*, 2003; Chase & Orchard, 2011; Schulson *et al.*, 2011; Swift *et al.*, 2012) and NCX on TATS has been shown to co-localize with RyRs (Thomas *et al.*, 2003; Jayasinghe *et al.*, 2009; Schulson *et al.*, 2011; Biesmans *et al.*, 2011). Loss of TATS in NCX knock-out has also been shown to be associated with abnormal Ca^{2+} cycling that impacts contractility and rhythm (Yue *et al.*, 2017). As such, TATS loss induces 1) decreased NCX expression and subsequent reduced local Ca^{2+} extrusion, 2) NCX-RyR decoupling, and localized inner subcellular Ca^{2+} accumulation. Our results support this mechanism and demonstrate that disrupted NCX-mediated Ca^{2+} removal caused by TATS loss contributes to SCRs by elevating $[Ca^{2+}]_{Cleft}$ and subsequently enhancing RyR P_O (**Fig. 2.7C**), especially in inner uncoupled CRUs (**Fig. 2.8A**). From this point of view, though the NCX upregulation that occurs in AF eventually enhances Ca^{2+}-voltage instability (Voigt *et al.*, 2012), it may act to limit enhanced SCRs and shortened APD responses to TATS loss and reduced I_{Ca} and therefore be an initial compensatory response. Increased TATS density with enhanced NCX expression in SERCA-KO mice is also believed to be a compensatory response (Swift *et al.*, 2012). While under these conditions reduced NCX contributes to a pro-arrhythmic state,

the opposite can also be true whereby altered NCX function can shift the balance between SCRs and Ca^{2+}-voltage instability coupling in an anti-arrhythmic manner (Antoons *et al.*, 2012). Though it is difficult to isolate the independent role of decreased NCX from reduced I_{Ca} and orphaning of RyRs that also occur with TATS loss, Ca^{2+} signal silencing and reduced central Ca^{2+} transient that may protect the cell from SCRs have been reported experimentally in atrial myocytes following 5-7 days of rapid atrial pacing (Wakili *et al.*, 2010; Greiser *et al.*, 2014). It is unclear whether this short-term protective effect of TATS loss is transient and whether the longer-term remodeling that occurs, for example in the transition between paroxysmal to chronic AF, leads to a swing towards the pro-arrhythmic state (Lenaerts *et al.*, 2009; Wakili *et al.*, 2010). Given our simulations of TATS loss and the resultant reduced NCX-mediated Ca^{2+} extrusion cause increased SCRs and DADs, we suggest that ultimately the pro-arrhythmic increase in $[Ca^{2+}]_{Cleft}$ overrides any benefit of reduced triggered central Ca^{2+} release. This tool can be used to investigate transitional remodeling that occurs during disease progression.

2.4.3 Arrhythmogenic waves in human atrial myocytes originate from the inner uncoupled CRUs

In addition to investigating the impact of variable TATS densities on the occurrence of SCRs and DADs, through incorporating different spatial CRU domains our model has permitted examination of the origin of these events. Experimental studies have previously shown diastolic Ca^{2+} sparks occur primarily around the cell periphery in atrial cells with no TATS (Brette *et al.*, 2005), suggesting that SCRs initiate in coupled CRUs. Interestingly, we observed this in the model at slow pacing rates (**Fig. 2.6B**), but with rapid pacing, as seen in atrial tachycardia and AF, SCRs were larger and showed greater incidence in inner uncoupled CRUs vs. coupled CRUs (**Fig. 2.8**). We suggest that these regional differences are indeed dependent on the stimulation rate and, notably, they are similar to those observed in HF ventricular myocytes,

where spark frequency increases in uncoupled vs. coupled release sites with increasing pacing frequency (Dries *et al.*, 2018).

At faster rates, the increase in SR Ca^{2+} loading and thus the increase in RyR leak (Shiferaw *et al.*, 2017) impact more strongly the inner uncoupled CRUs by enhancing SCRs, while local NCX Ca^{2+} extrusion eases Ca^{2+} sparks in coupled CRUs. Compared to coupled CRUs where Ca^{2+} is rapidly extruded by colocalized NCX thus limiting the magnitude of SCRs, Ca^{2+} leak from uncoupled CRUs is not readily removed from the cytosol and must diffuse to be extruded by NCX. As such, the inner Ca^{2+} concentration is relatively higher than that at the periphery. In addition to changes in SR load, fast pacing elevates inner diastolic $[Ca^{2+}]_{Cleft}$ causing increased RyR P_O and thus greater leak in inner uncoupled CRUs vs. surface CRUs due to spatial differences in NCX extrusion (**Fig. 2.7C**). This is in contrast to that at slower pacing rates where lower diastolic $[Ca^{2+}]_{Cleft}$ results in similar RyR P_O in coupled vs. uncoupled CRUs (**Fig. 2.2Bii** and **7Civ**). The higher simulated RyR P_O near the cell periphery vs. interior at lower pacing rates (**Fig. 2.6B**) is induced by the differences in Ca^{2+} diffusion characteristics at surface vs. inner CRUs and the presence of background Ca^{2+} currents on the external sarcolemma of detubulated cells.

In addition, varying TATS density does not appreciably change the SCR rate threshold in surface and inner uncoupled CRUs, with surface CRUs being generally more stable and inner uncoupled CRUs typically being more prone to SCR. Instead, varying TATS changes the balance between (stable) coupled and (unstable) uncoupled CRUs to determine the net effect for SCR, with the most remarkable changes seen in the TATS-dependence of SCR in inner coupled CRUs. Given that the extensive loss of TATS in HF and AF consequently increases the number of inner uncoupled CRUs, this may contribute to the increased arrhythmic activity observed in these diseases.

2.4.4 Model assumptions and limitations

We present, for the first time, a fully integrated human atrial ECC model that is coupled with an experimentally informed population of TATS structures. We incorporated TATS properties measured in an experimental manner to ensure the TATS population replicates experimental observations (**Fig. 2.1Bi-ii**) and allows for virtual-patient population and high-throughput simulation in future TATS studies. Model parameterization (**Fig. 2.1, 2A-B, 3**) and validation (**Fig. 2.2C, 4-6**) utilized extensive human-specific independent atrial datasets to generate human-specific results and conclusions that are highly translatable. Yet, due to lack of data availability for several features, experiments from rat or rabbit atrial or ventricular experiments were used, thus introducing some uncertainty. Using this model we have systematically evaluated the role of TATS disruption in Ca^{2+}-driven proarrhythmic behavior in the physiological range.

We acknowledge that other factors may contribute to the effect of varying TATS on local and global Ca^{2+} signaling, including variation in the volume of the release sites, non-uniform distribution of Ca^{2+} handling proteins (Herraiz-Martínez *et al.*, 2022), and alterations in their regulatory state (Brandenburg *et al.*, 2016), as discussed below. In our compartmental model, RyRs are sensitive to the rapid changes in cleft Ca^{2+} favored by the narrow cleft (i.e., the surrounding area near RyRs), which is critical for both CICR and Ca^{2+} sparks. While our model assumes that all coupled and uncoupled CRUs have the same Ca^{2+}compartments, as also done in previous computational studies (Shiferaw *et al.*, 2017, 2020*b*; Song *et al.*, 2018), it is conceivable that RyRs release Ca^{2+} in a larger compartment in CRUs that are not coupled with T-tubules. To address this possibility, we assessed the impact of altered Ca^{2+} compartmentation in orphaned/uncoupled CRUs. Namely, we performed simulations in which uncoupled CRUs had increased (+50%) submembrane volume (v_s), increased cleft volume (v_{Cleft}), or faster Ca^{2+} diffusion between cleft and submembrane ($\tau_{Cleft \leftrightarrow s}$ decreased by 50%). In all these simulated

conditions, our main conclusions on the local and global effects of TATS loss on SCR (and DAD) remained unaffected (**Fig. 2.10**). Additionally, we note that Ca^{2+} diffusion out of the cleft ($\tau_{Cleft \leftrightarrow s}$ ~0.022 ms, estimated by (Restrepo *et al.*, 2008)) is much faster than RyR opening and closure (0.7~1.9 ms) (Györke & Györke, 1998). Thus, sustained RyR flux due to longer channel openings (or fewer closures), dictated by RyR Ca^{2+} sensitivity and unitary flux, is most potent for maintaining high local Ca^{2+}.

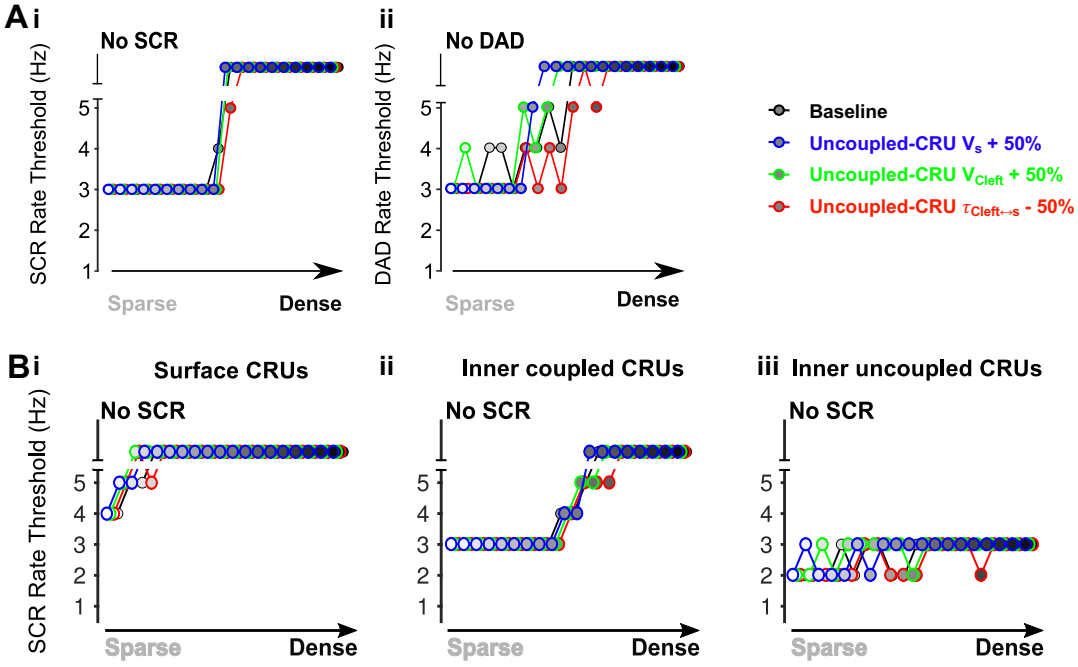

Figure 2.10 – Varying compartmentalization of uncoupled CRUs does not change the effects of TATS loss on SCRs and DADs.

A) Rate threshold for SCRs (i) and DADs (ii) with respect to increasing tubular density from detubulated to densely tubulated. Uncoupled CRU compartments retained the maximum ion flux strength but had 1) submembrane volume (v_s) increased by 50% (blue), 2) cleft volume (v_{Cleft}) increased by 50% (green), or 3) the time scale of Ca^{2+} diffusion between cleft and submembrane ($\tau_{Cleft \leftrightarrow s}$) decreased by 50% (red). **B)** TATS-loss-induced promotion of SCRs is greatest in inner uncoupled CRUs in cells with fewer tubules in all three conditions of varying uncoupled CRU compartments.

Our model assumes that all CRUs are composed of the same ensemble of ion channels and transporters, with the only differences being incorporated between CRUs that are coupled vs. uncoupled to the cell membrane. Nevertheless, heterogeneity has been reported in the distribution of Ca^{2+}-handling proteins (e.g., CSQ and RyR) in human atrial myocytes (Herraiz-Martínez *et al.*, 2022). Given that enhanced frequency of SCRs and DADs have been observed in isolated cells from AF vs. normal sinus rhythm patients (Voigt *et al.*, 2012, 2014) where both will have lost t-tubules due to enzymatic digestion, these differences are unlikely to be attributed to altered TATS density. For this study we assumed that all membrane ion channels and transporters are distributed uniformly to all coupled CRUs, with their density maintained (independent of TATS variation). This was supported by even distribution of LCC in TATS and on the surface membrane in human atrial cells (Glukhov *et al.*, 2015). While data regarding NCX distribution in human are lacking, in rat atrial myocytes, the Louch group showed that NCX current in tubulated cells was roughly double that of untubulated cells (Tazmini *et al.*, 2020), suggesting that NCX distribution may also be relatively equal between external sarcolemma and TATS. The effect of altering the expression and distribution of key Ca^{2+} handling proteins (i.e., NCX, RyR, and CSQ) on SCR and arrhythmogenic outcomes is the focus of a companion paper (Chapter 3).

Similarly, our model does not explicitly incorporate the mechanisms by which PKA and CaMKII influence the function of LCC, RyR, and PLB in normal physiology nor their regulatory state in the face of disease-induced ultrastructural remodeling. For example, RyR clusters at axial tubule-SR junctions are hyperphosphorylated to facilitate spontaneous macro Ca^{2+} sparks (duration and width) and rapid AP-evoked Ca^{2+} signals in mouse atria (Brandenburg *et al.*, 2016). A computational study predicted that this local hyperphosphorylation may increase the incidence at these sites but reduce the size of the SCRs (Sutanto *et al.*, 2018). However, the latency difference of AP-evoked Ca^{2+} release between

axial tubule coupled junctions and those at the surface is much more pronounced in mouse and rat atrial myocytes but less evident in the more human-like rabbit atrial myocyte (Brandenburg *et al.*, 2018). Such difference suggests the effects of RyR hyperphosphorylation differs between species. We carried out additional simulations in which hyperphosphorylation of the TATS-associated RyRs was modeled by increasing the Ca^{2+} sensitivity of RyR P_O (i.e., reducing k_{cp}) (**Fig. 2.2Bii-iii**). Our results indicated that this differential regulation at the TATS-associated RyRs is not necessary to explain the faster AP-evoked Ca^{2+} release at the axial tubule coupled junctions vs. surface region (**Fig. 2.11Aii-iii**) shown in rat atrial myocyte experiments (**Fig. 2.11Ai**) (Brandenburg *et al.*, 2016). In these experiments, higher LCC density in axial tubule junctions is reported (Brandenburg *et al.*, 2016), which may further contribute to the regional differences in AP-evoked Ca^{2+} signaling in rat atrial myocytes. On the other hand, our simulations also indicate that the presence of axial tubules can in itself lead to higher Ca^{2+} spark frequency near axial tubules (**Fig. 2.11Bii**), with hyperphosphorylation of TATS-associated RyRs only modestly further increasing the Ca^{2+} spark frequency at these sites (**Fig. 2.11Biii**), similar to experimental results (**Fig. 2.11Bi**) (Brandenburg *et al.*, 2016). When simulating the effects of varying TATS density in the presence of hyperphosphorylation at the TATS-associated RyRs, we observed that while TATS loss still promotes SCRs and DADs (**Fig. 2.11C-D**), cells with denser TATS exhibited a lower rate threshold for SCRs and DADs compared with our baseline model (**Figs. 2.7 and 2.11C**). On the other hand, in ventricular myocytes with HF-induced TATS loss, non-coupled RyRs are more sensitive to CaMKII-inhibition, which suggests CaMKII may preferentially phosphorylate RyRs in uncoupled vs. coupled CRUs to initiate SCRs in the uncoupled CRUs (Dries *et al.*, 2018). As such, CaMKII hyperphosphorylation of uncoupled RyRs may ensue to compensate for lower systolic Ca^{2+} release in uncoupled CRUs in atrial myocytes, with the maladaptive effect to increase diastolic

RyR leak. Simulating hyperphosphorylated RyRs in uncoupled CRUs does indeed predict enhanced diastolic $[Ca^{2+}]_{Cyto}$, especially in uncoupled CRUs (not shown).

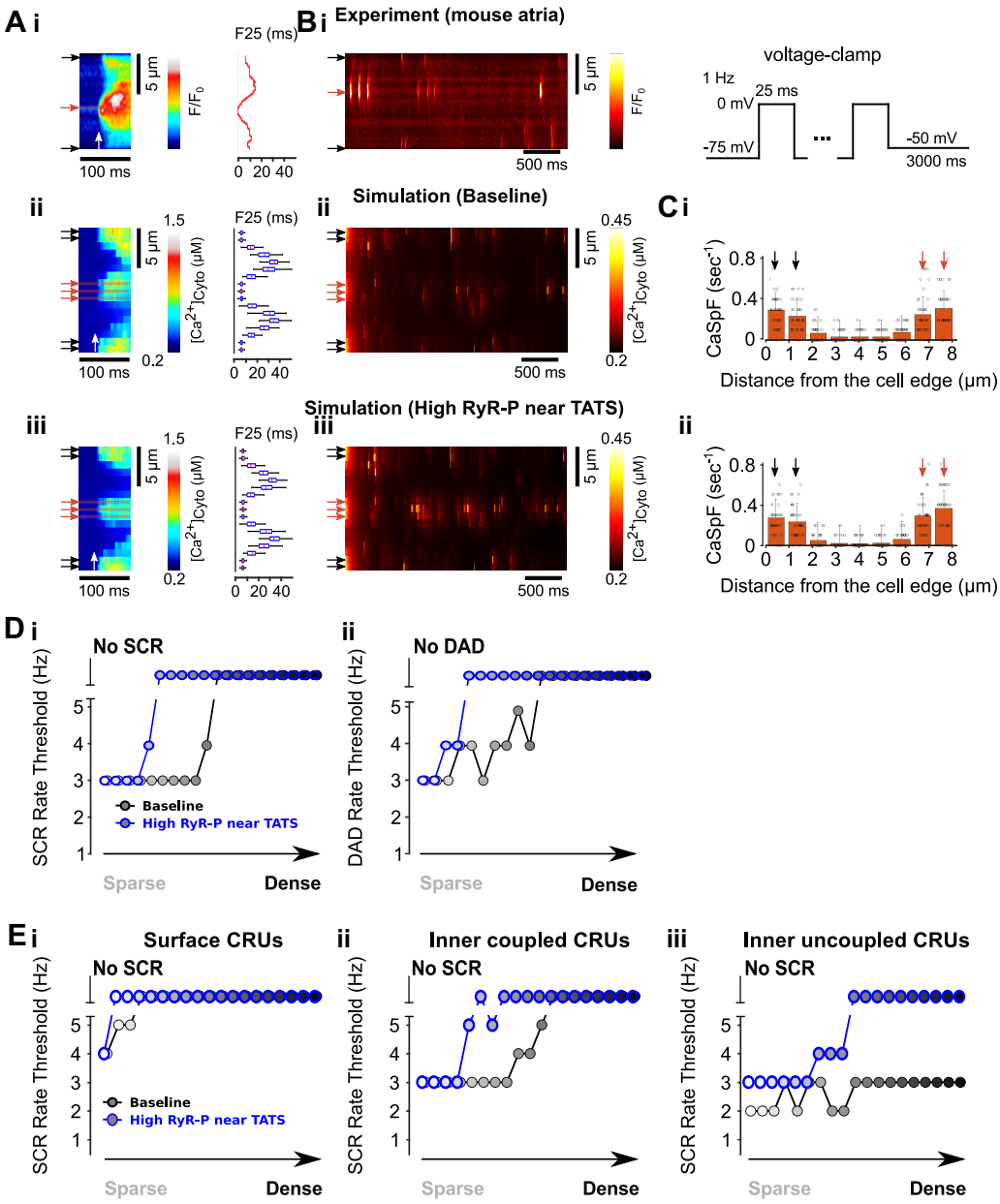

Figure 2.11 – TATS-associated RyR hyperphosphorylation does not change the effects of TATS loss on SCRs and DADs.

A) Experimental observations in a mouse atrial myocyte (i) showing the Ca^{2+} transient near TATS junctions (red arrow) vs. surface (black arrow) vs. uncoupled areas following stimulation (white arrow). The time to reach 25% of subcellular Ca^{2+} transient amplitude (F25) is reduced at TAT junctions suggesting Ca^{2+} release at TATS junctions occurs more rapidly following electrical stimulation

(Brandenburg *et al.*, 2016). Simulation of the model with axial tubules replicated the rapid response of subcellular Ca^{2+} signaling near tubules and surface without significant difference in F25 between surface and tubules (ii). This lack of difference remained unaltered with hyper-phosphorylation of TATS-associated RyRs (iii). **B)** During the voltage-holding period following 1-Hz voltage-clamp (protocol as an insert), Ca^{2+} spark occurrence is increased near tubules (red arrows) vs. other areas experimentally in mouse atrial myocytes (Brandenburg *et al.*, 2016) (i) and in the baseline (ii) and hyperphosphorylated TATS-associated RyR (iii) model simulation. **C)** Quantitative measurement of regional differences in Ca^{2+} spark frequency confirming increased spark occurrence at TATs in the baseline (i) and hyperphosphorylated RyR (ii) simulations. **D)** Relationship between SCR (i) and DAD (ii) occurrence in the baseline and hyperphosphorylated simulations with respect to increasing tubular density from detubulated to densely tubulated cells. Similar to the baseline model, TATS loss continues to reduce the rate threshold of SCRs (i) and DADs (ii) in the hyperphosphorylated RyR simulation, however this occurs at a lower TAT density. This is induced by lower SR load with leakier RyRs, which is in accordance with the conclusions in the companion paper (Chapter 3). **E)** SCR occurrence in surface (i), inner coupled (ii) and inner uncoupled (iii) CRUs with respect to increasing tubular density from detubulated to densely tubulated cells. When all RyRs in inner coupled CRUs are hyperphosphorylated, TATS-loss-induced promotion of SCRs in inner coupled and uncoupled CRUs remains apparent as in the baseline simulation. However, the threshold for SCRs is higher in following hyperphosphorylation with reduction in SCR threshold requiring more extensive TAT loss vs. baseline.

2.5 Conclusions

We developed a computational platform to study the interaction between changes in TATS organization/density, Ca^{2+} handling, and electrophysiology in human atrial myocytes. Our model explains the mechanisms by which atrial myocytes with sparse TATS exhibit greater vulnerability to SCRs and DADs and provides insight into ionic and Ca^{2+} handling remodeling that occurs alongside TATS loss in disease.

Chapter 3 Mechanisms of spontaneous Ca^{2+} release-mediated arrhythmia in a novel 3D human atrial myocyte model: II. Ca^{2+}-handling protein variation

The content of this chapter has been published in:

Zhang, X., Smith C., Morotti S., Edwards A., Sato D., Louch W., Ni H., Grandi E., "Mechanisms of spontaneous Ca2+ release-mediated arrhythmia in a novel 3D human atrial myocyte model: II Ca2+-handling protein variation" The Journal of Physiology (2022), DOI: 10.1113/JP283602

Abstract

Disruption of the transverse-axial tubule system (TATS) in diseases such as heart failure and atrial fibrillation occurs in combination with changes in the expression and distribution of key Ca^{2+}-handling proteins. Together this ultrastructural and ionic remodeling is associated with aberrant Ca^{2+} cycling and electrophysiological instabilities that underly arrhythmic activity. However, due to the concurrent changes in TATs and Ca^{2+}-handling protein expression and localization that occur in disease it is difficult to distinguish their individual contributions to the arrhythmogenic state. To investigate this, we applied our novel 3D human atrial myocyte model with spatially detailed Ca^{2+} diffusion and TATS to investigate the isolated and interactive effects of changes in expression and localization of key Ca^{2+}-handling proteins and variable TATS density on Ca^{2+}-handling abnormality driven membrane instabilities. We show that modulating the expression and distribution of the sodium-calcium exchanger, ryanodine receptors, and the sarcoplasmic reticulum (SR) Ca^{2+} buffer calsequestrin have varying pro and anti-arrhythmic effects depending on the balance of opposing influences on SR Ca^{2+} leak-load and Ca^{2+}-voltage relationships. Interestingly, the impact of protein remodeling on Ca^{2+}-driven proarrhythmic behavior varied dramatically depending on TATS density, with intermediately tubulated cells being more severely affected compared to detubulated and densely tubulated myocytes. This work provides novel mechanistic insight into the distinct and interactive consequences of TATS and Ca^{2+}-handling protein remodeling that underlies dysfunctional Ca^{2+} cycling and electrophysiological instability in disease.

3.1 Introduction

It is widely accepted that Ca^{2+} abnormalities can precipitate atrial fibrillation (AF), the most common cardiac arrhythmia. Both ionic remodeling and ultrastructural changes have been associated with aberrant Ca^{2+} signaling, excitation-contraction coupling, and AF (Nattel & Dobrev, 2012; Nattel & Harada, 2014; Dobrev & Wehrens, 2017; Denham *et al.*, 2018). Disruption of the transverse-axial tubular system (TATS) is one hallmark of AF structural remodeling that likely occurs early in disease progression and contributes to the dysfunction observed. In a companion paper, we developed a three-dimensional model of the human atrial myocyte coupling electrophysiology, whole-cell and local Ca^{2+} handling, and subcellular ultrastructural details, to interrogate the mechanisms by which TATS variability and loss affect human atrial physiology (Chapter 2). Our simulation predicted that TATS loss *per se* enhances vulnerability to proarrhythmic behaviors (i.e., spontaneous calcium releases, SCRs, delayed afterdepolarizations, DADs) by altering subcellular Ca^{2+} signaling. Nevertheless, SCRs and DADs occur more frequently in AF vs. sinus rhythm human atrial myocytes that both mostly lack TATS after isolation via enzymatic digestion (though a fairly robust TATS presence is seen in human atrial tissue (Richards *et al.*, 2011)). Indeed, the reduced density and regularity of the TATS is one aspect of disease remodeling, and it occurs concomitantly with altered channel and transporter expression, regulatory state, and function, as well as subcellular redistribution of ion channels, transporters, and Ca^{2+} handling proteins.

Well established hallmarks of ionic remodeling in AF include reduced L-type Ca^{2+} channel (LCC) current (Lenaerts *et al.*, 2009), increased inward rectifier K^+ current (I_{K1}) and constitutively activated acetylcholine-activated K^+ current ($I_{K,ACh}$) (Bosch *et al.*, 1999), enhanced Na^+/Ca^{2+} exchanger (NCX) activity (Lenaerts *et al.*, 2009; Voigt *et al.*, 2012), and hyperphosphorylated ryanodine receptors (RyRs) (Vest *et al.*, 2005; Neef *et al.*, 2010; Voigt *et al.*, 2012). The basal subcellular localization of these proteins in the atria, and whether they are

altered in disease, in not well understood. LCCs distribute equally in tubules and crest areas of the sarcolemma in control human atrial myocytes (Glukhov *et al.*, 2015). Given atrial LCC current amplitude likely depends on TATS density as shown in rat ventricular myocyte experiments (Frisk *et al.*, 2014), TATS loss in chronic AF might contribute to the observed reduction in current density. Recently, in human atrial myocytes from both normal sinus rhythm and chronic AF patients, RyR and the sarcoplasmic reticulum (SR) Ca^{2+} buffer calsequestrin (CSQ) were found more densely expressed near the cell periphery vs. the cell interior (Herraiz-Martínez *et al.*, 2022). This is similar to what has previously been shown in rat atrial myocytes, where RyR-CSQ colocalization was reduced in the cell interior vs. periphery (Schulson *et al.*, 2011). To our knowledge, NCX localization in human atrial myocytes has not yet been investigated, and while NCX is expressed at both the cell surface and in the TATS membrane, the precise quantitative distribution may vary in different species and cardiac regions (Melnyk *et al.*, 2005; Scriven *et al.*, 2010; Schulson *et al.*, 2011).

The available data on ion channels and Ca^{2+} handling protein expression, localization, and function in human atrial myocytes is limited and may not be representative of the heterogeneous human atrial myocyte population in tissue. There are known regional differences across the atria, e.g., in right vs. left atrium (Arora *et al.*, 2017), pulmonary vein vs. free atrial wall (Melnyk *et al.*, 2005), and insight from isolated cells is also complicated by TATS damage from the enzymatic digestion (Chen *et al.*, 2015). Furthermore, it remains unclear whether ionic and ultrastructural remodeling interacts to affect arrhythmogenic propensity. Indeed, because Ca^{2+} handling protein expression, localization, and regulatory states change simultaneously with TATs in disease (Brandenburg *et al.*, 2016; Yue *et al.*, 2017), their effects cannot easily be separated in experiments. To address this, we utilized our new 3D model of the human atrial myocyte with spatially detailed Ca^{2+} diffusion and TATS (Chapter 2) to investigate the isolated and interactive effects of altered TATS and changes in expression

and localization of key Ca^{2+}-handling proteins (i.e., NCX, RyR, and CSQ) on Ca^{2+}-driven membrane instabilities. We focused on these proteins because both 1) NCX and RyR are altered in AF and emerged as key mediators of TATS loss-induced diastolic instabilities in Ca^{2+} and membrane voltage (V_m), and 2) RyR and its regulator CSQ have been found to distribute non-uniformly between the cell periphery and interior. In this study, we found that TATS loss and Ca^{2+} handling protein remodeling collectively promote arrhythmia. Cells with intermediate TATS density were most sensitive to changes in protein expression and localization, whereby ultrastructural and Ca^{2+} handling remodeling synergistically contributed to the proarrhythmic outcomes. Conversely, when the TATS is depleted, changes in protein expression and distribution have little effect. Our study demonstrates the interactive contributions of TATS and Ca^{2+}-handling protein expression and distribution on maintaining Ca^{2+} and membrane potential stability in human atrial myocytes and provides novel model-based mechanistic insight that may guide future therapeutic anti-AF strategies.

3.2 Methods

We simulated human atrial myocyte electrophysiology and Ca^{2+} handling using our recently developed model, integrating transmembrane voltage dynamics, spatially-detailed Ca^{2+} diffusion, and varying TATS structure (Chapter 2). We modified the expression and subcellular distribution of various Ca^{2+} handling proteins (i.e., namely NCX, RyR, and CSQ), as detailed below. To investigate the interactive effects of altering protein expression and localization and varying tubular structures, we conducted simulations in cells with dense, median, and sparse TATS taken from the population of TATS structures described in our companion paper (Chapter 2).

3.2.1 Varying subcellular distribution of NCX, RyR, and CSQ

To investigate how the heterogeneous subcellular localization of NCX, RyR, and CSQ impact electrophysiology and Ca^{2+} handling, we systematically varied the relative density of NCX, RyR or CSQ localized to surface Ca^{2+} release units (CRUs, i.e., the 2 outer CRU layers near cell surface) vs. those localized to inner (i.e., non-surface) CRUs while keeping the whole-cell total expression unchanged (**Fig. 3.1**). Specifically, we varied the ratio of surface/inner CRU protein density between 0.5 and 2 to reflect the surface-to-central gradient in the subcellular distribution of RyR and CSQ observed in experiments (Herraiz-Martínez *et al.*, 2022).

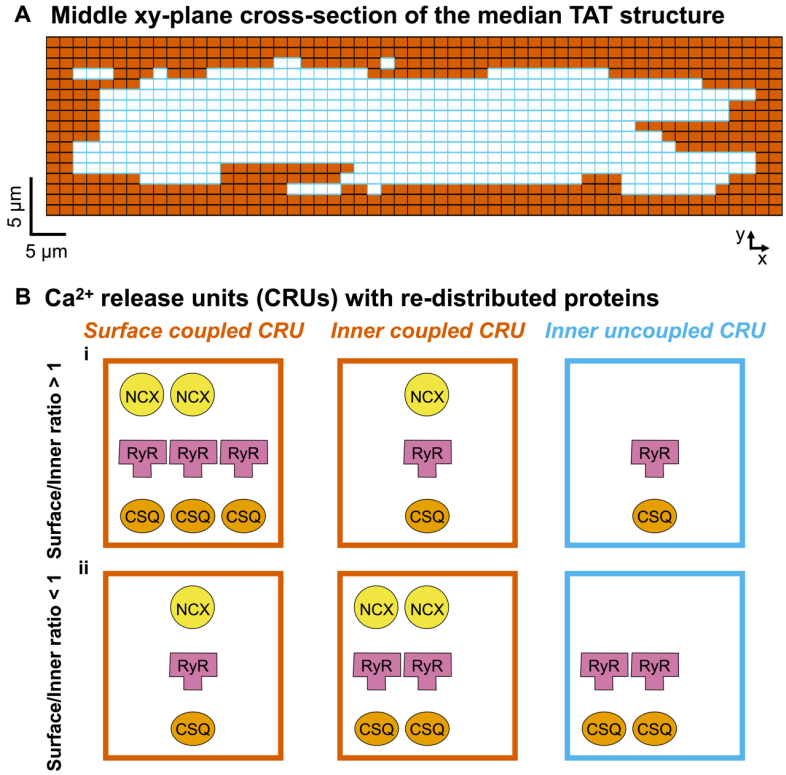

Figure 3.1 – Varying Ca^{2+} handling proteins (Na^{+}-Ca^{2+} exchanger, NCX, Ryanodine receptor, RyR, and calsequestrin, CSQ) distribution.

A) Two-dimensional section of a middle XY plane in the intermediate TAT structure shown in the companion paper (Zhang et al.). Surface coupled CRUs and inner coupled CRUs are in orange, and uncoupled CRUs are in light blue. **B)** Schematic of surface coupled (left), central coupled (middle), and

uncoupled (right) CRUs when surface/inner CRU protein expression ratio > 1 (**i**) or < 1 (**ii**). When varying the NCX (yellow) distribution, we scale the NCX current density in inner coupled and surface coupled CRUs accordingly. When varying the RyR distribution, we scale the relative expression of RyRs (pink) in the inner (coupled and uncoupled) CRUs vs. surface coupled CRUs. When varying the CSQ (orange) distribution, we scale the relative CSQ expression in the inner (coupled and uncoupled) CRUs vs. surface coupled CRUs.

3.2.2 Varying the whole-cell expression of NCX, RyR, and CSQ

The whole-cell expression (i.e., NCX maximal transport rate, number of RyRs per CRU, and CSQ maximum buffering capacity, B_{CSQ}) was scaled to explore the effects of experimentally-determined variation ranges of NCX (Schotten *et al.*, 2002; El-Armouche *et al.*, 2006; Lenaerts *et al.*, 2009; Voigt *et al.*, 2012; Yue *et al.*, 2017), RyR (Ohkusa *et al.*, 1999; Neef *et al.*, 2010; Voigt *et al.*, 2014; Greiser *et al.*, 2014), and CSQ (Lüss *et al.*, 1999; Faggioni *et al.*, 2014). Specifically, NCX was varied between 10% and 200%, RyR was varied between 10% and 140%, and CSQ was varied between 50% and 140% of the baseline expression outlined in Chapter 2

Since CSQ is not only a luminal SR Ca^{2+} buffer but also a regulator of RyR function (Terentyev *et al.*, 2003; Györke *et al.*, 2004; Knollmann *et al.*, 2006; Restrepo *et al.*, 2008), to dissect the relative and combined contributions of these processes we investigated three scenarios when performing simulations to study the impacts of varying CSQ: 1) only luminal SR Ca^{2+} buffering is affected; 2) only RyR regulation is affected; or 3) both SR buffering and RyR regulation are affected. To assess this, changes in Ca^{2+} buffering CSQ were implemented by modifying the B_{CSQ} in the equations of junctional SR (JSR) Ca^{2+} rapid equilibrium approximation, i.e., $\beta([Ca^{2+}]_{JSR})$ in the companion paper by Zhang et al; whereas changes in RyR gating were implemented by modifying the B_{CSQ} in RyR luminal-Ca^{2+}-dependent transient rate equations, i.e., k_{14} and k_{23} in Table 5 of the companion paper by Chapter 2

3.2.3 Numerical methods and simulation protocols

Simulation details are as in the companion paper (Chapter 2). Briefly, our human atrial myocyte model was implemented in C++ and parallelized using OpenMP 5.1 (Dagum & Menon, 1998). The ordinary differential equations (ODEs) and subcellular Ca^{2+} diffusion were solved using an explicit Forward Euler method except that LCC current (I_{Ca}) and RyR gating behaviors were described stochastically as in (Restrepo *et al.*, 2008; Sato & Bers, 2011), and that ODEs of fast Na^{+} current (I_{Na}) were solved using the Rush-Larsen scheme (Rush & Larsen, 1978). The time step was 0.01 ms.

3.2.4 Measurement of Ca^{2+}-handling abnormalities, V_m instabilities and differences in Ca^{2+} release between CRUs

To compare Ca^{2+} signaling in surface CRUs, inner coupled CRUs (those CRUs located away from the cell surface but coupled to tubules), and inner uncoupled CRUs, the $[Ca^{2+}]_{Cyto}$ within each group of CRUs throughout the cell was averaged. Ca^{2+}-handling abnormalities and V_m instabilities associated with changes in protein expression and distribution were examined for SCRs, DADs, and spontaneous action potentials (SAPs). Detailed descriptions of SCR and DAD measurements are provided in our companion paper (Chapter 2). Briefly, cells were paced to steady state with the stimulation then stopped and the subsequent diastolic period used for analysis in MATLAB R2021. SCRs were defined as Ca^{2+}-release events with an amplitude > 0.3 μM, with DADs defined as membrane depolarizations > 10 mV. SAPs were deemed present when the amplitude of a DAD exceeded 70 mV.

3.2.5 Measurements of alternans

To understand the effects of varying expression and distribution of Ca^{2+} handling proteins on the regularity of Ca^{2+} release, the occurrence of pacing-induced alternans in $[Ca^{2+}]_{Cyto}$ and V_m

traces were analyzed as done in experiments (Myles *et al.*, 2011; Hammer *et al.*, 2015). Specifically, Ca^{2+} alternans were distinguished when the calculated index (r) that compares the alternating averaged smaller (S) and larger (L) Ca^{2+} transient amplitudes (i.e., r = 1 – S/L) was over 0.08. APD alternans were identified when the difference between the averaged longer APD_{90} and the averaged shorter APD_{90} (ΔAPD_{90}) was over 10 ms.

3.3 Results

3.3.1 Lowering NCX promotes SCRs, but has biphasic effects on DADs and SAPs, depending on the balance between increased SCRs and reduced $\Delta V_m/\Delta Ca^{2+}$ gain

To reveal how NCX expression and TATS changes affect arrhythmic biomarkers (i.e., SCRs, DADs, and SAPs), we varied NCX expression in the human atrial myocyte models with sparse, intermediate, and dense TATS. We found that the SCR rate threshold monotonically decreases with reduced NCX expression and increased NCX associated with fewer SCRs, especially in cells with sparse TATS (**Fig. 3.2Ai**). While low NCX expression is associated with decreased SCR rate threshold, it conversely increases the rate thresholds of both DADs and SAPs when below 20%-40% of its baseline value. Interestingly, at low expression levels above 40% of baseline, DAD and SAP rate threshold is decreased matching SCR-NCX expression dependence (**Fig. 3.2Aii-iii**). This is demonstrated in the representative voltage (**i**) and $[Ca^{2+}]_{Cyto}$ (**ii**) traces in (**Fig. 3.2B**) where the biphasic effects of NCX reduction on DADs and SAPs (but not SCRs) are highlighted by the occurrence of SCRs at 0.2 and 0.5 NCX expression but DADs and SAPs solely occurring at 0.5. This result suggests that $[Ca^{2+}]_{Cyto}$-V_m coupling changes with low vs. high NCX expression. Interestingly, while the SCR pacing threshold is lower in cells with sparser TATS, SAPs occur at lower pacing rates in cells with intermediate and dense TATS, suggesting that NCX expression changes have the greatest impact on

$[Ca^{2+}]_{Cyto}$-V_m coupling in cells with relatively intact TATS. We further analyzed the model to understand the mechanism by which reducing NCX promotes SCRs but has biphasic effects on DADs and SAPs.

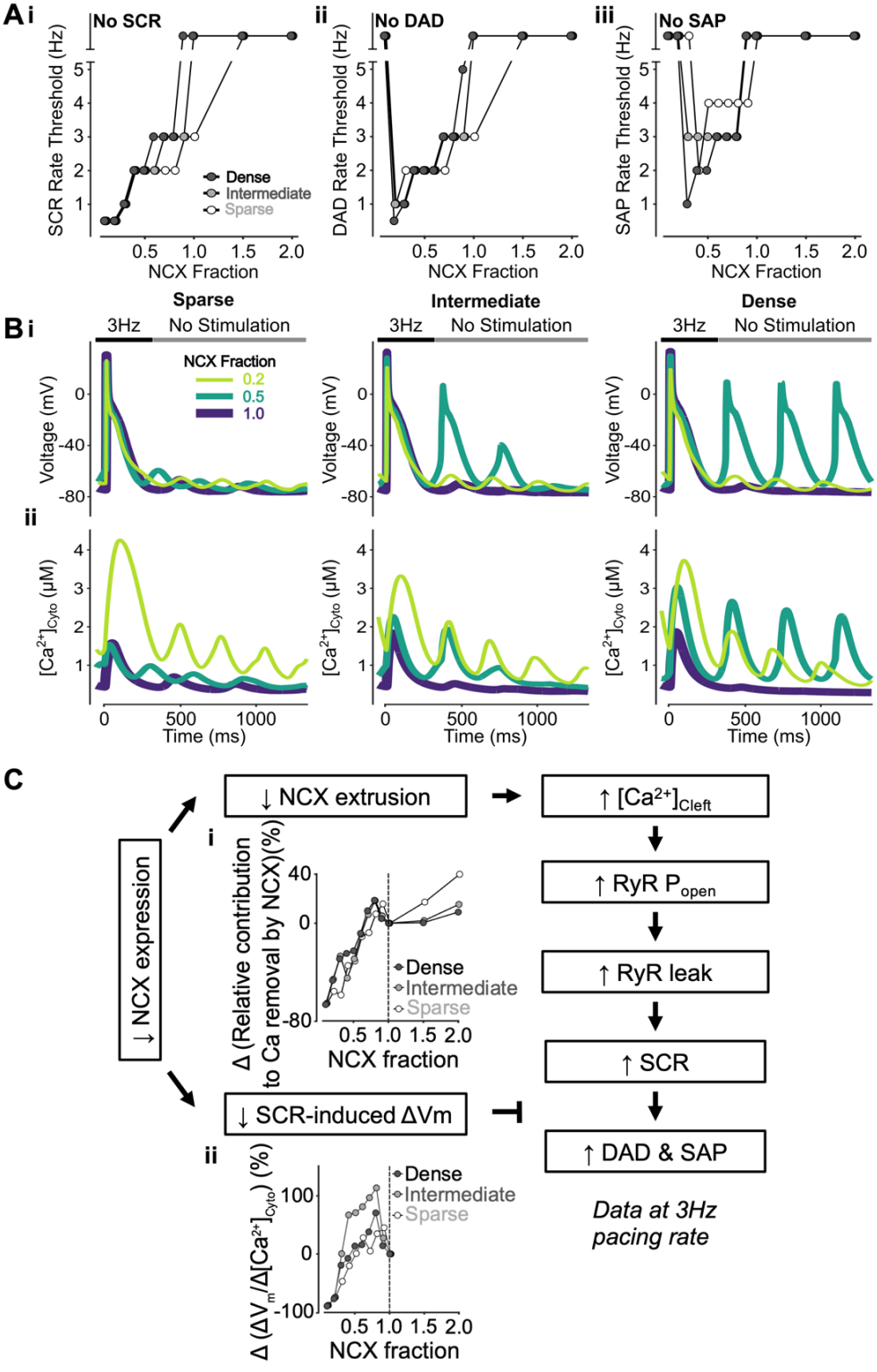

Figure 3.2 – Inhibition of NCX promotes SCRs but has biphasic effects on DADs and spontaneous APs (SAP).

A) Reducing NCX monotonically decreases the rate threshold of SCRs (i), whereas the rate thresholds of DADs (ii) and SAP, defined as DADs with amplitudes over 70 mV, (iii) display biphasic dependence. **B)** Effect of altered NCX fraction on voltage (i) and global cytosolic Ca^{2+} concentration (ii) in cells with sparse (left), intermediate (middle), and dense (right) tubules following pacing at 3 Hz to examine the occurrence of DADs, SAPs and SCRs. **C)** Mechanism underlying NCX inhibition promoting SCRs but having biphasic effects on DADs and SAP. Biomarkers were determined from the first 100 ms of no-stimulation period and normalized to those of cells with a retained NCX fraction of 1.0. Lower NCX expression is associated with reduced NCX contribution to Ca^{2+} extrusion (i) and smaller SCR-induced voltage changes/SCR amplitude ratio (ii). Less NCX extrusion results in elevated cleft Ca^{2+} concentration, augmented RyR P_o and leak leading to increased SCRs. While SCRs lead to DADs and SAP this transition is abated by the reduced SCR-induced changes in V_m, thus explaining the biphasic effects of reduced NCX.

We found that lowering NCX expression reduced NCX Ca^{2+} extrusion (**Fig. 3.2Ci**), leading to elevated diastolic cleft Ca^{2+} concentration, augmented diastolic RyR open probability (P_O) and leak, and increased SCRs and DADs. This mechanism resembles that suggested to be responsible for elevated SCR and DAD propensity in cells with sparse TATS in our companion paper (Chapter 2). Conversely, less NCX reduced SCR-induced ΔV_m, especially in cells with intermediate and dense TATS (**Fig. 3.2Cii**), leading to decoupling between SCR and DAD/SAPs and subsequent biphasic changes of DADs and SAPs.We further sought to determine whether regional variations exist in the effects of varying NCX expression and TATS density on the pacing threshold for SCR. To do so, we analyzed the averaged Ca^{2+} transient of surface CRUs, inner CRUs coupled to TATS (inner coupled), and inner CRUs that are not coupled to TATS (inner uncoupled) in each cell in the population with varying NCX expression and TATS density and quantified the biomarkers of local Ca^{2+} transient. As

expected, reduced NCX lowered the rate threshold for SCRs in all CRUs (**Fig. 3.3Ai**). The representative traces of average cytosolic Ca^{2+} concentration following pacing at 3 Hz in cells with dense (**Fig. 3.3Bi**), intermediate (**Fig. 3.3Bii**), and sparse TATS (**Fig. 3.3Biii**) also show larger SCRs with lower NCX expression. Interestingly, when NCX was severely reduced (scaling factor of 0.2 of baseline expression), Ca^{2+} alternans were observed in all CRUs from cells with intermediate and dense TATS (**Fig. 3.3Bi-ii**) indicating enhanced arrhythmic effect of lower NCX expression in tubulated cells.

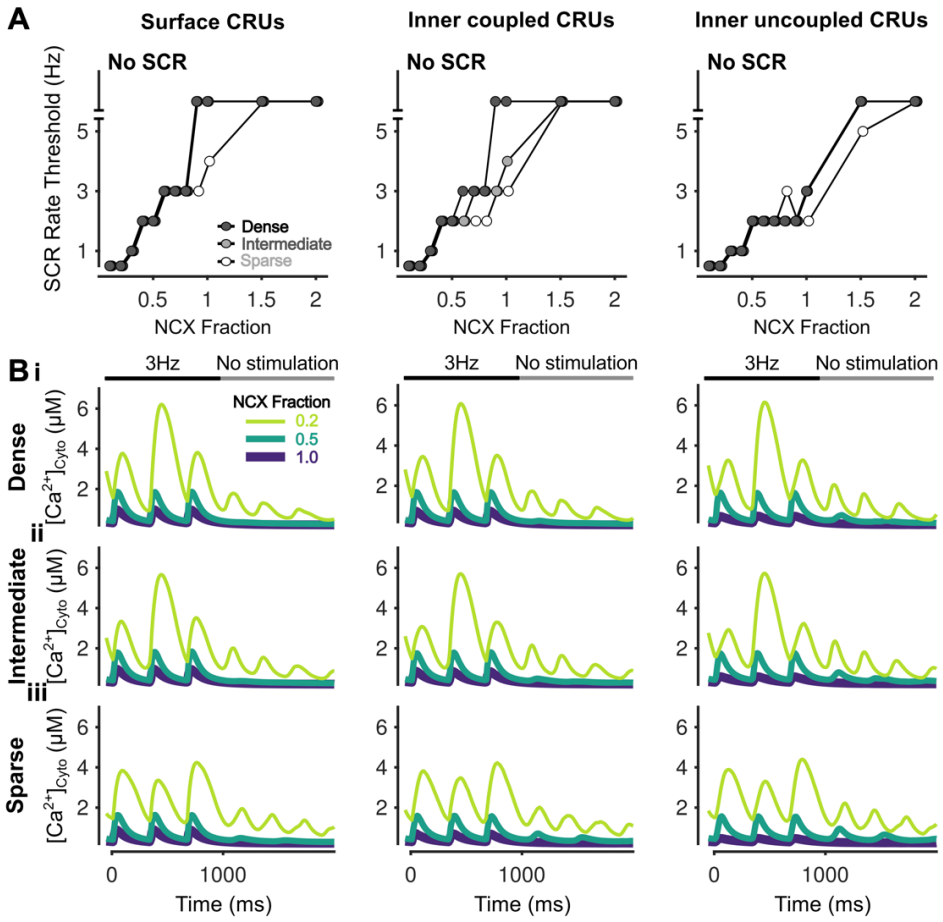

Figure 3.3 – Inhibition of NCX promotes simultaneous SCRs in all CRUs.

A) Rate threshold for local SCRs of surface (left), inner coupled (middle) and inner uncoupled (right) CRUs in dense, intermediate and sparsely tubulated cells. **B)** Cytosolic Ca^{2+} concentration of surface (left), inner coupled (middle) and inner uncoupled (right) CRUs from cells with dense (i), intermediate

(ii), and sparse (iii) tubules following pacing at 3 Hz showing SCRs and alternans for all CRUs at NCX Fraction of 0.2.

Overall, our simulations suggest that NCX inhibition shifts the balance between increased SCRs and reduced $\Delta V_m/\Delta Ca^{2+}$ gain. While cells with sparse TATS consistently display a lower SCR pacing threshold, when SCRs occur in more densely tubulated cells they are greater in magnitude and the SAP pacing threshold appears more sensitive to variations in NCX levels compared to sparsely tubulated cells.

3.3.2 Increasing surface/inner CRU NCX expression ratio promotes SCRs and DADs by elevating inner $[Ca^{2+}]_{Cleft}$ and RyR leak

After characterizing the impact of changes to global NCX expression on SCRs, DAD, and SAPs, we sought to investigate the effects of varying the spatial distribution of NCX and TATS density. To do this we altered the ratio of NCX in surface/inner CRUs in the human atrial myocyte models with sparse, intermediate, and dense TATS. Our simulations indicate that increasing the ratio of surface to inner CRU NCX expression decreases the rate threshold of SCRs (**Fig. 3.4Ai**) and DADs (**Fig. 3.4Aii**), without triggering SAPs (**Fig. 3.4Aiii**). This effect is more pronounced in cells with dense and intermediate TATS (**Fig. 3.4Ai-ii**), as also shown in the representative traces of V_m (**Fig. 3.4Bi**) and $[Ca^{2+}]_{Cyto}$ (**Fig. 3.2Bii**). We found that increasing the surface-to-inner CRU NCX expression ratio decreased inner NCX Ca^{2+} extrusion but enhanced NCX Ca^{2+} extrusion at the surface. While $[Ca^{2+}]_{Cleft}$ in surface CRUs remained unaffected (**Fig. 3.4Ci**), lower NCX expression in the inner CRUs lead to increased $[Ca^{2+}]_{Cleft}$ in both inner coupled (**Fig. 3.4Cii**) and uncoupled (**Fig. 3.4Ciii**) CRUs, thus causing elevated RyR P_O and leak, which promotes SCRs and DADs. The consequences of

heterogeneous NCX distribution were especially pronounced in inner coupled CRUs in cells with dense and intermediate TATS (**Fig. 3.5A-B**).

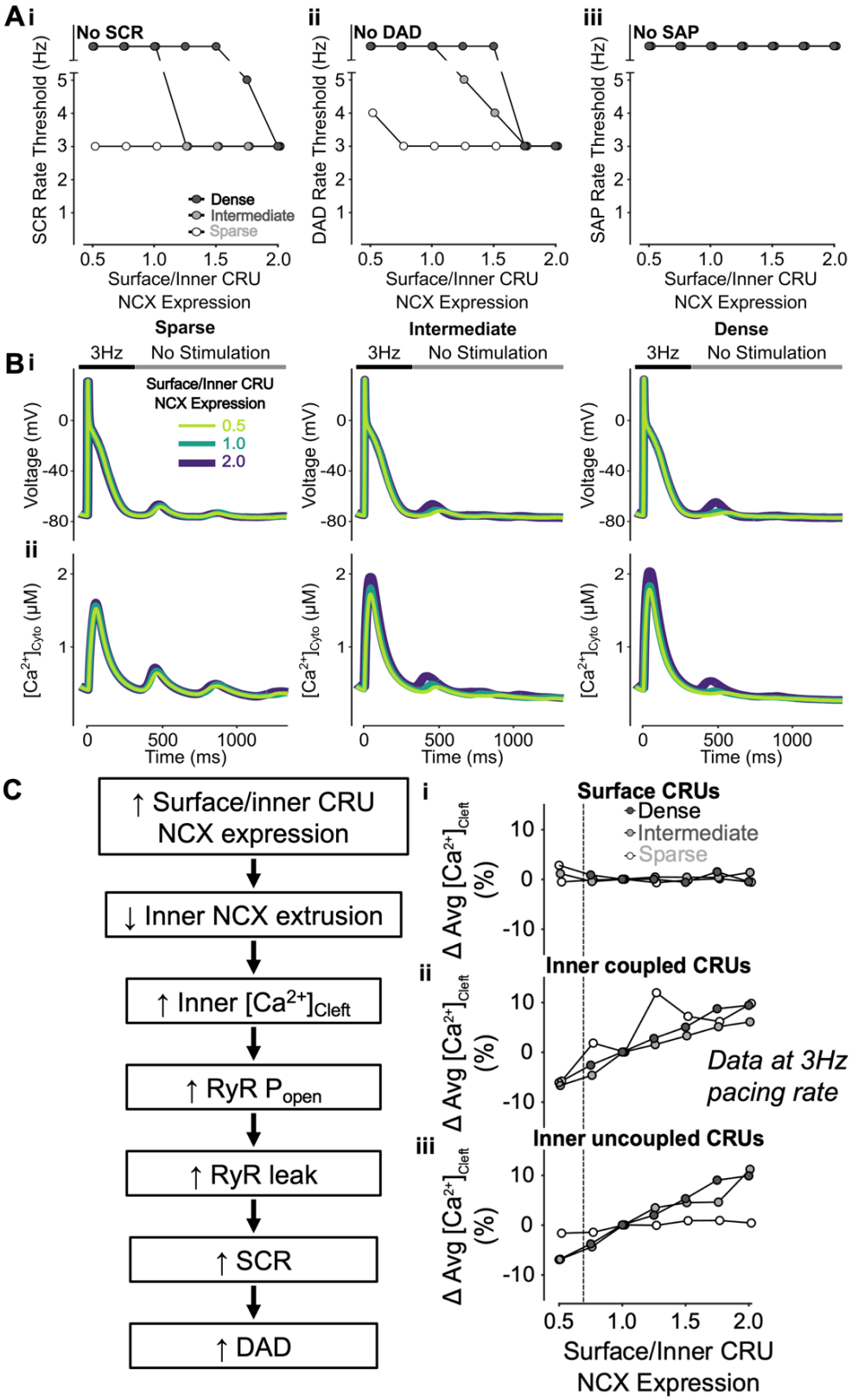

Figure 3.4 – Increasing surface/inner CRU NCX expression ratio enhances SCRs and DADs but does not affect SAPs.

A) Increasing surface/inner CRU NCX expression ratio (i.e., increasing NCX density in surface CRUs without changing whole-cell NCX expression) monotonically decreases the rate threshold of SCRs (i) and DADs (ii), whereas SAP remains absent in all conditions. This effect is greater in cells with dense and intermediate tubular structures vs cells with sparse tubules. **B)** Effect of altered surface/inner CRU NCX expression ratio on voltage (i) and global cytosolic Ca^{2+} concentration (ii) in cells with sparse (left), intermediate (middle), and dense (right) tubules following pacing at 3 Hz to examine the occurrence of DADs and SCRs. **C)** Mechanism underlying increasing surface/inner CRU NCX expression ratio inhibiting SCRs and DADs. Biomarkers were determined from the first 100 ms of no-stimulation period and normalized to those of cells with a retained surface/inner CRU NCX expression ratio of 1.0. Higher surface/inner CRU NCX expression ratio is associated with reduced NCX contribution to Ca^{2+} extrusion by inner coupled CRUs, resulting in higher cleft Ca^{2+} concentration in inner CRUs with no visible effect in surface CRUs. Higher inner cleft Ca^{2+} concentration in inner CRUs causes increased RyR P_o and RyR leak, leading to increased SCRs and DADs. Since fewer inner CRUs containing NCX exist in sparsely tubulated cells to begin with, the impact of varying NCX distribution is more pronounced in cells with tubules. As such, the consequence of changing cleft Ca^{2+} concentration is greater in cells with dense and intermediate tubules rather than those with sparse tubules, explaining the observed differences in SCRs and DADs between cells with varying tubule densities.

Overall, we found that increasing the surface/inner CRU NCX expression ratio promotes SCRs, especially in inner coupled CRUs, and DADs, but does not affect SAPs. These effects are marked in cells with intermediate and dense TATS, suggesting that loss of TATS and reduced NCX expression in inner CRUs favors SCRs and DADs via a similar mechanism, i.e., the elevation of inner $[Ca^{2+}]_{Cleft}$ and RyR leak.

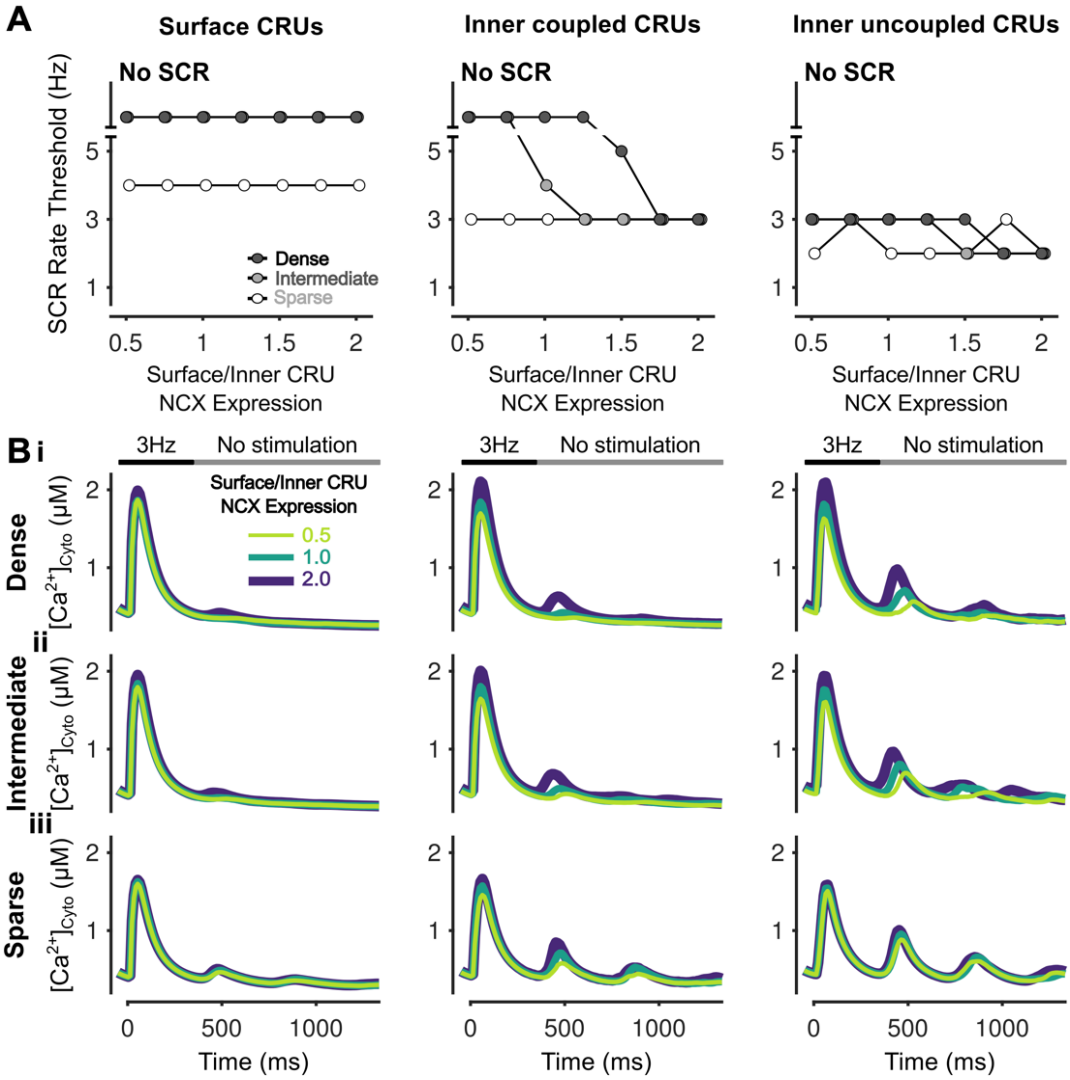

Figure 3.5 – Increasing surface/inner CRU NCX expression ratio enhances simultaneous SCRs in inner coupled CRUs.

A) Rate threshold for local SCRs of surface (left), inner coupled (middle) and inner uncoupled (right) CRUs in sparse, intermediate and densely tubulated cells with the impact of altered surface/inner NCX expression ratio greatest in inner coupled CRUs of cells with dense and intermediate tubules. **B)** Cytosolic Ca^{2+} concentration of surface (left), inner coupled (middle) and inner uncoupled (right) CRUs from cells with dense (i), intermediate (ii), and sparse (iii) tubules following pacing at 3 Hz showing observed SCRs with varying surface/inner CRU NCX expression ratios.

3.3.3 Inhibiting RyR has biphasic effects on SCRs, DADs, and SAPs, depending on the balance between the reduced number of RyRs and increased P_O

To understand the effects of varying RyR expression and TATS density on SCRs, DADs, and SAPs, we altered RyR expression in cells with sparse, intermediate, and dense TATS as described in the Methods. Slight lowering of RyR expression above 70% of its baseline value was proarrhythmic and reduced the rate thresholds of SCRs, DADs, and SAPs. RyR expression below 40-70% typically had the opposite effect with rate threshold increased (**Fig. 3.6Ai-iii**). Interestingly, in the cell with sparse TATs the SCR rate threshold was unaffected by varying RyR expression levels, despite the ability of SCRs to generate DADs and SAPs being altered in these cells. Indeed, DADs and SAPs occur at overall lower pacing rates in cells with sparse TATS vs. those with intermediate or dense TATS, suggesting that TATS loss further promotes arrhythmogenic behavior (due to larger SCRs, especially in inner uncoupled CRUs, **Fig. 3.7B**). The biphasic effects of RyR inhibition on SCRs, DADs, and SAPs are shown in representative traces of voltage (**Fig. 3.6Bi**) and $[Ca^{2+}]_{Cyto}$ (**Fig. 3.6Bii**) following 4-Hz pacing. Our model analysis indicates that the biphasic effects of RyR inhibition are mediated by the balance between two contrasting processes: on one hand, reduction in RyR expression reduces SR Ca^{2+} release and increases the SR Ca^{2+} load (**Fig. 3.6Ci**), which elevates unitary RyR P_O (**Fig. 3.6Cii**); on the other hand, the reduced RyR number limits the magnitude of diastolic Ca^{2+} release by affecting the number of unitary release events and thus their ability to recruit neighboring RyRs and CRUs. As with the impact on global Ca^{2+}, subcellular Ca^{2+} signaling also shows biphasic changes in SCR rate thresholds, which are most remarkable in surface CRUs of the cell with sparse TATS and in inner coupled CRUs of cells with intermediate and dense TATS (**Fig. 3.7A**).

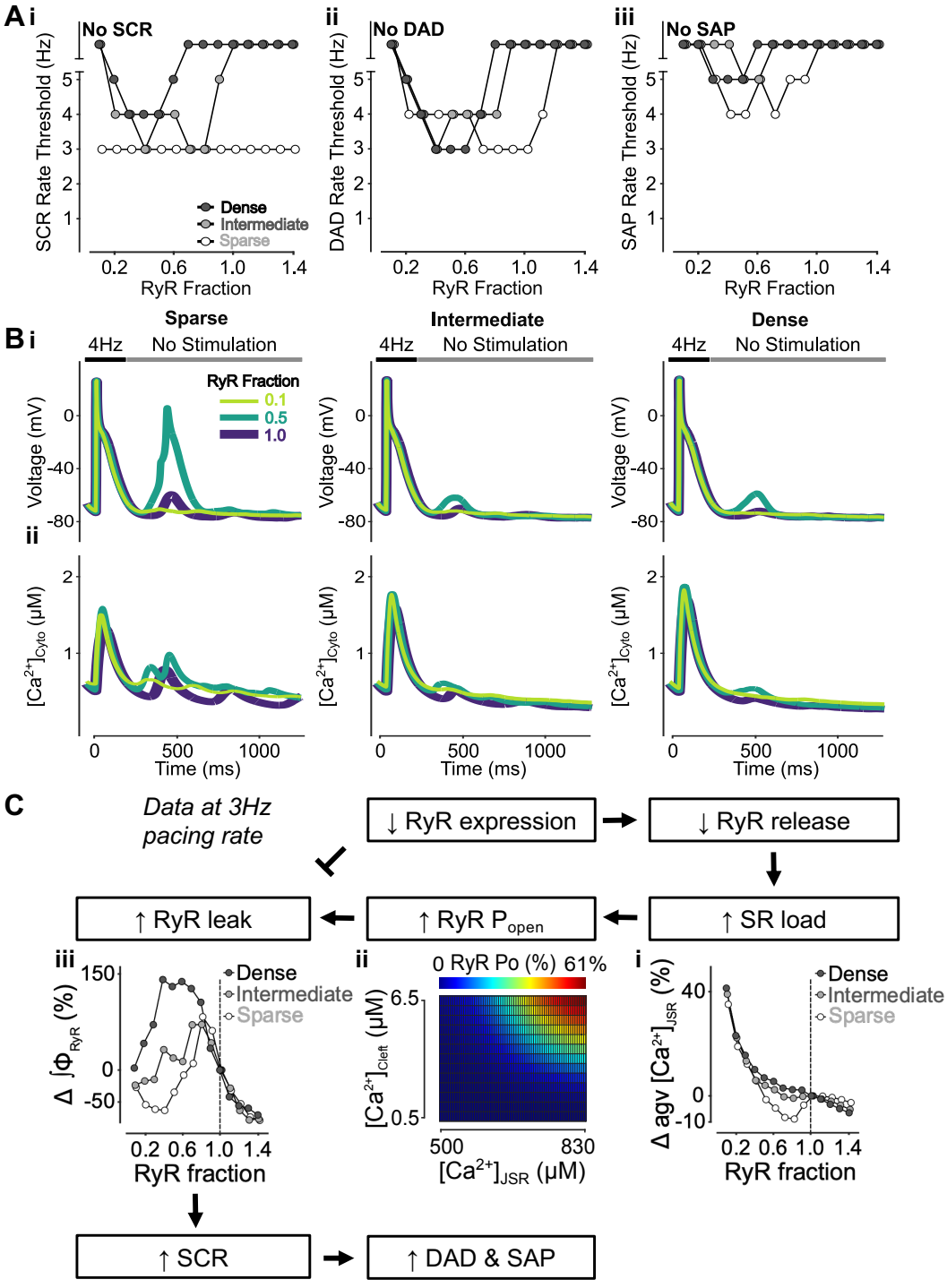

Figure 3.6 – Inhibition of RyR has biphasic effects on SCRs, DADs, and SAPs.

A) Rate threshold for SCRs (i), DADs (ii) and SAP (iii) in dense, intermediate and sparsely tubulated cells. Biphasic dependence on RyR inhibition is observed in all settings and cell types, with the exception of SCRs in sparsely tubulated cells. Here, the lowest observed baseline rate threshold for SCRs is unaltered by RyR inhibition. **B)** Effect of altered RyR fraction on voltage (i) and global cytosolic Ca^{2+} concentration

(ii) in cells with sparse (left), intermediate (middle), and dense (right) tubules following pacing at 4 Hz to examine the occurrence of DADs, SAPs and SCRs. **C)** Mechanism underlying RyR inhibition having biphasic effects on SCRs, DADs and SAP. Biomarkers were determined from the first 100 ms of no-stimulation period and normalized to those of cells with a retained RyR fraction of 1.0. Lower RyR expression is associated with reduced RyR release, leading to elevated SR load (i) and augmented RyR P_o (ii). While higher RyR P_o causes RyR leak leading to increased SCRs, lower RyR expression itself inhibits RyR leak. This results in the biphasic effect of RyR reduction on SCRs, DADs and SAPs.

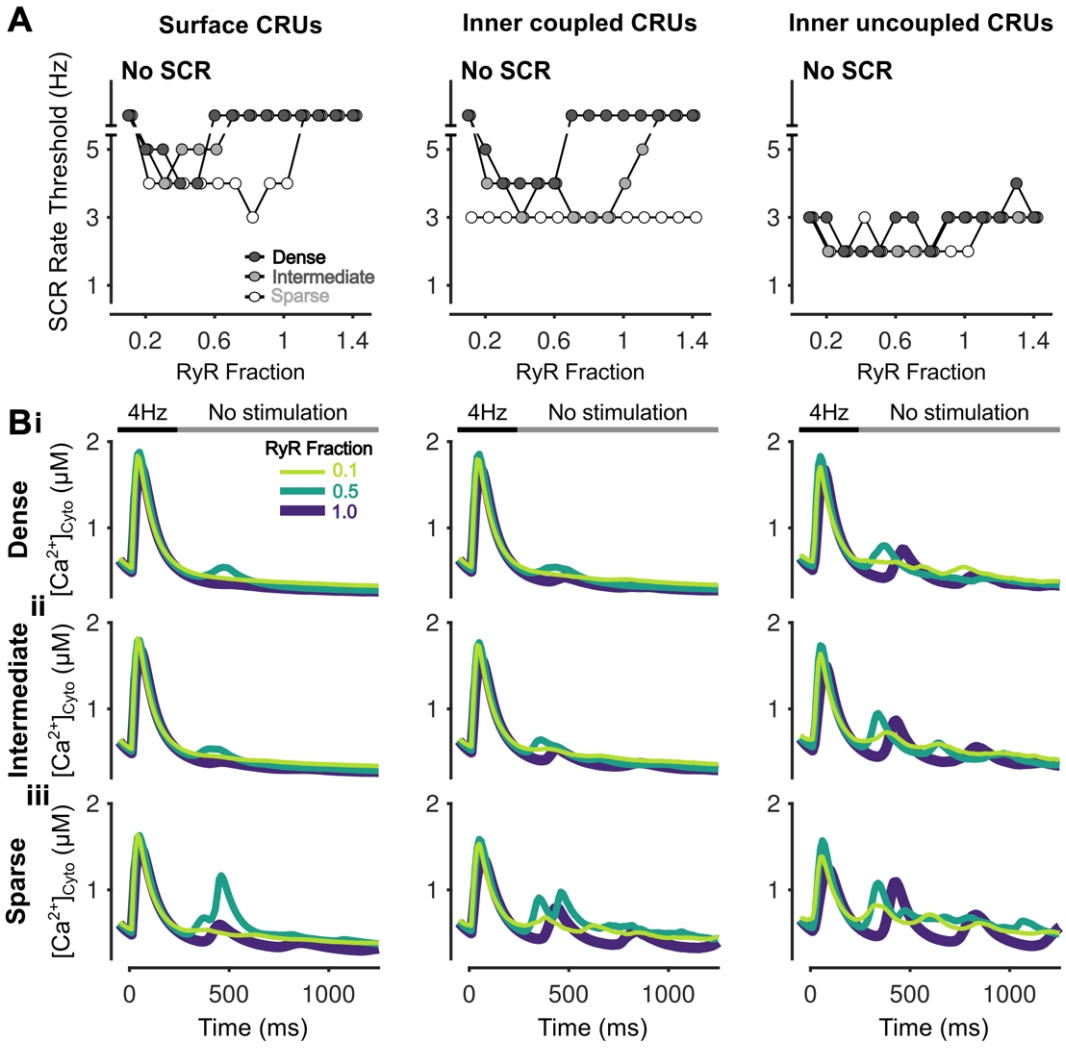

Figure 3.7 – Inhibition of RyR has biphasic effects on SCRs in all CRUs.

A) Rate threshold for local SCRs of surface (left), inner coupled (middle) and inner uncoupled (right) CRUs in sparse, intermediate and densely tubulated cells with the impact of altered RyR expression ratio greatest in surface CRUs of all cells and inner coupled CRUs of cells with dense and intermediate tubules.

B) Cytosolic Ca^{2+} concentration of surface (left), inner coupled (middle) and inner uncoupled (right) CRUs from cells with dense (i), intermediate (ii), and sparse (iii) tubules following pacing at 4 Hz showing observed SCRs with varying RyR fraction.

Interestingly, the rate threshold of inner coupled SCRs is similar to the whole cell SCR rate threshold (**Fig. 3.6Ai**), suggesting that SCRs in inner coupled CRUs dominantly affect whole cell SCR behavior. Furthermore, the rate threshold of surface SCRs (**Fig. 3.7A**) is similar to the rate thresholds of DADs and SAPs (**Fig. 3.6Aii-iii**), suggesting that surface CRU SCRs are more likely associated with the occurrence of DADs/SAPs.

3.3.4 Increasing RyR expression in surface vs. inner CRUs inhibits SCRs but has modest effects on DADs and SAPs

To reveal the effects of heterogenous CRU RyR localization and TATS on SCRs, DADs, and SAPs, we varied the surface-to-inner CRU RyR expression ratio in cells with sparse, intermediate, and dense TATS. The simulation results indicate that increasing the surface/inner CRU RyR expression ratio inhibits SCRs in the cell with sparse and intermediate TATS, with no changes observed in the densely tubulated cell (**Fig. 3.8Ai**). However, modest changes were seen in the DAD threshold and only for the most extreme changes (e.g., ratios of 0.5 and 1.75 - 2.0, **Fig. 3.8Aii**), while no changes were detected in the SAP rate threshold (**Fig. 3.8Aiii**). Both increasing and decreasing the RyR expression in surface vs. inner CRUs diminished DADs (i.e., reduced amplitude and increased pacing threshold) in the cell with sparse TATS, but enhanced DADs in the cell with intermediate TATS, as demonstrated in the representative traces (**Fig. 3.8Bi**). The representative traces of $[Ca^{2+}]_{Cyto}$ also show that SCRs are larger in cells with sparse/intermediate vs. dense TATS (**Fig. 3.8Bii**) with varying surface/inner CRU RyR expression, as we show in the companion paper (Chapter 2).

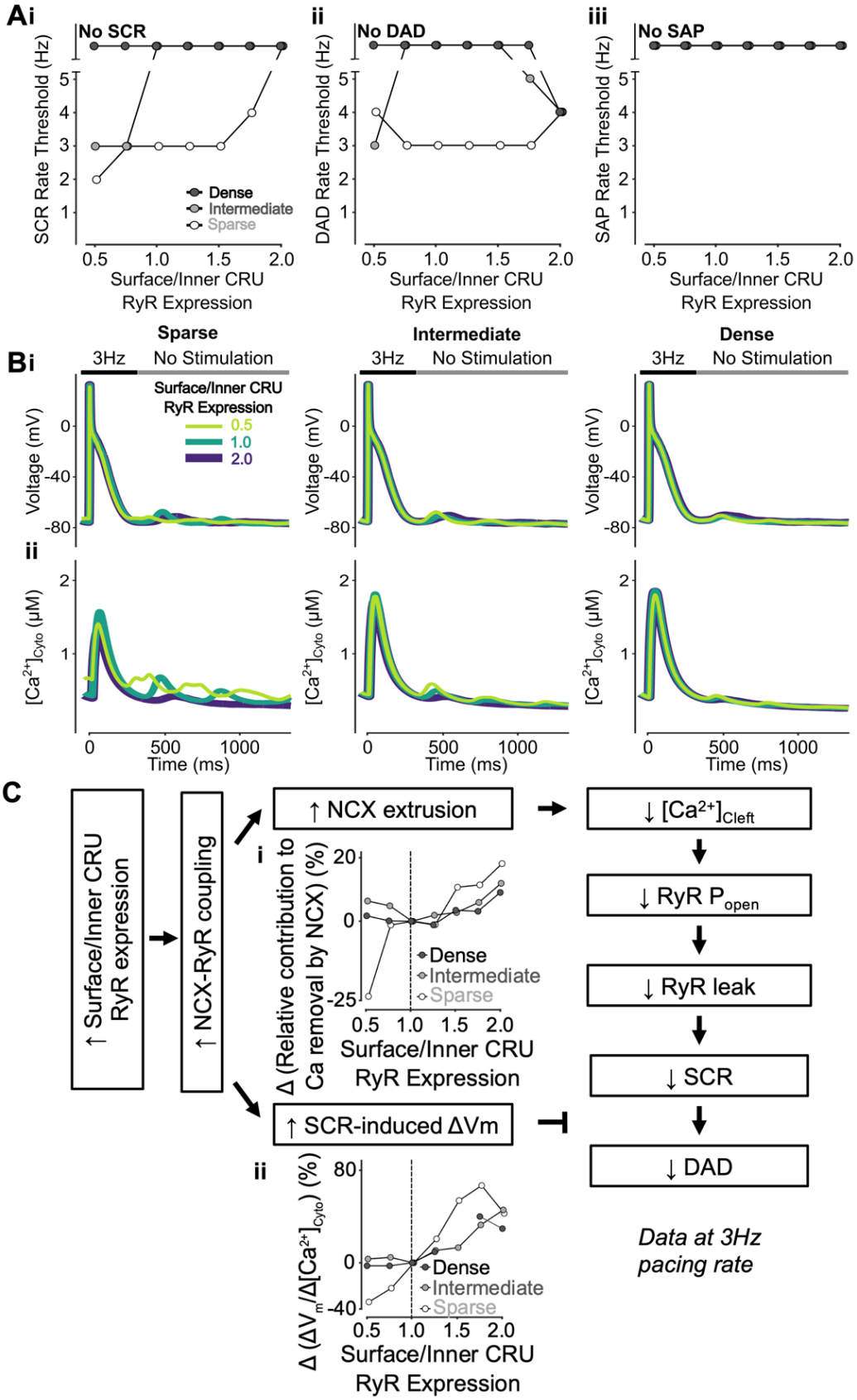

Figure 3.8 – Increasing surface/inner CRU RyR expression ratio inhibits SCRs, has biphasic effects on DADs but does not affect SAP.

A) Increasing surface/inner CRU RyR expression ratio (i.e., increasing RyR density in surface CRUs without changing whole-cell RyR expression) monotonically increases the rate threshold of SCRs (i), whereas DADs (ii) display biphasic dependence and SAP (iii) remains absent in all conditions. The effect on SCRs is greater in cells with sparse and intermediate tubular structures vs cells with dense tubules, whereas the biphasic effect on DADs is less pronounced in cells with sparse tubular structures vs cells with intermediate and dense tubules. **B)** Effect of altered surface/inner CRU RyR expression ratio on voltage (i) and global cytosolic Ca^{2+} concentration (ii) in cells with sparse (left), intermediate (middle), and dense (right) tubules following pacing at 3 Hz to examine the occurrence of DADs and SCRs. **C)** Mechanism underlying increasing surface/inner CRU RyR expression ratio inhibiting SCRs, having biphasic effects on DADs but not affecting SAP. Biomarkers were determined from the first 100 ms of no-stimulation period and normalized to those of cells with a retained surface/inner CRU RyR expression ratio of 1.0. Increasing surface/inner CRU RyR expression ratio means more RyRs are located closer to NCX, resulting in increased NCX-RyR coupling. This is associated with increased NCX contribution to Ca^{2+} extrusion (i) and higher SCR-induced voltage changes/SCR amplitude ratio (ii). Enhanced NCX extrusion results in lower cleft Ca^{2+} concentration, smaller RyR P_o and leak leading to milder SCRs. While this in itself limits DADs, DAD likelihood is promoted by the increased SCR-induced changes in V_m, thus explaining the biphasic effects of increasing surface/inner CRU RyR expression ratio.

The mechanistic analysis indicates increasing surface/inner CRU RyR expression enhances NCX-RyR coupling, thus leading to both larger NCX Ca^{2+} extrusion (**Fig. 3.8Ci**), with subsequent diminished SCRs that would attenuate DADs, and enhanced $\Delta V_m/\Delta Ca^{2+}$ gain that would favor DADs (**Fig. 3.8Cii**). The balance of these two competing processes underlies the modest effects of varying RyR relative distribution in surface and inner CRUs on DADs. The analysis of subcellular Ca^{2+} signaling indicates that increasing surface RyR expression increases the SCR rate threshold in all CRUs, especially in inner CRUs, and that TATS loss exacerbates the effects of reducing RyR expression in inner CRUs (**Fig. 3.9A-B**).

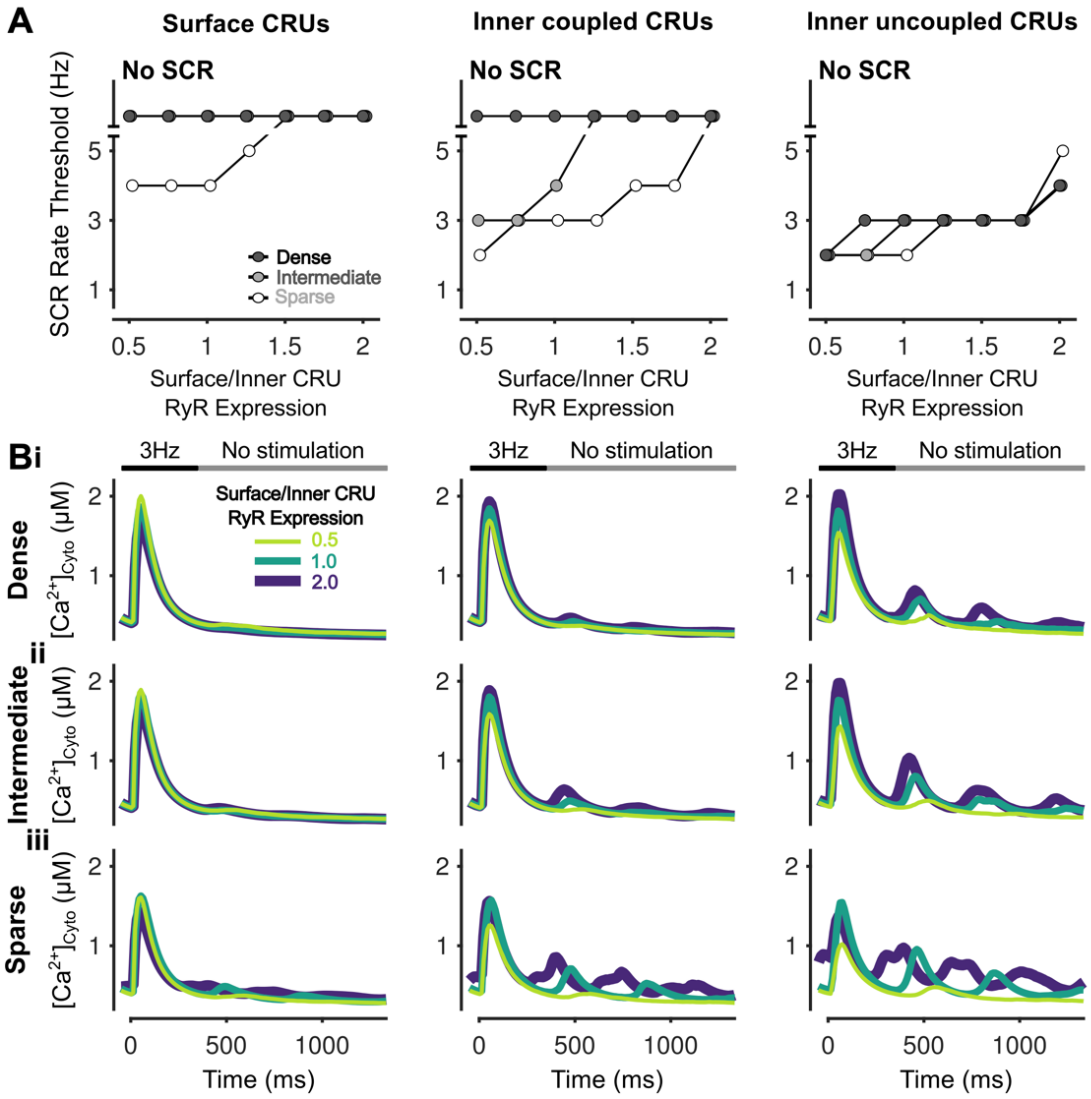

Figure 3.9 – Increasing surface/inner CRU RyR expression ratio inhibits simultaneous SCRs in all CRUs.

A) Rate threshold for local SCRs of surface (left), inner coupled (middle) and inner uncoupled (right) CRUs in sparse, intermediate and densely tubulated cells with the impact of altered surface/inner RyR expression ratio greatest in inner coupled CRUs of cells with sparse and intermediate tubules. **B)** Cytosolic Ca^{2+} concentration of surface (left), inner coupled (middle) and inner uncoupled (right) CRUs from cells with dense (i), intermediate (ii), and sparse (iii) tubules following pacing at 3 Hz showing observed SCRs with varying surface/inner CRU RyR expression ratios.

3.3.5 Loss of CSQ promotes SCRs and DADs, primarily through diminished CSQ Ca^{2+} buffering, with no effect on SAPs

The impact of CSQ expression levels and TATS density on SCRs, DADs, and SAPs was examined by varying the expression of CSQ in cells with sparse, intermediate, and dense TATS. Because CSQ both affects luminal Ca^{2+} buffering and RyR P_O, we simulated the changes in CSQ expression level by 1) only changing the Ca^{2+} buffering parameters (**Figs. 3.10-3.11**), 2) only modifying the parameters associated with CSQ regulation of RyR gating (**Figs. 3.11-3.12**), and 3) modulating both processes (**Figs. 3.13-3.14**), as described in the Methods. Reducing CSQ-mediated luminal SR Ca^{2+} buffering promotes SCRs, DADs, and SAPs (**Figs. 3.10A-B**), and enhances subcellular SCRs in all CRUs (**Fig. 3.11**). However, inhibiting CSQ RyR-regulation, i.e., decreasing SR Ca^{2+} sensitivity of RyR P_O, conversely increases pacing rate thresholds of SCRs, DADs, and SAPs, especially in cells with sparse TATS (**Fig. 3.12A-B**). Inhibiting CSQ RyR-regulation also reduces subcellular SCRs in all CRUs, especially in inner CRUs (**Fig. 3.13A-B**). When concomitantly simulating the changes in both luminal Ca^{2+} buffering and RyR regulation, we found that CSQ inhibition promotes SCRs and DADs, without changing the SAP rate threshold (**Fig. 3.14A-B**), i.e., similar to the effects of inhibiting CSQ Ca^{2+} buffering alone (**Fig. 3.10A-B**).

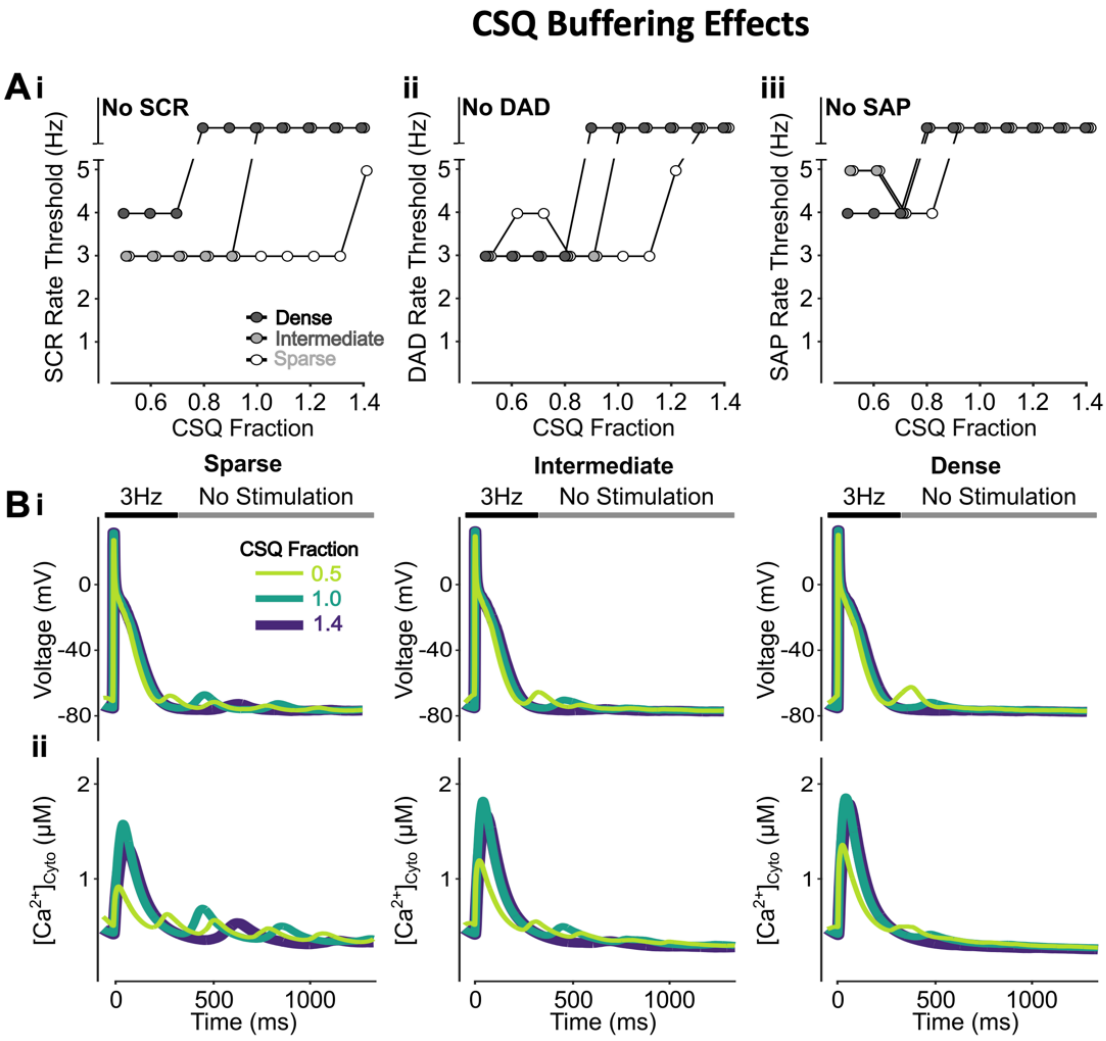

Figure 3.10 – Promotion of CSQ Ca^{2+} buffering effects inhibits SCRs, DADs and SAPs.

A) Promoting Ca^{2+} buffering by CSQ monotonically increases the rate threshold of SCRs (i), DADs (ii), and SAPs (iii). This effect is enhanced in cells with dense and intermediate tubular structures vs cells with sparse tubules. **B)** Effect of altered CSQ-mediated Ca^{2+} buffering on voltage (i) and global cytosolic Ca^{2+} concentration (ii) in cells with sparse (left), intermediate (middle), and dense (right) tubules following pacing at 3 Hz to examine the occurrence of DADs and SCRs.

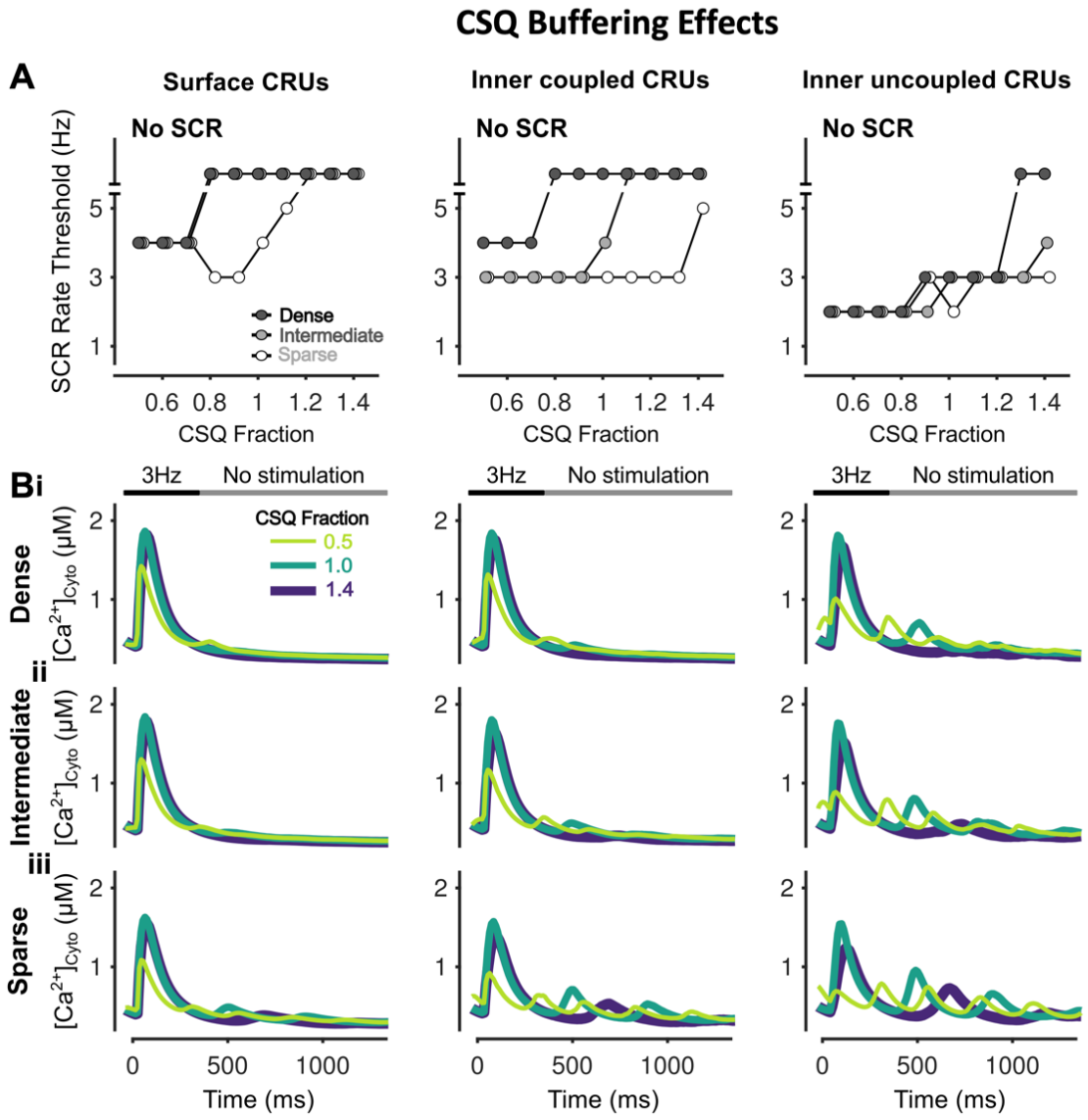

Figure 3.11 – Inhibition of CSQ Ca^{2+} buffering effects promotes SCRs in all CRUs.

A) Rate threshold for local SCRs of surface (left), inner coupled (middle) and inner uncoupled (right) CRUs in sparse, intermediate and densely tubulated cells with the impact of altered CSQ Ca^{2+} buffering effects greatest in inner coupled/uncoupled CRUs of cells with dense and intermediate tubules. **B)** Cytosolic Ca^{2+} concentration of surface (left), inner coupled (middle) and inner uncoupled (right) CRUs from cells with dense (i), intermediate (ii), and sparse (iii) tubules following pacing at 3 Hz showing observed SCRs with varying fraction of CSQ Ca^{2+} buffering effects.

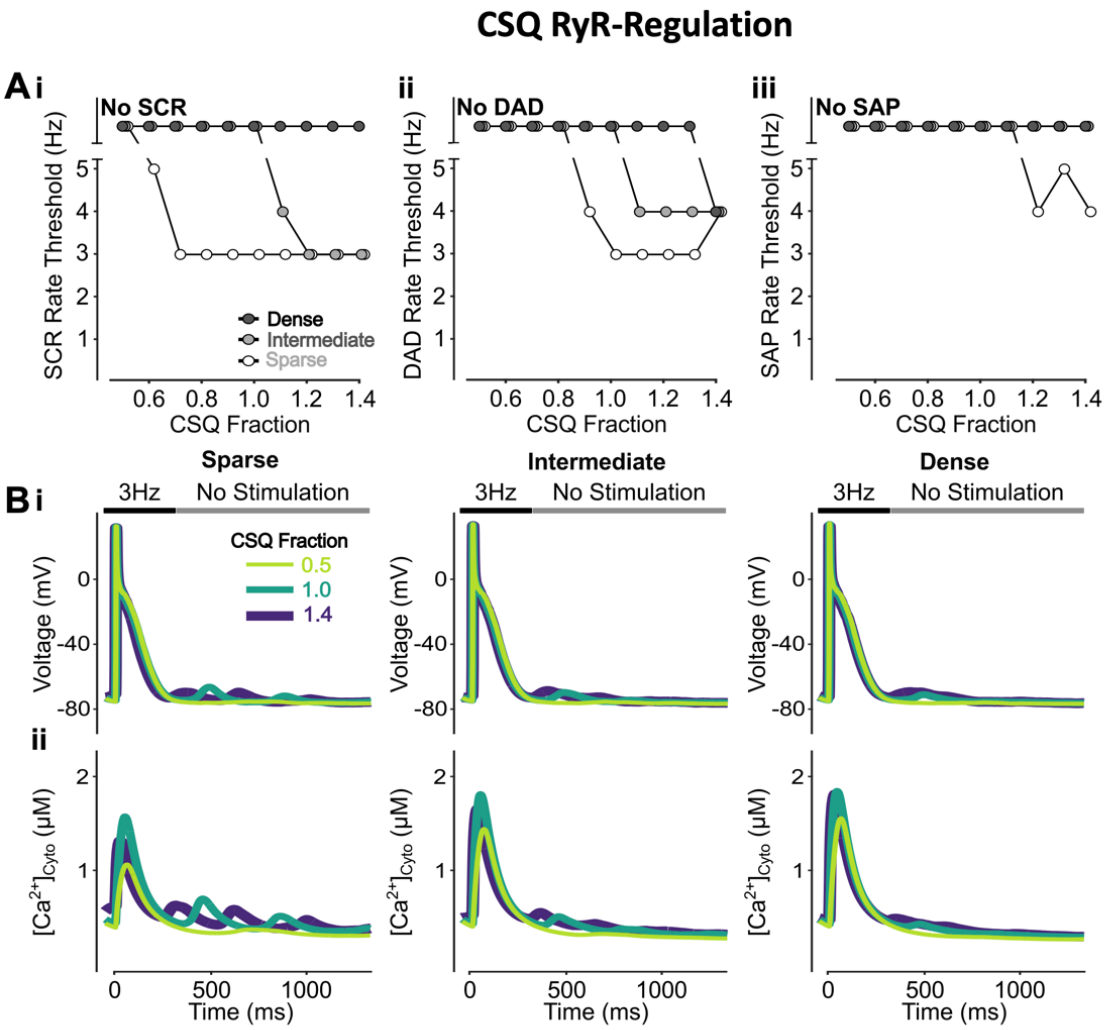

Figure 3.12 – Increasing CSQ-RyR regulation promotes SCRs, DADs and SAPs.

A) Increasing CSQ-RyR regulation monotonically decreases the rate threshold of SCRs (i), DADs (ii), and SAPs (iii) with the effect greater in cells with sparse and intermediate tubular structures vs cells with dense tubules. **B)** Effect of altered CSQ-RyR regulation on voltage (i) and global cytosolic Ca^{2+} concentration (ii) in cells with sparse (left), intermediate (middle), and dense (right) tubules following pacing at 3 Hz to examine the occurrence of DADs and SCRs.

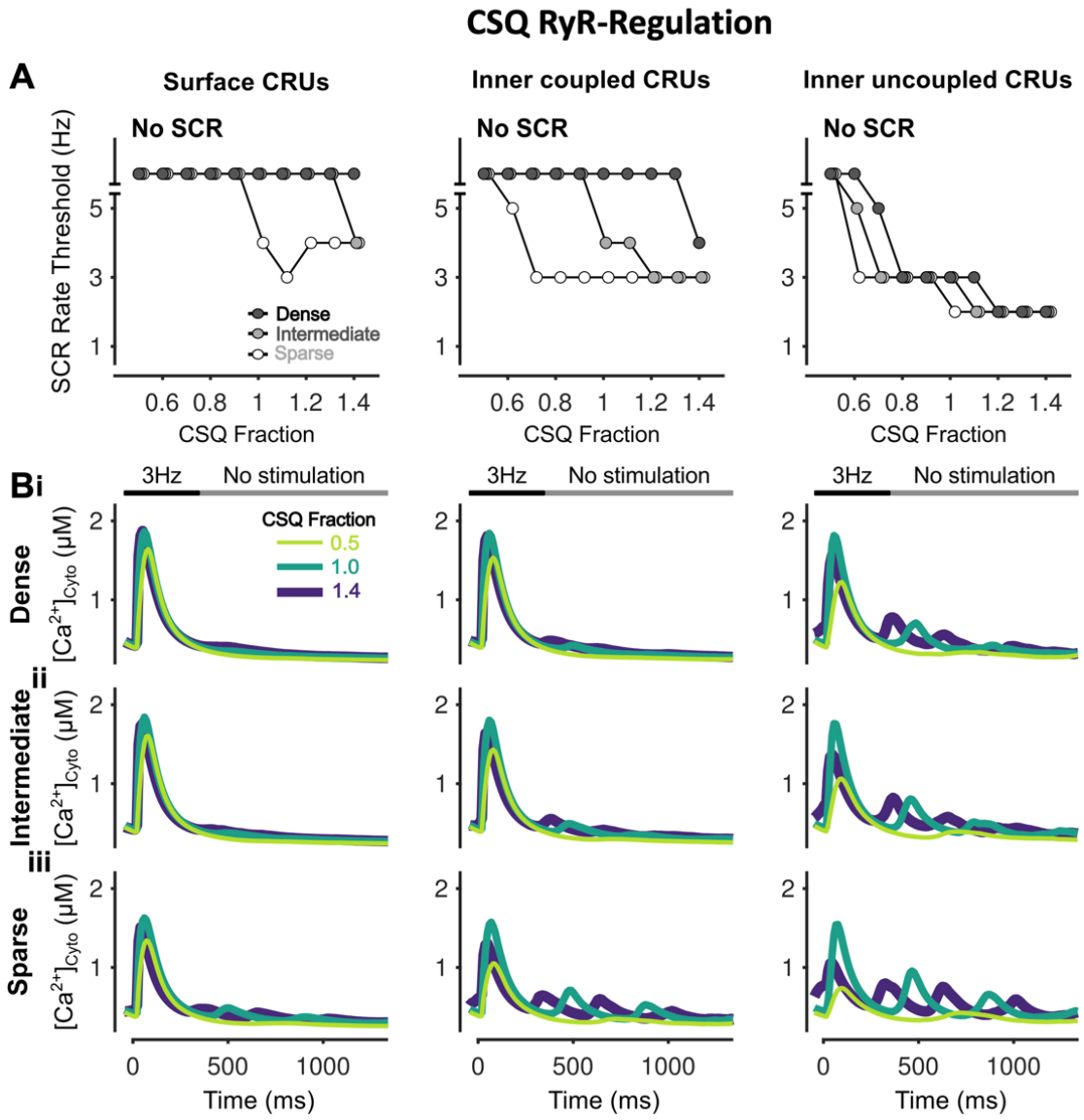

Figure 3.13 – Inhibition of CSQ-RyR regulation suppresses SCRs in all CRUs.

A) Rate threshold for local SCRs of surface (left), inner coupled (middle) and inner uncoupled (right) CRUs in sparse, intermediate and densely tubulated cells with the impact of altered CSQ-RyR regulation greatest in inner coupled/uncoupled CRUs. **B)** Cytosolic Ca^{2+} concentration of surface (left), inner coupled (middle) and inner uncoupled (right) CRUs from cells with dense (i), intermediate (ii), and sparse (iii) tubules following pacing at 3 Hz showing observed SCRs with varying fraction of CSQ RyR-regulation.

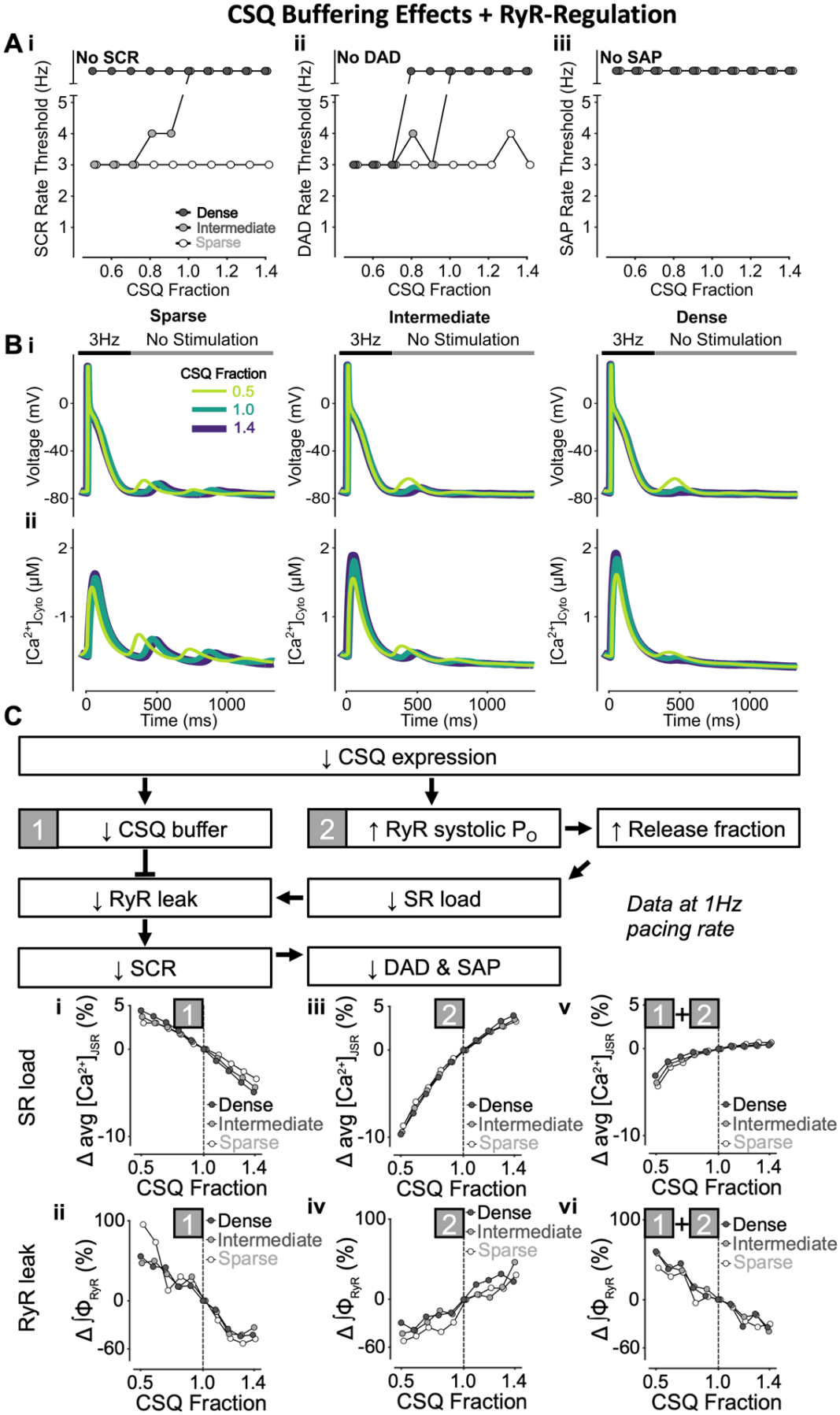
CSQ Buffering Effects + RyR-Regulation
A i
No SCR
SCR Rate Threshold (Hz)
Dense
Intermediate
Sparse
CSQ Fraction
ii
No DAD
DAD Rate Threshold (Hz)
iii
No SAP
SAP Rate Threshold (Hz)
B i
Sparse
Intermediate
Dense
3Hz
No Stimulation
CSQ Fraction
0.5
1.0
1.4
Voltage (mV)
ii
[Ca2+]Cyto (μM)
Time (ms)
C
↓ CSQ expression
1 ↓ CSQ buffer
2 ↑ RyR systolic Po
↑ Release fraction
↓ RyR leak
↓ SR load
↓ SCR
↓ DAD & SAP
Data at 1Hz pacing rate
SR load
RyR leak
Δ avg [Ca2+]JSR (%)
Δ ∫ΦRyR (%)
CSQ Fraction

Figure 3.14 – Increasing CSQ fraction inhibits SCRs and DADs with no effect on SAPs.

A) Increasing CSQ fraction (i.e., both CSQ-mediated Ca^{2+} buffering and RyR regulation) monotonically raises the rate threshold of SCRs (i) and DADs (ii), with SAP (iii) remaining absent in all conditions. While CSQ-mediated changes in SCRs are solely observed in cells with intermediate tubular structures, the effect of reduced CSQ fraction on DADs is greater in cells with dense and intermediate tubular structures vs cells with sparse tubules. **B)** Effect of altered CSQ fraction on voltage (i) and global cytosolic Ca^{2+} concentration (ii) in cells with sparse (left), intermediate (middle), and dense (right) tubules following pacing at 3 Hz to examine the occurrence of DADs and SCRs. **C)** Mechanism underlying increased CSQ fraction inhibiting SCRs and DADs without affecting SAPs. Biomarkers were determined from the first 100 ms of no-stimulation period and normalized to those of cells with a retained CSQ fraction of 1.0. Since CSQ is a jSR Ca^{2+} buffer and regulates RyR P_o, there is interplay between varying CSQ buffering effects (1), CSQ-RyR regulation (2) and CSQ fraction (1+2). Lower CSQ expression is associated with reduced CSQ-mediated jSR Ca^{2+} buffering (1) and increased RyR systolic P_o (2). Reduced CSQ Ca^{2+} buffering (1) decreases SR load (i) but promotes RyR leak (ii), and thus SCRs. Conversely, enhanced systolic RyR P_o (2) increases SR release fraction, which lowers SR load (iii) and diminishes RyR leak (iv), leading to reduced SCRs. Combining these two effects, although decreasing CSQ expression lowers down SR Ca^{2+} load (v), RyR leak is enhanced (vi), which leads to promotion of SCRs, DADs, and SAPs.

Indeed, our mechanistic analysis suggests that luminal Ca^{2+} buffering by CSQ plays a more important role in affecting arrhythmic outcomes than its role on RyR gating. On one hand, inhibiting CSQ Ca^{2+} buffering (**Fig. 3.14C, 1**) increased the SR load (**Fig. 3.14Ci**) and RyR leak (**Fig. 3.14Cii**) to promote SCRs and DADs. On the other hand, inhibition of CSQ RyR-regulation (**Fig. 3.14C, 2**) elevated RyR systolic P_O and enhanced SR release fraction, and decreased SR load (**Fig. 3.14Ciii**), leading to subsequent smaller RyR leak (**Fig. 3.14Civ**) and reduced SCRs and DADs, especially in inner coupled CRUs (**Fig. 3.15**). When combining the two opposing effects, we found an overall net increase in RyR leak (**Fig.**

3.14Cvi), which was dominant over the slight decrease in SR load (**Fig. 3.14Cv**), and promoted SCRs, DADs, and SAPs. In these settings, the rate thresholds of SCRs, DADs, and SAPs are consistently lower in the cell with sparse TATS (in agreement with results in the companion Chapter 2 paper), but cells with intermediate and dense TATS are more susceptible to changes in CSQ expression.

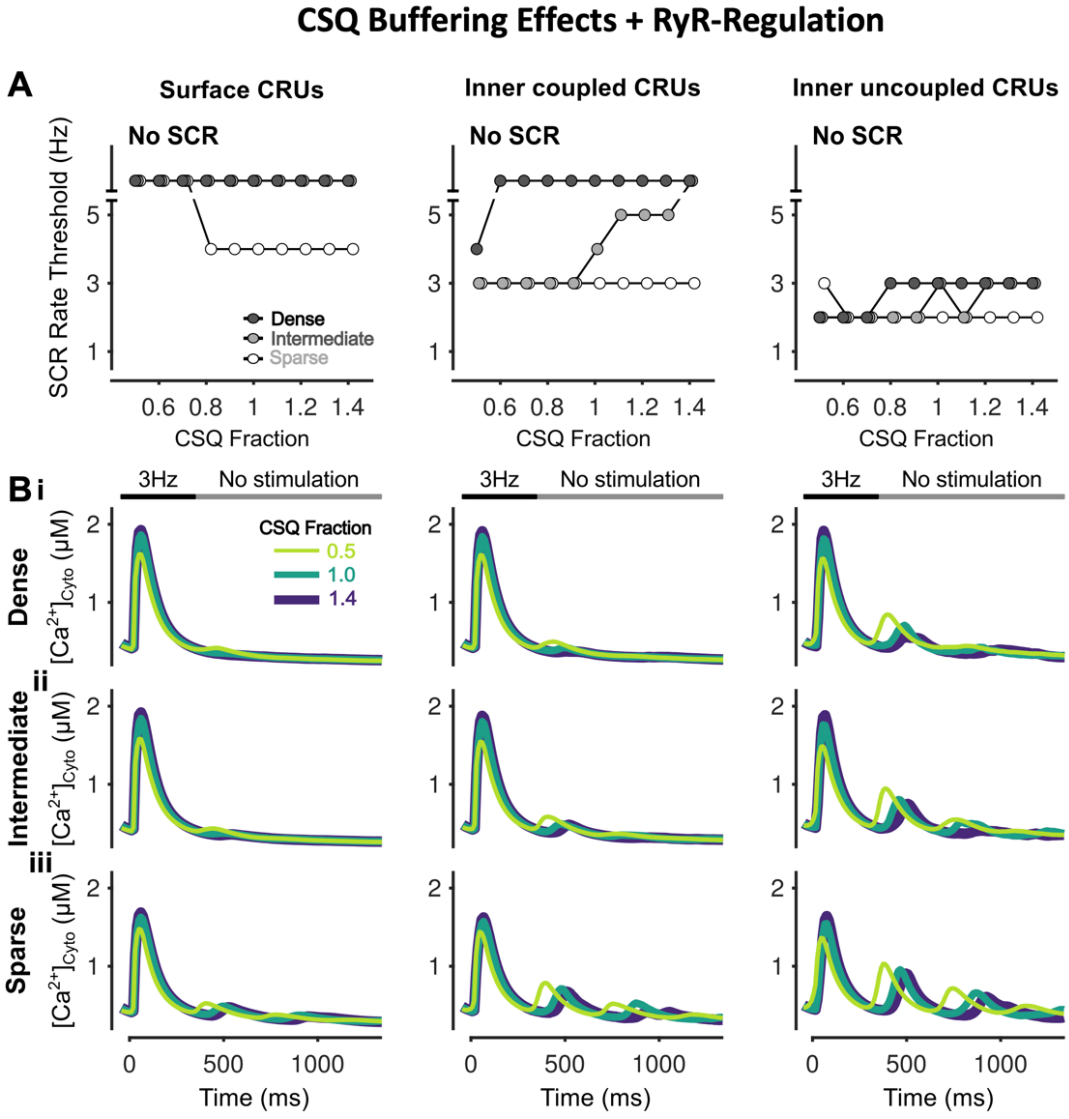

Figure 3.15 – Varying CSQ fraction has differing effects on SCR dependent on CRU location.

A) Rate threshold for local SCRs of surface (left), inner coupled (middle) and inner uncoupled (right) CRUs in sparse, intermediate and densely tubulated cells. Whereas CSQ downregulation raises the SCR rate threshold in cells with sparse tubules, it lowers the threshold in inner coupled/uncoupled CRUs of

cells with intermediate and dense tubular structures. **B)** Cytosolic Ca^{2+} concentration of surface (left), inner coupled (middle) and inner uncoupled (right) CRUs from cells with dense (i), intermediate (ii), and sparse (iii) tubules following pacing at 3 Hz showing observed SCRs with varying CSQ fraction.

3.3.6 Increasing surface vs. inner CRU CSQ expression promotes SCRs but inhibits DADs by elevating inner RyR leak but decreasing surface RyR leak

To reveal the effects of heterogeneous subcellular CSQ distribution and TATS density on SCRs, DADs, and SAPs, we simulated various surface/inner CRU CSQ expression ratios in cells with sparse, intermediate, and dense TATS. The simulation results indicate that increasing surface vs. inner CRU CSQ expression lowers the pacing threshold for SCRs (in cells with intermediate TATS, **Fig. 3.16Ai**), but increased the pacing threshold for DADs (in cells with sparse and intermediate TATS, **Fig. 3.16Aii**), without remarkable effects on SAP rate threshold (**Fig. 3.16Aiii**). These results are also illustrated by the representative traces of $[Ca^{2+}]_{Cyto}$ and V_m (**Fig. 3.16B**). We found that increasing surface-to-inner CRU CSQ expression ratio changes RyR leak locally, i.e., decreasing RyR leak at the periphery and increasing it at the cell interior. A larger inner RyR leak favors SCRs and DADs (**Fig. 3.16Ci**), but a smaller RyR leak in the periphery area (**Fig. 3.16Cii**) reduces NCX Ca^{2+} extrusion (**Fig. 3.16Ciii**), $\Delta V_m/\Delta Ca^{2+}$ gain (**Fig. 3.16Civ**) and DADs. The effects of varying surface-to-inner CRU CSQ expression ratio on $\Delta V_m/\Delta Ca^{2+}$ gain are stronger in cells with sparse TATS (**Fig. 3.16Civ**), which is reflected in DAD rate threshold changes being more marked compared to intermediate/densely tubulated cells (**Fig. 3.16Aii**). Examination of the subcellular Ca^{2+} signals suggests that increasing surface vs. inner CSQ expression reduces the SCR rate threshold in inner coupled CRUs of the cell with intermediate TATS (**Fig. 3.17A**), matching the changes in SCR rate threshold (**Fig. 3.16Ai**), and in all cases, SCRs are favored in cells with sparse TATS (**Fig. 3.17A-B**).

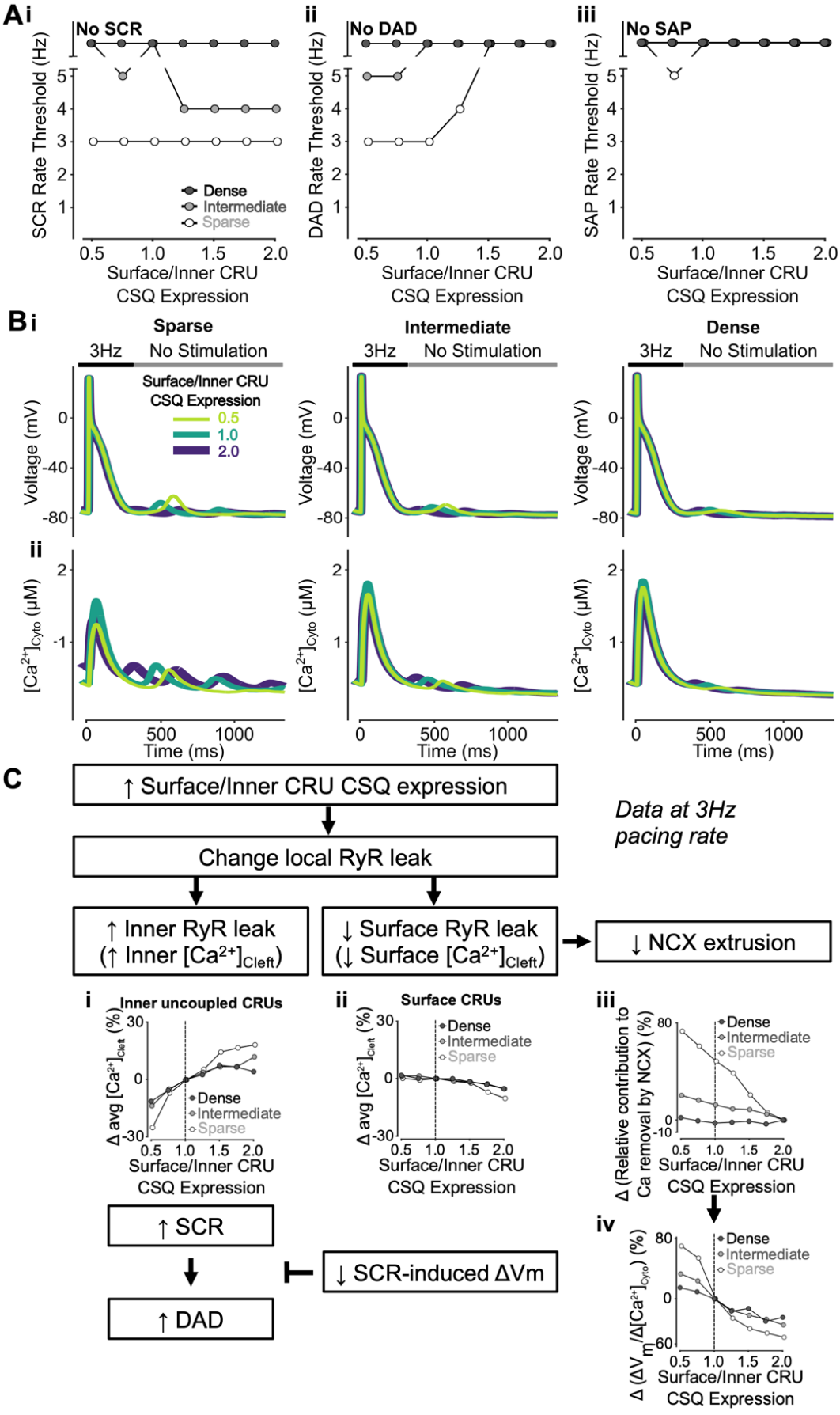
A i
No SCR
SCR Rate Threshold (Hz)
Dense
Intermediate
Sparse
Surface/Inner CRU
CSQ Expression
ii
No DAD
DAD Rate Threshold (Hz)
iii
No SAP
SAP Rate Threshold (Hz)
B i
Sparse
Intermediate
Dense
3Hz
No Stimulation
Surface/Inner CRU
CSQ Expression
0.5
1.0
2.0
Voltage (mV)
ii
[Ca2+]Cyto (μM)
Time (ms)
C
↑ Surface/Inner CRU CSQ expression
Change local RyR leak
↑ Inner RyR leak
(↑ Inner [Ca2+]Cleft)
↓ Surface RyR leak
(↓ Surface [Ca2+]Cleft)
↓ NCX extrusion
Data at 3Hz
pacing rate
i
Inner uncoupled CRUs
Δ avg [Ca2+]Cleft (%)
ii
Surface CRUs
iii
Δ (Relative contribution to
Ca removal by NCX) (%)
iv
Δ (ΔVm/Δ[Ca2+]Cyto) (%)
↑ SCR
↑ DAD
↓ SCR-induced ΔVm

Figure 3.16 – Increasing surface/inner CRU CSQ expression ratio promotes SCRs but inhibits DADs and does not affect SAP.

A) Increasing surface/inner CRU CSQ expression ratio (i.e., increasing CSQ density in surface CRUs without changing whole-cell CSQ expression) monotonically decreases the rate threshold of SCRs (i) and increases the rate threshold of DADs (ii), whereas SAPs (iii) only appear in cells with sparse tubules and surface/inner CRU CSQ expression ratio of 0.75. The effect on SCRs is greater in cells with intermediate tubular structures vs cells with sparse and dense tubules, whereas the effect on DADs is enhanced in cells with sparse and intermediate tubular structures vs cells with dense tubules. **B)** Effect of altered surface/inner CRU CSQ expression ratio on voltage (i) and global cytosolic Ca^{2+} concentration (ii) in cells with sparse (left), intermediate (middle), and dense (right) tubules following pacing at 3 Hz to examine the occurrence of DADs and SCRs. **C)** Mechanism underlying increasing surface/inner CRU CSQ expression ratio promoting SCRs, inhibiting DADs with no effect on SAPs. Biomarkers were determined from the first 100 ms of no-stimulation period and normalized to those of cells with a retained surface/inner CRU CSQ expression ratio of 1.0. As similarly described when altering overall CSQ expression (**Figure 13**), increasing surface/inner CRU CSQ expression ratio is associated with increased RyR leak in inner uncoupled CRUs (i) and decreased RyR leak in surface CRUs (ii). Enhanced RyR leak in inner uncoupled CRUs leads to stronger SCRs and DADs. However, less RyR leak in surface CRUs reduces NCX contribution to Ca^{2+} extrusion (iii) and lowers SCR-induced voltage changes/SCR amplitude ratio (iv). As such, while SCRs typically lead to DADs, this transition is prohibited by the decreased SCR-induced changes in V_m, thus explaining the opposing effects of increasing surface/inner CRU RyR expression ratio on SCRs and DADs.

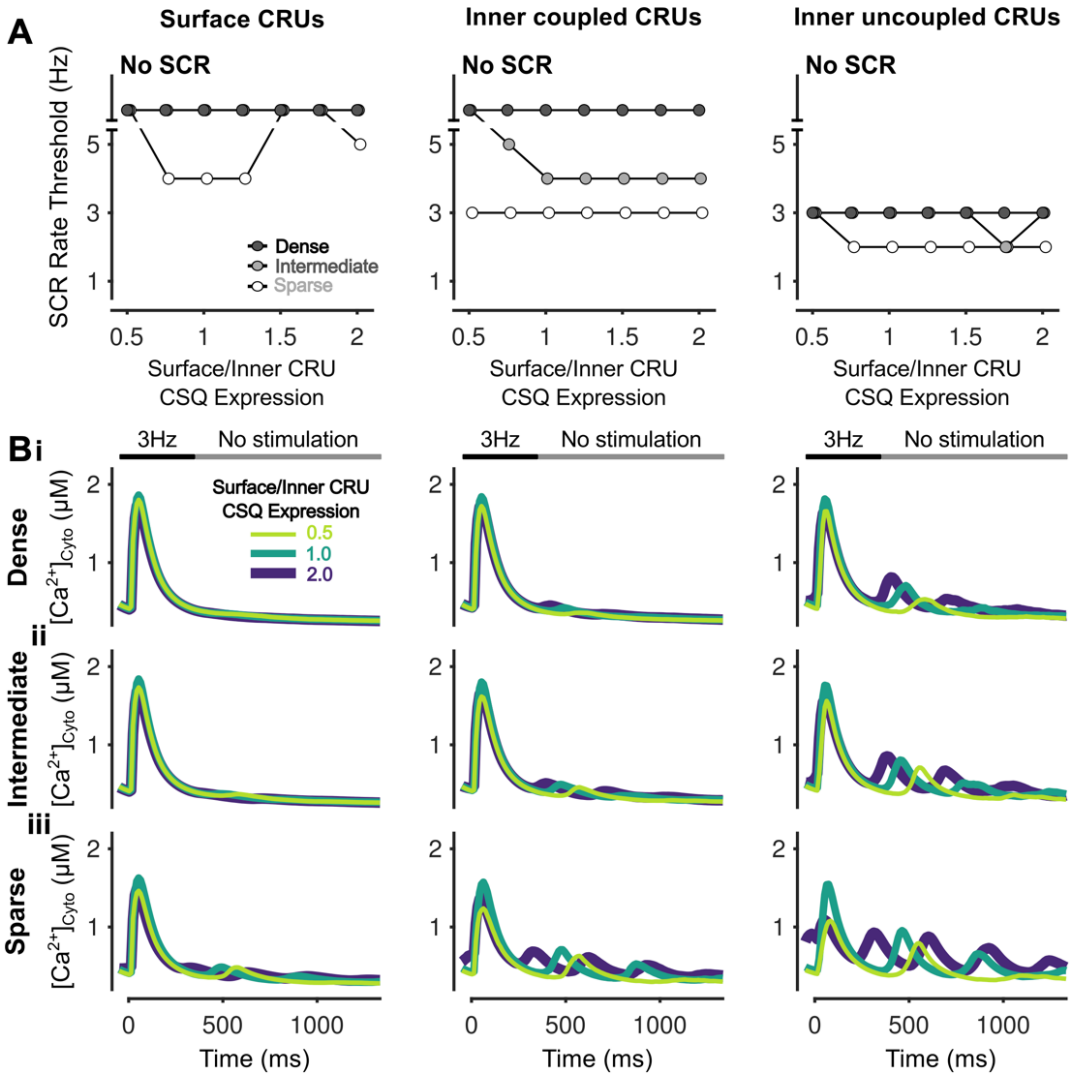

Figure 3.17 – Increasing surface/inner CRU CSQ expression ratio promotes simultaneous SCRs in inner coupled CRUs of cells with intermediate tubules.

A) Rate threshold for local SCRs of surface (left), inner coupled (middle) and inner uncoupled (right) CRUs in sparse, intermediate and densely tubulated cells with the impact of altered surface/inner CSQ expression ratio greatest in inner coupled CRUs of cells with intermediate tubules. **B)** Cytosolic Ca^{2+} concentration of surface (left), inner coupled (middle) and inner uncoupled (right) CRUs from cells with dense (i), intermediate (ii), and sparse (iii) tubules following pacing at 3 Hz showing observed SCRs with varying surface/inner CRU CSQ expression ratios.

3.4 Discussion

In this study, we utilized our integrative model of the human atrial myocyte (Chapter 2) to predict and quantitatively explain how TATS loss interacts with varying expression and localization of key Ca^{2+} handling proteins to disrupt diastolic Ca^{2+} homeostasis and electrophysiological stability in human atrial cells. Specifically, we demonstrated that arrhythmogenic effects of Ca^{2+} handling protein remodeling are especially exaggerated in cells with intermediate TATS, with densely tubulated myocytes being more resilient, and detubulated myocytes being rather insensitive to the superimposed ionic remodeling. Recent studies have investigated t-tubule restoration as a therapeutic maneuver in cardiac disease, especially in HF, and suggest that therapeutic t-tubule protection and repair may benefit inotropy while inhibiting arrhythmia (Manfra *et al.*, 2017). Analogously, several groups endeavored to optimize experimental conditions to produce human induced pluripotent derived cardiomyocytes with functional t-tubule networks (Parikh *et al.*, 2017). Our findings provide mechanistic insight into the interactive contributions of TATS and Ca^{2+}-handling protein expression and distribution on Ca^{2+}-driven proarrhythmic behavior that underlie AF pathophysiology and may help to predict the effects of antiarrhythmic strategies at varying stages of ultrastructural remodeling.

3.4.1 NCX expression and distribution

In the healthy heart, NCX inhibition prevents Ca^{2+} extrusion, leading to Ca^{2+} overload (Bers, 2002) and thus enhancement of SCRs (Lotteau *et al.*, 2021). This is seen in our simulations, whereby a decrease in NCX is associated with a reduction in the pacing threshold for SCRs. While increased SCRs are typically expected to promote V_m instabilities, drug-induced NCX block enhanced SCRs but reduced DADs in rabbit atrial myocyte experiments (Hohendanner

et al., 2015). We also observed this in our simulations where inhibiting NCX (both globally or locally in the cell interior vs. periphery) varied the balance between increased SCRs and reduced $\Delta V_m/\Delta Ca^{2+}$ gain that determines the net impact on SCRs, DADs, and SAPs (**Fig. 3.2**). As such, our model provides quantitative spatially-detailed insight into the interaction of these two opposing effects. Furthermore, our simulation results suggest that SCR is further enhanced with TATS loss, and the effects of inhibiting NCX on $[Ca^{2+}]_{Cyto}$-voltage coupling is stronger in cells with intermediate and dense TATS (**Figs. 3.2** and **3.4**). This suggests that with severe ultrastructural remodeling and TATS loss, additional changes in Ca^{2+} extrusion may not strongly modulate Ca^{2+} homeostasis and arrhythmogenesis. Interestingly, atrial myocytes from NCX knock-out mice also have reduced TATS density (Yue *et al.*, 2017). It is reasonable to speculate that TATS loss in this setting may be a compensatory adaptation to Ca^{2+} overload, to limit Ca^{2+}-V_m coupling and attenuate DAD and SAP risk. Indeed, this is supported by our sparsely tubulated myocyte model having a higher SAP rate threshold than the models with intermediate and dense TATS.

Interestingly, lower NCX promotes CaT alternans in cells with sparse and intermediate TATS but has biphasic effects on the rate threshold of CaT alternans in the densely tubulated cell (**Fig. 3.18Ai**), with the same effect observed in all CRU locations (**Fig. 3.3Bi**). Similarly, NCX inhibition has biphasic effects on the rate threshold of APD alternans (**Fig. 3.18Aii**), alongside changes in rate thresholds of DADs and SAPs (**Fig. 3.2Aii-iii**). Though these effects were observed when altering NCX expression, varying surface/inner CRU NCX localization had no effect on rate threshold of APD alternans besides initiating some CaT alternans at 5Hz (**Fig. 3.18B**). Taken together, these results suggest that atrial cells are more sensitive to whole-cell rather than subcellular changes in NCX-mediated Ca^{2+} extrusion.

As NCX is upregulated in disease (Voigt *et al.*, 2012), we also considered the impact of increased, not just decreased, NCX expression on arrhythmogenesis. Based on our

simulation results, enhanced NCX expression may be an adaptive ionic remodeling process to protect the cells against Ca^{2+} overload-induced arrhythmia, although this can also be proarrhythmic with increased Ca^{2+}-V_m coupling. Indeed, in AF, enhanced NCX expression increases diastolic Ca^{2+}-V_m coupling to augment the arrhythmogenic effects of enhanced SR Ca^{2+}-leak, causing transient inward current and subsequent DADs (Hove-Madsen *et al.*, 2004; Lenaerts *et al.*, 2009; Neef *et al.*, 2010; Voigt *et al.*, 2012). Because of this, NCX inhibition is thought to be a suitable therapeutic AF treatment (Hobai & O'Rourke, 2004).

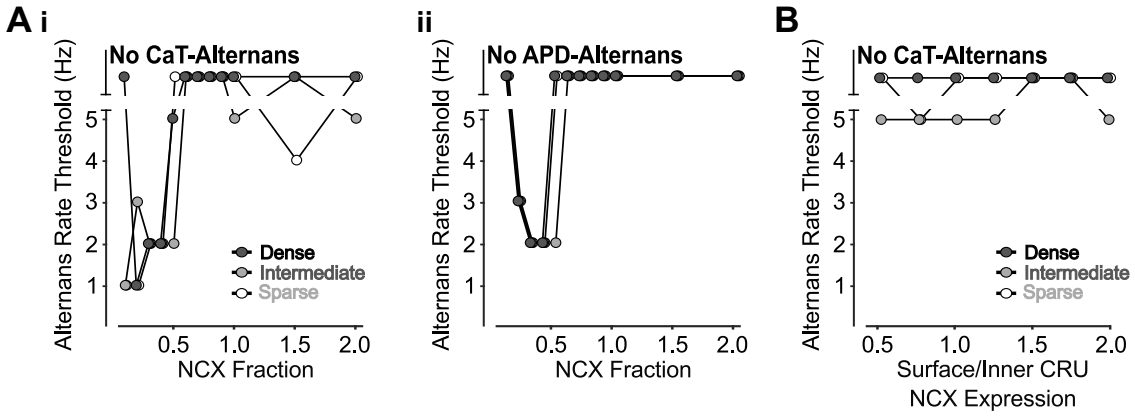

Figure 3.18 – Inhibition of NCX has biphasic effects on CaT and APD alternans but increasing surface/inner CRU NCX expression ratio only exhibits CaT alternans at 5 Hz.

A) The rate thresholds of CaT alternans (i) and APD alternans (ii) display biphasic dependence on NCX reduction. **B)** Varying surface/inner CRU NCX expression ratio induces CaT alternans at 5 Hz, especially in cells with intermediate TATS.

Our simulation suggests that varying degrees of NCX inhibition could have opposite effects on arrhythmias with NCX inhibition treatment potentially having better effects in cells with intermediate and dense TATS than in cells with sparse TATS. In atrial myocytes, NCX likely distributes on both the cell surface and TATS (Melnyk *et al.*, 2005; Scriven *et al.*, 2010), with localization disrupted with TATS remodeling in disease. As such, altered NCX distribution alongside TATS loss promotes arrhythmia, while increasing NCX density within

remaining TATS may preserve NCX-mediated Ca^{2+}-extrusion and rescue the cells from Ca^{2+} overload. While NCX inhibition is thought to be more relevant to cardiac disease clinically, it is interesting to note that pharmacological NCX activators are emerging as promising strategies to ameliorate certain neurodegenerative diseases (Annunziato *et al.*, 2020), such as stroke, neonatal hypoxia, multiple sclerosis, amyotrophic lateral sclerosis, Alzheimer's disease, Parkinson's disease, and spinal muscular atrophy. In neuronal cells, various NCX isoforms work to maintain Na^+ and Ca^{2+} homeostasis in the cytosol, endoplasmic reticulum, and mitochondria via both forward and reverse mode operation; and have been shown to increase survival of neuronal and glial-derived cells in pathophysiologic conditions (Annunziato *et al.*, 2020; Pannaccione *et al.*, 2020).

3.4.2 RyR expression and distribution

Previous computational studies using a ventricular myocyte model show that enhanced RyR expression *per se* increased SR Ca^{2+} leak, while the subsequent reduction SR Ca^{2+} load reduced RyR P_O (Sato *et al.*, 2016), similar to experimental data showing that SR Ca^{2+} leak reduces SR load (Bers, 2002), which can reduce the RyR P_O (Sitsapesan & Williams, 1994). On the other hand, a recent experimental study found RyR loss-of-function mutations, which are associated with arrhythmia and sudden cardiac death, cause elevated SR Ca^{2+} load (Li *et al.*, 2021), which can increase the RyR P_O. These data suggest that increasing RyR expression might be pro- or anti-arrhythmic depending on the prevailing mechanism. Indeed, our simulations indicate that altering RyR expression shifts the balance between RyR number-associated release flux and opposite SR load changes that determine the net impact on RyR leak, and subsequent SCRs, DADs, and SAPs (**Fig. 3.6**). While RyR number does affect SCR in the cell with sparse TATS, DADs and SAPs are similarly affected in all cell types (**Fig. 3.6A**). Interestingly, these contrasting outcomes are similar to those reported following use of two different RyR-

modulating drugs in ventricular myocytes from catecholaminergic polymorphic ventricular tachycardia (CPVT) mice. Here RyR inhibition by tetracaine decreased Ca^{2+} sparks and leak thus increasing SR Ca^{2+} load, whereas flecainide reduced Ca^{2+} spark mass and increased Ca^{2+} spark frequency with no effect on spark-mediated SR Ca^{2+} leak or content (Hilliard *et al.*, 2010).

SCRs are increased in myocytes isolated from patients with paroxysmal AF lacking TATS likely because of increased RyR channel expression (Beavers *et al.*, 2013; Voigt *et al.*, 2014). Conversely, a reduction in RyR expression is seen in several animal models of atrial tachycardia remodeling as part of the underlying proarrhythmic substrate (Lenaerts *et al.*, 2009; Wakili *et al.*, 2010; Lugenbiel *et al.*, 2015). Notably, despite reduced total RyR protein levels in the atria of patients with systolic HF, RyR function was found to be increased (Molina *et al.*, 2018). As such, changes in RyR expression may not fully reflect changes in RyR regulation, as previously discussed (Chapter 2), which may further affect the balance between adaptive and maladaptive responses. For example, mouse knock-in RyR mutations that result in increased diastolic Ca^{2+} leak are associated with CPVT and AF, which are inhibited with the RyR stabilizer S107 that reduces diastolic SR Ca^{2+} leak in atrial myocytes and decreases burst pacing-induced AF in vivo (Shan *et al.*, 2012). Additionally, AF is associated with RyR hyperphosphorylation (Vest *et al.*, 2005; Neef *et al.*, 2010; Voigt *et al.*, 2012) and thus larger diastolic SR leak and elevated Ca^{2+} levels (Neef *et al.*, 2010).

In human atrial myocytes from both normal sinus rhythm and AF patient samples, RyR density is higher at the sarcolemma than in the cell interior (Herraiz-Martínez *et al.*, 2022), but the physiological significance of heterogeneous subcellular RyR distribution is not understood. In our model, increasing RyR expression at the surface vs. inner CRUs enhances NCX-RyR coupling, which on one hand reduces SCRs due to NCX-mediated Ca^{2+} extrusion, but on the other hand, increases $\Delta V_m/\Delta Ca^{2+}$ gain (**Fig. 3.8**). Our simulations suggest that the observed increase in peripheral RyR distribution might be a protective mechanism that allows achieving

the optimal balance that guarantees stable Ca^{2+} and V_m homeostasis. Whilst these spatial differences exist in the healthy atria, complex remodeling occurs in AF involving RyR cluster fragmentation and redistribution to inter-z-line areas, with Ca^{2+} sparks increased in fragmented CRUs (Macquaide *et al.*, 2015). This subcellular remodeling of RyR distribution in AF is outside the scope of this study but can be examined in future investigations. In the companion paper (Zhang et al), we highlighted that NCX-mediated Ca^{2+} extrusion inhibits SCRs in coupled CRUs, whereas SCRs persist in uncoupled CRUs due to Ca^{2+} released having to diffuse to coupled CRUs to be extruded by NCX. In line with this, spatial differences in subcellular Ca^{2+} dynamics may be differentially affected by RyR subcellular remodeling in coupled vs. uncoupled CRUs.

3.4.3 CSQ expression and distribution

CSQ is a major luminal Ca^{2+} buffer and RyR regulator (Terentyev *et al.*, 2003; Györke *et al.*, 2004; Knollmann *et al.*, 2006; Restrepo *et al.*, 2008). Reduced atrial CSQ expression promotes arrhythmia in HF (Yeh *et al.*, 2008), with CSQ loss enhancing SCRs and DADs to increase AF risk (Faggioni *et al.*, 2014). Our model confirms these findings and demonstrates that diminished Ca^{2+} buffering associated with lower CSQ expression has a predominant effect promoting SCRs and DADs (**Figs. 3.10** and **3.14**), with associated changes to RyR gating having the opposing (and more modest) effect of decreasing SR load to limit SCRs and DADs (**Figs. 3.12** and **3.14**). Indeed, while impaired SR Ca^{2+} buffering is a well-accepted mechanism for CPVT-associated CSQ mutations (Wleklinski *et al.*, 2020), CSQ-RyR interaction may also be altered by some of these mutations (Terentyev *et al.*, 2006). Notably, despite SCRs and DADs being consistently greater in the cell with sparse TATS, cells with intermediate and dense TATS are more susceptible to changes in CSQ expression (**Fig. 3.14**).

In human atrial myocytes, CSQ is more abundant near the cell periphery vs. the inner area (Schulson *et al.*, 2011; Herraiz-Martínez *et al.*, 2022). Our simulations suggest that this baseline subcellular CSQ distribution gradient might be protective against arrhythmia, as increasing surface vs. inner CRU CSQ expression promotes SCRs but inhibits DADs (**Fig. 3.16**). The protection from DADs is stronger in cells with sparse and intermediate TATS (**Fig. 3.16**), and might be relevant for chronic AF, where a cell surface to interior gradient in CSQ expression is seen and there is TATS loss (Lenaerts *et al.*, 2009).

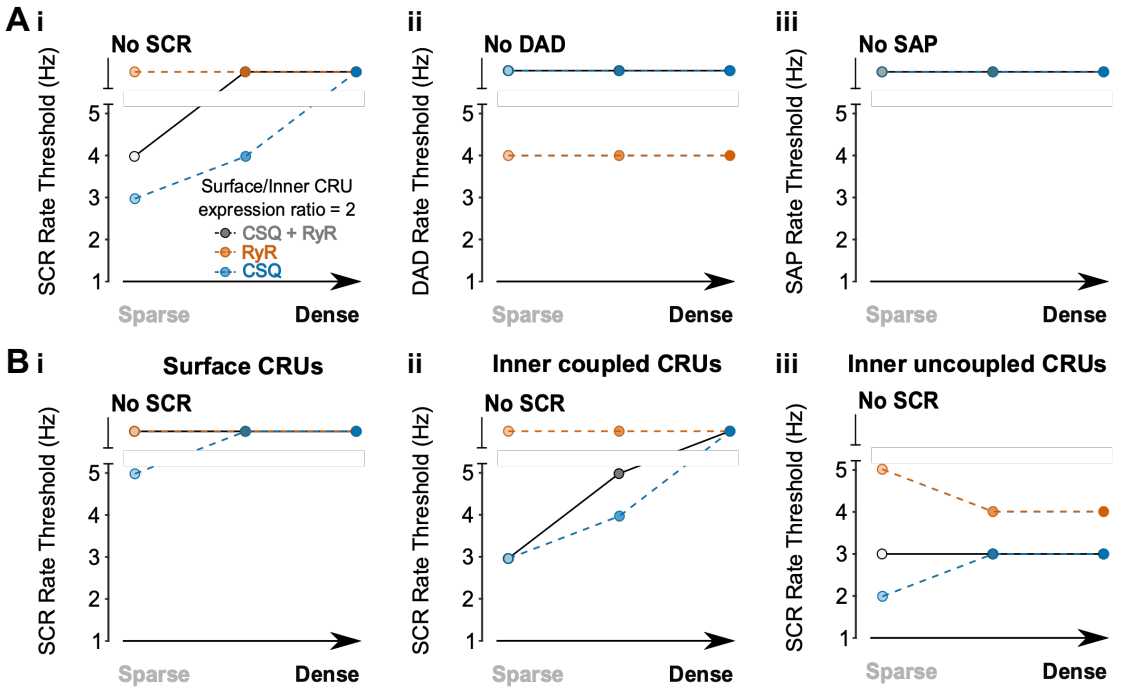

Figure 3.19 – Effect of concomitantly increasing surface/inner CRU expression ratio of CSQ and RyR to 2.0.

A) With increased CRU CSQ and RyR expression ratio, tubule loss decreases the rate threshold of SCRs (i), whereas DADs (ii) and SAPs (iii) remain absent in all conditions. The simulation results with surface/inner CRU expression ratio of RyR (orange) or CSQ (blue) at 2.0 are superimposed for comparison. **B)** Rate threshold for local SCRs from surface (i), inner coupled (ii) and inner uncoupled (iii) CRUs in sparse, intermediate, and densely tubulated cells. The impact of altered tubular density is greatest in inner coupled CRUs, with less change in SCR rate threshold associated with changes in tubule density in surface or inner uncoupled CRUs.

Notably, when we simulated concomitant changes in surface/inner CRU expression ratios (ratio = 2) of both RyR and CSQ to mimic experimental findings (Herraiz-Martínez *et al.*, 2022), we found that the pacing threshold for SCRs increased vs varying CSQ distribution only, and varying-RyR-induced DADs are ultimately prevented by concomitant changes (i.e., CSQ + RyR) (**Fig. 3.19**). This indicates that appropriate relative expression of RyR and CSQ through non-uniform surface/inner CRU expression ratios, as seen in human atrial myocyte experiments (Herraiz-Martínez *et al.*, 2022), provides protection against arrhythmia. Of note, adaptive changes to CSQ deficiency in CPVT include increased RyR expression, which on one hand maintains excitation-contraction coupling but also increases RyR leakiness (Song *et al.*, 2007).

3.4.4 LCC expression and localization

In human atrial myocytes, LCCs are evenly distributed in TATS and surface membrane (Glukhov *et al.*, 2015). While LCC current is decreased in AF (Christ T. *et al.*, 2004), to our knowledge LCC subcellular distribution in AF is yet to be elucidated. In HF ventricular myocytes, altered colocalization between LCCs and RyRs may impair the ability of the LCC to trigger RyR Ca^{2+} release (Gómez *et al.*, 1997). Indeed, computational atrial myocyte simulations indicate that disrupted LCC localization (i.e., removal of LCCs away from the dyadic cleft) changes subcellular Ca^{2+} dynamics to elevate SR load and enhance AP-evoked Ca^{2+} wave propagation (Shiferaw *et al.*, 2020*a*). In our preliminary simulations, we found that varying LCC expression and distribution *per se* did not change SCR and DAD properties (data not shown). Nevertheless, LCCs play a critical role in systolic Ca^{2+} signaling, as well as in setting the steady-state conditions for diastolic behavior (e.g., cellular Ca^{2+} loading and removal, which we take into account by simulating at various pacing frequencies).

3.5 Future Directions

The limitations of this model are discussed in our companion paper (Zhang et al). Taking those into account, our novel 3D human atrial myocyte model provides a valuable platform that can be further adapted for future investigations. These could include, but are not limited to, incorporating immunofluorescence microscopy-based protein distributions and localization information of other proteins, calibrating additional experimental results of SR Ca^{2+} dynamics, and integrating extracellular ion dynamics.

3.5.1 Estimation of protein localization

While spatial localization and activity of key Ca^{2+} handling proteins in the ventricle have been characterized experimentally using immunofluorescence microscopy and/or detubulation (Kawai *et al.*, 1999; Despa *et al.*, 2003; Gadeberg *et al.*, 2017), little is currently known regarding the atria. However, various experimental data indicate heterogeneous Ca^{2+} handling proteins function, expression, and localization (Chen-Izu *et al.*, 2006; Macquaide *et al.*, 2015; Brandenburg *et al.*, 2016; Galice *et al.*, 2018; Herraiz-Martínez *et al.*, 2022), and variable TATs (Trafford *et al.*, 2013; Brandenburg *et al.*, 2016, 2018) in atrial myocytes, which may destabilize Ca^{2+} homeostasis and the bidirectional interaction between electrical excitation and Ca^{2+} signaling. LCCs have been shown to distribute equally in tubules and crest areas of the sarcolemma (Glukhov *et al.*, 2015), and rabbit atrial experiments confirm that LCCs are colocalized with RyRs as in the ventricle (Carl *et al.*, 1995). Compared to the ventricle, however, atrial cells are much more diverse, with varied cell width, sarcomere spacing (Arora *et al.*, 2017), and heterogeneity in the TATS between cells and across the atrium (Frisk *et al.*, 2014; Gadeberg *et al.*, 2016). Indeed, the subcellular distribution and expression of K^+ ion channels, LCC, and NCX are heterogeneous in canine pulmonary veins vs. left atrium (Melnyk

et al., 2005). While the distribution of these proteins in the healthy atria has begun to be identified, more work is needed, especially to provide insight into the remodeling that occurs in disease. Once experimental data on protein localization of human atrial myocytes becomes more readily available, this model has the potential to integrate all the spatial information to investigate how varying expression and subcellular structures may affect Ca^{2+} and voltage homeostasis.

3.5.2 Effect on extracellular ion concentrations

The TATS permits rapid AP propagation but slows ion (i.e., Na^{+}, Ca^{2+}, and K^{+}) diffusion between the extracellular space and TATS lumen (Yao *et al.*, 1997; Blatter & Niggli, 1998; Shepherd & McDonough, 1998; Swift *et al.*, 2006). However, myocyte contraction and relaxation cause distortion of the TATS that aids pumping the fluid to accelerate the diffusion (Savio-Galimberti *et al.*, 2008; Rog-Zielinska *et al.*, 2021*b*). A computational model of Ca^{2+} diffusion within a 10-μm long tubule suggests there is a high-to-low Ca^{2+} concentration dynamic gradient between peripheral, central and deep sections, which are regulated by tubule diameters, depth, and buffering effects, extracellular ion concentration and diffusion coefficient (Pásek *et al.*, 2008*b*). Experimental observations and mathematical models indicate the difference between tubules and surface membrane on membrane space, specific membrane capacitance and distribution of membrane ion channels, transporters and pumps in rat ventricular myocytes (Pásek *et al.*, 2008*a*). Computational models of tubules in rat (Pásek *et al.*, 2006) and guinea-pig (Pásek *et al.*, 2008*c*) ventricular myocytes both indicate that current-clamp pacing brings transient K^{+} accumulation but Ca^{2+} depletion in the TATS lumen, whereas fast pacing weakens K^{+} accumulation but increases Ca^{2+} depletion to decrease SR load and Ca^{2+} transient amplitude. These ion concentration gradients could also be integrated into our model to investigate not only intracellular but also extracellular local Ca^{2+} dynamics.

3.6 **Conclusions**

We utilized our novel 3D human atrial myocyte model to examine the arrhythmic effect of varying the expression and distribution of key Ca^{2+}-handling proteins alongside changes in TATS density. We reveal a balance between the pro- and anti-arrhythmic effects of protein remodeling and that this is differentially impacted by TATS density. These findings mechanistically elucidate how remodeling underlies Ca^{2+}-handling abnormalities and V_m instabilities that may precipitate AF.

Chapter 4 Discussion and Conclusions

4.1 Summary of Major Findings and Significance

This dissertation work aimed to develop a novel 3D, spatially detailed human atrial myocyte model that couples electrophysiology and Ca^{2+}-handling with variable TATS organization and density to link mechanistically cardiac ultrastructure to functional Ca^{2+} signaling. This study has shown that 1) varying TATS density, expression, and subcellular distribution of Ca^{2+}-handling proteins individually and collectively have variable pro- and anti-arrhythmic effects 2) the location and coupling status of CRUs determines their vulnerability to Ca^{2+}-driven arrhythmias with intracellular uncoupled CRUs most susceptible to SCRs, 3) the impact of Ca^{2+}-handling protein remodeling varies depending on TATS density with the most severe pro-arrhythmic behavior observed in cells with intermediate TATS (**Fig. 4.1**).

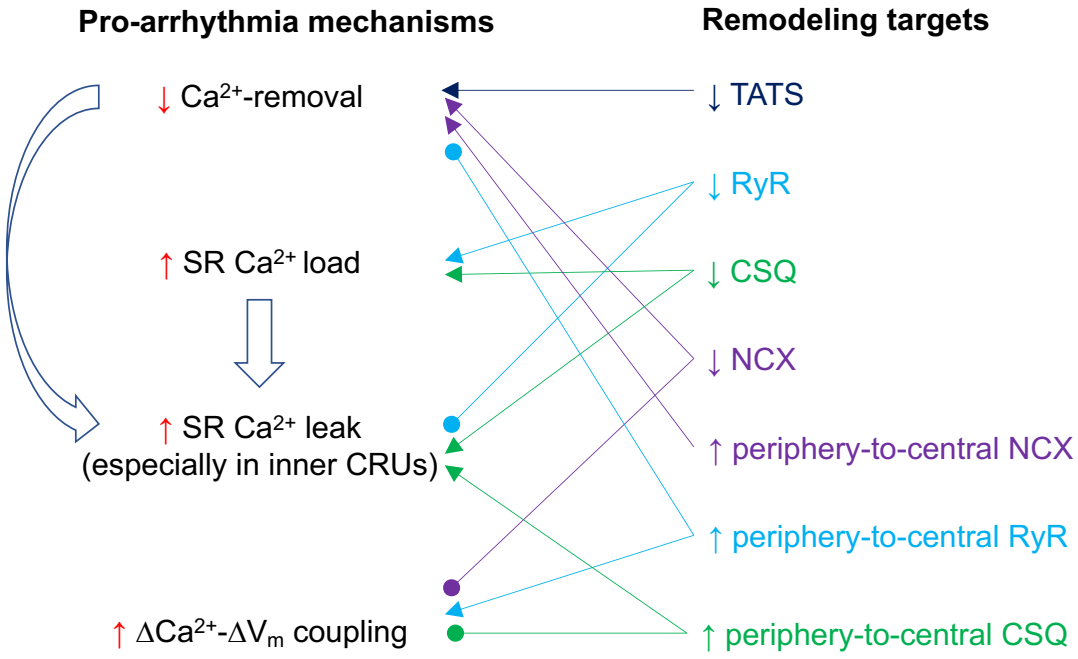

Figure 4.1 – The correlation between multiple remodeling targets and major pro-arrhythmia mechanisms.

TATS remodeling and the variations of Ca^{2+}-handling proteins mediate the balance of multiple anti- and pro-arrhythmia mechanism thus regulate the vulnerability to Ca^{2+}-driven arrhythmia. The arrows with triangular head represent that the remodeling factor promoting pro-arrhythmic mechanism, while the arrows with round head accounts for the inhibition effects.

In Chapter 2, we developed the model and extensively parameterized and validated it against a broad and diverse experimental dataset to build a robust platform evaluating the role of TATS remodeling on global and subcellular Ca^{2+} handling. We demonstrated that varying TATS density and subsequential changes in the localization of key Ca^{2+}-handling proteins have profound effects on Ca^{2+} handling. In this setting, TATS loss reduced NCX and thus increased cleft Ca^{2+} concentration through decreased Ca^{2+} extrusion. As a result, RyR open probability increased by elevated Ca^{2+} concentration, which enhanced SCRs, arrhythmogenic waves (especially in the cell interior), and consequential voltage instabilities through DADs. In summary, this study reveals the mechanism underlying how TATS remodeling promotes Ca^{2+}-driven proarrhythmic behavior.

In Chapter 3, we further developed the model presented in Chapter 2 by integrating varying expressions and localization of key Ca^{2+}-handling proteins. In this study, we investigated the isolated and interactive effects of changes in the expression and localization of key Ca^{2+}-handling proteins and variable TATS density on Ca^{2+} and voltage instabilities. The simulation results indicate that modulating the expression and distribution of NCX, RyR, and CSQ have different pro- and anti-arrhythmic effects, which depend on the balance of opposing influences on SR Ca^{2+} leak–load and Ca^{2+}–voltage relationships. Interestingly, the proarrhythmic impact of Ca^{2+}-handling protein remodeling changes dramatically in cells with varying TATS density, with intermediately tubulated cells more sensitive to these proarrhythmic insults compared to detubulated and densely tubulated myocytes. This work provides novel mechanistic insight into the distinct and interactive consequences of TATS and

Ca^{2+}-handling protein remodeling that underlies dysfunctional Ca^{2+} cycling and electrophysiological instability in disease.

In summary, while previous studies have focused on the consequential reduction in I_{Ca} following TATS loss, our study shows that the concomitant loss of NCX is also highly detrimental, especially in the generation of arrhythmias. Using the model, we were able to characterize how independent and combined Ca^{2+}-handling protein and TATS remodeling is pro- or anti-arrhythmic at the level and coupling status of the CRU. We identified that intracellular uncoupled CRUs are more prone to SCR-mediated triggered inward NCX current and thus membrane depolarization that causes DADs and spontaneous APs. Typically, diastolic Ca^{2+} removal via NCX on TATS inhibits SCRs from forming a whole-cell Ca^{2+} wave, and thus stabilizes both Ca^{2+} signaling and voltage dynamics. In line with this, densely tubulated cells appear to be protected from the arrhythmia induced by Ca^{2+} handling protein remodeling. Due to experimental limitations, the independent effects of TATS loss and Ca^{2+} handling protein remodeling in the atria have not been studied previously and this work highlights the mechanistic impact of these separate and interactive factors on arrhythmia generation. This approach is of great importance in examining arrhythmia mechanisms and potential therapeutic targets in diseases such as HF and AF where there is combined patchy t-tubule loss and altered expression and distribution of key Ca^{2+} handling proteins.

4.2 Limitations and Future Work

In recent years, more advanced super-resolution imaging techniques have allowed the development of spatially detailed Ca^{2+} signaling models to replicate nanodomain structures within myocytes and reveal the fundamental structure-function relationship between ultrastructure (e.g., TATS) and Ca^{2+} handling protein properties in both health and disease, from the nanometer to the whole-heart scale (Colman *et al.*, 2022). The beauty of mechanistic

models is to enable us to comprehensively test hypotheses and explore fundamental theories when developing new therapies (Grandi & Maleckar, 2016), which will be further enhanced by increased computational power and improved experimental imaging techniques.

While our model provides novel insight into spatially-detailed Ca^{2+} handling and its governing by the TATS and changes in Ca^{2+} handling proteins, there are limitations in its scope, as discussed in detail in Chapters 2 and 3. Briefly, our model does not account for other sources of subcellular heterogeneity, including differences in ca diffusion and compartmentalization in coupled vs. uncoupled CRUs. Furthermore, an obvious next step will be to integrate our model with descriptions of PKA- and CaMKII-signaling, which importantly regulate Ca^{2+} handling. Indeed, RyR phosphorylation was reported to be higher near TATS, which could be another source of subcellular Ca^{2+} heterogeneity. In addition, our model could evolve to address several unresolved questions:

1) Substantial sex differences have been reported in the prevalence, pathophysiology, treatment, and prognosis of AF (Tadros *et al.*, 2014; Ko *et al.*, 2016; Gillis, 2017; Magnussen *et al.*, 2017; Andrade *et al.*, 2018; Odening *et al.*, 2019). Knowledge of sex differences in the underlying arrhythmogenic substrate may improve therapy. Recent experimental studies revealed differences in cell geometry, TATS density, and expression, function, and phosphorylation status of Ca^{2+} handling proteins in female vs. male atrial myocytes, and in their remodeling in AF (Yue *et al.*, 2017; Herraiz-Martínez *et al.*, 2022). However, how these sex-dependent differences contribute (individually or collectively) to arrhythmia propensity in females vs. males remains unknown. We plan to use our new human atrial myocyte model discussed in Chapters 2 and 3 to integrate these sex-specific features and build sex-specific models of both nSR and AF conditions (Zhang *et al.*, 2022). We also plan to conduct a systematic parametric study to understand the precise contribution of

each sex-dependent change (i.e., TATS density, cell dimension, and Ca^{2+}-handling protein expression or function) to SCR generation and Ca^{2+} spark properties. This study will interrogate the interactive contributions of subcellular structural and ionic sex differences to intracellular Ca^{2+} instability and provide novel model-based mechanistic insight that may guide future therapeutic sex-specific anti-AF strategies.

2) This model also has the potential to be integrated with more subcellular spatial details, such as the local distribution of Ca^{2+}-handling proteins and TATS determined by super-resolution microscopy (Kohl *et al.*, 2013; Walker *et al.*, 2014; Brandenburg *et al.*, 2016; Sutanto *et al.*, 2018; Galice *et al.*, 2018; Pritchard *et al.*, 2018).
3) Our model assumes a constant extracellular ion concentration. However, during myocyte contraction and relaxation external fluid exchange occurs via distortion of the TATS that aids in pumping the fluid to accelerate the diffusion (Savio-Galimberti *et al.*, 2008; Rog-Zielinska *et al.*, 2021*b*). Previous computational studies have illustrated the effects of extracellular ion dynamics (not only Ca^{2+} but also Na^{+} and K^{+}) fluid in TATS (Pásek *et al.*, 2006, 2008*a*, 2008*c*) and in intercalated disk (Moise *et al.*, 2021), which could be integrated into our model.
4) Na^{+} dynamics have been shown to regulate Ca^{2+} and voltage dynamics in a common-pool atrial myocyte model (Grandi *et al.*, 2011) and in a super-resolution model of Ca^{2+} spark dyad-space ventricular myocyte model (Chu *et al.*, 2016). The model discussed in this dissertation could be further adapted to include subcellular Na^{+} dynamics to understand the interaction between Na^{+} and Ca^{2+}.
5) Ca^{2+} signaling regulates electrophysiology and contractility (Bers, 2002). Computational models integrated with descriptions of myofilament contraction

allow us to evaluate the effects of additional drug targets and more complex mechanisms (Negroni *et al.*, 2015). Our model also has the potential to be extended to include modulation of the myofilaments and thus cell contractility.

6) Tissue/organ computational models commonly show more translational insights into clinical treatments, especially precise medicine, compared to single myocyte models (Trayanova *et al.*, 2020; Colman *et al.*, 2022). In both health and disease atrial tissue, there is a variety of TATS within cells and TATS may contribute to organ-level phenomena. As a result, tissue models could help to address how spatial heterogeneity in TATS affects tissue- and organ-level function.
7) To reduce the demand for computational power for running tissue simulations, simpler phenomenological and statistical models are developed to replicate major EC coupling properties in each cell by using much fewer ODEs (Shiferaw *et al.*, 2018, 2020*a*; Colman, 2019). In these settings, the dissertation work could be used to develop a new phenomenological and/or statistical model of Ca^{2+} release with varying TATS for use in tissue simulations.

4.3 Translational Relevance

Computational models of cardiac electrophysiology have interacted with experimental research in a 'ping-pong' interplay to provide real-world impact (Heijman *et al.*, 2021), such as simulation-guided ablation of routine pulmonary vein isolation in AF rhythm-control (ClinicalTrials.gov NCT04101539) and cardiac safety screening by cardiomyocyte models ('Comprehensive In Vitro Proarrhythmia Assay') by the Food and Drug Administration and pharmaceutical industry (Heijman & Dobrev, 2022). The clinical understanding of ectopic activity-promoting Ca^{2+}-handling abnormalities remains unclear and the lack of approved drugs targeting individual Ca^{2+}-handling abnormalities limits the direct evaluation in patients

(Dobrev & Wehrens, 2017). A recent clinical study indicates that R-propafenone (a drug that inhibits cardiac RyRs) and S-propafenone (a drug that does not inhibit cardiac RyRs) have no significant difference in AF inducibility of patients scheduled for AF ablation (Shoemaker *et al.*, 2022). However, the Na^+-channel and β-adrenoceptor-blocking effects of propafenone make it challenging to evaluate these findings. The model developed in this dissertation work represents a useful tool to assess the distinct mechanisms underlying the beneficial (and adverse) effects of treatment. Simulation of this model allows applying systematic approaches to translate implications of subcellular-scale Ca^{2+}-signaling remodeling to organ-level arrhythmia.

Given that t-tubule loss in disease is structurally and functionally detrimental to Ca^{2+} handling and arrhythmia susceptibility, we will briefly discuss the significance of restoring TATS and Ca^{2+}-handling protein properties and potential target proteins for drug development, with the focus on both TATS preservation and restoration and Ca^{2+}-handling abnormality. Several proteins have been implicated in TATS regulation, such as Junctophilin 2 (JPH2), Amphiphysin II (AMPII, BIN-1), Telethonin (TCAP), and Caveolin 3 (CAV3), with their respective roles in biogenesis, organization, and preservation of TATS still under investigation.

1) JPH2 has been shown to facilitate the dyad formation (Takeshima *et al.*, 2000; Jayasinghe *et al.*, 2012) by anchoring SR to t-tubules. Lower expression of JPH2 reduces the number of dyads and disrupts tubular organization and formation, thus impairing Ca^{2+} handling and cell contractility (van Oort *et al.*, 2011; Chen *et al.*, 2013; Reynolds *et al.*, 2013). Whereas lack of JPH2 is detrimental to the t-tubule organization, t-tubules still form in its absence (Chen *et al.*, 2013; Reynolds *et al.*, 2013; Caldwell *et al.*, 2014). In addition, loss of t-tubules in the HF atria is not associated with reduced JPH2 expression (Caldwell *et al.*, 2014), and as such JPH2 may play a key role in t-tubule regulation but not initial formation.

2) AMPII/BIN-1 is concentrated in tubules (Butler *et al.*, 1997; Lee *et al.*, 2002; Hong *et al.*, 2014) and has been shown to induce t-tubule formation in vitro (Caldwell *et al.*, 2014; Zhou *et al.*, 2021). AMPII knockdown decreases the tubular density, thus disrupting Ca^{2+} signaling and cell contraction (Hong *et al.*, 2014; Caldwell *et al.*, 2014). Expression of AMPII is reduced in HF and is associated with a reduced t-tubule density (Caldwell *et al.*, 2014). In addition to its role in the t-tubule formation, AMPII also assists LCC trafficking to the t-tubule membrane, and as such downregulation of AMPII as in HF has a compounding effect on Ca^{2+} handling (Hong *et al.*, 2010).
3) TCAP was reported to facilitate tubule maintenance by mediating the association between tubules and the 'stretch sensitive complex' along the z-disc (Knöll *et al.*, 2002; Ibrahim *et al.*, 2013). Both TCAP disruption and knockout induce abnormal tubules and dysregulation of the Ca^{2+} signaling (Zhang *et al.*, 2009; Ibrahim *et al.*, 2013).
4) CAV3 is a cardiac-specific caveolin protein in the sarcolemma and tubules, associated with JPH2 (Minamisawa *et al.*, 2004). Though t-tubules are still formed in CAV3 knock-out they are disordered and longitudinally oriented vs control (Galbiati *et al.*, 2001).

While all these mentioned proteins regulate TATS in varying aspects, BIN1 has emerged as a promising candidate for TATS repair. Circulating cardiac BIN1 has been identified as a biomarker correlating with cardiovascular risk and severity of remodeling in humans (Nikolova *et al.*, 2018; Hitzeman *et al.*, 2020). In animal studies, exogenous BIN1 delivered has also been reported to both protect hearts before HF induction and restore cardiac function under pre-existing failure (Li *et al.*, 2020; Liu *et al.*, 2020), and gene therapy involving JPH2 has similarly improved outcomes in HF (Reynolds *et al.*, 2013). As such, both BIN1 and

JPH2 have the potential to limit TATS remodeling and thus maintain Ca^{2+} handling. Some well-established clinic therapies also benefit the reversal of TATS remodeling. Both mechanical unloading and biventricular pacing improve the homogeneity of TATS, RyRs, and Ca^{2+} release in the HF (Ibrahim *et al.*, 2012; Sachse *et al.*, 2012; Li *et al.*, 2015). The treatment using tadalafil, a PDE5 inhibitor typically used to treat erectile dysfunction, has similar effects of restoration, which is associated with varied BIN1 expression-level (Lawless *et al.*, 2019). These widely used treatments could be ideal treatments for reversing ultrastructural remodeling in HF. The model built in this dissertation work deepens our mechanistic understanding of how TATS regulate SCR-mediated arrhythmia and sheds new insight into developing ultrastructure-targeted anti-arrhythmia therapeutic strategies. Indeed, based on all these clinical and experimental observations, the quantitative evaluation of the effects of TATS loss on Ca^{2+} handling and electrophysiology in Chapter 2 can inform the preclinical development of human atria-specific therapy.

The properties of Ca^{2+}-handling proteins are also changed in disease and contribute to the pathophysiology (Dobrev & Wehrens, 2017; Denham *et al.*, 2018). Although many targets (e.g., expression and phosphorylation of ion channels, transporters, and pumps, and organ-level structures changes) have been studied (Grandi & Maleckar, 2016), the heterogeneous subcellular distribution of Ca^{2+}-handling proteins has not yet been treated as a potential treatment target. While TATS repair significantly benefits normal Ca^{2+} handling, dyadic disruption impairs Ca^{2+} dynamics in HF ventricle, even with TATS remaining (Lipsett *et al.*, 2019). In addition, BIN1 and JPH2 also regulate LCCs and RyRs trafficking (Hong *et al.*, 2010; Jayasinghe *et al.*, 2012; Fu *et al.*, 2016; Gross *et al.*, 2021), thus regulating the dyadic localization of Ca^{2+} handling protein and medicate Ca^{2+} signaling. The disruption of subcellular localization of Ca^{2+}-handling proteins (and dyadic/SR ultrastructure) may impair Ca^{2+} signaling. Recently, in human atrial myocytes from both nSR and AF patients, RyR and CSQ

were found more densely expressed near the cell periphery vs. the cell interior (Herraiz-Martínez et al., 2022). This is similar to what has previously been shown in rat atrial myocytes, where RyR-CSQ colocalization was reduced in the cell interior vs. periphery (Schulson et al., 2011). The ultrastructural adaptive differences in atrial cells from neonatal vs adult sheep (i.e., enlarged surface SR and larger, more closely spaced surface and central RyR clusters) enhance Ca^{2+} release at the sarcolemma and aid Ca^{2+} wave propagation to compensate for reduced TATS density (Smith et al., 2022). Consistent with these experimental observations, computational studies also highlighted the important role of Ca^{2+}-handling protein localization in the Ca^{2+} dynamics (Sutanto *et al.*, 2018; Galice *et al.*, 2018). Aligning with all these findings, Chapter 3 quantitatively evaluates the detrimental impact of expression loss and redistribution of Ca^{2+}-handling proteins in addition to TATS loss that is similar to that typically observed in the disease, thus revealing the interactive arrhythmogenic effects of TATS loss and varied Ca^{2+}-handling protein properties. As such, independently and collectively, spatial targeting of TATS and Ca^{2+}-handling protein restoration may be ideal therapeutic targets to reduce arrhythmias in HF and AF. Understanding how these numerous factors integrate to modulate Ca^{2+} handling and affect cardiac myocyte physiology can yield valuable mechanistic insights that can lead to the development of therapeutic strategies for treating cardiac disease.

4.4 Concluding Remarks

This dissertation has facilitated the development of a physiology-based computational 3D model of a human atrial myocyte coupling electrophysiology and Ca^{2+} dynamics with subcellular spatial details. It demonstrates that independent and combined subcellular structural and Ca^{2+}-handling protein remodeling (i.e., disruption of TATS and altered expression and localization of Ca^{2+}-handling proteins) have individual and collective effects on Ca^{2+}-driven arrhythmias. Insight from this detailed novel model suggests that subcellular structural

remodeling is an ideal target for anti-arrhythmia therapeutics. Further development of this in-silico platform will provide significant additional mechanistic insight into arrhythmia mechanisms in the healthy and diseased atrium.

Reference

Allbritton NL, Meyer T & Stryer L (1992). Range of messenger action of calcium ion and inositol 1,4,5-trisphosphate. *Science* **258,** 1812–1815.

Alvarez-Lacalle E, Echebarria B, Spalding J & Shiferaw Y (2015). Calcium Alternans is Due to an Order-Disorder Phase Transition in Cardiac Cells. *Phys Rev Lett* **114,** 108101.

Andersson T, Magnuson A, Bryngelsson I-L, Frøbert O, Henriksson KM, Edvardsson N & Poçi D (2013). All-cause mortality in 272 186 patients hospitalized with incident atrial fibrillation 1995–2008: a Swedish nationwide long-term case–control study. *Eur Heart J* **34,** 1061–1067.

Andrade J, Khairy P, Dobrev D & Nattel S (2014). The Clinical Profile and Pathophysiology of Atrial Fibrillation. *Circ Res* **114,** 1453–1468.

Andrade JG, Deyell MW, Lee AYK & Macle L (2018). Sex Differences in Atrial Fibrillation. *Can J Cardiol* **34,** 429–436.

Annunziato L, Secondo A, Pignataro G, Scorziello A & Molinaro P (2020). New perspectives for selective NCX activators in neurodegenerative diseases. *Cell Calcium* **87,** 102170.

Anon (2022). File:Heart diagram-en.svg. *Wikipedia*. Available at: https://en.wikipedia.org/w/index.php?title=File:Heart_diagram-en.svg&oldid=1087408793 [Accessed October 17, 2022].

Anon (n.d.). File:SinusRhythmLabels.svg - Wikipedia. Available at: https://commons.wikimedia.org/wiki/File:SinusRhythmLabels.svg [Accessed October 17, 2022].

Antoons G, Willems R & Sipido KR (2012). Alternative strategies in arrhythmia therapy: Evaluation of Na/Ca exchange as an anti-arrhythmic target. *Pharmacol Ther* **134,** 26–42.

Arora R, Aistrup GL, Supple S, Frank C, Singh J, Tai S, Zhao A, Chicos L, Marszalec W, Guo A, Song L-S & Wasserstrom JA (2017). Regional distribution of T-tubule density in left and right atria in dogs. *Heart Rhythm* **14,** 273–281.

Asfaw M, Alvarez-Lacalle E & Shiferaw Y (2013). The Timing Statistics of Spontaneous Calcium Release in Cardiac Myocytes. *PLOS ONE* **8,** e62967.

Balijepalli RC, Lokuta AJ, Maertz NA, Buck JM, Haworth RA, Valdivia HH & Kamp TJ (2003). Depletion of T-tubules and specific subcellular changes in sarcolemmal proteins in tachycardia-induced heart failure. *Cardiovasc Res* **59,** 67–77.

Beavers DL, Wang W, Ather S, Voigt N, Garbino A, Dixit SS, Landstrom AP, Li N, Wang Q, Olivotto I, Dobrev D, Ackerman MJ & Wehrens XHT (2013). Mutation E169K in

Junctophilin-2 Causes Atrial Fibrillation Due to Impaired RyR2 Stabilization. *J Am Coll Cardiol* **62,** 2010–2019.

Benson AP, Stevenson-Cocks HJ, Whittaker DG, White E & Colman MA (2021). Multi-scale approaches for the simulation of cardiac electrophysiology: II – Tissue-level structure and function. *Methods* **185,** 60–81.

Bers D (2001). *Excitation-Contraction Coupling and Cardiac Contractile Force*. Springer Science & Business Media.

Bers DM (2002). Cardiac excitation–contraction coupling. *Nature* **415,** 198–205.

Bers DM & Grandi E (2009). Calcium/Calmodulin-dependent Kinase II Regulation of Cardiac Ion Channels. *J Cardiovasc Pharmacol* **54,** 180–187.

Bers DM & Grandi E (2011). Human Atrial Fibrillation: insights from computational electrophysiological models. *Trends Cardiovasc Med* **21,** 145–150.

Bers DM & Morotti S (2014). Ca2+ current facilitation is CaMKII-dependent and has arrhythmogenic consequences. *Front Pharmacol*; DOI: 10.3389/fphar.2014.00144.

Bers DM & Shannon TR (2013). Calcium Movements Inside the Sarcoplasmic Reticulum of Cardiac Myocytes. *J Mol Cell Cardiol* **58,** 59–66.

Biesmans L, Macquaide N, Heinzel FR, Bito V, Smith GL & Sipido KR (2011). Subcellular Heterogeneity of Ryanodine Receptor Properties in Ventricular Myocytes with Low T-Tubule Density. *PLOS ONE* **6,** e25100.

Blatter LA, Kockskämper J, Sheehan KA, Zima AV, Hüser J & Lipsius SL (2003). Local calcium gradients during excitation–contraction coupling and alternans in atrial myocytes. *J Physiol* **546,** 19–31.

Blatter LA & Niggli E (1998). Confocal nearmmembrane detection of calcium in cardiac myocytes. *Cell Calcium* **23,** 269–279.

Bosch RF, Zeng X, Grammer JB, Popovic K, Mewis C & Kühlkamp V (1999). Ionic mechanisms of electrical remodeling in human atrial fibrillation. *Cardiovasc Res* **44,** 121–131.

Boyd D, Workman A & Macquaide N (2018). Super Resolution Imaging of Ryanodine Receptor Cluster Morphology in Rabbit and Human Atrial Myocytes. *Biophys J* **114,** 621a.

Brandenburg S, Kohl T, Williams GSB, Gusev K, Wagner E, Rog-Zielinska EA, Hebisch E, Dura M, Didié M, Gotthardt M, Nikolaev VO, Hasenfuss G, Kohl P, Ward CW, Lederer WJ & Lehnart SE (2016). Axial tubule junctions control rapid calcium signaling in atria. *J Clin Invest* **126,** 3999–4015.

Brandenburg S, Pawlowitz J, Eikenbusch B, Peper J, Kohl T, Mitronova GY, Sossalla S, Hasenfuss G, Wehrens XHT, Kohl P, Rog-Zielinska EA & Lehnart SE (2019). Junctophilin-2 expression rescues atrial dysfunction through polyadic junctional membrane complex biogenesis. *JCI Insight* **4(12),** e127116.

Brandenburg S, Pawlowitz J, Fakuade FE, Kownatzki-Danger D, Kohl T, Mitronova GY, Scardigli M, Neef J, Schmidt C, Wiedmann F, Pavone FS, Sacconi L, Kutschka I, Sossalla S, Moser T, Voigt N & Lehnart SE (2018). Axial Tubule Junctions Activate Atrial Ca2+ Release Across Species. *Front Physiol* **9,** 1227.

Brette F, Despa S, Bers D & Orchard C (2005). Spatiotemporal characteristics of SR Ca uptake and release in detubulated rat ventricular myocytes. *J Mol Cell Cardiol* **39,** 804–812.

Brette F, Sallé L & Orchard CH (2006). Quantification of Calcium Entry at the T-Tubules and Surface Membrane in Rat Ventricular Myocytes. *Biophys J* **90,** 381–389.

Burashnikov A & Antzelevitch C (2010). New developments in atrial antiarrhythmic drug therapy. *Nat Rev Cardiol* **7,** 139–148.

Butler MH, David C, Ochoa G-C, Freyberg Z, Daniell L, Grabs D, Cremona O & Camilli PD (1997). Amphiphysin II (SH3P9; BIN1), a Member of the Amphiphysin/Rvs Family, Is Concentrated in the Cortical Cytomatrix of Axon Initial Segments and Nodes of Ranvier in Brain and around T Tubules in Skeletal Muscle. *J Cell Biol* **137,** 1355–1367.

Caldwell JL, Smith CER, Taylor RF, Kitmitto A, Eisner DA, Dibb KM & Trafford AW (2014). Dependence of Cardiac Transverse Tubules on the BAR Domain Protein Amphiphysin II (BIN-1). *Circ Res* **115,** 986–996.

Campos FO, Shiferaw Y, Prassl AJ, Boyle PM, Vigmond EJ & Plank G (2015). Stochastic spontaneous calcium release events trigger premature ventricular complexes by overcoming electrotonic load. *Cardiovasc Res* **107,** 175–183.

Campos FO, Shiferaw Y, Vigmond EJ & Plank G (2017). Stochastic spontaneous calcium release events and sodium channelopathies promote ventricular arrhythmias. *Chaos Interdiscip J Nonlinear Sci* **27,** 093910.

Campos FO, Shiferaw Y, Weber dos Santos R, Plank G & Bishop MJ (2018). Microscopic Isthmuses and Fibrosis Within the Border Zone of Infarcted Hearts Promote Calcium-Mediated Ectopy and Conduction Block. *Front Phys*. Available at: https://www.frontiersin.org/articles/10.3389/fphy.2018.00057 [Accessed October 14, 2022].

Campos FO, Whitaker J, Neji R, Roujol S, O'Neill M, Plank G & Bishop MJ (2019). Factors Promoting Conduction Slowing as Substrates for Block and Reentry in Infarcted Hearts. *Biophys J* **117,** 2361–2374.

Cannell MB, Crossman DJ & Soeller C (2006). Effect of changes in action potential spike configuration, junctional sarcoplasmic reticulum micro-architecture and altered t-tubule structure in human heart failure. *J Muscle Res Cell Motil* **27,** 297–306.

Cantalapiedra IR, Alvarez-Lacalle E, Peñaranda A & Echebarria B (2017). Minimal model for calcium alternans due to SR release refractoriness. *Chaos Interdiscip J Nonlinear Sci* **27,** 093928.

Carl SL, Felix K, Caswell AH, Brandt NR, Ball WJ, Vaghy PL, Meissner G & Ferguson DG (1995). Immunolocalization of sarcolemmal dihydropyridine receptor and sarcoplasmic

reticular triadin and ryanodine receptor in rabbit ventricle and atrium. *J Cell Biol* **129,** 673–682.

Chase A & Orchard CH (2011). Ca efflux via the sarcolemmal Ca ATPase occurs only in the t-tubules of rat ventricular myocytes. *J Mol Cell Cardiol* **50,** 187–193.

Chen B, Guo A, Zhang C, Chen R, Zhu Y, Hong J, Kutschke W, Zimmerman K, Weiss RM, Zingman L, Anderson ME, Wehrens XHT & Song L-S (2013). Critical roles of junctophilin-2 in T-tubule and excitation–contraction coupling maturation during postnatal development. *Cardiovasc Res* **100,** 54–62.

Chen B, Zhang C, Guo A & Song L-S (2015). In situ single photon confocal imaging of cardiomyocyte T-tubule system from Langendorff-perfused hearts. *Front Physiol* **6,** 134.

Chen W, Aistrup G, Wasserstrom JA & Shiferaw Y (2011). A mathematical model of spontaneous calcium release in cardiac myocytes. *Am J Physiol-Heart Circ Physiol* **300,** H1794–H1805.

Chen W, Asfaw M & Shiferaw Y (2012). The Statistics of Calcium-Mediated Focal Excitations on a One-Dimensional Cable. *Biophys J* **102,** 461–471.

Cheng H, Lederer WJ & Cannell MB (1993). Calcium Sparks: Elementary Events Underlying Excitation-Contraction Coupling in Heart Muscle. *Science* **262,** 740–744.

Chen-Izu Y, McCulle SL, Ward CW, Soeller C, Allen BM, Rabang C, Cannell MB, Balke CW & Izu LT (2006). Three-Dimensional Distribution of Ryanodine Receptor Clusters in Cardiac Myocytes. *Biophys J* **91,** 1–13.

Christ T., Boknik P., Wöhrl S., Wettwer E., Graf E.M., Bosch R.F., Knaut M., Schmitz W., Ravens U., & Dobrev D. (2004). L-Type Ca2+ Current Downregulation in Chronic Human Atrial Fibrillation Is Associated With Increased Activity of Protein Phosphatases. *Circulation* **110,** 2651–2657.

Chu L, Greenstein JL & Winslow RL (2016). Modeling Na+-Ca2+ exchange in the heart: Allosteric activation, spatial localization, sparks and excitation-contraction coupling. *J Mol Cell Cardiol* **99,** 174–187.

Chugh SS, Havmoeller R, Narayanan K, Singh D, Rienstra M, Benjamin EJ, Gillum RF, Kim Y-H, McAnulty JH, Zheng Z-J, Forouzanfar MH, Naghavi M, Mensah GA, Ezzati M & Murray CJL (2014). Worldwide Epidemiology of Atrial Fibrillation. *Circulation* **129,** 837–847.

Clancy CE & Rudy Y (1999). Linking a genetic defect to its cellular phenotype in a cardiac arrhythmia. *Nature* **400,** 566–569.

Clarke JD, Caldwell JL, Horn MA, Bode EF, Richards MA, Hall MCS, Graham HK, Briston SJ, Greensmith DJ, Eisner DA, Dibb KM & Trafford AW (2015). Perturbed atrial calcium handling in an ovine model of heart failure: Potential roles for reductions in the L-type calcium current. *J Mol Cell Cardiol* **79,** 169–179.

Colman MA (2019). Arrhythmia mechanisms and spontaneous calcium release: Bi-directional coupling between re-entrant and focal excitation. *PLOS Comput Biol* **15,** e1007260.

Colman MA, Alvarez-Lacalle E, Echebarria B, Sato D, Sutanto H & Heijman J (2022). Multi-Scale Computational Modeling of Spatial Calcium Handling From Nanodomain to Whole-Heart: Overview and Perspectives. *Front Physiol*. Available at: https://www.frontiersin.org/article/10.3389/fphys.2022.836622 [Accessed March 11, 2022].

Colman MA, Perez Alday EA, Holden AV & Benson AP (2017). Trigger vs. Substrate: Multi-Dimensional Modulation of QT-Prolongation Associated Arrhythmic Dynamics by a hERG Channel Activator. *Front Physiol*. Available at: https://www.frontiersin.org/articles/10.3389/fphys.2017.00757 [Accessed October 14, 2022].

Colman MA, Sarathy PP, MacQuiaide N & Workman AJ (2016*a*). A new model of the human atrial myocyte with variable T-tubule organization for the study of atrial fibrillation. In *2016 Computing in Cardiology Conference (CinC)*, pp. 221–224.

Colman MA, Sarathy PP, MacQuiaide N & Workman AJ (2016*b*). A new model of the human atrial myocyte with variable T-tubule organization for the study of atrial fibrillation. In *2016 Computing in Cardiology Conference (CinC)*, pp. 221–224.

Conesa D, Echebarria B, Peñaranda A, Cantalapiedra IR, Shiferaw Y & Alvarez-Lacalle E (2020). Two-variable nullcline analysis of ionic general equilibrium predicts calcium homeostasis in ventricular myocytes. *PLOS Comput Biol* **16,** e1007572.

Cordeiro JM, Spitzer KW, Giles WR, Ershler PE, Cannell MB & Bridge JHB (2001). Location of the initiation site of calcium transients and sparks in rabbit heart Purkinje cells. *J Physiol* **531,** 301–314.

Courtemanche M, Ramirez RJ & Nattel S (1998). Ionic mechanisms underlying human atrial action potential properties: insights from a mathematical model. *Am J Physiol-Heart Circ Physiol* **275,** H301–H321.

Dagum L & Menon R (1998). OpenMP: An Industry-Standard API for Shared-Memory Programming. *IEEE Comput Sci Eng* **5,** 46–55.

Dan G-A & Dobrev D (2018). Antiarrhythmic drugs for atrial fibrillation: Imminent impulses are emerging. *IJC Heart Vasc* **21,** 11–15.

Denham NC, Pearman CM, Caldwell JL, Madders GWP, Eisner DA, Trafford AW & Dibb KM (2018). Calcium in the Pathophysiology of Atrial Fibrillation and Heart Failure. *Front Physiol* **9,** 1380.

Despa S, Brette F, Orchard CH & Bers DM (2003). Na/Ca Exchange and Na/K-ATPase Function Are Equally Concentrated in Transverse Tubules of Rat Ventricular Myocytes. *Biophys J* **85,** 3388–3396.

Dibb KM, Clarke JD, Horn MA, Richards MA, Graham HK, Eisner DA & Trafford AW (2009). Characterization of an Extensive Transverse Tubular Network in Sheep Atrial Myocytes and its Depletion in Heart Failure. *Circ Heart Fail* **2,** 482–489.

Dobrev D & Ravens U (2003). Remodeling of cardiomyocyte ion channels in human atrial fibrillation. *Basic Res Cardiol* **98,** 137–148.

Dobrev D, Voigt N & Wehrens XHT (2011). The ryanodine receptor channel as a molecular motif in atrial fibrillation: pathophysiological and therapeutic implications. *Cardiovasc Res* **89,** 734–743.

Dobrev D & Wehrens XHT (2017). Calcium-mediated cellular triggered activity in atrial fibrillation. *J Physiol* **595,** 4001–4008.

Dolber PC, Bauman RP, Rembert JC & Greenfield JC (1994). Regional changes in myocyte structure in model of canine right atrial hypertrophy. *Am J Physiol-Heart Circ Physiol* **267,** H1279–H1287.

Donahue BS & Abercrombie RF (1987). Free diffusion coefficient of ionic calcium in cytoplasm. *Cell Calcium* **8,** 437–448.

Dries E, Santiago DJ, Gilbert G, Lenaerts I, Vandenberk B, Nagaraju CK, Johnson DM, Holemans P, Roderick HL, Macquaide N, Claus P & Sipido KR (2018). Hyperactive ryanodine receptors in human heart failure and ischaemic cardiomyopathy reside outside of couplons. *Cardiovasc Res* **114,** 1512–1524.

Dzhura I, Wu Y, Colbran RJ, Balser JR & Anderson ME (2000). Calmodulin kinase determines calcium-dependent facilitation of L-type calcium channels. *Nat Cell Biol* **2,** 173–177.

ecgpedia (2011). *English: Shapes of the cardiac action potential in the heart*. Available at: https://commons.wikimedia.org/wiki/File:Shapes_of_the_cardiac_action_potential_in_the_heart.svg [Accessed October 17, 2022].

Eisner DA (2018). Ups and downs of calcium in the heart. *J Physiol* **596,** 19–30.

Eisner DA, Caldwell JL, Kistamás K & Trafford AW (2017). Calcium and Excitation-Contraction Coupling in the Heart. *Circ Res* **121,** 181–195.

El-Armouche A, Boknik P, Eschenhagen T, Carrier L, Knaut M, Ravens U & Dobrev D (2006). Molecular Determinants of Altered Ca2+ Handling in Human Chronic Atrial Fibrillation. *Circulation* **114,** 670–680.

Ellinwood N, Dobrev D, Morotti S & Grandi E (2017*a*). In Silico Assessment of Efficacy and Safety of IKur Inhibitors in Chronic Atrial Fibrillation: Role of Kinetics and State-Dependence of Drug Binding. *Front Pharmacol*. Available at: https://www.frontiersin.org/articles/10.3389/fphar.2017.00799 [Accessed October 3, 2022].

Ellinwood N, Dobrev D, Morotti S & Grandi E (2017*b*). Revealing kinetics and state-dependent binding properties of IKur-targeting drugs that maximize atrial fibrillation selectivity. *Chaos Interdiscip J Nonlinear Sci* **27,** 093918.

Fabiato A (1983). Calcium-induced release of calcium from the cardiac sarcoplasmic reticulum. *Am J Physiol-Cell Physiol* **245,** C1–C14.

Faggioni M, Savio-Galimberti E, Venkataraman R, Hwang HS, Kannankeril PJ, Darbar D & Knollmann BC (2014). Suppression of Spontaneous Ca Elevations Prevents Atrial Fibrillation in Calsequestrin 2-Null Hearts. *Circ Arrhythm Electrophysiol* **7,** 313–320.

Fill M & Gillespie D (2018). Ryanodine Receptor Open Times Are Determined in the Closed State. *Biophys J* **115,** 1160–1165.

Freedman B, Potpara TS & Lip GYH (2016). Stroke prevention in atrial fibrillation. *The Lancet* **388,** 806–817.

Frisk M, Koivumäki JT, Norseng PA, Maleckar MM, Sejersted OM & Louch WE (2014). Variable t-tubule organization and Ca2+ homeostasis across the atria. *Am J Physiol-Heart Circ Physiol* **307,** H609–H620.

Fu Y, Shaw SA, Naami R, Vuong CL, Basheer WA, Guo X & Hong T (2016). Isoproterenol Promotes Rapid Ryanodine Receptor Movement to Bridging Integrator 1 (BIN1)–Organized Dyads. *Circulation* **133,** 388–397.

Gadeberg HC, Bond RC, Kong CHT, Chanoit GP, Ascione R, Cannell MB & James AF (2016). Heterogeneity of T-Tubules in Pig Hearts. *PLOS ONE* **11,** e0156862.

Gadeberg HC, Kong CHT, Bryant SM, James AF & Orchard CH (2017). Sarcolemmal distribution of I_{Ca} and I_{NCX} and Ca^{2+} autoregulation in mouse ventricular myocytes. *Am J Physiol-Heart Circ Physiol* **313,** H190–H199.

Galbiati F, Engelman JA, Volonte D, Zhang XL, Minetti C, Li M, Hou H, Kneitz B, Edelmann W & Lisanti MP (2001). Caveolin-3 Null Mice Show a Loss of Caveolae, Changes in the Microdomain Distribution of the Dystrophin-Glycoprotein Complex, and T-tubule Abnormalities*. *J Biol Chem* **276,** 21425–21433.

Galice S, Xie Y, Yang Y, Sato D & Bers DM (2018). Size Matters: Ryanodine Receptor Cluster Size Affects Arrhythmogenic Sarcoplasmic Reticulum Calcium Release. *J Am Heart Assoc* **7,** e008724.

Gaspo R, Bosch RF, Bou-Abboud E & Nattel S (1997). Tachycardia-Induced Changes in Na+ Current in a Chronic Dog Model of Atrial Fibrillation. *Circ Res* **81,** 1045–1052.

Gassanov N, Brandt MC, Michels G, Lindner M, Er F & Hoppe UC (2006). Angiotensin II-induced changes of calcium sparks and ionic currents in human atrial myocytes: Potential role for early remodeling in atrial fibrillation. *Cell Calcium* **39,** 175–186.

Gillis AM (2017). Atrial Fibrillation and Ventricular Arrhythmias. *Circulation* **135,** 593–608.

Glukhov AV, Balycheva M, Sanchez-Alonso JL, Ilkan Z, Alvarez-Laviada A, Bhogal N, Diakonov I, Schobesberger S, Sikkel MB, Bhargava A, Faggian G, Punjabi PP, Houser SR & Gorelik J (2015). Direct Evidence for Microdomain-Specific Localization and Remodeling of Functional L-Type Calcium Channels in Rat and Human Atrial Myocytes. *Circulation* **132,** 2372–2384.

Gómez AM, Valdivia HH, Cheng H, Lederer MR, Santana LF, Cannell MB, McCune SA, Altschuld RA & Lederer WJ (1997). Defective Excitation-Contraction Coupling in Experimental Cardiac Hypertrophy and Heart Failure. *Science* **276,** 800–806.

González de la Fuente M, Barana A, Gómez R, Amorós I, Dolz-Gaitón P, Sacristán S, Atienza F, Pita A, Pinto Á, Fernández-Avilés F, Caballero R, Tamargo J & Delpón E (2013). Chronic atrial fibrillation up-regulates β1-Adrenoceptors affecting repolarizing currents and action potential duration. *Cardiovasc Res* **97,** 379–388.

Grandi E, Dobrev D & Heijman J (2019). Computational modeling: What does it tell us about atrial fibrillation therapy? *Int J Cardiol* **287,** 155–161.

Grandi E & Maleckar MM (2016). Anti-arrhythmic strategies for atrial fibrillation: The role of computational modeling in discovery, development, and optimization. *Pharmacol Ther* **168,** 126–142.

Grandi E, Pandit SV, Voigt N, Workman AJ, Dobrev D, Jalife J & Bers DM (2011). Human Atrial Action Potential and Ca2+ Model. *Circ Res* **109,** 1055–1066.

Greene D & Shiferaw Y (2021). Mechanistic link between CaM-RyR2 interactions and the genesis of cardiac arrhythmia. *Biophys J* **120,** 1469–1482.

Greiser M, Kerfant B-G, Williams GSB, Voigt N, Harks E, Dibb KM, Giese A, Meszaros J, Verheule S, Ravens U, Allessie MA, Gammie JS, Velden J van der, Lederer WJ, Dobrev D & Schotten U (2014). Tachycardia-induced silencing of subcellular Ca^{2+} signaling in atrial myocytes. *J Clin Invest* **124,** 4759–4772.

Gross P et al. (2021). Interaction of the Joining Region in Junctophilin-2 With the L-Type Ca2+ Channel Is Pivotal for Cardiac Dyad Assembly and Intracellular Ca2+ Dynamics. *Circ Res* **128,** 92–114.

Guo A, Zhang C, Wei S, Chen B & Song L-S (2013). Emerging mechanisms of T-tubule remodelling in heart failure. *Cardiovasc Res* **98,** 204–215.

Györke I & Györke S (1998). Regulation of the Cardiac Ryanodine Receptor Channel by Luminal Ca 2+ Involves Luminal Ca 2+ Sensing Sites. *Biophys J* **75,** 2801–2810.

Györke I, Hester N, Jones LR & Györke S (2004). The Role of Calsequestrin, Triadin, and Junctin in Conferring Cardiac Ryanodine Receptor Responsiveness to Luminal Calcium. *Biophys J* **86,** 2121–2128.

Hammer KP, Ljubojevic S, Ripplinger CM, Pieske BM & Bers DM (2015). Cardiac myocyte alternans in intact heart: Influence of cell–cell coupling and β-adrenergic stimulation. *J Mol Cell Cardiol* **84,** 1–9.

Heijman J, Abdoust PE, Voigt N, Nattel S & Dobrev D (2016). Computational models of atrial cellular electrophysiology and calcium handling, and their role in atrial fibrillation. *J Physiol* **594,** 537–553.

Heijman J & Dobrev D (2022). Determinants and therapeutic potential of calcium handling abnormalities in atrial fibrillation: what can we learn from computer models? *J Physiol*; DOI: 10.1113/JP283817.

Heijman J, Sutanto H, Crijns HJGM, Nattel S & Trayanova NA (2021). Computational models of atrial fibrillation: achievements, challenges, and perspectives for improving clinical care. *Cardiovasc Res* **117,** 1682–1699.

Hernandez-Hernandez G, Alvarez-Lacalle E & Shiferaw Y (2015). Role of connectivity and fluctuations in the nucleation of calcium waves in cardiac cells. *Phys Rev E* **92,** 052715.

Herraiz-Martínez A, Tarifa C, Jiménez-Sábado V, Llach A, Godoy-Marín H, Colino-Lage H, Nolla-Colomer C, Casabella-Ramon S, Izquierdo-Castro P, Benítez I, Benítez R, Roselló-Díez E, Rodríguez-Font E, Viñolas X, Ciruela F, Cinca J & Hove-Madsen L (2022). Influence of sex on intracellular calcium homoeostasis in patients with atrial fibrillation. *Cardiovasc Res* **118,** 1033–1045.

Hilgemann DW & Noble D (1987). Excitation-contraction coupling and extracellular calcium transients in rabbit atrium: reconstruction of basic cellular mechanisms. *Proc R Soc Lond B Biol Sci* **230,** 163–205.

Hilliard FA, Steele DS, Laver D, Yang Z, Marchand SJL, Chopra N, Piston DW, Huke S & Knollmann BC (2010). Flecainide inhibits arrhythmogenic Ca2+ waves by open state block of ryanodine receptor Ca2+ release channels and reduction of Ca2+ spark mass. *J Mol Cell Cardiol* **48,** 293–301.

Hitzeman TC et al. (2020). cBIN1 Score (CS) Identifies Ambulatory HFrEF Patients and Predicts Cardiovascular Events. *Front Physiol*. Available at: https://www.frontiersin.org/articles/10.3389/fphys.2020.00503 [Accessed October 24, 2022].

Hobai IA & O'Rourke B (2004). The potential of Na+/Ca2+ exchange blockers in the treatment of cardiac disease. *Expert Opin Investig Drugs* **13,** 653–664.

Hodgkin AL & Huxley AF (1952). A quantitative description of membrane current and its application to conduction and excitation in nerve. *J Physiol* **117,** 500–544.

Hohendanner F, Walther S, Maxwell JT, Kettlewell S, Awad S, Smith GL, Lonchyna VA & Blatter LA (2015). Inositol-1,4,5-trisphosphate induced Ca2+ release and excitation–contraction coupling in atrial myocytes from normal and failing hearts. *J Physiol* **593,** 1459–1477.

Hong T, Yang H, Zhang S-S, Cho HC, Kalashnikova M, Sun B, Zhang H, Bhargava A, Grabe M, Olgin J, Gorelik J, Marbán E, Jan LY & Shaw RM (2014). Cardiac BIN1 folds T-tubule membrane, controlling ion flux and limiting arrhythmia. *Nat Med* **20,** 624–632.

Hong T-T, Smyth JW, Gao D, Chu KY, Vogan JM, Fong TS, Jensen BC, Colecraft HM & Shaw RM (2010). BIN1 Localizes the L-Type Calcium Channel to Cardiac T-Tubules. *PLOS Biol* **8,** e1000312.

Hove-Madsen L, Llach A, Bayes-Genís A, Roura S, Font ER, Arís A & Cinca J (2004). Atrial Fibrillation Is Associated With Increased Spontaneous Calcium Release From the Sarcoplasmic Reticulum in Human Atrial Myocytes. *Circulation* **110,** 1358–1363.

Hund TJ & Mohler PJ (2015). Role of CaMKII in cardiac arrhythmias. *Trends Cardiovasc Med* **25,** 392–397.

Hüser J, Lipsius SL & Blatter LA (1996). Calcium gradients during excitation-contraction coupling in cat atrial myocytes. *J Physiol* **494,** 641–651.

Ibrahim M, Navaratnarajah M, Siedlecka U, Rao C, Dias P, Moshkov AV, Gorelik J, Yacoub MH & Terracciano CM (2012). Mechanical unloading reverses transverse tubule remodelling and normalizes local Ca2+-induced Ca2+release in a rodent model of heart failure. *Eur J Heart Fail* **14,** 571–580.

Ibrahim M, Siedlecka U, Buyandelger B, Harada M, Rao C, Moshkov A, Bhargava A, Schneider M, Yacoub MH, Gorelik J, Knöll R & Terracciano CM (2013). A critical role for Telethonin in regulating t-tubule structure and function in the mammalian heart. *Hum Mol Genet* **22,** 372–383.

Jacquemet V (2007). Steady-state solutions in mathematical models of atrial cell electrophysiology and their stability. *Math Biosci* **208,** 241–269.

Jafri MS, Rice JJ & Winslow RL (1998). Cardiac Ca2+ Dynamics: The Roles of Ryanodine Receptor Adaptation and Sarcoplasmic Reticulum Load. *Biophys J* **74,** 1149–1168.

January CT, Wann LS, Alpert JS, Calkins H, Cigarroa JE, Cleveland JC, Conti JB, Ellinor PT, Ezekowitz MD, Field ME, Murray KT, Sacco RL, Stevenson WG, Tchou PJ, Tracy CM & Yancy CW (2014). 2014 AHA/ACC/HRS Guideline for the Management of Patients With Atrial Fibrillation. *J Am Coll Cardiol* **64,** e1–e76.

Jayasinghe ID, Baddeley D, Kong CHT, Wehrens XHT, Cannell MB & Soeller C (2012). Nanoscale Organization of Junctophilin-2 and Ryanodine Receptors within Peripheral Couplings of Rat Ventricular Cardiomyocytes. *Biophys J* **102,** L19–L21.

Jayasinghe ID, Cannell MB & Soeller C (2009). Organization of Ryanodine Receptors, Transverse Tubules, and Sodium-Calcium Exchanger in Rat Myocytes. *Biophys J* **97,** 2664–2673.

Kang C, Qiao Y, Li G, Baechle K, Camelliti P, Rentschler S & Efimov IR (2016). Human Organotypic Cultured Cardiac Slices: New Platform For High Throughput Preclinical Human Trials. *Sci Rep* **6,** 28798.

Kawai M, Hussain M & Orchard CH (1999). Excitation-contraction coupling in rat ventricular myocytes after formamide-induced detubulation. *Am J Physiol-Heart Circ Physiol* **277,** H603–H609.

Kettlewell S, Burton FL, Smith GL & Workman AJ (2013). Chronic myocardial infarction promotes atrial action potential alternans, afterdepolarizations, and fibrillation. *Cardiovasc Res* **99,** 215–224.

Kim MH, Johnston SS, Chu B-C, Dalal MR & Schulman KL (2011). Estimation of Total Incremental Health Care Costs in Patients With Atrial Fibrillation in the United States. *Circ Cardiovasc Qual Outcomes* **4,** 313–320.

Kirk MM, Izu LT, Chen-Izu Y, McCulle SL, Wier WG, Balke CW & Shorofsky SR (2003). Role of the Transverse-Axial Tubule System in Generating Calcium Sparks and Calcium Transients in Rat Atrial Myocytes. *J Physiol* **547,** 441–451.

Kneller J, Sun H, Leblanc N & Nattel S (2002). Remodeling of Ca2+-handling by atrial tachycardia: evidence for a role in loss of rate-adaptation. *Cardiovasc Res* **54,** 416–426.

Knöll R et al. (2002). The Cardiac Mechanical Stretch Sensor Machinery Involves a Z Disc Complex that Is Defective in a Subset of Human Dilated Cardiomyopathy. *Cell* **111,** 943–955.

Knollmann BC, Chopra N, Hlaing T, Akin B, Yang T, Ettensohn K, Knollmann BEC, Horton KD, Weissman NJ, Holinstat I, Zhang W, Roden DM, Jones LR, Franzini-Armstrong C & Pfeifer K (2006). *Casq2* deletion causes sarcoplasmic reticulum volume increase, premature Ca^{2+} release, and catecholaminergic polymorphic ventricular tachycardia. *J Clin Invest* **116,** 2510–2520.

Ko CY, Liu MB, Song Z, Qu Z & Weiss JN (2017). Multiscale Determinants of Delayed Afterdepolarization Amplitude in Cardiac Tissue. *Biophys J* **112,** 1949–1961.

Ko D, Rahman F, Schnabel RB, Yin X, Benjamin EJ & Christophersen IE (2016). Atrial fibrillation in women: epidemiology, pathophysiology, presentation, and prognosis. *Nat Rev Cardiol* **13,** 321–332.

Kohl T, Westphal V, Hell SW & Lehnart SE (2013). Superresolution microscopy in heart — Cardiac nanoscopy. *J Mol Cell Cardiol* **58,** 13–21.

Koivumäki JT, Korhonen T & Tavi P (2011). Impact of Sarcoplasmic Reticulum Calcium Release on Calcium Dynamics and Action Potential Morphology in Human Atrial Myocytes: A Computational Study. *PLOS Comput Biol* **7,** e1001067.

Kolstad TR, van den Brink J, MacQuaide N, Lunde PK, Frisk M, Aronsen JM, Norden ES, Cataliotti A, Sjaastad I, Sejersted OM, Edwards AG, Lines GT & Louch WE (2018). Ryanodine receptor dispersion disrupts Ca2+ release in failing cardiac myocytes ed. Dietz HC & Vunjak-Novakovic G. *eLife* **7,** e39427.

Krijthe BP, Kunst A, Benjamin EJ, Lip GYH, Franco OH, Hofman A, Witteman JCM, Stricker BH & Heeringa J (2013). Projections on the number of individuals with atrial fibrillation in the European Union, from 2000 to 2060. *Eur Heart J* **34,** 2746–2751.

Kushmerick MJ & Podolsky RJ (1969). Ionic Mobility in Muscle Cells. *Science* **166,** 1297–1298.

Lawless M, Caldwell JL, Radcliffe EJ, Smith CER, Madders GWP, Hutchings DC, Woods LS, Church SJ, Unwin RD, Kirkwood GJ, Becker LK, Pearman CM, Taylor RF, Eisner DA, Dibb KM & Trafford AW (2019). Phosphodiesterase 5 inhibition improves contractile function and restores transverse tubule loss and catecholamine responsiveness in heart failure. *Sci Rep* **9,** 6801.

Lee E, Marcucci M, Daniell L, Pypaert M, Weisz OA, Ochoa G-C, Farsad K, Wenk MR & De Camilli P (2002). Amphiphysin 2 (Bin1) and T-Tubule Biogenesis in Muscle. *Science* **297,** 1193–1196.

Lenaerts I, Bito V, Heinzel FR, Driesen RB, Holemans P, D'hooge J, Heidbüchel H, Sipido KR & Willems R (2009). Ultrastructural and Functional Remodeling of the Coupling Between Ca2+ Influx and Sarcoplasmic Reticulum Ca2+ Release in Right Atrial Myocytes From Experimental Persistent Atrial Fibrillation. *Circ Res* **105,** 876–885.

Li D, Fareh S, Leung TK & Nattel S (1999). Promotion of Atrial Fibrillation by Heart Failure in Dogs. *Circulation* **100,** 87–95.

Li GR & Nattel S (1997). Properties of human atrial ICa at physiological temperatures and relevance to action potential. *Am J Physiol-Heart Circ Physiol* **272,** H227–H235.

Li H, Lichter JG, Seidel T, Tomaselli GF, Bridge JHB & Sachse FB (2015). Cardiac Resynchronization Therapy Reduces Subcellular Heterogeneity of Ryanodine Receptors, T-Tubules, and Ca2+ Sparks Produced by Dyssynchronous Heart Failure. *Circ Heart Fail* **8,** 1105–1114.

Li J, Agvanian S, Zhou K, Shaw RM & Hong T (2020). Exogenous Cardiac Bridging Integrator 1 Benefits Mouse Hearts With Pre-existing Pressure Overload-Induced Heart Failure. *Front Physiol*. Available at: https://www.frontiersin.org/articles/10.3389/fphys.2020.00708 [Accessed October 24, 2022].

Li Q, O'Neill SC, Tao T, Li Y, Eisner D & Zhang H (2012). Mechanisms by which Cytoplasmic Calcium Wave Propagation and Alternans Are Generated in Cardiac Atrial Myocytes Lacking T-Tubules—Insights from a Simulation Study. *Biophys J* **102,** 1471–1482.

Li Y, Wei J, Guo W, Sun B, Estillore JP, Wang R, Yoruk A, Roston TM, Sanatani S, Wilde AAM, Gollob MH, Roberts JD, Tseng ZH, Jensen HK & Chen SRW (2021). Human RyR2 (Ryanodine Receptor 2) Loss-of-Function Mutations. *Circ Arrhythm Electrophysiol* **14,** e010013.

Lipsett DB, Frisk M, Aronsen JM, Nordén ES, Buonarati OR, Cataliotti A, Hell JW, Sjaastad I, Christensen G & Louch WE (2019). Cardiomyocyte substructure reverts to an immature phenotype during heart failure. *J Physiol* **597,** 1833–1853.

Liu MB, Ko CY, Song Z, Garfinkel A, Weiss JN & Qu Z (2016). A Dynamical Threshold for Cardiac Delayed Afterdepolarization-Mediated Triggered Activity. *Biophys J* **111,** 2523–2533.

Liu MB, de Lange E, Garfinkel A, Weiss JN & Qu Z (2015). Delayed afterdepolarizations generate both triggers and a vulnerable substrate promoting reentry in cardiac tissue. *Heart Rhythm* **12,** 2115–2124.

Liu Y, Zhou K, Li J, Agvanian S, Caldaruse A-M, Shaw S, Hitzeman TC, Shaw RM & Hong T (2020). In Mice Subjected to Chronic Stress, Exogenous cBIN1 Preserves Calcium-Handling Machinery and Cardiac Function. *JACC Basic Transl Sci* **5,** 561–578.

Lotteau S, Zhang R, Hazan A, Grabar C, Gonzalez D, Aynaszyan S, Philipson KD, Ottolia M & Goldhaber JI (2021). Acute Genetic Ablation of Cardiac Sodium/Calcium Exchange in Adult Mice: Implications for Cardiomyocyte Calcium Regulation, Cardioprotection, and Arrhythmia. *J Am Heart Assoc* **10,** e019273.

Louch WE, Bito V, Heinzel FR, Macianskiene R, Vanhaecke J, Flameng W, Mubagwa K & Sipido KR (2004). Reduced synchrony of Ca2+ release with loss of T-tubules—a comparison to Ca2+ release in human failing cardiomyocytes. *Cardiovasc Res* **62,** 63–73.

Louch WE, Mørk HK, Sexton J, Strømme TA, Laake P, Sjaastad I & Sejersted OM (2006). T-tubule disorganization and reduced synchrony of Ca2+ release in murine cardiomyocytes following myocardial infarction. *J Physiol* **574,** 519–533.

Lugenbiel P, Wenz F, Govorov K, Schweizer PA, Katus HA & Thomas D (2015). Atrial Fibrillation Complicated by Heart Failure Induces Distinct Remodeling of Calcium Cycling Proteins. *PLOS ONE* **10,** e0116395.

Lüss I, Boknik P, Jones LR, Kirchhefer U, Knapp J, Linck B, Lüss H, Meissner A, Müller FU, Schmitz W, Vahlensieck U & Neumann J (1999). Expression of Cardiac Calcium Regulatory Proteins in Atrium v Ventricle in Different Species. *J Mol Cell Cardiol* **31,** 1299–1314.

Macquaide N, Tuan H-TM, Hotta J, Sempels W, Lenaerts I, Holemans P, Hofkens J, Jafri MS, Willems R & Sipido KR (2015). Ryanodine receptor cluster fragmentation and redistribution in persistent atrial fibrillation enhance calcium release. *Cardiovasc Res* **108,** 387–398.

Magnussen C et al. (2017). Sex Differences and Similarities in Atrial Fibrillation Epidemiology, Risk Factors, and Mortality in Community Cohorts. *Circulation* **136,** 1588–1597.

Mahajan A, Shiferaw Y, Sato D, Baher A, Olcese R, Xie L-H, Yang M-J, Chen P-S, Restrepo JG, Karma A, Garfinkel A, Qu Z & Weiss JN (2008). A Rabbit Ventricular Action Potential Model Replicating Cardiac Dynamics at Rapid Heart Rates. *Biophys J* **94,** 392–410.

Maleckar MM, Greenstein JL, Giles WR & Trayanova NA (2009). K+ current changes account for the rate dependence of the action potential in the human atrial myocyte. *Am J Physiol-Heart Circ Physiol* **297,** H1398–H1410.

Manfra O, Frisk M & Louch WE (2017). Regulation of Cardiomyocyte T-Tubular Structure: Opportunities for Therapy. *Curr Heart Fail Rep* **14,** 167–178.

Mangold K & Silva JR (2020). Modeling the molecular details of ion channels. *Model Simulating Card Electr Act*; DOI: 10.1088/978-0-7503-2064-1ch2.

Marchena M & Echebarria B (2018). Computational Model of Calcium Signaling in Cardiac Atrial Cells at the Submicron Scale. *Front Physiol* **9,** 1760.

Marchena M & Echebarria B (2020*a*). Influence of the tubular network on the characteristics of calcium transients in cardiac myocytes. *PLOS ONE* **15,** e0231056.

Marchena M & Echebarria B (2020*b*). Influence of the tubular network on the characteristics of calcium transients in cardiac myocytes. *PLOS ONE* **15,** e0231056.

Melnyk P, Ehrlich JR, Pourrier M, Villeneuve L, Cha T-J & Nattel S (2005). Comparison of ion channel distribution and expression in cardiomyocytes of canine pulmonary veins versus left atrium. *Cardiovasc Res* **65,** 104–116.

Melnyk P, Zhang L, Shrier A & Nattel S (2002). Differential distribution of Kir2.1 and Kir2.3 subunits in canine atrium and ventricle. *Am J Physiol-Heart Circ Physiol* **283,** H1123–H1133.

Minamisawa S, Oshikawa J, Takeshima H, Hoshijima M, Wang Y, Chien KR, Ishikawa Y & Matsuoka R (2004). Junctophilin type 2 is associated with caveolin-3 and is down-regulated in the hypertrophic and dilated cardiomyopathies. *Biochem Biophys Res Commun* **325,** 852–856.

Miyasaka Y, Barnes ME, Gersh BJ, Cha SS, Bailey KR, Abhayaratna WP, Seward JB & Tsang TSM (2006). Secular Trends in Incidence of Atrial Fibrillation in Olmsted County, Minnesota, 1980 to 2000, and Implications on the Projections for Future Prevalence. *Circulation* **114,** 119–125.

Moise N, Struckman HL, Dagher C, Veeraraghavan R & Weinberg SH (2021). Intercalated disk nanoscale structure regulates cardiac conduction. *J Gen Physiol* **153,** e202112897.

Molina CE, Abu-Taha IH, Wang Q, Roselló-Díez E, Kamler M, Nattel S, Ravens U, Wehrens XHT, Hove-Madsen L, Heijman J & Dobrev D (2018). Profibrotic, Electrical, and Calcium-Handling Remodeling of the Atria in Heart Failure Patients With and Without Atrial Fibrillation. *Front Physiol* **9,** 1383.

Morotti S, Grandi E, Summa A, Ginsburg KS & Bers DM (2012). Theoretical study of L-type Ca2+ current inactivation kinetics during action potential repolarization and early afterdepolarizations. *J Physiol* **590,** 4465–4481.

Morotti S, Koivumäki JT, Maleckar MM, Chiamvimonvat N & Grandi E (2016*a*). Small-Conductance Ca2+-Activated K+ Current in Atrial Fibrillation: Both Friend and FOE. *Biophys J* **110,** 274a.

Morotti S, McCulloch AD, Bers DM, Edwards AG & Grandi E (2016*b*). Atrial-selective targeting of arrhythmogenic phase-3 early afterdepolarizations in human myocytes. *J Mol Cell Cardiol* **96,** 63–71.

Myles RC, Burton FL, Cobbe SM & Smith GL (2011). Alternans of action potential duration and amplitude in rabbits with left ventricular dysfunction following myocardial infarction. *J Mol Cell Cardiol* **50,** 510–521.

Narolska NA, van Loon RB, Boontje NM, Zaremba R, Penas SE, Russell J, Spiegelenberg SR, Huybregts M a. JM, Visser FC, de Jong JW, van der Velden J & Stienen GJM (2005). Myocardial contraction is 5-fold more economical in ventricular than in atrial human tissue. *Cardiovasc Res* **65,** 221–229.

Nattel S (2011). From Guidelines to Bench: Implications of Unresolved Clinical Issues for Basic Investigations of Atrial Fibrillation Mechanisms. *Can J Cardiol* **27,** 19–26.

Nattel S (2013). Paroxysmal Atrial Fibrillation and Pulmonary Veins: Relationships Between Clinical Forms and Automatic Versus Re-entrant Mechanisms. *Can J Cardiol* **29,** 1147–1149.

Nattel S, Burstein B & Dobrev D (2008). Atrial Remodeling and Atrial Fibrillation. *Circ Arrhythm Electrophysiol* **1,** 62–73.

Nattel S & Dobrev D (2012). The multidimensional role of calcium in atrial fibrillation pathophysiology: mechanistic insights and therapeutic opportunities. *Eur Heart J* **33,** 1870–1877.

Nattel S & Harada M (2014). Atrial Remodeling and Atrial Fibrillation: Recent Advances and Translational Perspectives. *J Am Coll Cardiol* **63,** 2335–2345.

Nattel S, Maguy A, Le Bouter S & Yeh Y-H (2007). Arrhythmogenic Ion-Channel Remodeling in the Heart: Heart Failure, Myocardial Infarction, and Atrial Fibrillation. *Physiol Rev* **87,** 425–456.

Neef S, Dybkova N, Sossalla S, Ort KR, Fluschnik N, Neumann K, Seipelt R, Schöndube FA, Hasenfuss G & Maier LS (2010). CaMKII-Dependent Diastolic SR Ca2+ Leak and Elevated Diastolic Ca2+ Levels in Right Atrial Myocardium of Patients With Atrial Fibrillation. *Circ Res* **106,** 1134–1144.

Negroni JA, Morotti S, Lascano EC, Gomes AV, Grandi E, Puglisi JL & Bers DM (2015). β-adrenergic effects on cardiac myofilaments and contraction in an integrated rabbit ventricular myocyte model. *J Mol Cell Cardiol* **81,** 162–175.

Ni H, Fogli Iseppe A, Giles WR, Narayan SM, Zhang H, Edwards AG, Morotti S & Grandi E (2020). Populations of in silico myocytes and tissues reveal synergy of multiatrial-predominant K+-current block in atrial fibrillation. *Br J Pharmacol* **177,** 4497–4515.

Nikolova AP, Hitzeman TC, Baum R, Caldaruse A-M, Agvanian S, Xie Y, Geft DR, Chang DH, Moriguchi JD, Hage A, Azarbal B, Czer LS, Kittleson MM, Patel JK, Wu AHB, Kobashigawa JA, Hamilton M, Hong T & Shaw RM (2018). Association of a Novel Diagnostic Biomarker, the Plasma Cardiac Bridging Integrator 1 Score, With Heart Failure With Preserved Ejection Fraction and Cardiovascular Hospitalization. *JAMA Cardiol* **3,** 1206–1210.

Nivala M, Song Z, Weiss JN & Qu Z (2015). T-tubule disruption promotes calcium alternans in failing ventricular myocytes: Mechanistic insights from computational modeling. *J Mol Cell Cardiol* **79,** 32–41.

Noble D (1960). Cardiac Action and Pacemaker Potentials based on the Hodgkin-Huxley Equations. *Nature* **188,** 495–497.

Nygren A, Fiset C, Firek L, Clark JW, Lindblad DS, Clark RB & Giles WR (1998). Mathematical Model of an Adult Human Atrial Cell. *Circ Res* **82,** 63–81.

Odening KE, Deiß S, Dilling-Boer D, Didenko M, Eriksson U, Nedios S, Ng FS, Roca Luque I, Sanchez Borque P, Vernooy K, Wijnmaalen AP & Yorgun H (2019). Mechanisms of sex differences in atrial fibrillation: role of hormones and differences in electrophysiology, structure, function, and remodelling. *EP Eur* **21,** 366–376.

Ohkusa T, Ueyama T, Yamada J, Yano M, Fujumura Y, Esato K & Matsuzaki M (1999). Alterations in cardiac sarcoplasmic reticulum Ca2+regulatory proteins in the atrial tissue of patients with chronic atrial fibrillation. *J Am Coll Cardiol* **34,** 255–263.

van Oort RJ, Garbino A, Wang W, Dixit SS, Landstrom AP, Gaur N, De Almeida AC, Skapura DG, Rudy Y, Burns AR, Ackerman MJ & Wehrens XHT (2011). Disrupted Junctional Membrane Complexes and Hyperactive Ryanodine Receptors After Acute Junctophilin Knockdown in Mice. *Circulation* **123,** 979–988.

Packer DL et al. (2019). Effect of Catheter Ablation vs Antiarrhythmic Drug Therapy on Mortality, Stroke, Bleeding, and Cardiac Arrest Among Patients With Atrial Fibrillation: The CABANA Randomized Clinical Trial. *JAMA* **321,** 1261–1274.

Pannaccione A, Piccialli I, Secondo A, Ciccone R, Molinaro P, Boscia F & Annunziato L (2020). The Na+/Ca2+exchanger in Alzheimer's disease. *Cell Calcium* **87,** 102190.

Parikh SS, Blackwell DJ, Gomez-Hurtado N, Frisk M, Wang L, Kim K, Dahl CP, Fiane A, Tønnessen T, Kryshtal DO, Louch WE & Knollmann BC (2017). Thyroid and Glucocorticoid Hormones Promote Functional T-Tubule Development in Human-Induced Pluripotent Stem Cell–Derived Cardiomyocytes. *Circ Res* **121,** 1323–1330.

Pásek M, Brette F, Nelson A, Pearce C, Qaiser A, Christe G & Orchard CH (2008*a*). Quantification of t-tubule area and protein distribution in rat cardiac ventricular myocytes. *Prog Biophys Mol Biol* **96,** 244–257.

Pásek M, Šimurda J & Christé G (2006). The functional role of cardiac T-tubules explored in a model of rat ventricular myocytes. *Philos Trans R Soc Math Phys Eng Sci* **364,** 1187–1206.

Pásek M, Šimurda J, Christé G & Orchard CH (2008*b*). Modelling the cardiac transverse-axial tubular system. *Prog Biophys Mol Biol* **96,** 226–243.

Pásek M, Šimurda J, Orchard CH & Christé G (2008*c*). A model of the guinea-pig ventricular cardiac myocyte incorporating a transverse–axial tubular system. *Prog Biophys Mol Biol* **96,** 258–280.

Picht E, Zima AV, Shannon TR, Duncan AM, Blatter LA & Bers DM (2011). Dynamic Calcium Movement Inside Cardiac Sarcoplasmic Reticulum During Release. *Circ Res* **108,** 847–856.

Polontchouk L, Haefliger J-A, Ebelt B, Schaefer T, Stuhlmann D, Mehlhorn U, Kuhn-Regnier F, De Vivie ER & Dhein S (2001). Effects of chronic atrial fibrillation on gap junction distribution in human and rat atria. *J Am Coll Cardiol* **38,** 883–891.

Porciatti F, Pelzmann B, Cerbai E, Schaffer P, Pino R, Bernhart E, Koidl B & Mugelli A (1997). The pacemaker current If in single human atrial myocytes and the effect of β-adrenoceptor and A1-adenosine receptor stimulation. *Br J Pharmacol* **122,** 963–969.

Pritchard HAT, Pires PW, Yamasaki E, Thakore P & Earley S (2018). Nanoscale remodeling of ryanodine receptor cluster size underlies cerebral microvascular dysfunction in Duchenne muscular dystrophy. *Proc Natl Acad Sci* **115,** E9745–E9752.

Qu Z, Shiferaw Y & Weiss JN (2007). Nonlinear dynamics of cardiac excitation-contraction coupling: An iterated map study. *Phys Rev E* **75,** 011927.

Rasmussen HB, Møller M, Knaus H-G, Jensen BS, Olesen S-P & Jørgensen NK (2004). Subcellular localization of the delayed rectifier K+ channels KCNQ1 and ERG1 in the rat heart. *Am J Physiol-Heart Circ Physiol* **286,** H1300–H1309.

Restrepo JG, Weiss JN & Karma A (2008). Calsequestrin-Mediated Mechanism for Cellular Calcium Transient Alternans. *Biophys J* **95,** 3767–3789.

Reynolds JO, Chiang DY, Wang W, Beavers DL, Dixit SS, Skapura DG, Landstrom AP, Song L-S, Ackerman MJ & Wehrens XHT (2013). Junctophilin-2 is necessary for T-tubule maturation during mouse heart development. *Cardiovasc Res* **100,** 44–53.

Richards MA, Clarke JD, Saravanan P, Voigt N, Dobrev D, Eisner DA, Trafford AW & Dibb KM (2011). Transverse tubules are a common feature in large mammalian atrial myocytes including human. *Am J Physiol-Heart Circ Physiol* **301,** H1996–H2005.

Rog-Zielinska EA, Moss R, Kaltenbacher W, Greiner J, Verkade P, Seemann G, Kohl P & Cannell MB (2021*a*). Nano-scale morphology of cardiomyocyte t-tubule/sarcoplasmic reticulum junctions revealed by ultra-rapid high-pressure freezing and electron tomography. *J Mol Cell Cardiol* **153,** 86–92.

Rog-Zielinska EA, Scardigli M, Peyronnet R, Zgierski-Johnston CM, Greiner J, Madl J, O'Toole ET, Morphew M, Hoenger A, Sacconi L & Kohl P (2021*b*). Beat-by-Beat Cardiomyocyte T-Tubule Deformation Drives Tubular Content Exchange. *Circ Res* **128,** 203–215.

Romero L, Alvarez-Lacalle E & Shiferaw Y (2019). Stochastic coupled map model of subcellular calcium cycling in cardiac cells. *Chaos Interdiscip J Nonlinear Sci* **29,** 023125.

Rosa GM, Dorighi U, Ferrero S, Brunacci M, Bertero G & Brunelli C (2015). Ranolazine for the treatment of atrial fibrillation. *Expert Opin Investig Drugs* **24,** 825–836.

Rovetti R, Das KK, Garfinkel A & Shiferaw Y (2007). Macroscopic consequences of calcium signaling in microdomains: A first-passage-time approach. *Phys Rev E* **76,** 051920.

Rush S & Larsen H (1978). A Practical Algorithm for Solving Dynamic Membrane Equations. *IEEE Trans Biomed Eng* **BME-25,** 389–392.

Sacconi L, Ferrantini C, Lotti J, Coppini R, Yan P, Loew LM, Tesi C, Cerbai E, Poggesi C & Pavone FS (2012). Action potential propagation in transverse-axial tubular system is impaired in heart failure. *Proc Natl Acad Sci* **109,** 5815–5819.

Sachse FB, Torres NS, Savio-Galimberti E, Aiba T, Kass DA, Tomaselli GF & Bridge JH (2012). Subcellular Structures and Function of Myocytes Impaired During Heart Failure Are Restored by Cardiac Resynchronization Therapy. *Circ Res* **110,** 588–597.

Sato D & Bers DM (2011). How Does Stochastic Ryanodine Receptor-Mediated Ca Leak Fail to Initiate a Ca Spark? *Biophys J* **101,** 2370–2379.

Sato D, Bers DM & Shiferaw Y (2013). Formation of Spatially Discordant Alternans Due to Fluctuations and Diffusion of Calcium. *PLOS ONE* **8,** e85365.

Sato D, Dixon RE, Santana LF & Navedo MF (2018). A model for cooperative gating of L-type Ca2+ channels and its effects on cardiac alternans dynamics. *PLOS Comput Biol* **14,** e1005906.

Sato D, Shannon TR & Bers DM (2016). Sarcoplasmic Reticulum Structure and Functional Properties that Promote Long-Lasting Calcium Sparks. *Biophys J* **110,** 382–390.

Saucerman JJ, Brunton LL, Michailova AP & McCulloch AD (2003). Modeling β-Adrenergic Control of Cardiac Myocyte Contractility in Silico. *J Biol Chem* **278,** 47997–48003.

Savio-Galimberti E, Frank J, Inoue M, Goldhaber JI, Cannell MB, Bridge JHB & Sachse FB (2008). Novel Features of the Rabbit Transverse Tubular System Revealed by Quantitative Analysis of Three-Dimensional Reconstructions from Confocal Images. *Biophys J* **95,** 2053–2062.

Schmidt C et al. (2015*a*). Upregulation of K2P3.1 K+ Current Causes Action Potential Shortening in Patients With Chronic Atrial Fibrillation. *Circulation* **132,** 82–92.

Schmidt C et al. (2015*b*). Upregulation of K2P3.1 K+ Current Causes Action Potential Shortening in Patients With Chronic Atrial Fibrillation. *Circulation* **132,** 82–92.

Schotten U, Greiser M, Benke D, Buerkel K, Ehrenteidt B, Stellbrink C, Vazquez-Jimenez JF, Schoendube F, Hanrath P & Allessie M (2002). Atrial fibrillation-induced atrial contractile dysfunction: a tachycardiomyopathy of a different sort. *Cardiovasc Res* **53,** 192–201.

Schulson MN, Scriven DRL, Fletcher P & Moore EDW (2011). Couplons in rat atria form distinct subgroups defined by their molecular partners. *J Cell Sci* **124,** 1167–1174.

Schwarz N, Kuniss M, Nedelmann M, Kaps M, Bachmann G, Neumann T, Pitschner H-F & Gerriets T (2010). Neuropsychological decline after catheter ablation of atrial fibrillation. *Heart Rhythm* **7,** 1761–1767.

Scriven DRL, Asghari P, Schulson MN & Moore EDW (2010). Analysis of Cav1.2 and Ryanodine Receptor Clusters in Rat Ventricular Myocytes. *Biophys J* **99,** 3923–3929.

Shan J, Xie W, Betzenhauser M, Reiken S, Chen B-X, Wronska A & Marks AR (2012). Calcium Leak Through Ryanodine Receptors Leads to Atrial Fibrillation in 3 Mouse Models of Catecholaminergic Polymorphic Ventricular Tachycardia. *Circ Res* **111,** 708–717.

Shannon TR, Wang F, Puglisi J, Weber C & Bers DM (2004). A Mathematical Treatment of Integrated Ca Dynamics within the Ventricular Myocyte. *Biophys J* **87,** 3351–3371.

Sheehan KA & Blatter LA (2003). Regulation of junctional and non-junctional sarcoplasmic reticulum calcium release in excitation-contraction coupling in cat atrial myocytes. *J Physiol* **546,** 119–135.

Shepherd N & McDonough HB (1998). Ionic diffusion in transverse tubules of cardiac ventricular myocytes. *Am J Physiol-Heart Circ Physiol* **275,** H852–H860.

Shiferaw Y, Aistrup GL, Louch WE & Wasserstrom JA (2020*a*). Remodeling Promotes Proarrhythmic Disruption of Calcium Homeostasis in Failing Atrial Myocytes. *Biophys J* **118,** 476–491.

Shiferaw Y, Aistrup GL, Louch WE & Wasserstrom JA (2020*b*). Remodeling Promotes Proarrhythmic Disruption of Calcium Homeostasis in Failing Atrial Myocytes. *Biophys J* **118,** 476–491.

Shiferaw Y, Aistrup GL & Wasserstrom JA (2017). Mechanism for Triggered Waves in Atrial Myocytes. *Biophys J* **113,** 656–670.

Shiferaw Y, Aistrup GL & Wasserstrom JA (2018). Synchronization of Triggered Waves in Atrial Tissue. *Biophys J* **115,** 1130–1141.

Shiferaw Y, Sato D & Karma A (2005). Coupled dynamics of voltage and calcium in paced cardiac cells. *Phys Rev E* **71,** 021903.

Shinagawa K, Shi Y-F, Tardif J-C, Leung T-K & Nattel S (2002). Dynamic Nature of Atrial Fibrillation Substrate During Development and Reversal of Heart Failure in Dogs. *Circulation* **105,** 2672–2678.

Shoemaker MB, Yoneda ZT, Crawford DM, Akers WS, Richardson T, Montgomery JA, Phillips S, Shyr Y, Saavedra P, Estrada JC, Kanagasundram A, Shen ST, Michaud GF, Crossley G, Ellis CR & Knollmann BC (2022). A Mechanistic Clinical Trial Using (R)-Versus (S)-Propafenone to Test RyR2 (Ryanodine Receptor) Inhibition for the Prevention of Atrial Fibrillation Induction. *Circ Arrhythm Electrophysiol* **15,** e010713.

Sitsapesan R & Williams AJ (1994). Regulation of the gating of the sheep cardiac sarcoplasmic reticulum ca2+-release channel by luminal Ca2+. *J Membr Biol* **137,** 215–226.

Smith CER, Pinali C, Eisner DA, Trafford AW & Dibb KM (2022). Enhanced calcium release at specialised surface sites compensates for reduced t-tubule density in neonatal sheep atrial myocytes. *J Mol Cell Cardiol* **173,** 61–70.

Smyrnias I, Mair W, Harzheim D, Walker SA, Roderick HL & Bootman MD (2010). Comparison of the T-tubule system in adult rat ventricular and atrial myocytes, and its role in excitation–contraction coupling and inotropic stimulation. *Cell Calcium* **47,** 210–223.

Soltis AR & Saucerman JJ (2010). Synergy between CaMKII Substrates and β-Adrenergic Signaling in Regulation of Cardiac Myocyte Ca2+ Handling. *Biophys J* **99,** 2038–2047.

Song L, Alcalai R, Arad M, Wolf CM, Toka O, Conner DA, Berul CI, Eldar M, Seidman CE & Seidman JG (2007). Calsequestrin 2 (CASQ2) mutations increase expression of calreticulin and ryanodine receptors, causing catecholaminergic polymorphic ventricular tachycardia. *J Clin Invest* **117,** 1814–1823.

Song L-S, Sobie EA, McCulle S, Lederer WJ, Balke CW & Cheng H (2006). Orphaned ryanodine receptors in the failing heart. *Proc Natl Acad Sci* **103,** 4305–4310.

Song Z, Karma A, Weiss JN & Qu Z (2016). Long-Lasting Sparks: Multi-Metastability and Release Competition in the Calcium Release Unit Network. *PLOS Comput Biol* **12,** e1004671.

Song Z, Ko CY, Nivala M, Weiss JN & Qu Z (2015). Calcium-Voltage Coupling in the Genesis of Early and Delayed Afterdepolarizations in Cardiac Myocytes. *Biophys J* **108,** 1908–1921.

Song Z, Liu MB & Qu Z (2018). Transverse tubular network structures in the genesis of intracellular calcium alternans and triggered activity in cardiac cells. *J Mol Cell Cardiol* **114,** 288–299.

Sutanto H, van Sloun B, Schönleitner P, van Zandvoort MAMJ, Antoons G & Heijman J (2018). The Subcellular Distribution of Ryanodine Receptors and L-Type Ca2+ Channels Modulates Ca2+-Transient Properties and Spontaneous Ca2+-Release Events in Atrial Cardiomyocytes. *Front Physiol* **9,** 1108.

Swietach P, Spitzer KW & Vaughan-Jones RD (2010). Modeling calcium waves in cardiac myocytes: importance of calcium diffusion. *Front Biosci Landmark Ed* **15,** 661–680.

Swift F, Franzini-Armstrong C, Øyehaug L, Enger UH, Andersson KB, Christensen G, Sejersted OM & Louch WE (2012). Extreme sarcoplasmic reticulum volume loss and compensatory T-tubule remodeling after Serca2 knockout. *Proc Natl Acad Sci* **109,** 3997–4001.

Swift F, Strømme TA, Amundsen B, Sejersted OM & Sjaastad I (2006). Slow diffusion of K+ in the T tubules of rat cardiomyocytes. *J Appl Physiol* **101,** 1170–1176.

Tadros R, Ton A-T, Fiset C & Nattel S (2014). Sex Differences in Cardiac Electrophysiology and Clinical Arrhythmias: Epidemiology, Therapeutics, and Mechanisms. *Can J Cardiol* **30,** 783–792.

Takeshima H, Komazaki S, Nishi M, Iino M & Kangawa K (2000). Junctophilins: A Novel Family of Junctional Membrane Complex Proteins. *Mol Cell* **6,** 11–22.

Tanaami T, Ishida H, Seguchi H, Hirota Y, Kadono T, Genka C, Nakazawa H & Barry WH (2005). Difference in Propagation of Ca^{2+} Release in Atrial and Ventricular Myocytes. *Jpn J Physiol* **55,** 81–91.

Tazmini K, Frisk M, Lewalle A, Laasmaa M, Morotti S, Lipsett DB, Manfra O, Skogested J, Aronsen JM, Sejersted OM, Sjaastad I, Edwards AG, Grandi E, Niederer SA, Øie E & Louch WE (2020). Hypokalemia Promotes Arrhythmia by Distinct Mechanisms in Atrial and Ventricular Myocytes. *Circ Res* **126,** 889–906.

Terentyev D, Nori A, Santoro M, Viatchenko-Karpinski S, Kubalova Z, Gyorke I, Terentyeva R, Vedamoorthyrao S, Blom NA, Valle G, Napolitano C, Williams SC, Volpe P, Priori SG & Gyorke S (2006). Abnormal Interactions of Calsequestrin With the Ryanodine Receptor Calcium Release Channel Complex Linked to Exercise-Induced Sudden Cardiac Death. *Circ Res* **98,** 1151–1158.

Terentyev D, Viatchenko-Karpinski S, Györke I, Volpe P, Williams SC & Györke S (2003). Calsequestrin determines the functional size and stability of cardiac intracellular calcium stores: Mechanism for hereditary arrhythmia. *Proc Natl Acad Sci* **100,** 11759–11764.

Thomas MJ, Sjaastad I, Andersen K, Helm PJ, Wasserstrom JA, Sejersted OM & Ottersen OP (2003). Localization and function of the Na+/Ca2+-exchanger in normal and detubulated rat cardiomyocytes. *J Mol Cell Cardiol* **35,** 1325–1337.

Thul R, Coombes S, Roderick HL & Bootman MD (2012). Subcellular calcium dynamics in a whole-cell model of an atrial myocyte. *Proc Natl Acad Sci* **109,** 2150–2155.

Tomek J, Bueno-Orovio A, Passini E, Zhou X, Minchole A, Britton O, Bartolucci C, Severi S, Shrier A, Virag L, Varro A & Rodriguez B (2019). Development, calibration, and validation of a novel human ventricular myocyte model in health, disease, and drug block ed. Faraldo-Gómez JD, Barkai N, Hund T & Maleckar M. *eLife* **8,** e48890.

Trafford AW, Clarke JD, Richards MA, Eisner DA & Dibb KM (2013). Calcium signalling microdomains and the t-tubular system in atrial mycoytes: potential roles in cardiac disease and arrhythmias. *Cardiovasc Res* **98,** 192–203.

Tran K, Smith NP, Loiselle DS & Crampin EJ (2009). A Thermodynamic Model of the Cardiac Sarcoplasmic/Endoplasmic Ca2+ (SERCA) Pump. *Biophys J* **96,** 2029–2042.

Trayanova NA, Doshi AN & Prakosa A (2020). How personalized heart modeling can help treatment of lethal arrhythmias: A focus on ventricular tachycardia ablation strategies in post-infarction patients. *WIREs Syst Biol Med* **12,** e1477.

Vagos MR, Arevalo H, Heijman J, Schotten U & Sundnes J (2021). A Computational Study of the Effects of Tachycardia-Induced Remodeling on Calcium Wave Propagation in Rabbit Atrial Myocytes. *Front Physiol*; DOI: 10.3389/fphys.2021.651428.

Van Wagoner David R., Pond Amber L., Lamorgese Michelle, Rossie Sandra S., McCarthy Patrick M., & Nerbonne Jeanne M. (1999). Atrial L-Type Ca2+ Currents and Human Atrial Fibrillation. *Circ Res* **85,** 428–436.

Van Wagoner DR, Pond AL, Lamorgese M, Rossie SS, McCarthy PM & Nerbonne JM (1999). Atrial L-Type Ca2+ Currents and Human Atrial Fibrillation. *Circ Res* **85,** 428–436.

van der Velden HMW, Ausma J, Rook MB, Hellemons AJCGM, van Veen TAAB, Allessie MA & Jongsma HJ (2000). Gap junctional remodeling in relation to stabilization of atrial fibrillation in the goat. *Cardiovasc Res* **46,** 476–486.

Verrier RL & Belardinelli L (2020). Pulmonary Delivery of Antiarrhythmic Drugs for Rapid Conversion of New-Onset Atrial Fibrillation. *J Cardiovasc Pharmacol* **75,** 276–283.

Vest JA, Wehrens XHT, Reiken SR, Lehnart SE, Dobrev D, Chandra P, Danilo P, Ravens U, Rosen MR & Marks AR (2005). Defective Cardiac Ryanodine Receptor Regulation During Atrial Fibrillation. *Circulation* **111,** 2025–2032.

Voigt N, Heijman J, Trausch A, Mintert-Jancke E, Pott L, Ravens U & Dobrev D (2013). Impaired Na+-dependent regulation of acetylcholine-activated inward-rectifier K+ current modulates action potential rate dependence in patients with chronic atrial fibrillation. *J Mol Cell Cardiol* **61,** 142–152.

Voigt N, Heijman J, Wang Q, Chiang DY, Li N, Karck M, Wehrens XHT, Nattel S & Dobrev D (2014). Cellular and Molecular Mechanisms of Atrial Arrhythmogenesis in Patients With Paroxysmal Atrial Fibrillation. *Circulation* **129,** 145–156.

Voigt N, Li N, Wang Q, Wang W, Trafford AW, Abu-Taha I, Sun Q, Wieland T, Ravens U, Nattel S, Wehrens XHT & Dobrev D (2012). Enhanced Sarcoplasmic Reticulum Ca2+

Leak and Increased Na+-Ca2+ Exchanger Function Underlie Delayed Afterdepolarizations in Patients With Chronic Atrial Fibrillation. *Circulation* **125,** 2059–2070.

Wakili R et al. (2010). Multiple Potential Molecular Contributors to Atrial Hypocontractility Caused by Atrial Tachycardia Remodeling in Dogs. *Circ Arrhythm Electrophysiol* **3,** 530–541.

Wakili R, Voigt N, Kääb S, Dobrev D & Nattel S (2011). Recent advances in the molecular pathophysiology of atrial fibrillation. ; DOI: 10.1172/JCI46315. Available at: https://www.jci.org/articles/view/46315/pdf [Accessed October 11, 2022].

Walden AP, Dibb KM & Trafford AW (2009). Differences in intracellular calcium homeostasis between atrial and ventricular myocytes. *J Mol Cell Cardiol* **46,** 463–473.

Walker MA, Williams GSB, Kohl T, Lehnart SE, Jafri MS, Greenstein JL, Lederer WJ & Winslow RL (2014). Superresolution Modeling of Calcium Release in the Heart. *Biophys J* **107,** 3018–3029.

Wang JH (1953). Tracer-diffusion in Liquids. IV. Self-diffusion of Calcium Ion and Chloride Ion in Aqueous Calcium Chloride Solutions1. *J Am Chem Soc* **75,** 1769–1770.

Wang Z, Fermini B & Nattel S (1993). Delayed rectifier outward current and repolarization in human atrial myocytes. *Circ Res* **73,** 276–285.

Wang Z, Fermini B, & Nattel S (1993). Sustained depolarization-induced outward current in human atrial myocytes. Evidence for a novel delayed rectifier K+ current similar to Kv1.5 cloned channel currents. *Circ Res* **73,** 1061–1076.

Wattigney WA, Mensah GA & Croft JB (2002). Increased Atrial Fibrillation Mortality: United States, 1980–1998. *Am J Epidemiol* **155,** 819–826.

Weber CR, Ginsburg KS, Philipson KD, Shannon TR & Bers DM (2001). Allosteric Regulation of Na/Ca Exchange Current by Cytosolic Ca in Intact Cardiac Myocytes. *J Gen Physiol* **117,** 119–132.

Wei S, Guo A, Chen B, Kutschke W, Xie Y-P, Zimmerman K, Weiss RM, Anderson ME, Cheng H & Song L-S (2010). T-Tubule Remodeling During Transition From Hypertrophy to Heart Failure. *Circ Res* **107,** 520–531.

Wettwer E, Hála O, Christ T, Heubach JF, Dobrev D, Knaut M, Varró A & Ravens U (2004). Role of IKur in Controlling Action Potential Shape and Contractility in the Human Atrium. *Circulation* **110,** 2299–2306.

Williams AJ, Thomas NL & George CH (2018). The ryanodine receptor: advances in structure and organization. *Curr Opin Physiol* **1,** 1–6.

Williams GSB, Huertas MA, Sobie EA, Jafri MS & Smith GD (2007). A Probability Density Approach to Modeling Local Control of Calcium-Induced Calcium Release in Cardiac Myocytes. *Biophys J* **92,** 2311–2328.

Williams GSB, Huertas MA, Sobie EA, Jafri MS & Smith GD (2008). Moment Closure for Local Control Models of Calcium-Induced Calcium Release in Cardiac Myocytes. *Biophys J* **95,** 1689–1703.

Wleklinski MJ, Kannankeril PJ & Knollmann BC (2020). Molecular and tissue mechanisms of catecholaminergic polymorphic ventricular tachycardia. *J Physiol* **598,** 2817–2834.

Woo S-H, Cleemann L & Morad M (2005). Diversity of atrial local Ca2+ signalling: evidence from 2-D confocal imaging in Ca2+-buffered rat atrial myocytes. *J Physiol* **567,** 905–921.

Wu X & Bers DM (2006). Sarcoplasmic Reticulum and Nuclear Envelope Are One Highly Interconnected Ca2+ Store Throughout Cardiac Myocyte. *Circ Res* **99,** 283–291.

Xie Y, Sato D, Garfinkel A, Qu Z & Weiss JN (2010). So Little Source, So Much Sink: Requirements for Afterdepolarizations to Propagate in Tissue. *Biophys J* **99,** 1408–1415.

Yang P-C, DeMarco KR, Aghasafari P, Jeng M-T, Dawson JRD, Bekker S, Noskov SY, Yarov-Yarovoy V, Vorobyov I & Clancy CE (2020). A Computational Pipeline to Predict Cardiotoxicity. *Circ Res* **126,** 947–964.

Yao A, Spitzer KW, Ito N, Zaniboni M, Lorell BH & Barry WH (1997). The restriction of diffusion of cations at the external surface of cardiac myocytes varies between species. *Cell Calcium* **22,** 431–438.

Yeh Y-H, Wakili R, Qi X-Y, Chartier D, Boknik P, Kääb S, Ravens U, Coutu P, Dobrev D & Nattel S (2008). Calcium-Handling Abnormalities Underlying Atrial Arrhythmogenesis and Contractile Dysfunction in Dogs With Congestive Heart Failure. *Circ Arrhythm Electrophysiol* **1,** 93–102.

Yuchi Z & Van Petegem F (2016). Ryanodine receptors under the magnifying lens: Insights and limitations of cryo-electron microscopy and X-ray crystallography studies. *Cell Calcium* **59,** 209–227.

Yue DT, Herzig S & Marban E (1990). Beta-adrenergic stimulation of calcium channels occurs by potentiation of high-activity gating modes. *Proc Natl Acad Sci* **87,** 753–757.

Yue X, Zhang R, Kim B, Ma A, Philipson KD & Goldhaber JI (2017). Heterogeneity of transverse-axial tubule system in mouse atria: Remodeling in atrial-specific Na+–Ca2+ exchanger knockout mice. *J Mol Cell Cardiol* **108,** 50–60.

Zhang R, Yang J, Zhu J & Xu X (2009). Depletion of zebrafish Tcap leads to muscular dystrophy via disrupting sarcomere–membrane interaction, not sarcomere assembly. *Hum Mol Genet* **18,** 4130–4140.

Zhang X, Smith C, Morotti S, Grandi E & Ni H (2022). Sex-dependent differences in Ca2+-related arrhythmia revealed by human atrial myocyte models. *Biophys J* **121,** 231a.

Zhou J, Singh N, Monnier C, Marszalec W, Gao L, Jin J, Frisk M, Louch WE, Verma S, Krishnamurthy P, Nico E, Mulla M, Aistrup GL, Kishore R & Wasserstrom JA (2021). Phosphatidylinositol-4,5-Bisphosphate Binding to Amphiphysin-II Modulates T-

Tubule Remodeling: Implications for Heart Failure. *Front Physiol*. Available at: https://www.frontiersin.org/articles/10.3389/fphys.2021.782767 [Accessed October 16, 2022].

Zou R, Kneller J, Leon LJ & Nattel S (2005). Substrate size as a determinant of fibrillatory activity maintenance in a mathematical model of canine atrium. *Am J Physiol-Heart Circ Physiol* **289,** H1002–H1012.